Bioactive Self-Assembled Protein Nanosheets for Stem Cell-Based Biotechnologies

Hassan Kanso

2019-2024

Submitted in partial fulfilment of the requirements of the Degree of Doctor of Philosophy.

Statement of originality for inclusion in research degree theses:

I, Hassan Kanso, confirm that the research included within this thesis is my own work or that where it has been carried out in collaboration with, or supported by others, that this is duly acknowledged below, and my contribution indicated. Previously published material is also acknowledged below.

I attest that I have exercised reasonable care to ensure that the work is original and does not to the best of my knowledge break any UK law, infringe any third party's copyright or other Intellectual Property Right, or contain any confidential material.

I accept that Queen Mary University of London has the right to use plagiarism detection software to check the electronic version of the thesis.

I confirm that this thesis has not been previously submitted for the award of a degree by this or any other university.

Signature: Hassan Kanso

Date: 23/01/2024

Details of collaboration and publications:

Acknowledgments:

Completing my doctoral journey in the Gautrot Lab has been an unforgettable experience, enriched by the support of my fellow colleagues in the lab. This endeavour was made possible by the dedicated pursuit of knowledge and tireless support by Julien Gautrot to help guide my research. I am forever grateful for your trust, guidance and wisdom you have provided to me on this path.

My gratitude extends to Minerva, Stefania, Will, Elijah, Alexandra and the rest of the Gautrot lab for the endless support I have received for my experiments and the positive impact on my mental health. I wish to express my appreciation for Dr. Ruth Rose for sacrificing her time to aid in my research and mentoring me throughout my experimentation with recombinant technology, I am eternally grateful to have met someone as kind as you.

Thank you to Dr. Roberto Buccafusca for his help with Mass spectroscopy measurements. Giulia Mastroianni for her help with TEM trainings and support. Michaela Egertová for her help with Cryostat training and support.

I thank my parents for the boundless encouragement and motivation they provided me through these four years, and their belief in me gave me the strength to push forward and persevere.

I wish to convey my gratitude towards the reviewers who took the time to help in improving my work and moulding it to reach its final form.

This thesis is not just a product of my own undertaking but a collaborative effort of the scientific community and my professor Julien Gautrot.

Abstract:

Tissue and stem cell culture methods have been dominated by glass and plastic substrates such as Tissue culture plastic. These solid substrates, although widely used, are associated with poor scalability for adherent stem cell expansion in systems such as 3D bioreactors and the design of parallel culture systems. Therefore, investigating strategies to bypass these obstacles in stem cell expansion is essential to enable the wider translation of stem cell technologies. An alternative strategy recently proposed consists in using a liquid surface instead, such as an oil, and associated oil droplets.

Indeed, emulsions can be formed using protein nanosheets to stabilise oil/water interfaces to promote the adhesion of stem cells and enable their proliferation. These nanosheets exhibit enhanced interfacial mechanics and allow the introduction of bioactive components via recombinant protein expression to promote bioactivity. Beyond the application of resulting bioemulsions for the expansion of Mesenchymal stem cells, the impact of these bioactive interfaces on the differentiation of iPSCs and the development of cerebral organoids will be presented.

The Bovine serum albumin protein was recombinantly modified to attach an N-terminal Avi-Tag, this was expressed and purified from the yeast *P. pastoris* expression system. The Avi-tag was then biotinylated *in vitro* by recombinantly expressed BirA. Emulsions of a specific size were formed using the newly biotinylated Bt-BSA protein and functionalized with a cascade of components to mimic cell-cell ligands, this resulted in bioemulsions with a bioactive surface that can interact with surrounding cells. These functionalised droplets were integrated into developing cerebral organoids and their impact on phenotype was studied. The droplets were

found not to deform sufficiently to allow mechanical forces to be measured, yet the many of these droplets were retained within the organoids which led to an interesting phenotype within the organoids. The developing rosettes were found to develop enlarged lumens shown by an increase in area, this phenotype did not impact the differentiation into the cerebral lineage depicted by immunohistochemistry of hallmark marker of neuronal differentiation within organoids retaining droplets.

The interfacial mechanics of fibrinogen nanosheets treated with varying concentrations of thrombin was studied using interfacial shear rheology. The effect of thrombin significantly altered the interfacial mechanics with the lower concentration of thrombin significantly increasing the toughness multiple folds and decreasing the elasticity of the nanosheets. Additionally, the nanostructure of nanosheets was studied using SEM and TEM and traditional fibrin fibres were found to not form at these interfaces, but local rearrangements and retractions in the thrombin treated nanosheets were observed. Finally, these enhanced mechanical properties promoted the proliferation and expansion of Mesenchymal stem cells on quasi-2D and 3D interfaces.

Contents

Abbreviations:

2-dimensional (2D)
3-dimensional (3D)
488-tagged Streptavidin (f-strep)
4′,6-diamidino-2-phenylindole (DAPI)
Alcohol Oxidase Enzyme (AOX)
Arginylglycylaspartic Acid (RGD)
Atomic Force Microscopy (AFM)
Biotin Ligase - *E. coli* (BirA)
Bovine Serum Albumin (BSA)
β-tubulin (tuj1)
Calcium (Ca2+)
Outer Radial Glia Cells (oRGs)
Canine Serum Albumin (CSA)
Central Nervous System (CNS)
Chinese Hamster Ovary (CHO)
Circular Dichroism (CD)
Cortical Plate (CP)
Deoxyribonucleic Acid (DNA)
Discovery Hybrid Rheometer (DHR-3)
Droplet-based Sensors (DS)
Du Noüy Ring (DDR)
Dulbecco's Phosphate Buffered Saline (dPBS)
E-cadherin (E-cad)
Embryoid Body (EB)
Embryonic Stem Cells (ESCs)
Endoplasmic Reticulum (ER)
Engelbreth-holm-swarm (EHS)
Equine Serum Albumin (ESA)
Escherichia coli (*E. coli*)
Extracellular Matrix (ECM)
Fluorescein Isothiocyanate (FITC)
Fourier-transform Infrared (FTIR)
Forkhead-box G1 (FOXG1)
Glutathione-s-transferase Tagged (GST-x)
Green Fluorescent Protein (GFP)
Guanine/Cytosine (GC)
Horse Radish Peroxidase (HRP)
Human Keratinocytes (hPK)
Human Mesenchymal Stem Cells (hMSCs)
Human Serum Albumin (HSA)
Imaging Ellipsometry (IE)
Immunoglobulin (igG)
Induced Pluripotent Stem Cells (iPSCs)
Inner Subventricular Zone (ISVZ)
Integrated μ-fluidic Cartridge (IFC)
Intermediate Progenitors (IP)

International Society for Cellular Therapy (ISCT)
Isopropyl ß-D-1-thiogalactopyranoside (IPTG)
Leporine Serum Albumin (LSA)
Maltose Binding Protein Tagged (MBP-x)
Maltose-binding Protein (MBP)
Methanol Utilisation Slow (Mut^{s})
Methanol Utilising Minus (Mut^{-})
Methanol Utilising Plus (Mut^{+})
Minimal Dextrose (MD)
Molecular Dynamics (MD)
N-cadherin (N-Cad)
Neuroepithelial (NE)
Optimal Cutting Temperature (OCT)
Outer Subventricular Zone (OSVZ)
Paired Box 6 (PAX6)
Pentafluorobenzyl Chloride (PFBC)
Phosphate Buffered Saline (PBS)
Pichia pastoris (*P. pastoris*)
Plasma HSA (pHSA)
Pluripotent Stem Cell (PSC)
Poly (dimethyl Siloxane) (PDMS)
Poly(l-lysine) (PLL)
Poly(l-lysine)-graft-polyethylene Glycol (PLL-g-peg)
Polymerase Chain Reaction (PCR)
Post Translational Modifications (PTM)
Proteinase B (prb1)
Proteinase a (pep4)
Quartz Crystal Microbalance with Dissipation (QCM-d)
Radial Glia (RG)
Recombinant BSA (rBSA)
Recombinant Human Serum Albumin (rHSA)
Ribonucleic Acid (RNA)
Rock Inhibitor (Y-27632)
Room Temperature (RT)
Scanning Electron Microscopy (SEM)
Serum-free Floating Culture of Embryoid Body-like Aggregates (SFEBQ)
Sodium Dodecyl Sulphate (SDS)
Spectroscopic Ellipsometry (SE)
SRY-box 2 (SOX2)
Subventricular Zone (SVZ)
Sumo Tagged (S3C-x)
Surface Plasmon Resonance (SPR)
Tissue Culture Plastic (TCP)
Tobacco Etch Virus (TEV)
Transmission Electron Microscopy (TEM)
Ultra-low Attachment (ULA)
Ventricular Zone (VZ)
Yes-associated Protein (YAP)
Zonula Occludens-1 (ZO-1)

List of Figures and Tables:

Figures:

Tables:

1. Introduction

1.1. Recombinant protein technologies:

1.1.1 Albumins and Human Serum Albumin

Proteins have been used as scaffolding for cell attachment in fluid-fluid systems and we are beginning to appreciate that these adsorbed proteins have potential to engineer bioactive materials[1]. However, introducing this bioactivity to materials and controlling the correct presentation of functionality are challenges that still need to be addressed[2].

Albumins are globular proteins that are known to be found in blood plasma, egg whites, milks and plants[3–6]. Serum albumins are the most abundant proteins in the vertebrate plasma (roughly 60% in healthy humans [7,8]) with the human variant Human serum albumin (HSA) composed of 585 amino acids and carries a molecular weight of 66.5 kDa[9]. The protein is primarily synthesised in the liver by hepatocytes as the precursor pre-pro-albumin[10], the pre sequence aids the transportation to the endoplasmic reticulum where the pre sequence is cleaved into pro-albumin[11]. Before secretion out of hepatocytes the pro sequence is cleaved at the Golgi apparatus by Furin [11]; the final mature sequence is composed of the 585 amino acid sequence previously mentioned.

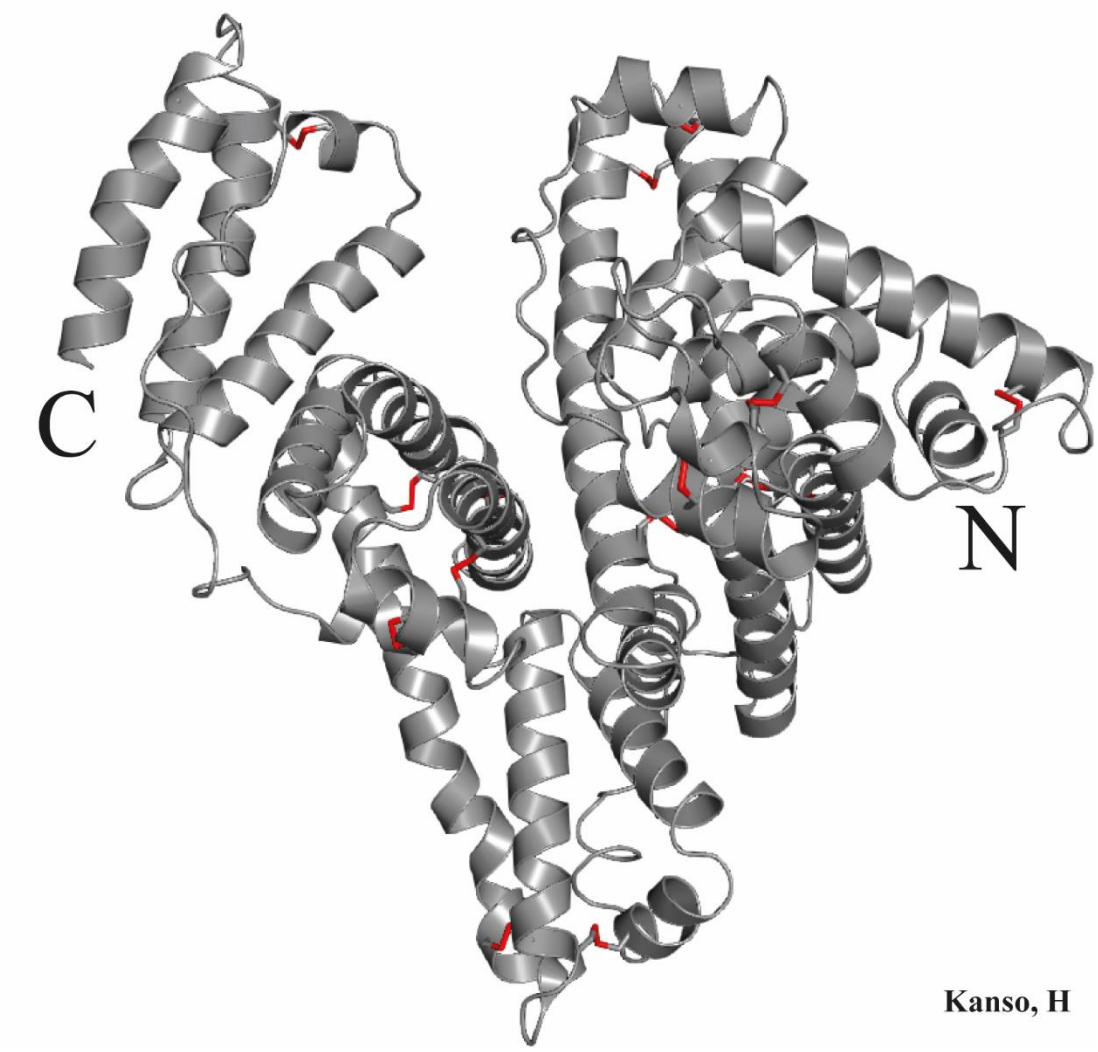

Figure 1: Pymol generated image of the crystal structure of globular Human serum albumin protein (PDB: 1AO6). The secondary structure depicts the heart-shaped structure, in grey the backbone of the protein and highlighted in red the disulphide bonds (rendered as sticks).

The globular HSA protein (Figure 1) forms a monomeric heart-shaped tertiary structure stabilised by 17 disulphide bonds and is primarily composed of three homologous domains: I (1–195), II (196–383), and III (384–585) [7,12,13]; each domain also consists of two subdomains A and B[14]. Additionally, it is primarily composed of 67% α-helices, 10% beta turns and 23% random coils with no β-sheets[15]. Additionally, there are 35 cysteines with 34 of them forming 17 disulphide bonds that form between the different domains mainly between α-helices are essential for the stability and

rigidity of the protein [16]. Interestingly, HSA is known to not possess any intracellular post-translational glycosylation, however it is at times glycated during the blood circulation of diabetic subjects [7,17]; the protein is also known to undergo phosphorylation by extracellular kinases[18].

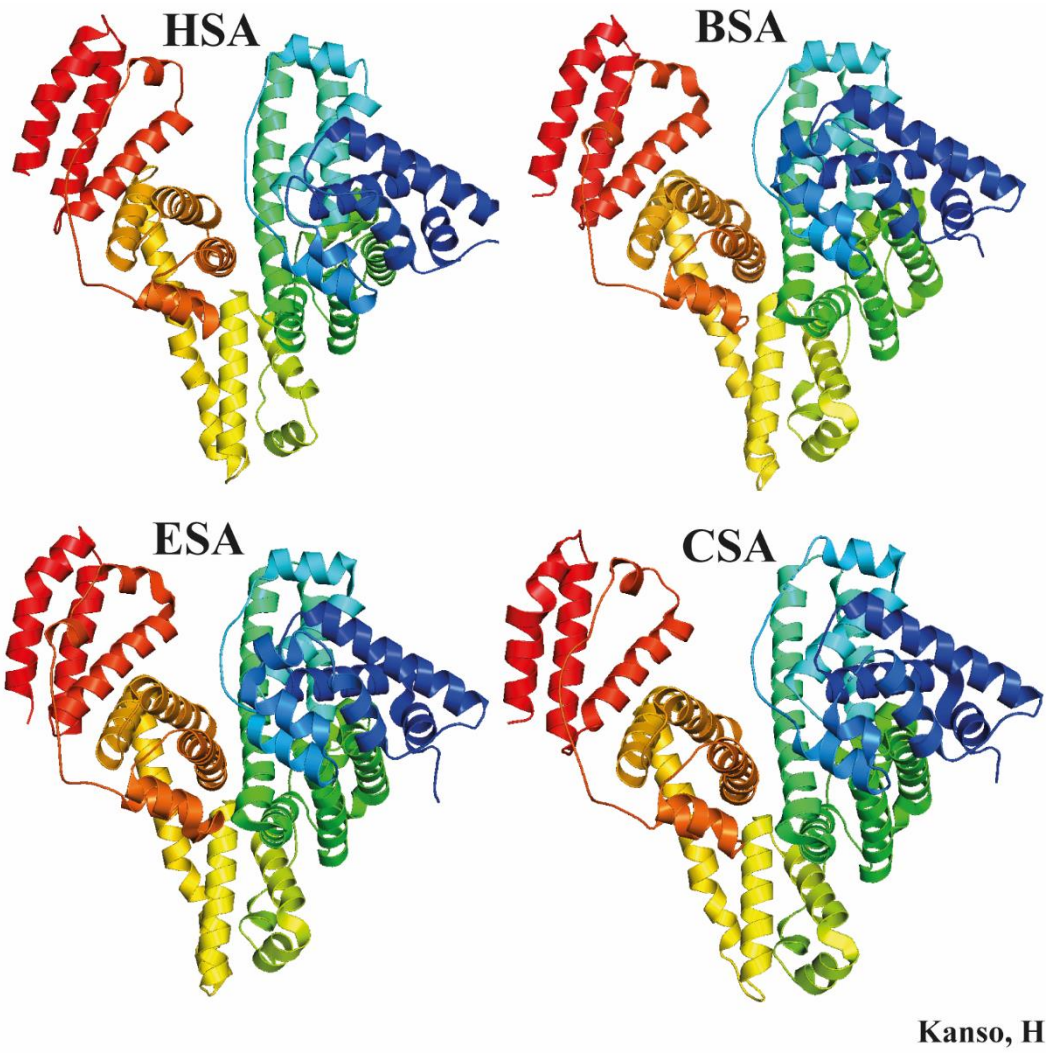

Figure 2: Pymol reprasentation of the crystal structures of different albumin proteins HSA (1AO6), BSA (3V03), ESA (4F5U) and CSA (5GHK), rendered using the elemental carbon spectrum. The figure shows the overall similarity and conservation of the structure of the albumin protein between different species.

Furthermore, there is a significant degree of similarity existing between the sequences and structures of HSA and its counterparts (Figure 2) derived from bovine (BSA),

equine (ESA), leporine (LSA) and canine (CSA)[19–21]. The structural similarity and the 76% sequence identity between HSA and BSA[22] are the primary reasons why HSA can be substituted with BSA for cell culture practices and other biotechnological applications[23].

Albumin proteins such as HSA have been demonstrated to play essential roles in regulating pH and blood pressure[24,25] and functions as a carrier for endogenous compounds such as: steroids, fatty acids, thyroid hormones, metabolites, metal ions and exogenous compounds such as drugs [26–31]. These functions open avenues for HSA to become a target for clinical and biotechnological studies[9]. Some studies have used HSA as a carrier of oxygen [32], a nanocarrier of drugs [33] and to extend the half-life of other proteins[34].

1.1.2. Recombinant protein expression

In the past the classic fractionation of HSA from human plasma was practiced to commercially produce the protein, however the supply of human plasma is always limited and the variations between batches lead to unreliability and a decrease in quality of the final protein[35]. Furthermore, risk of contamination with blood borne infectious pathogens such as HIV and hepatitis is always an issue for commercial use [36,37]. Therefore, finding alternative techniques that prevent these risks are valuable.

Recombinant DNA technology first came to fruition in the 1960s with the discovery of restriction enzymes by Werner Arber[38], and was further advanced in 1972 by the collaborative work completed by Stanley Cohen and Herbert Boyer [39]. Utilising this concept, scientists take advantage of this technique to produce a diverse range of proteins that are modified at the DNA level[40]. These newly synthesised proteins

contain amino acids that are modified by the insertion or deletion of genes or segments that can vary from a single amino acid, to as large as full protein domains [40].

The modularity of adding and removing domains can introduce additional functionality to proteins [40]; the simplest of functionalities can be in the form of a short amino acid segment known as a Tag, that is introduced onto a specific site of a protein (usually the terminus), the most common being the Hexa-Histidine-Tag which introduces the ability of protein purification via immobilised metal ion affinity chromatography (IMAC), specifically Nickel (Ni^{2+}) ions [41].

The scalability of recombinant expression makes this a very attractive technique to produce large amounts of modified highly sought-after proteins that can be cheaply mass produced in the cost-effective expression systems at yields suitable for commercial use, this has significant implications for the biotechnological and pharmaceutical industry[42]. Additionally, the translation machinery used to produce these proteins have been labelled as high-fidelity systems (ability to highly produce proteins with minimal variations)[40], hence the variation in the final amino acid sequence is almost not present. On the other hand, natural proteins and polymers that are harvested from nature can commonly accommodate slight variations between batches due to mutations occurring within the host; hence it can be appreciated that recombinant technology can ensure tight control over material properties[40].

Moreover, recombinant proteins have been increasing in popularity for utilisation outside of the biochemical, biological and biotherapeutics fields, and are being integrated into other disciplines such as material sciences and medical engineering[43,44].

1.1.3. Recombinant expression of Human Serum Albumin in Prokaryotic systems

In the past various expression systems have been used to recombinantly express recombinant human serum albumin (rHSA) including, eukaryotic organisms such as yeast [45–50], transgenic plants [51–55] and transgenic animals [56]. So far, the only system that has been able to produce rHSA that is as safe as plasma HSA (pHSA) and approved for therapeutic applications is the yeast *Pichia pastoris* (*P. pastoris*) expression system [57]. However, the industrial production of rHSA at a large-scale need to fit specific minimum requirements such as, a large market volume of several grams per litre, no adverse side effects caused by impurities [16] and low production cost, of which is still challenging for the field of recombinant expression [58].

Efforts have been directed towards the expression of rHSA in the most common expression system, the prokaryotic system such as *Escherichia coli* (*E. coli*), this is due to the fact that prokaryotic expression systems lack the machinery to post-translationally modify rHSA[59]; this is potentially useful as the native form lacks glycosylated post translational modifications (PTM)[7,17]. A cDNA encoding the HSA gene has been inserted into the *E. coli* expression cassette and produced functional rHSA at final yield of 2.5 g/L, however the system was known to suffer from the expression of the protein into the insoluble inclusion body form (nonfunctional), this is caused by the lack of proper folding and aggregation in the cytoplasm [60,61]. To solve this problem, scientists utilise *in vitro* purification steps such as denaturation of the protein followed by a refolding process to potentially obtain the active form of the protein; however, this does not always work for all proteins [62,63].

Scientists have still tried to push the method further successfully engineering *E. coli* strains that co-express chaperones and foldases to aid in cytoplasmic folding, this promotes the correct folding of disulphide-rich recombinant proteins[61]. Additionally, studied have attempted to optimise expression conditions such as induction temperatures and terminal fusion of varying solubility tags to increase solubility to push the protein into the soluble cytoplasm [64,65].

A study by Nguyen et al demonstrated that fusion of rHSA with the maltose-binding protein (MBP) tag significantly improved the cytoplasmic expression and solubility of rHSA; with 9.46 mg or rHSA purified from a 500ml Origami 2 *E. coli* culture [66]. They varied the induction temperatures and found that utilising a lower expression temperature of 18°C significantly improve solubility of rHSA compared to the standard 37°C [66]. The rHSA protein was purified and denatured with 6M guanidine-HCl, then refolded to obtain the active form [66]. The utilisation of the Origami 2 strain promoted an oxidative cytoplasmic environment due to mutations in the thioredoxin reductase and glutathione reductase genes; this promoted the formation of correct disulphide bonds between the free cysteines [64]. Additionally, insertion of a Tobacco Etch Virus (TEV) recognition site allowed the removal of the MBP tag by TEV proteases to obtain the 66.7 kDa rHSA protein [66]; this is important for downstream therapeutic application to prevent unwanted immune responses [66]. To verify the removal of the MBP-tag, the protein can be mixed with amylose resin to observe whether the newly untagged protein complementary binds to the resin or flows through without any interactions.

1.1.4. Recombinant expression in Eukaryotic systems

The production of pharmaceutical proteins such as those used for vaccines and antibodies is dominated by animal expression systems such as Chinese hamster ovary (CHO) cells[67], this is due to their high-quality protein production that have identical biochemical features compared to the human variants; these include their tertiary structures, biological activity, solubility and PTMs [68]. However, these systems lack the ability for high expression yields that suit the high dosage clinical applications and market demand [68]; this is due to their slow growth and expensive media compositions[69].

1.1.5. The *P. pastoris* recombinant expression system

The *P. pastoris* system has started to draw more attention in recent times due to its simplicity of genetic manipulation, high cell density, cheap medium compositions, high scale-up potentials and expression yields[70]. Since it is a eukaryotic system, it also carries advantages such as compatible protein folding and PTMs of human-derived proteins and the ability to secrete the expressed protein into the medium; this reduces the necessary steps of purification increasing the potential yield [70]. The system has the ability to perform PTMs such as O- and N-linked glycosylation (within the endoplasmic reticulum or Golgi apparatus) and disulphide bond formations within the cytoplasm, this is very attractive for the production of mammalian proteins, as some require the attachment of carbohydrates through glycosylation to the backbone of the protein, promoting correct folding, stability, activity and solubility[71]. However, the

system does possess disadvantages, the first being the requirement of large amounts of plasmid for the transformation steps, paired with the lower transformation efficiency per µg of DNA (~10^3–10^4) when compared to E. coli (~10^8–10^{11})[72]. Additionally, due to the nature of preparations and growth conditions there is a high occurrence of contamination with fungi and bacteria observed during the transformation and expression steps[73]. There are also potential risks of the secreted protein being hydrolysed by native secreted proteases[74]. However, this is currently solved in more novel *P. pastoris* strains that lack such proteases by the disruption of proteinase A (pep4) and proteinase B (prb1), strains include: SMD1163, SMD1165 and *Pichia pink*[75].

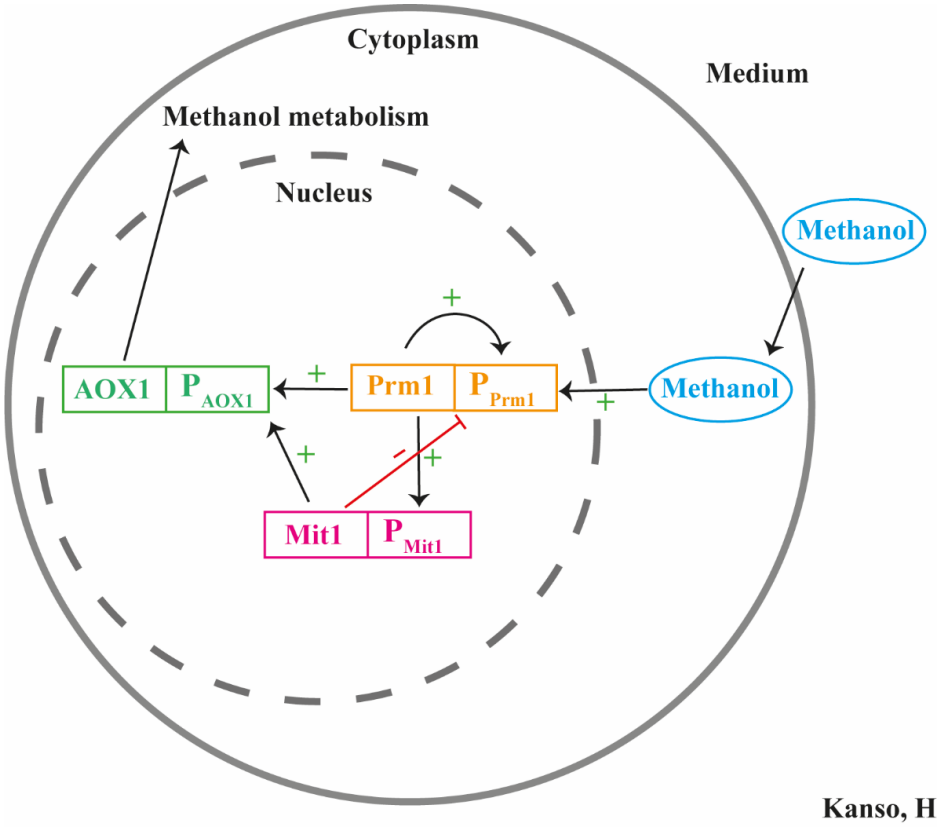

Figure 3: Methanol utilisation pathway in *P. pastoris* using the AOX1 promoter. Prm1 expression is induced when methanol is the sole carbon source, Prm1 can self induce its promoter and induces both the AOX1 and Mit1 promoter. The Mit1 promoter transribes the Mit1 protein which also strongly induces the AOX1 promoter. Figure reproduced from Wang et al [76].

The *P. pastoris* GS115 strain encodes two genes for the alcohol oxidase enzyme (AOX) AOX1 and AOX2, in the presence of methanol these genes are transcribed and produce the AOX enzyme [77]; the AOX1 gene has been demonstrated to exhibit a stronger response to methanol and produces more AOX enzyme[78]. An AOX1 knockout will produce the methanol utilisation slow (Mut^s) phenotype as the slow AOX2 gene is used instead, this leads to a slower growth on methanol plates or in methanol containing media[78]. If the AOX2 gene is knocked out the methanol utilising plus (Mut^+) phenotype is observed, this does not affect the growth rate on methanol as the AOX1 gene is still activated [78]. It has been reported that the AOX2 activity is roughly 10% compared to the 90% activity utilised by the AOX1 promoter [79]. However, the knockout of both AOX1 and AOX2 genes will lead to the methanol utilising minus (Mut^-) phenotype preventing the growth on methanol [78]. Utilising these different phenotypes can be beneficial for the production of different recombinant proteins that may require slower or faster expression conditions for correct folding[80]. The *P. pastoris* system has the ability to utilise methanol as its sole carbon source for metabolism, the induction pathway for AOX1 expression is regulated by the activation of the Prm1 promoter through methanol binding, this has the ability to self-activate itself and activates the Mit1 promoter [76]. Both Mit1 and Prm1 (Figure 3) strongly activate the AOX1 promoter which leads to the expression of alcohol oxidase 1, AOX1 acts an alternative pathway to the cytochrome pathway of the electron transport chain by transferring electrons directly from ubiquinol to oxygen, this bypasses the standard proton gradient pathway used to generate ATP [76].

1.1.6. Recombinant expression of Human serum albumin in *P. pastoris*

Kobayashi et al has demonstrated a methanol feeding strategy that achieved a 7g/L rHSA yield, increasing the yield to 11g/L by adding a 4x fed-batch fermentation strategy [81,82]. Mallem et al established that controlling the growth rate and induction cell density can help optimise the yield of protein production [83]. Furthermore, a study by Mallem et al utilised the Mut^{s} phenotype of *P. pastoris* to express rHSA at a high level of 10g/L indicating that the slow production of rHSA can benefit the expression of the protein. However, the studies mentioned had lengthy induction times reaching over 250 hours, which paired with methanol can be of potential hazard for the scale up industry [70]. On the other hand, Zhu et al improved these systems and established a protocol for secreted rHSA expression in *P. pastoris* that yielded 8.86 g/L in only 96 hours of methanol induction [84].

The composition of growth and induction medias used for *P. pastoris* are now well established [85]. Studies have continuously attempted to optimise the growth and induction media compositions to improve the final yield of rHSA. The most common carbon sources used by *P. pastoris* for growth are glycerol and glucose, these are found to be superior over other carbon sources such as sorbitol and sucrose, leading to a significant increase in cell biomass and densities[70]. A study by Zhu et al, investigated the effect of the supplementing different amino acids into the induction medium based on the residues with the highest frequency in the sequence of HSA [84]. The addition of amino acids such as: Alanine, Histidine, Glycine, Glutamate, Leucine and Lysine at

1g/L increased the rHSA yield by 20%. Additionally, the combination of 0.5% Casamino acid and 10mM ascorbic acid further increased the yield by 10% [84].

Additionally, it is well documented that *P. pastoris* has the ability to tolerate high concentrations of methanol at 28ºC, with studies going up to 5% (v/v) methanol [86]. However, it was demonstrated that 2% is the optimal concentration of methanol before cell viability becomes an issue [84]. Furthermore, the induction temperature was also found to play an essential role in the cell biomass, viability and expression yield [84]. Although a higher temperature promoted an increase in cell biomass the optimal temperature for the expression of rHSA was 28ºC; with higher temperatures increases the damaging effects of methanol and promotes the release of proteases from the dead cells [84]. Moreover, studies are consistently finding that the increase in temperature further increases the degradation products generated in the induction phase, hence it is generally accepted that lower temperatures are more optimal for protein expression in *P. pastoris* cultures [87–89].

1.2. Organoids:

1.2.1. Derivation of organoids

Since the 1960s, the term 'Organoid' has been used to describe all 3-dimensional (3D) organotypic cultures [90], and defined as mini-clusters of cells that grow in an *in vitro* 3D environment that self-organise and differentiate into functional cell types closely resembling the structure and functions of an organ; hence termed "Mini-organs" [91]. Organoids are defined by three attributes: self-organisation, multicellularity and functionality [92]. The organoid must contain more than one cell type from the resembling organ that it models, they should demonstrate specific functions that are characteristic of the target organ and partially mirror the arrangement and organisation of cells [93]. Additionally, a study takes the definition a step further by adding the development of several cell types from stem cell progenitors that self-organise through cell sorting and lineage commitments [93].

Recent advancements in stem cell technologies have facilitated the progression of human pluripotent stem cell (PSC)-based 3D cultures [94] and enhanced our ability to investigate human development [95]. These organoid technologies are built from the foundations of developmental biology and cell co-culture experiments and represent a vital link that bridges traditional 2D cultures and *in vivo* human models [93]. Furthermore, organoid protocols have already been successfully developed for numerous organ systems such as: retina[96], intestine[97], thyroid[98], liver[99], pituitary[100], inner ear[101], kidney[102–104] and brain[105]. These *in vitro* systems have evolved from another similar *in vitro* system called the Embryoid body (EB) [93]. EBs are 3D aggregates of PSCs[106] that closely resemble the development of an early pre-

gastrulating embryo [107]. Additionally, they also parallel the differentiation of teratomas to form various organised tissues [93]. However, not all organoid protocols utilise the EB stage [93]. Yet, organoids can be derived from various sources: primary tissues, embryonic stem cells (ESCs) and induced pluripotent stem cells (iPSCs)[90].

1.2.2. Applications of organoid technologies

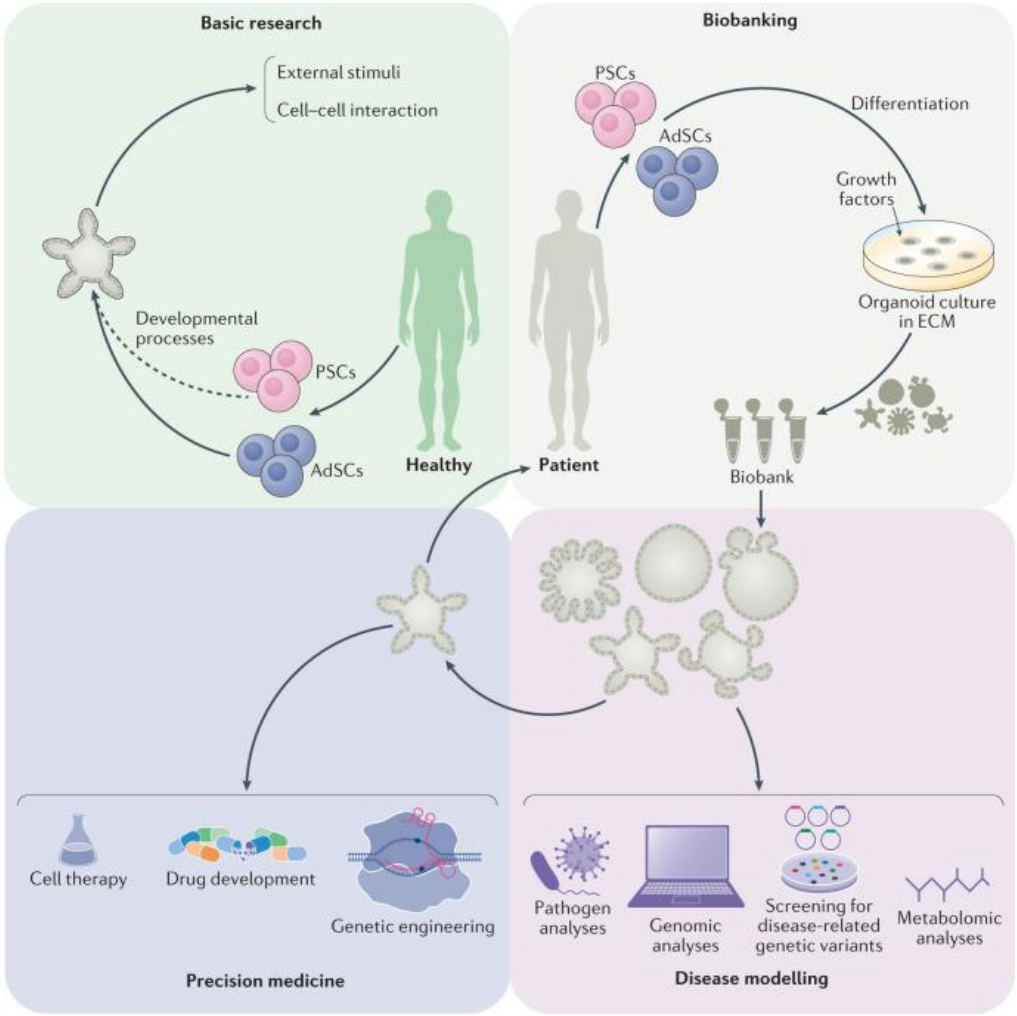

Figure 4: Schematic summarising the applications of organoid technologies in the academic and industrial settings. Figure obtained from Kim et al[95].

Advantages of using organoids include the ability to indefinitely expand, cryopreserve in biobanks and easily manipulate genetic makeup [93]. Furthermore, to bypass the

scarcity of primary human material, the utilisation of patient-derived human ESCs and iPSCs can help bypass this issue [93].

These self-organising tissues have multiple potential applications in drug discovery, disease research and regenerative medicine [108,109]. A major advantage of this system is the capacity to culture both tissue specific stem cells and their differentiated counterparts with a limited amount of starting material; this introduces a potential for patient specific disease modelling and screening [93]. However, the lack of surrounding vasculature and Extracellular matrix (ECM) niche microenvironments limits the growth potential of organoids, this creates a reliance on specific nutrients and growth factors to pattern the cells[110].

Studying tissue development and disease. Organoid systems facilitate the study of processes that govern embryonic development, stem cell lineage differentiation and the onset of diseases. Furthermore, the ESCs, iPSCs and fetal tissues preserve their characteristics that are inherent to their original development [93]. Some studies have deployed the CRISPR/Cas9 gene editing system to introduce mutations into healthy human colon organoids, promoting the growth of cancerous organoids which could be used to study the mechanism of cancer development and formation [111–113]. Additionally, some diseases found in humans have been difficult to study in animals due to their complexities such as those that effect the human brain [93]. Patient-derived iPSCs from patients suffering of neuronal diseases were differentiated into the neural organoids and used to model these pathologies *in vitro* [105].

Organoids application in therapeutics and drug development. Patient derived organoids provide a promising resource to develop technologies for personalised treatments. The cells would be taken from the disease carrying biopsy and would

supply enough material to generate patient-derived organoids for phenotypic profiling and in-depth genetic sequencing [93]. Moreover, growing healthy organoids with their diseased counterparts enables clinical screens for drug combinations to selectively target the disease; this aids in the identification of more efficacious treatments whilst minimising potential side effects to the patient [93]. Similarly, the disease organoids can also be potentially used to predict drug resistance for upcoming drugs that target patient-specific diseases[93]. However, organoids do have a drawback that potentially hinders these technological advancements, which is they are often suffer from heterogeneity in viability, size and shape; hence can obscure drug efficacy and toxicity [93]. This variability between batches has raised doubts regarding the feasibility of replicating the human brain developmental process with a degree of reproducibility comparable to the endogenous tissue [114].

Organoids in the field of regenerative medicine. In modern times, medicine has the capability to replace damaged tissue through the process of allogenic transplantation. However, this is reliant on the scarce supply of healthy donor tissues with the problem associated with tissue rejection [93]. In recent times, there have been cases of successful transplantation of patient derived organoids engrafted into the colon, pancreas and liver [99,115–120]; this technology aids to bypass the highlighted problem with rejection.

1.2.3. Germ layers and their resulting organoid

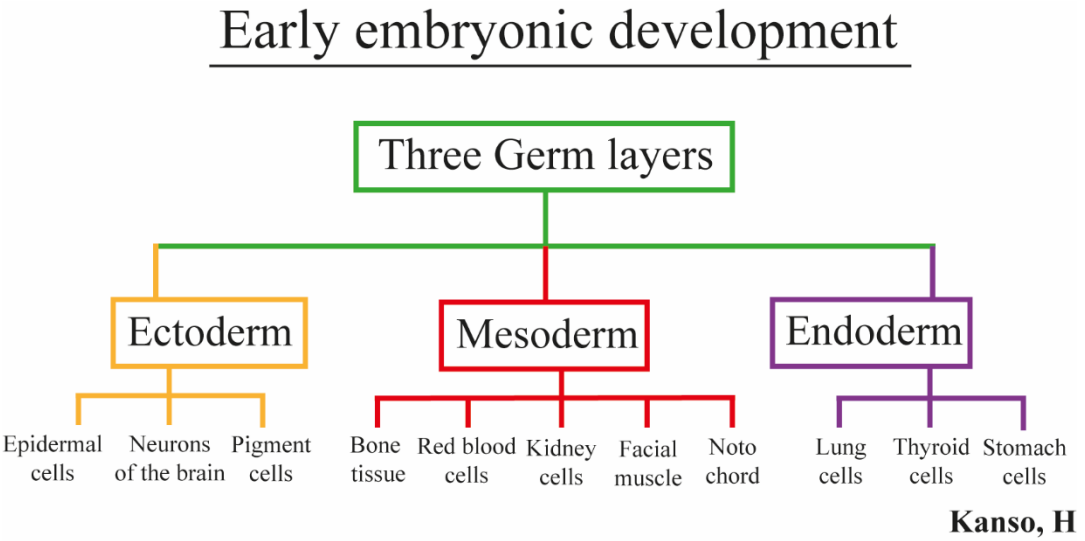

Figure 5: Schematic depicting the three germ layers that form during early embryonic development, the Ectoderm, Mesoderm and Endoderm consequently give rise to specific cells types. Figure reproduced from Nico Heins, Mikael C.O. Englund et al[121].

There are three germ layers (Figure 5) that form during early embryonic development, the endoderm, mesoderm and ectoderm; all of which have their own specific differentiation lineages. In recent times, protocols have been established to derive organoids from all three germ layers [122].

The endoderm layer is responsible for generating the epithelial linings of the digestive and respiratory tracts, and organs such as lung, liver, gall bladder, pancreas and urinary bladder [122]. The first endodermal organoids were intestinal organoids that were derived from adult stem cells (ASCs) [97]. Intestinal stem cells grow to form small cysts which then form buds that expand into 3D structures outwards into the surrounding matrix [97]. This method has been adapted to generate a variety of organoids such as stomach[123–125], pancreas[116,126,127], liver[117], prostate[128,129], oesophagus[130,131], gall bladder[132,133]and

taste buds[134]. Furthermore, endodermal organoids have been derived from human PSCs to mimic the small intestine[135], lung[136–138], liver[139], thyroid[140,141], stomach[142,143] and pancreatic[144] and bile duct tissues[145].

The mesoderm layer is responsible for generating the mesenchyme, haematopoietic system, muscles, cartilage, bone, kidneys, spleen, gonads and genital ducts[122].

The final layer is the ectoderm and this gives rise to all forms of neural tissues, including the central nervous system (CNS), sensory epithelia, pituitary gland, the epidermis and mammary glands [122]. Yoshiki sasai et al first developed a protocol where they seeded ESCs in non-adhesive plates with serum-free medium; the cells then aggregated to form an EB [146]. From these EBs they used specific growth factor mixes to generate organoids [122] that resembled the optic cup [96,147], cerebellum [148], hippocampus[149] and adenohypophysis [150].

Furthermore, Madeline Lancaster generated a neuroectoderm organoid from EBs that were embedded into Matrigel (a laminin rich ECM mimicking scaffold that provides structural support and growth factors); this promoted the outgrowth of neuroepithelial buds that developed into several types of brain regions [105]. From single cell analysis the cells generated in these brain organoids resembled the human foetal brain [151]. Additionally, the different brain regions can be generated from ESCs by manipulating growth factors such as Hedgehog, FGF, BMP, and Wnt [152–154].

Nevertheless, regardless of the germ layer identity it has been established that the Wnt signalling pathway is the core process for the maintenance of these organoids from ASCs and PSCs[122].

Utilising iPSC lines for organoid formation requires an extra step when compared to ESCs as they come from patient-derived somatic cells [155–157], these are converted into

iPSCs by the adjustment of gene expression; genes included are OCT4, KLF4, SOX2 and MYC [156]. The ESCs and iPSCs are then exposed to patterning growth factors specific to a germ layer lineage, followed by embedding into a scaffold matrix such as Matrigel; this directs the development of organoids into a 3D architecture[93].

1.2.4. Human neurodevelopment and cerebral organoids

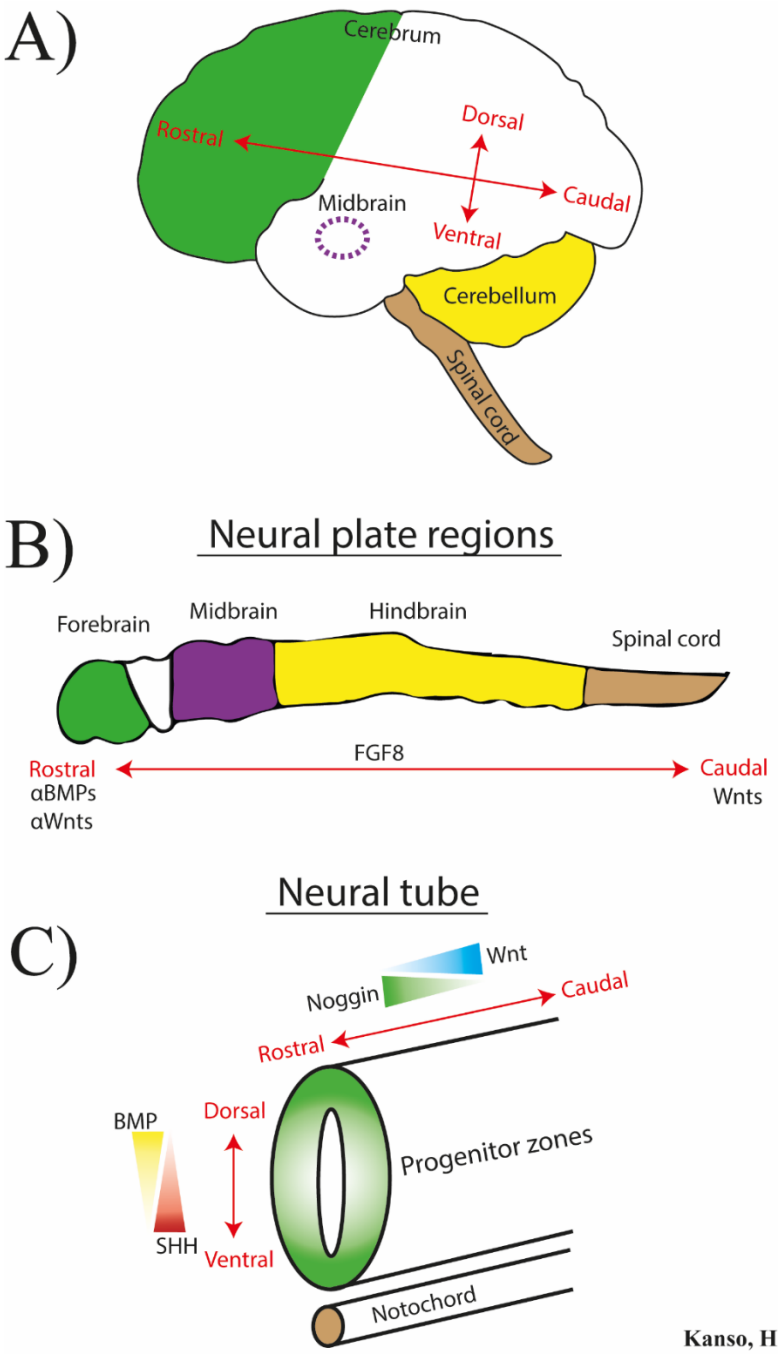

Figure 6: A) Summary of the human brain with its Dorsal-Ventral and Rostral-Caudal axes. B) Neural plate regions that form pre-neural tube closure, with the various morphogen gradients in the Rostral-Caudal axes. BMPS and WNT pathways are inhibited to form the Forebrain region. C) Summary of the morphogen gradients present post-neural tube closure. BMP-SHH gradients exist in the Dorsal-Ventral axis and Noggin-WNT gradients exist in the Rostral-Causal axis. Highlighted in Green = Forebrain region. Purple = Midbrain. Yellow = Hindbrain. Brown = spinal cord. Figure reproduced from Melanie V. Brady, Flora M. Vaccarino[158].

The development of the human nervous system and its underlying mechanisms that contribute to brain disorders, currently represent a very challenging pursuit within the field of neurobiology. A major contributor to this issue is the restricted access to healthy and diseased human brain tissues for functional studies[159,160]. In the past, research was very limited to animal modelling which does not necessarily translate directly to the development, architect and species-specific features of the human brain [161]. Hence, there is a demand for a model that reprises these features of human CNS development.

The human brain is part of the CNS that as mentioned previously is derived from the neuroectoderm during development [162]. This organ is highly complex and divided into three main regions: the forebrain, midbrain and hindbrain (Figure 6). All three of which are primarily composed of neurons and glia cells [91]. The neuroectoderm first forms a neural plate that is then patterned and shaped into a neural tube which is closed through folding and fusion [162]. *In vivo* the neural plate gives rise to radially arranged neuroepithelial cells that expand to shape various structures within the brain [110]; the epithelium generates an apical-basal polarity radially organised around a fluid filled lumen that forms the brain ventricles [93]. These axes are generated by morphogen gradients such as the Shh-Wnt/BMP axis (Figure 6) and influenced by factors including retinoic acid/FGF [163]. It is these axes that divides the neural tube into the four major regions of the CNS [93]. *In vitro* this process can be partially mimicked to spontaneously acquire radial organisation similar to the neuroepithelium; this occurs in the form of neural rosettes [110]. Additionally, the neural ectoderm that is derived from iPSC derived EBs spontaneously initiates apicobasal polarity to form neuroepithelial buds [110]. However, these *in vitro* models lack the *in vivo* basement membrane which leads to incorrect orientation and a discontinuous epithelium [164].

Recent breakthroughs [105,165–167] in human iPSCs technologies and 3D culture systems have paved the way for exploration of human cortical development [168]. Human cerebral organoids present a pioneering approach to investigate the molecular and cellular processes of this process [168]. Protocols have been successful in generating specific brain regions such as: midbrain organoids[169], hippocampal organoids[149] and cerebellar organoids[148].They exhibit complex structures that replicate a wide variety of aspects of neurogenesis, including the formation of an apical-basal axis, polarised neuroepithelia, the formation of layered cortex like features and maturation of synapses [170,171].

Protocols exist for generating 2D rosettes, and these replicate certain aspects of brain development such as: lineage progression [105,172] and neuronal specification [173]. Furthermore, they are less prone to producing heterogenous cultures which organoids do suffer from [174,175]. However, they lack the 3D complex organisation that is demonstrated by cerebral organoids, by the formation of continuous neuroepithelia and defined progenitor zones [110]. Lancaster et al has pioneered the generation of 3D cerebral organoids that contain these different brain regions within a single organoid [105]. However, these cerebral organoids were prone to hypoxia and generated necrotic cores due to the lack of diffusion of nutrients into the core [105]. To solve this problem the “mini-brains” were further matured and developed into the several brain regions by the transfer into a spinner-flask bioreactor (a small portable flask with a spinning module that allows intake of media and removal of waste) [91], this formed organoids that were several millimetres in size. Another study took this approach and cultured these organoids in a spinner-flask bioreactor (Figure 7), this enabled the extension of development without the requirement of intervention to treat hypoxia [176]. Interestingly, these brain organoids generated from both methods exhibited defined cortical layers,

proliferating progenitor zones and neurons that were capable of electrical excitation [96,105,177].

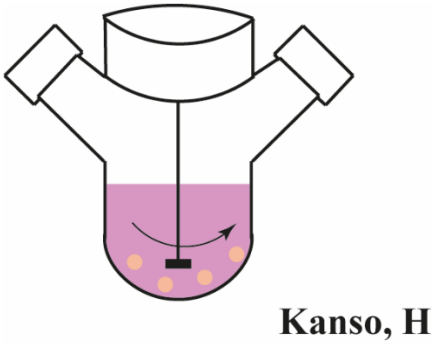

Figure 7: Example of a Spinner flask bioreactor used in the long term growth and development of organoids.

The process of organ self-assembly is theorised to follow the Steinberg differential adhesion hypothesis, this states that the cells segregate to form the most thermodynamically stable pattern, this pattern is thought to be composed of domains that comprise of cells that possess similar adhesive properties mediated by surface adhesion proteins such as Cadherins[178,179]. This results in less adhesive cells (that express a low amount of cadherins) sorting towards the periphery and enveloping highly adhesive cells that highly express cadherins within the centre of the cell aggregate; this hypothesis was found to be demonstrated in the vertebrate neural and epidermal ectoderm [180,181].

Classical cadherins are classed as transmembrane proteins that form intercellular bonds between their relevant extracellular domains on neighbouring cells [182]. The cytoplasmic Cadherin domain binds β-catenin, that binds α-catenin [182] which in turn binds to the actin cytoskeleton through activated vinculin or epithelial protein lost in neoplasm (EPLIN) [183–188]. These complexes are found in most metazoan cohesive tissues [189], and play a role in the transduction of mechanical forces that shapes cells, involved in regeneration and diseases [190]. Furthermore, changes in the actin

cytoskeleton are proposed to induce conformational changes in α-catenin which recruits vinculin to promote cell-cell contacts through cadherins [191].

1.2.5. Hippo Pathway – YAP/TAZ signalling in Neuroepithelial organoids

The acto-myosin contractile machinery plays crucial role in tissue development and functioning in muscle and non-muscle systems and cell types. It underpins the assembly of actomyosin bundles or stress fibres that contribute to important cell behaviours such as migration, epithelial junction formation and maturation, as well as polarisation [192–194]. This machinery is known to also regulate downstream signalling pathways such as the mechanosensitive pathways such as the SRF pathway[195] and the Hippo signalling pathway, which is crucial for determining cell fate in response to extracellular cues [196–199]. The Hippo pathway functions as a mediator of molecular signals detected through changes in the cytoskeleton, such as: cell polarity, adhesion, GPCR signalling, and mechanical forces [200]. Additionally, the pathway interacts with other developmental and regulatory signals such as Wnt, Notch, and TGF[200], conferring it key roles in development, homeostasis and regeneration [200].

The Yes-associated protein (YAP) involved in the Hippo pathway (The YAP/Hippo pathway can be referred to in Figure 59) responds to extracellular geometrical cues such as surface topographies and confinement [196–199], it has been demonstrated in human iPSCs that the active form of YAP is localised within the nuclei of cells and is translocated into the cytoplasm where it is inactivated [201]; this is also found to be the

case in Neuroepithelial (NE) organoids, with YAP cytoplasmic localisation occurring towards the end of NE organoid formation [201]. Furthermore, YAP was found to be essential in the maintenance of the apical-basal polarity of lumens during the NE cyst formation [201]. Studies utilising 2D substrates have also demonstrated that YAP activity can be manipulated by the tuning of its biophysical microenvironment, such as topography, geometry, and confinement [196,202–205]. Moreover, YAP has been shown to be an important requirement for early ectodermal specification, by inhibiting YAP transcriptional activity using verteporfin at early neural induction cell death was observed [206].

1.2.6. Bioengineering extracellular scaffolds for organoid technologies

Recently, scientists have begun to explore the effect of engineering physical extracellular cues to guide organoid cell-fate and organisation [207–210]. For example, the generation of artificial physical boundaries during cellular organisation by the addition of substrate geometries (a scaffold material with variations in its shape, surface roughness, size and composition) have been demonstrated to promote shape-guided organoid morphogenesis [208–210].

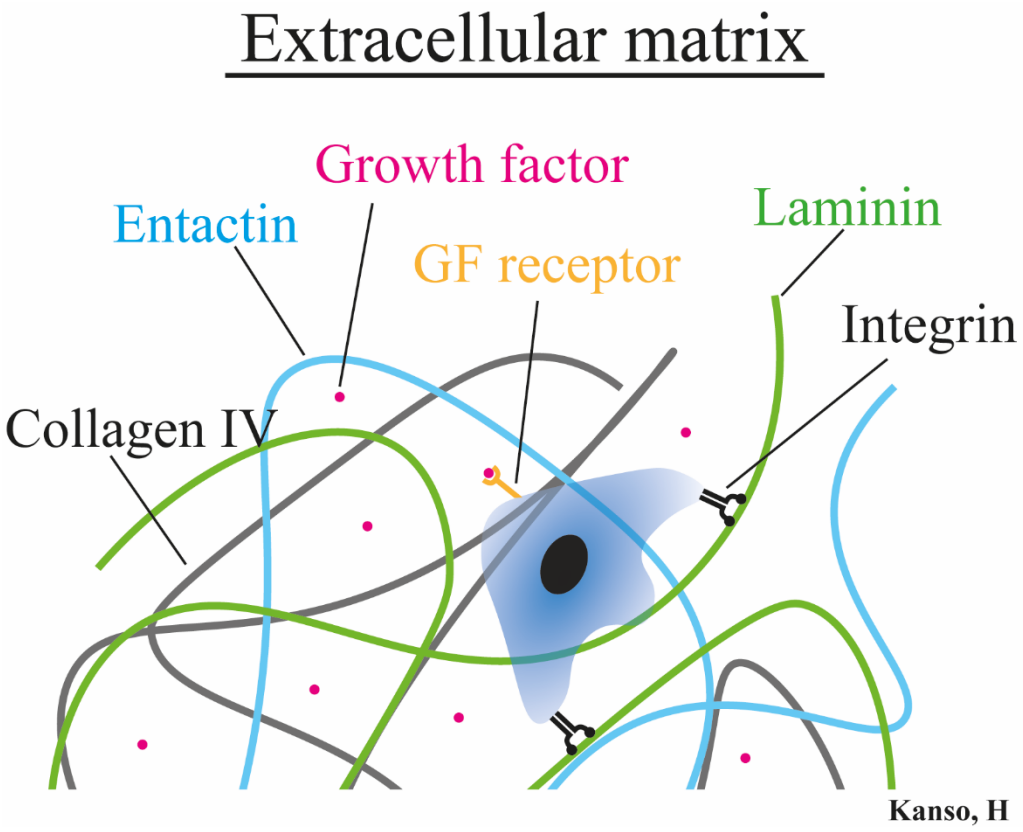

Figure 8: Summary of the extracellular matrix (Matrigel) and the various proteins that compose it: Growth factors, Laminin, Entactin and Collagen IV. Cells interact with this matrix using cell surface adhesion proteins such as integrins, and bind the growth factors via surface growth factor receptors.

Likewise biological or synthetic scaffolds have been used to mimic the characteristics of the natural ECM, with the most frequently used being Matrigel (Figure 8) – secreted from Engelbreth-Holm-Swarm (EHS) mouse sarcoma cells[211]. Matrigel provides structural support and growth factors to the embedded cells through adhesive proteins such as collagen, entactin, laminin and proteoglycans [211]; hence cerebral organoids take advantage of this laminin-rich environment to protrude and extend neuroepithelial buds outwards [105,212]. In addition, studies have confirmed the formation of intestinal 3D complex organised epithelia within ECM hydrogels [97]. Also, some scaffold free

techniques exist to culture cells by the hanging of droplets containing medium from a plate by gravity and surface tension [213].

However, complications arise when organoids become too large in size, restricting the oxygen diffusion and nutrient exchange into the core, thus agitation bioreactors have become a big player in organoid technology [214–216]. A study by Lancaster et al found that static cultures of organoids are limited by the stationary diffusion of oxygen, this led to the formation of necrotic cores [105]. Hence, they utilised spinning bioreactors optimised for cerebral organoids to increase the diffusion of nutrients into the core. Additionally, microfluidic technologies can be utilised to improve oxygen and nutrient exchange, maintain tissue health and homeostasis [168].

1.2.7. Mechanical forces, morphogenesis and organoid development

Over the years, mechanical forces such as cellular adhesion, cytoskeletal tension, cell migration, stretching and compression have been recognised to play an essential role in shaping embryonic structures, and their influence on this process have been well established [217–224]. Furthermore, these mechanical forces have been demonstrated to induce the expression of important developmental genes [225,226]. This is supported through various *in vitro* studies that found that cellular forces can also affect the direction of movement[227–229], orientation of the cell division axis [230–232] and differentiation [233–237] and the rate of proliferation [238–241]. In recent studies. It was also discovered that not only biochemical signalling but mechanical stress plays a role in

mechanical cues for tissue morphogenesis and homeostasis, for example the neural tube closure and extension in vertebrates [242]. However, the exact mechanism to which these forces influence cell behaviour *in vivo* is still relatively unknown [243].

Cellular forces have been quantified by the development of techniques that aided in measurements within cell culture systems [243]. Cells within tissues are affected by different tissue-associated forces such as hydrostatic pressure, shear stress, compression and tension [243]. Of those forces, only some have the ability to be measured using current techniques, for example, cellular tensions are measured using femtosecond-pulsed laser ablation (lasers directed at a target surface to remove material) of cell-cell junctions [244,245]. Whenever a cell movement is measured there is an underlying force that generates it [246]; these forces originate within the cell with cellular substructures contributing towards their generation [222,247–252]. It is generally accepted that forces generated within the cell are mainly caused by the acto-myosin contractility at the cell cortex and some through traction forces [248,249,253,254]. These forces are transmitted to adjacent cells in the tissue by adhesion mediated connections of the cytoskeleton or through connection to the ECM[255].

The ECM is also known to play a role in mechanical cues of tissue remodelling, and it is the composition and organisation that are important for acquiring tissue-specific mechanical properties [256–258]. Of the four major components of the ECM being laminin, nidogen, perlecan and collagen, some have been already established to play a role in mechanically maintaining tissue shape [257,258]. 2D substrates and 3D scaffolds with controlled stiffnesses have demonstrated that cell migration [259], cell differentiation [234,236] and tumour progression [260] all are dependent on the stiffness of the extracellular microenvironment.

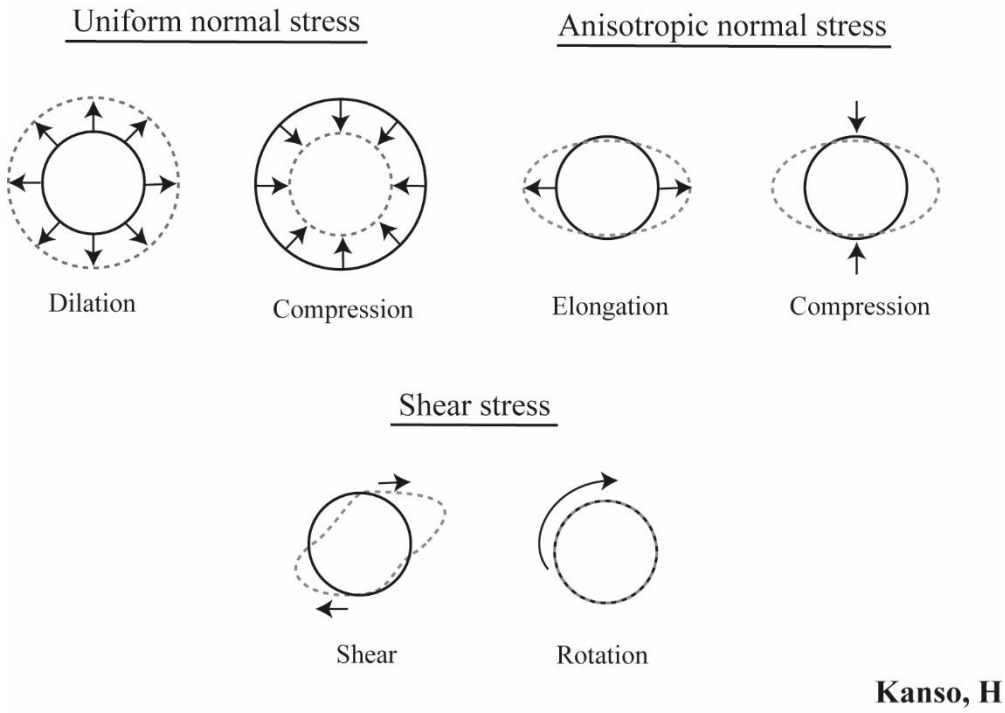

Figure 9: The different forms of stress that can be exerted onto a material. Normal stresses are made of either, uniform normal stress or Anisotropic normal stress. Shear stresses result in either shear (elongations) or rotation or a combination of both of the material. Figure reproduced from Campas et al [246].

Living tissues are exposed to spatial and temporal variations of mechanics, such as stresses (forces) and mechanical properties [246]. In tissues that have high cell densities the mechanics at the tissue scale can be described by continuum mechanics (an approach to study the response of materials to deformation, including normal and shear stresses)[219,261–265,246]. Normal stresses can lead to two outcomes: uniform normal stresses lead to dilation or compressions whereas anisotropic normal stresses lead to elongations and compressions in specific directions (Figure 9) [246]. On the contrary, shear stresses lead to shear (elongations) and rotations of the volume elements (Figure 9) [219,261,266]. This includes the visco-elasticity of the matrices involved, impacting the resistance to flow and resistance to mechanical deformation [246]. Lastly, to characterise the local relative deformation, the strain and strain rates applied can be measured to

quantify the local tissue deformations that occur from cell movements, rearrangements and changes in cell shape [219,220,261,263].

Morphogenic flows and tissue deformations observed during embryonic development have been shown to directly result from two mechanical factors: the spatial distribution of stresses generated by the cells and the mechanical properties of the tissue (elasticity or fluidity) [246]. If the tissue exhibits elastic properties, once a force is applied it will deform but return to the original configuration when the force is removed[246]. On the other hand, if the tissue is fluid, then the deformation will increase over time but the original configuration would be lost once the force is removed [246].

In vitro studies have concluded that cellular aggregates such as EBs behave similar to viscoelastic materials, that display both and elastic and a viscous response [267–271]. However, the timescale at which the force is applied is important. For example, if the force is applied over a short period of time (seconds) the cellular aggregates would follow an elastic response with the deformation. In contrast, application of forces over a longer period of time, would result in rearrangements and flowing of cells that deforms the tissue after the force is removed; interestingly the aggregate's surface tension partially restores its spherical shape over time[268–271].

1.2.8. Measuring mechanical forces in biology

Various techniques exist to measure mechanical properties of subcellular structures at the micron/second scales [272–277], these measurements are known to be different from the supracellular tissue level mechanical properties that control tissue organisation and morphogenesis [247,248,253,278]. Techniques such as atomic force microscopy [279,280],

micropipette aspiration [281,282] and magnetic cytometry [283] have been used to measure cell mechanics and adhesion forces. Additionally, to measure molecular tension in cell cultures, fluorescent resonance energy transfer-based molecular force sensors have been used [284,285]. Furthermore, to quantify traction forces generated by cell cultures *in vitro* experiments using soft gel substrates such as elastic micropillars [286,287], gel matrices[288,289] and traction force microscopy [227,290,291] have been applied.

To measure mechanical contact between cells and tissues, contact manipulation methods exist whereby a push or pull force is applied to the sample. This gives direct measurements of the applied forces. This method can only be used on samples that are accessible to a probe [292]. Examples of a pushing tools are microplates or indenters [293,294], these will output information about the mechanical properties such as stiffnesses, viscosity and stresses [292]. Pulling tools such as micromanipulators pull on a cell or tissue sample leading to a deformation caused by aspiration through an aperture; this provides information about the surface tension [295,296]. On the contrary, recording forces *in vivo* has proven very difficult and to date only laser ablation has been able to ablate cell-cell junctions in the living embryo [244]. However, laser ablation only provides qualitative information about the tension at cell junctions [244,297] and sections of tissues [245,298], and cannot provide quantitative measurements of cellular forces [243].

1.2.9. Droplet-based force sensors

Currently, the majority of measurement techniques have access to the mechanical forces and properties found at the surface of living tissues. However, other techniques such as droplet-based sensors (DS) have been developed to measure mechanical stresses generated within living embryonic tissues [243,299]. DS use biocompatible oil microdroplets that are coated with specific ligands promoting adhesion to cell receptors with a size similar to the physiological size of cells [246]. To quantify the mechanical forces that cells apply on the surface of these oil droplets, the relation between the geometry of the droplet and the local cellular forces that cause deformation must be related; this relation can be explained by Laplace's law [300].

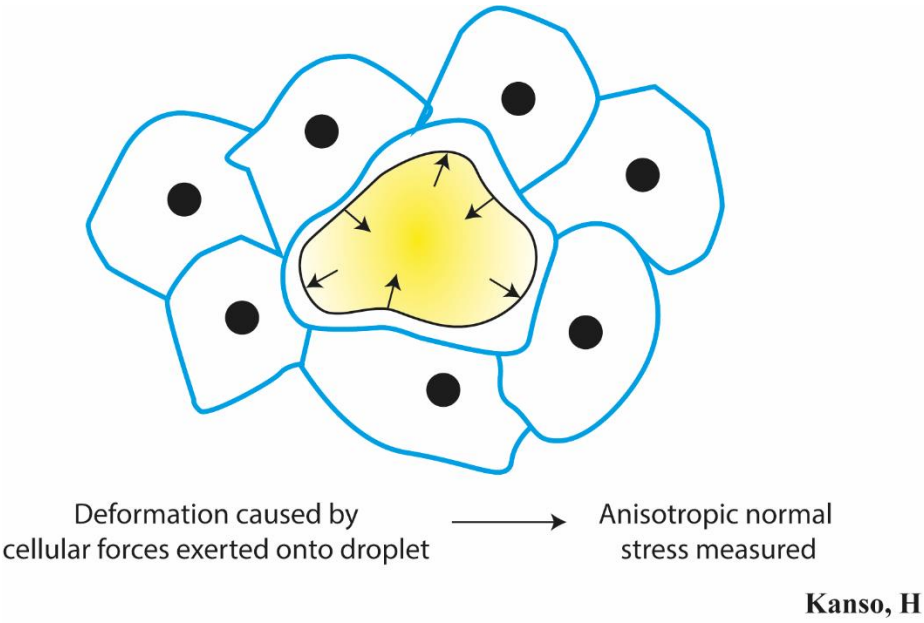

Figure 10: Example of a droplet being deformed by its surrounding cells; Anisotropic normal stress can be extracted from this. Figure reproduced from Campas et al [243].

These calibrated droplets with a known interfacial tension, are either microinjected or mixed with cells within a tissue or aggregate [246]. The applied forces and mechanical stresses from the surrounding cells cause the deformation of the droplet, and paired

with fluorescent microscopy techniques, the reconstruction of its shape in 3D allow quantitative measurement of the mechanical stresses applied to the droplet [246]. A major advantage of this system is that it allows quantitative measurements of endogenous stresses *in vivo*, otherwise known to be difficult to record [246]. Additionally, spatial and temporal measurements of the stresses can be recorded by measuring these deformations over time [246]. Furthermore, specific targeting of different cells can be achieved by varying the droplet surface ligands or stresses induced by specific molecules [246]. Also, the droplets have the ability to be left within the 3D system for days and it has been shown to not affect embryonic development [292]. However, it is limited to measuring the anisotropic stresses generated and cannot measure the local shear stresses applied by individual cells on a given point on the surface of the droplet [246]. Furthermore, this technique is specific to 3D tissues and cannot be used as easily for 2D monolayers [246].

The Campas group used different surface ligands functionalisation and droplet types to measure anisotropic stresses within living tissues[243]. The first method they used was to generate a ferrofluid based microdroplet that was controlled using a uniform magnetic field that deforms it along the direction of magnetic field [301]. By imaging the droplet's deformation, they obtained the mechanical properties of a small region in the tissue [301], and coating the ferrofluid droplet with a cell adhesion receptor ligand like RGD could allow the droplet to function as an *in vivo* force sensor [243]. The second method they employed is the formation of an oil droplet with inert FC70 fluorocarbon oil from 3M, and coated with DSPE-PEG-biotin that allowed the binding of fluorescent 488-streptavidin [243]. This generated an oil droplet that can bind biotinylated ligands of all types, they utilised biotinylated mE-cadherin antibodies to measure mechanical stresses in mammary epithelial cell aggregates [243]. Additionally,

coating with a RGD peptide allowed the group to measure the mechanical stresses in tooth mesenchymal cell aggregates [243].

1.3. Protein nanosheets assembled at liquid-liquid interfaces

1.3.1. Interfacial rheology

There are a variety of ways to study self-assembly processes at fluid interfaces, such as: Circular dichroism (CD) spectroscopy[302], Fourier-transform infrared (FTIR) spectroscopy[303], quartz crystal microbalance with dissipation (QCM-D), spectroscopic ellipsometry (SE)[304], neutron reflectometry[305] and interfacial rheology[306].

Interfacial rheology studies the response of interfacial films to deformations[306], and has been shown to be a very sensitive technique to measure the impact of surfactants on the mechanics of adsorbed protein layers[307,308]. Furthermore, it can be used in conjugation with other traditional methods such as: atomic force microscopy (AFM), imaging ellipsometry (IE) and surface plasmon resonance (SPR)[302].

These deformations are usually performed in two ways. The first being shear rheology which involves subjecting the adsorbed film to shear stress whilst maintaining a constant area[309]; directly measuring the strain that is generated by applied mechanical stress[310]. On the other hand, the second method is dilation rheology which applies area variations (compression and dilation) to the adsorbed film[306,308], or measuring the response to the compression of the surface[310].

Interfacial shear rheology has been found to excel in the measurement of interfacial mechanics of adsorbed protein and mixed protein-surfactant layers at 2D liquid/liquid or liquid/gas interfaces[311,312,313,314,315,316]. On the contrary, interfacial dilatational rheology has been identified to perform in the range of short-term stability[317] and monitoring the structure and concentration of single emulsifiers at interfaces[311].

There is a multitude of factors that are important for interfacial rheology summarized in the table below:

Table 1: Factors that are important to consider for interfacial rheology. Information compiled from Julia Maldonado-Valderrama et al.[306]

Factor	Examples
The native conformation of the protein of interest	Random disordered (Caseins) or Globular (Albumins, Milk proteins)
The type of surfactant used	Ionic/non-ionic, water soluble or oil soluble
The nature of the interface	Air/Water or Oil/Water
Properties of the aqueous phase	pH and ionic strength
Forces and interactions between components at the interface	Vander Waals, hydrophobic, hydrogen bonding and crosslinks

1.3.2. Proteins and their mechanics

Proteins are natural, non-toxic and often low-cost compounds commonly used in the food industry[310]. In particular, milk proteins are valued for their ability to stabilise food emulsions and foams[318]. Proteins are amphiphilic and have a complex structure that is formed by the combination of ionic, polar and non-polar amino acids, generating regions of varying hydrophilicity and hydrophobicity[318]. The core of the protein contains the buried hydrophobic residues and an actively charged surface presents hydrophilic residues, this enables proteins to strongly interact with food components[318].

Due to their similarities in structural (secondary, tertiary and quaternary subunits that interconnect) and surface properties, proteins have been recognised as polymers[319]. A polymer typically takes into account very long chains of randomly organised repeating copolymer subunits[319], whereas proteins such as the globular BSA (583 residues in length), and the disordered β-Casein being (only composed of 209 amino acids) are of defined size and secondary/tertiary structures.

The main classes of milk proteins are whey proteins with a globular tertiary structure and caseins with a disordered and more flexible structure[302]. Alongside albumins, milk proteins have been widely studied for their adsorption onto various fluid interfaces, such as air/water and oil/water interfaces. It is thought that an interface is not just a dividing region between two fluids, but a region of finite thickness containing molecules with properties differing from the bulk phases (this is due to the reduce interfacial tension generated by adsorption)[320]. In the case of proteins, their adsorption

onto these fluid interfaces is largely influenced by their surface charge[321] and hydrophobicity.[322,323]

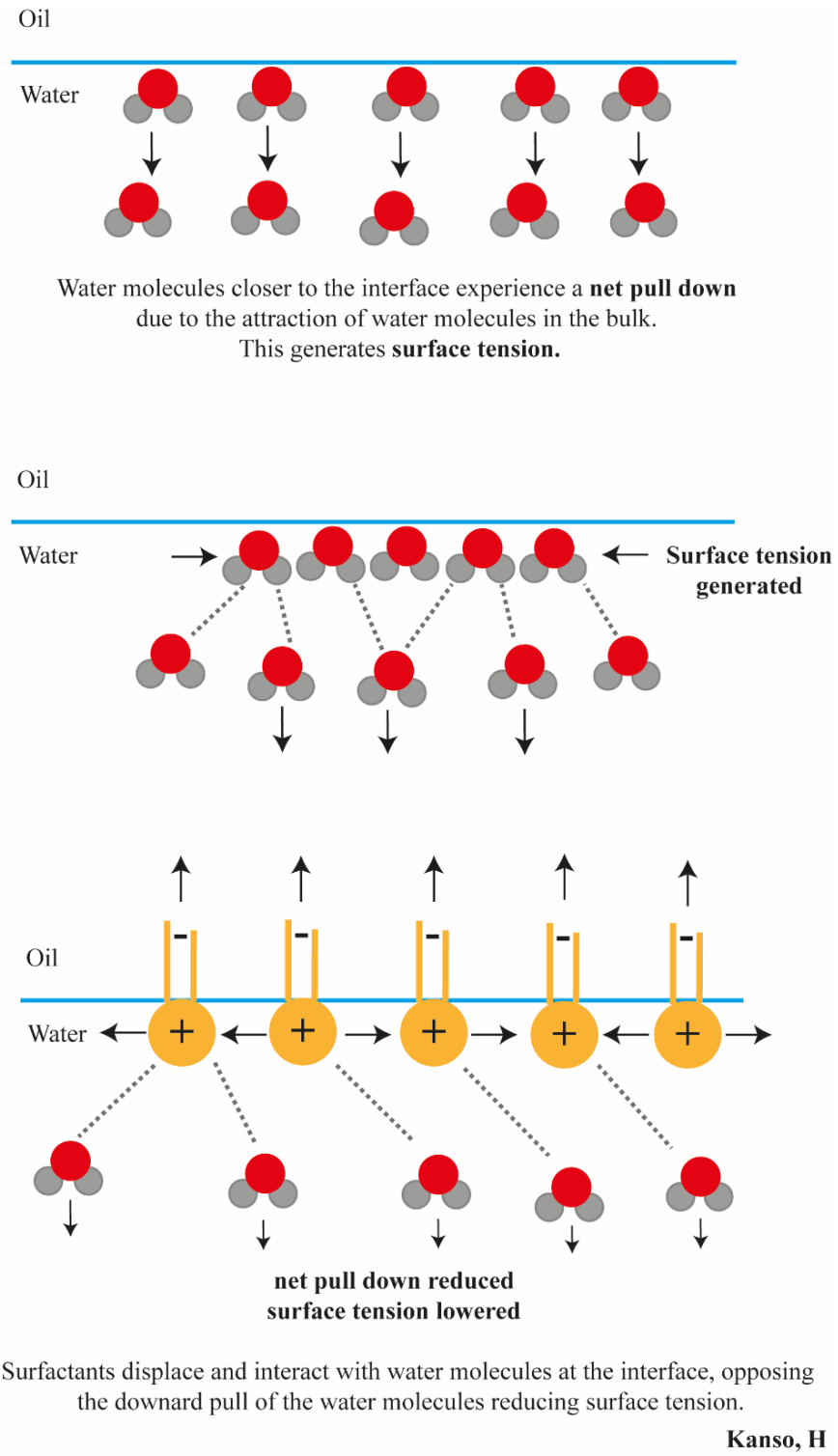

Figure 11: Schematic summarising the effect of surfactants on the surface tension at the Oil/water interface. The surfactant displaces water molecules at the interface reducing the downward pull of water molecules on the interface, reducing surface tension.

Proteins are known to exhibit both elastic and viscous responses, therefore are recognised to be viscoelastic[309]. In protein-polymer systems, viscoelasticity has been found to correlate directly to the thermodynamic stability of biological components such as emulsions[309]. It is widely known that the emulsification process is not thermodynamically favoured (not spontaneous) as a large interfacial area is generated once an emulsion is formed; this makes emulsions prone to destabilisation through mechanisms such as coalescence, creaming and flocculation[324]. Methods exist to bypass this problem, through the addition of stabilizers such as surfactants which stabilise emulsions through the Gibbs-Marangoni mechanism[310] and decreasing the energy required to form a stable interface, this is caused by the reduction in interfacial tension (Figure 11)[308,318,325,326,327,328]. Protein adsorption stabilises emulsions by forming a thin, viscoelastic film[307], this displaces water molecules on the interface reducing the interfacial tension, and allows the fluid interface to resist tangential stresses (shear stress that is parallel to the film) generated by the neighbouring fluid phase[308,318,326,327]; this will facilitate the breakup of droplets during the emulsification process[324]. Furthermore, another potential strategy to improving emulsion stability is to strengthen the viscoelastic protein film through the addition of protein crosslinks[318].

1.3.3. Protein nanosheets and their formation at oil/water interfaces

Protein nanosheets at the oil/water interface are formed by the diffusion of proteins from the bulk phase towards the interface; on arrival at the interface, the protein molecules partially unfold to expose hydrophobic amino acid residues towards the

hydrophobic oil phase [329]. Moreover, once the protein adsorbs at the interface it has been established that some degree of structural change will occur to the tertiary structure, be it rearrangement or complete unfolding and spreading over the interface[330,331]. This unfolding process mediates the rearrangement of hydrophobic residues to face the oil phase, whilst hydrophilic amino acids will arrange towards the hydrophilic aqueous phase [329]. It is this reorientation and assembly on the interface that results in the minimisation of thermodynamic energy of the system leading to a negative ΔG promoting a more spontaneous process [329].

The rate of protein adsorption onto a material is determined by three major driving factors: the protein concentration, the molecular weight of the protein and the affinity of the protein for the surface [332]. The interactions between the protein and the surface are non-covalent forces, such as hydrophobic, electrostatic (Vander Waals) and hydrogen bonding[333]. Protein adsorption is also known to be a spontaneous process, however for this to be true the Gibbs free energy of the system must be negative[334].

As discussed, the hydrophobicity of the interface plays a big role in the thermodynamics of protein adsorption, for example the energy barrier of adsorption to the air/water interface is roughly 2-20 kT is for globular proteins, however at the triolein-water interface this energy barrier is significantly lower[335] – this is due to the stronger interactions between the protein and the hydrophobic oil phase. It has been demonstrated that proteins have a higher binding affinity and tend to adsorb more substantially to hydrophobic surfaces than hydrophilic[318,336] , this is accredited to a greater degree of unfolding at hydrophobic surfaces caused by the withdrawal of buried hydrophobic residues from the protein core, of which are now able to interact and form new, stronger interactions with the surface [318]. The extent of protein

conformational changes is dependent on the protein structure and solvent conditions [337].

Furthermore, for similar reasons, it is thought that at oil-water interfaces, protein chains are able to penetrate into the non-aqueous phase more freely[318,338]; thus, can move around more freely at the surface of the oil. One can manipulate the energy barrier of adsorption onto the interface by altering the physiochemical properties of adsorbed proteins, this was demonstrated by Wierenga et al[339], by increasing the hydrophobicity of Ovalbumin through the addition of four hydrophobic Capryl groups onto its surface; it was revealed that the energy barrier of adsorption had decreased and the rate of adsorption to the interface had increased[339]. Similarly, this was also studied by Gautrot et al[340], whereby they altered the charges on the surfaces of proteins generating supercharged albumins; these were to form strong elastic protein nanosheets that mediated ECM protein adsorption and cellular adhesion [340].

Moreover, the reduction in surface tension caused by protein adsorption is explained by the displacement of water from the interface and is associated with the ordered packing of globular proteins at the surface[320]. The adsorption process of protein molecules will continue to occur at the surface, until the maximum surface saturation has been reached[332]. Therefore, the size of a protein has an impact on the rate of protein adsorption as the larger the size, the smaller the amount of moles required to achieve a given surface tension[320]. Additionally, flexible proteins such as β-Casein are able to adsorb at a rapid rate forming a layer of low ordered packing. Whereas, a globular protein such as BSA observe a slower rate of adsorption but a higher order of packing at the Oil/water interface [337].

Also, the concentration of protein in the bulk phase can influence the stability of an interface, as the lower the concentration of protein, the degree of crowding at the interface is reduced; thus, proteins can undergo a higher degree of molecular relaxation and spreading at the surface – granting a higher affinity to the surface[341], and an increased likelihood of adopting the lowest energy configuration state once unfolded[318]. However, external factors such as temperature and pH can also impact the extent of unfolding and the final structural configuration of protein at the interface[318].

In addition, an example of a solution that contains a mixture of proteins such as serum, has been demonstrated to have a dynamic adsorption process and conveys competitive adsorption[332]. Proteins that adsorbed first to the interface were displaced by proteins displaying a larger molecular weight, a higher degree of conformational flexibility and a higher affinity to the surface; this phenomenon is referred to as the Vroman Effect [332,342,343] and is an example of reversible adsorption. However, it is known that proteins tend to adsorb less reversibly at hydrophobic surfaces and the extent of exchange between the protein film and the bulk aqueous phase is greatly reduced[318]; this is due to penetration of hydrophobic residues into the oil phase leading to the majority of the unfolding occurring within the oil bulk phase as opposed to the aqueous or gas phase[344].

1.3.4. Bioemulsions

Bioactive emulsions, or bioemulsions, were recently proposed and defined as emulsions displaying inherent and direct bioactivity, for example promoting cell adhesion[345]. In the context of this thesis, this will be extended to the stimulation of other cell membrane receptors. Bioemulsions are a subtype of emulsion that are activated using a bioactive component and have the capabilities to support the culture of adherent cells[329]. This tool is emerging as appealing option for the scale up of cellular manufacturing [346,347]. However, to be used at the industrial scale the cost of these microcarriers must be reduced to minimise the cost of cell-based therapies. Presently, the cost of cultivating 1 billion cells falls within the range of £800-1900; with up to 65% of the costs corresponding to the cost of consumables for cell culture and recovery and the majority of the rest of the costs corresponding to the media [348,349].

In order to be classed as a suitable microcarrier, bioemulsions must possess essential characteristics, notably: the ability to provide sufficient anchorage for cell growth, a display of adequate physical mechanical properties and enable the convenient and efficient harvesting of the expanded cells [350]. The core material, surface properties and particle size are all essential factors that contribute to cell adhesion and proliferation on such carriers. Therefore, commercially available microcarriers exhibit variations in size, protein coating and surface charges – this provides a wide variety of applications and accommodation of different cell types [351,352].

Furthermore, the protein nanosheet that enables the proliferation of cells on the bioemulsion must also possess key characteristics: First, the ability to stabilise the oil droplet and persist during the long-term cell culture at physiological conditions [350].

Second, the formation of a robust protein network that is capable of withstanding cell-induced contractile forces generated during the processes of cellular migrations and spreading[350]. Finally, the capacity to efficiently adsorb ECM proteins at the surface of the nanosheets [350], or to directly promote cell adhesion (e.g. via integrin ligands).

Recently, it was proposed that the formation of mechanically strong protein/polymer nanosheets at the liquid-liquid interfaces of bioemulsions, provided a local mechanical microenvironment that promoted cellular adhesion [353,354]. It was discovered that the interfacial viscoelasticity of these protein nanosheets assembled at liquid-liquid interfaces was able to regulate the proliferative capacity of adherent stem cells on liquid substrates, despite the absence of bulk elastic properties of the oil phase (viscosities comparable to those of aqueous solutions) [355].

Human Mesenchymal Stem cells (hMSCs) have been effectively cultivated on microcarriers [348,356–359], typically composed of solid particles, 200-300 μm in size and made up of a variety of materials [360]. Whilst quantitative analysis of the data obtained from microcarriers proves to be challenging, the majority of research in this field has highlighted the significance of microcarrier surface coating promoting cell adhesion, proliferation and preservation of phenotype [350]. Examples of such ECM protein-coated microcarriers used for MSC cultures include, cross-linked dextran-based and denatured collagen-coated microporous Cytodex-3 and a cross-linked gelatin-based macroporous CultiSpher-S[348,359,361–365].

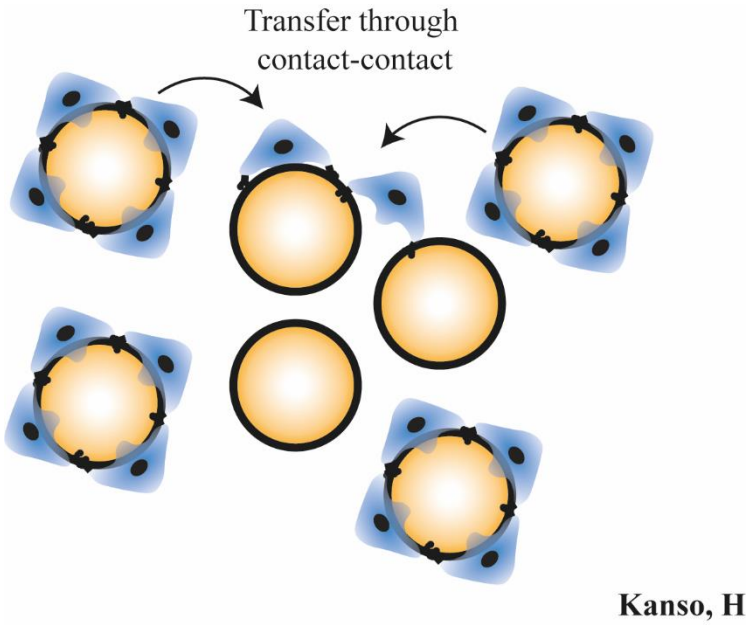

Figure 12: Schematic depicting the droplet-droplet transfer of cells through contact, this can allow passaging without the need for enzymatic detachment.

In addition, microcarriers also offer the advantage of cell passaging via bead-bead transfer without the need for enzymatic treatment, this occurs by seeding fresh microcarriers into the ongoing culture (as seen in Figure 12)[356,366]. This approach not only allows more efficient use of labour-intensive nature of the cell passaging process (the harvesting and transfer of cells to start new cultures), but also reduces the risk of contaminations [367].

Other types of bioactive functional microcarriers (both protein and non-protein based) exist such as temperature-responsive[368–370] and dissolvable microcarriers [371]. Temperature-responsive microcarriers possess the ability for non-enzymatic cell harvesting via the manipulation of culture temperatures; this is as a result of a gradual change in hydrophilicity promoting incremental cellular release [360]. However, this method requires the engraftment of temperature-responsive polymers such as poly(N-isopropylacrylamide) onto existing Chloromethylated poly(styrene) (CMPS) beads[372], which requires specialist knowledge and equipment [360]. Furthermore, it is necessary to

assess the effects of the temperature change on the quality of the cells [360]. Dissolvable microcarriers use modified hydrogels that can be enzymatically digested to release cells without breaking the bonds proteolytically; the Corning™ Synthemax II dissolvable microcarriers (Comprised of polygalacturonic acid polymer chains cross linked via calcium ions) were tested and were shown to successfully expand iPSCs, with a cell harvest recovery rate of 92% [371]; but Corning has now discontinued this product.

Globular proteins are an attractive platform for the proliferation of cell cultures, as they have the capability to act as scaffold proteins to form viscoelastic nanosheets that stabilise bioemulsions. Furthermore, they can be readily sourced and are mostly approved for food industry and in some cases therapeutics [373]. However, to date most of these successful systems such as poly(l-lysine) (PLL) paired with reactive surfactant acyl chlorides[353,354], have supported cell adhesion at these liquid substrates have been based on the co-assembly of protein and a co-surfactant; this hinders potential therapeutic applications of the bioemulsions as the co-surfactants have been identified as cytotoxic[329]. Nevertheless, there are studies that have demonstrated a high cell proliferation on bioemulsions without the need of a cosurfactant, but scalability is still an issue [329].

These protein-oil micro-droplets provide a large surface-to-volume ratio which in turn generates a significantly larger surface area than traditional 2-Dimensional (2D) cultures; this is suitable for the cultivation of a wide variety of adherent cells, including MSCs [329]. The Gautrot et al group [350] demonstrated that bioemulsions stabilised by a protein nanosheet such as PLL displayed both strong interfacial mechanics, allowed ECM proteins adsorption and cell-adhesive ligands; this enabled the long-term expansion of adherent stem cells such as MSCs[350]. Additionally, the MSCs retained

their multipotent phenotype for up to six passages (~47 days) on these bioemulsions when compared to solid microcarriers [350]. A study by Hanga et al [360] also observed a stretch in the deposited protein layer at the oil/water interface as a result of the proliferating MSCs deforming the interface; this altered the shape from a sphere to a tear-shaped droplet and exhibited morphologies similar to those cultured on solid substrates [360].

Although this technology provides a range of advantages for culturing and processing adherent cells, the application of these bioemulsions is still in its early stages. Yet studies are beginning to scale-up these techniques for long-term expansion of MSCs into spinner flask bioreactors (seen in figure 7) [347]. Amongst these microcarrier based bioreactors, conical flasks, stirred tanks or expandable bag systems have been demonstrated to be successful [374,375]. Furthermore, the processing of these microcarriers to harvest cells (to detach the cells completely, not passaging) still requires enzymatic digestion, which still has the possibility to damage cell membrane receptors and impact cellular phenotypes [349]. This is a very difficult problem to solve when scaled to industrial production as the concentration of enzymes and incubation times are difficult to control, which can impact cell viability and recovery efficiencies [349,376]. Bioemulsions based on biomedical grade oils (metabolizable or not) could alleviate these issues.

1.3.5. Cell adhesion to fluid interfaces and surfactants

It was previously thought that cells cannot adhere to fluid substrates due to the inability to sustain the actomyosin-based contractility because of rapid relaxations at the interfaces[377]. However, in recent studies it has been demonstrated that cell cultures are capable of proliferating, spreading and adhering to low viscosity liquids such as Silicone and Fluorinated oils. Moreover, cell cultures such as Fibroblasts[378,379] and Myoblasts[380] have been studied and observed to proliferate on Fluorinated Novec 7500 oil and Poly (Dimethyl siloxane) (PDMS)[381]. However, this was only made possible by the self-assembly of mechanically strong protein nanosheets at the interface between the culture medium and the supporting oil[381,382]. An example of such behaviour was seen in the Poly(L-Lysine) protein (PLL), it was discovered that PLL generated strong polyelectrolyte nanosheets in the presence of the pro-surfactant pentafluorobenzyl chloride (PFBC) at pH 10.5, this facilitated the adsorption of Fibronectin which promoted the adhesion, proliferation and spreading of primary human keratinocytes (HPKs) and HaCaT cells at the surface of fluorinated Novec 7500 oil[383]; these results were found to be comparable to the traditional Tissue culture plastic (TPS) substrate[383].

Solid substrates with a bulk modulus within the range of kPa (soft protein-based hydrogels such as those comprised of hyaluronic acid) to gPa (Tissue culture plastic) are typically employed for culturing adherent cells and stem cells [384]. Over the years, tissue and stem cell culture methods have been dominated by these solid substrates although widely used, they lack in poor scalability for adherent stem cell expansion in systems such as 3D bioreactors and the design of parallel culture systems[383,385,386,387].

Furthermore, adhesion to these solid substrates has been demonstrated to promote a variety of cell phenotypes such as: proliferation[388], apoptosis[389], differentiation[390–392], endocytosis, motility[388,393] and spreading[394–396]. Therefore, investigating strategies to bypass these obstacles in stem cell expansion is desirable; a possible alternative strategy would be to use a liquid surface instead, such as an oil.

The fundamental study conducted by Keese and Giaever in 1980s paved the way for the cultivation of cells on liquid-liquid interfaces. They first reported the culture of adherent Fibroblast cells at liquid interfaces and identified the significance of introducing a surfactant to the interface mediated such processes [397,398]. However, the factors that control the molecular structures of these assemblies, the precise mechanism and the impact on interfacial mechanics remains unclear [397,399]. Direct cell adhesion to low viscosity liquid is surprising as they are thought to relax too fast (not allowing the formation of focal adhesions) to facilitate attachment [400], this suggested when compared to cell adhesion to solid substrates that a different mechanism was governing such processes [401]. The attachment of cells onto liquid-liquid interfaces was revealed to be caused by the self-assembly of mechanically strong viscoelastic protein nanosheets at these interfaces; and with the supplementation with the pro-surfactant PFBC the proliferation rates were comparable to cells proliferating on solid substrates[401].

Moreover, it was also revealed that the concentration of the prosurfactant PFBC had a clear correlation with the proliferation of HaCaTs at the surface of Fluorinated Novec 7500 oil. This led to the idea that cell proliferation at the surface of low viscosity liquids was mediated by surfactants[382]. The study by Gautrot et al.[382] proposed that acyl chlorides such as the PFBC surfactant used formerly, can react with the proteins that assembled at the interface to generate hydrophobic cross links, resulting in

mechanically strong protein nanosheets that are capable of sustaining cell proliferation[382]; these physical cross-links promote a more interconnected protein network which is associated with an increase in interfacial elasticity [402].

1.3.6. Cell adhesion to the extracellular matrix and its effect on Stem cell fate

Stem cells grow in a microenvironment composed of neighbouring cells, the surrounding ECM and the soluble factors present in the media; these factors combined establishes a stem cell niche [403]. The fate of stem cells can be modulated by the aspects of its surrounding ECM, for example the stiffness [404–406], surface nano-topography [407–410] and its chemical characteristics[406,411]. Additionally, stem cell differentiation is further modulated by cell size[412,413], cell shape [414,415], cell–cell contact, and cell density [416–418].

The ECM is a non-cellular component that provides the physical scaffolding for cellular adhesion[419], the regulation of cell adhesion to the ECM is controlled by molecular processes that physically connect the cell's actin cytoskeleton to the ECM via self-assembled proteins[420] such as integrins and fibronectin. This adhesion is known to induce downstream biochemical pathways that are fundamental in the regulation of cellular phenotypes, including such as cycling[421], cell spreading and motility[394,396,422], apoptosis[423], stem cell self-renewal[424], and differentiation[391,392]. These cellular phenotypes have been demonstrated to be regulated by mechanisms

such as ERK, SMAD, MAL/SRF and YAP signalling (as discussed in section 5.2.5) [425–427].

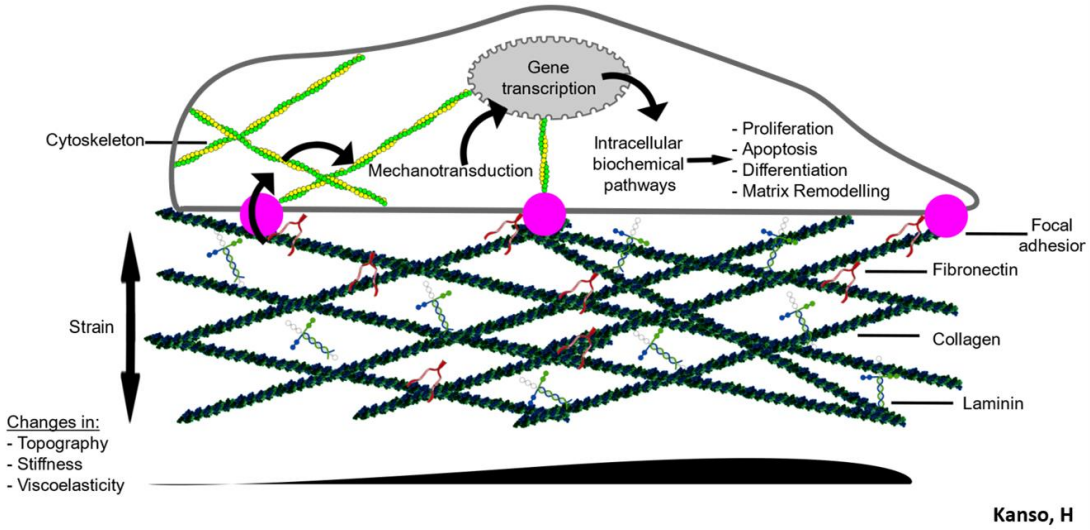

Figure 13: The effect of cell adhesion to the ECM and its effect on cell fate. Cells can sense the changes in substrate topography, stiffness and viscoelasticity through mechanosensitive focal adhesions which alter the intracellular cytoskeleton. The adhesion to these matrix substrates such as Matrigel triggers mechanotransduction pathways that alter gene transcription which promotes cellular proliferation, differentiation and matrix remodelling, thus influencing cell fate.

It has been demonstrated that cells are capable of adhering and applying contractile forces onto the ECM and 2D materials via the formation of focal adhesions[428,429,430,431]; these forces are typically in the range of 1-20nN[432,433] and are mediated by internal actin polymerization[434]. Cells use this process to actively sense the nanoscale biophysical properties of their surrounding environment[377] in particular stiffness[435], topography[436] and viscoelasticity[437]. Furthermore, cells will respond to the mechanical cues generated resulting in the actuation of biochemical pathways, leading to the activation of gene transcription[438] consequently, modulating the cellular phenotypes mentioned previously.

With the advancement in nanotechnology and engineering techniques, it is now possible to generate synthetic biomaterials that mimic this physical microenvironment however, for cells to successfully 'feel' their surroundings, it is conditional on the sensing of nanoscale physical properties of the synthetic biomaterial[420]. These nanoscale physical properties include: the nanoscale geometry, topography and mechanics[420].

There are two main approaches that allow the fabrication of synthetic nano-biomaterials that have control over their physical properties[420]. The first being the 'Top down' approach, this involves the modification of the macroscopic bulk material, which is then scaled down to nanoscale components[420]. On the other hand, the 'Bottom up' approach utilises the interaction of smaller components (building blocks) to generate self-assembled, larger and more organised nanostructures[420,439,440].

An example of a synthetic biomaterial is Polydimethylsiloxane (PDMS) hydrogels, these have been extensively utilised to study cell behaviour due to its biocompatibility and ability to tune the mechanical properties of its physical microenvironment; this allows it to cover a range of biological tissue stiffnesses [441,442]. It was also previously reported, that hMSCs differentiated in response to altered PDMS substrate stiffness [405,443]. It was also proposed that local viscoelastic deformation by the cells regulated cell adhesion, which modulated the molecular clutch mechanism; this mechanism has been put forth to explain how cells sense the stiffness of their surrounding matrix influencing the fate of differentiating MSCs [444,445].

Additionally, single-molecular force probe microscopy has confirmed that cells sensing their surroundings through these deformations on the matrix measure <200 nm [446,447]. However, some recent reports have highlighted that cellular phenotypes do

not necessarily directly correlate with the bulk mechanics of ECM mimicking biomaterials [425]. This was demonstrated in studies with MSCs cultured on varying stiffness of 3D hydrogel. The first cultured MSCs on a hydrogel primarily based on hyaluronic acid, with the cells committing towards osteogenic lineages on the soft variant and adipocytes differentiation on the stiffer matrix variant [448]. Whereas, the opposite trend was observed on 2D poly(acrylamide) hydrogels[405] and within nondegradable 3D hydrogels [449]. This contrast in cell fate was proposed to be caused by the cells' capability to rapidly degrade softer hydrogels, enabling them to spread faster than those on stiffer hydrogels which adopted more rounded morphologies [384].

Interestingly, PLL nanosheets form stiffer interfaces at the Oil/water interface but have been demonstrated to successfully promote hMSCs proliferation, elongation and spreading. This was thought to be consequence of the increased positive charge of the interface which promotes the rapid adsorption of fibronectin; which facilitated the connection of cell surface ligands such as integrins to the ECM, this was proposed to mediate mechano-sensing through the cytoskeleton-integrin-ECM link [384]. Furthermore, the reported direct adsorption of fibronectin to hydrophobic interfaces was discovered to facilitate the attachment of hMSCs, however their ability to stabilise emulsions was unsuccessful; hence limiting their use for cell culture on bioemulsions[450].

1.4. Aims and objectives

The aims of this thesis were split into two, the first aim was to introduce bioactivity to self-assembled protein nanosheets and then apply this technology to study forces and introduce ligands within complex tissues such as cerebral organoids. An Avi-tag was introduced onto the Bovine serum albumin protein which became the scaffold that adsorbed and stabilised the Oil/water interface, this allowed the formation of bioemulsions in the physiological range of 20-30 μm. The albumin protein was recombinantly expressed in the *P. pastoris* expression system, followed by its *in vitro* biotinylation by the *E. coli* biotin ligase BirA. Bioactivity was introduced onto our bioemulsions through three surface active ligands, N-Cadherin, E-Cadherin and RGD, these were chosen to mimic cell-cell interactions that allowed interactions between the droplets and cells within cerebral organoids. Markers of neuronal development and maturation were studied to characterise whether the droplets have an effect on the lineage commitment and/or development of the cerebral organoids.

The second aim was to search for proteins that promoted the direct strengthening of interfacial mechanics of protein nanosheets without the need of a toxic co-surfactant. We proposed to explore this through the assembly of fibrinogen that is known to adsorb to both hydrophobic and hydrophilic surfaces and to we studied the impact of the addition of thrombin on the interfacial liquid-liquid mechanics and whether these enhanced nanosheets promoted the adherence and proliferation of highly contractile cells such as Mesenchymal stem cells. The interfacial mechanics of the fibrinogen nanosheet such as stiffness, toughness and elasticity were characterised through interfacial shear rheology and compared to other proteins and materials in the

literature. After which, these enhanced protein nanosheets were tested to discern whether they are capable of facilitating the proliferation and growth of 2D and 3D cell cultures for prolonged periods of time.

2. Materials and methods

2.1. Expression and purification of rBSA in *P. pastoris*

JM109, Rosetta D3 and DH5α *E. coli* cells were kindly provided by Dr. R. Rose's Lab. GS115 *P. pastoris* yeast strain ordered from Life Technologies, Invitrogen. SHuffle® T7 Express Competent *E. coli* cells, Amylose resin and OneTaq® Quick-Load® 2X Master Mix were ordered from New England Biolabs. The pPIC9K plasmid was ordered from Gentaur Ltd. Restriction enzymes Fast Digest SnaBI, AvrII and SacI were ordered from ThermoFisher. Ampicillin, DTT, glycerol, 100mM ATP solution, D-biotin, 1M $MgCl_2$, PBS, PageRuler Unstained Broad Range Protein Ladder, Pierce biotin quantitation kit and Potassium phosphate dibasic were ordered from ThermoFisher. D (+)-glucose, G-418, lithium acetate and PD10 desalting columns were ordered from Sigma Aldrich. Agar, TAE 50X buffer and tris-glycine-SDS buffer, D-sorbitol, potassium phosphate monobasic and Lennox L Broth capsules, HEPES powder were ordered from Melford Scientific. Casamino acid powder, Yeast extract, peptone and Yeast synthetic drop out medium (without histidine) was ordered from ForMedium. 5M NaCl was ordered from Invitrogen. Imidazole powder was ordered Acros Organics.

2.1.1 Plasmid design and cloning

The BSA protein sequence used for this experiment was the 3V03 *Bos Taurus* sequence. The expression vector 6xHis-3C-Avi-rBSA was designed manually using the SnapGene software and ordered via the ThermoFisher GeneArt services. The *Bos Taurus* BSA codons were optimised using this service to the *P. pastoris* host codons to ensure the highest reliability in expression. The inserts were then ordered and synthesised in a ThermoFisher standard pEX-A2 vector containing the Amp® ampicillin resistance gene. The inserts were then ordered synthesised in a ThermoFisher standard pEX-A2 vector containing the Amp® ampicillin resistance gene.

1 µL of pEX-A2-rBSA vector was transformed into 50 µL of JM109 bacterial cells via standard heat shock at 42^{o}C and plated onto 100 µg/mL ampicillin LB plates overnight at 37^{o}C. One colony was picked, transferred into 5 mL of 100 µg/mL ampicillin LB media and incubated overnight at 37^{o}C, 220rpm. 2 mL of the resulting starter culture was centrifuged at 14k rpm and the pellet was mini-prepped using a QIAGEN QIAprep miniprep kit with a final elution volume of 50 µL. pEX-A2-BSA and pPIC9K vectors were both digested with SnaBI and AvrII restriction enzymes at 37^{o}C for 15 minutes using the digestion master mix in Table 2.

Table 2: Digestion master mix for the digestion of pEX-A2-BSA and pPIC9K plasmids. 16 µL of each plasmid was digested in separate Eppendorf tubes. Total reaction volume is 20 µL.

	pEX-A2-rBSA	pPIC9K
10x FD Green buffer	2 µL	1 µL
AvrII endonuclease	1 µL	0.5 µL
SnaBI endonuclease	1 µL	0.5 µL

20 µL of the digested plasmids were characterised on a 1% agarose gel for 30 minutes at 120V. 5 µL of DNA ladder were also used and loaded into the first lane. The recombinant BSA (rBSA) insert (1852 bp) and pPIC9K (9276 bp) were purified out of 1% agarose gel using a GeneJET gel extraction kit with a final elution volume of 50 µL. 4.5 µL of digested rBSA was mixed with 0.5 µL of digested pPIC9K and 5 µL of Instant sticky end master mix. 5 µL of the resultant ligated pPIC9K-rBSA vector was transformed into DH5α *E. coli* (high competency) cells using the standard heat shock procedure and 200 µL of the transformation was plated onto a 100 µg/mL ampicillin LB plate and incubated overnight at 37ºC.

Six colonies were picked from the plates to form 5 mL starter cultures and subsequently 2 mL of culture was miniprepped. 500 µL of each starter culture was mixed with 500 µL of 30% Glycerol, vortexed, snap frozen with liquid nitrogen then stored at -80ºC. Analytical digests were incubated at 37ºC for 15 minutes using the digestion mix in Table 3, and were setup for the miniprepped plasmids, before characterisation on 1% agarose gels at 120V for 30 minutes.

Table 3: Digestion master mix for the analytical digest of miniprepped pPIC9K-rBSA plasmids. SnaBI recognizes TAC^GTA sites. AvrII recognizes C^CTAGG sites.

Component	Volume (µL)
10x FastDigest Green buffer	1
SnaBI endonuclease	0.5
AvrII endonuclease	0.5
ddH_2O	5
pPIC9K-rBSA	3

The gel was observed for the generation of two bands, one for the cleaved empty pPIC9K plasmid (9.27 kbp) and another for the rBSA insert (1.85 kbp).

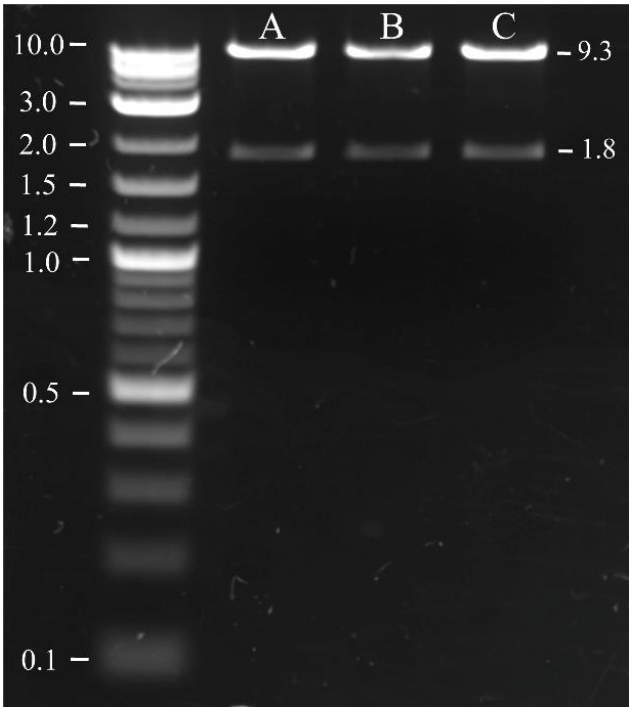

Figure 14: 1% agarose gel of analytical digests of DH5α *E. coli* cells transformed with pPIC9K-Avi-rBSA (A-C). Successful transformants should generate two bands, one for the empty cleaved pPIC9K plasmid (~9.27 kbp) and another for the Avi-rBSA insert (~1.85 kbp), kbp = kilobase pairs.

10 µL of successful plasmids were sent off for sequencing to further verify the sequence along with 10 µM 5' AOX1 forward primer. A successful transformant was streaked onto a 100 µg/mL ampicillin LB plate and incubated at 37°C overnight. Colonies were picked and transferred into 50 mL 100 µg/mL ampicillin LB media and incubated overnight at 37°C. The culture was midi-prepped using the QIAGEN plasmid plus midi prep kit to obtain at least 10 µg of plasmid DNA. Plasmids were stored at -20°C until required.

2.1.2. Generating electrocompetent *P. pastoris* cells

GS115 *Pichia pastoris* strain was streaked onto a YPD-agar plate and incubated at 30°C for 2 days. Single colonies were then streaked into patches of roughly 4 cm^2 onto YPD-agar and incubated at 30°C for 18 hours, ensuring patches do not get too thick (Figure 15).

Figure 15: Example of a patched GS115 *P. pastoris* cells, with an area of ~4 cm^2 on YPD-Agar.

920 µL of YPD was prepared in a sterile 1.5 mL Eppendorf tube, 40 µL of fresh 1M DTT and 40 µL of 1M HEPES-NaOH (pH 8.0) was added to the mix. Cells from one patch were scraped and transferred to the mix using a sterile pipette tip, the mix was vortexed to allow for uniform suspension. The tube was incubated at 30^{o}C for 15 minutes at 100 rpm, then pelleted at 3000 x g for 3 minutes. The cells were washed twice with ice cold sterile water then twice with ice cold 1M sorbitol, with a final volume of 50 µL. The *P. pastoris* cells are now considered electrocompetent and can be stored at -80^{o}C for long term storage.

2.1.3. Transformation of pPIC9K into *P. pastoris*

The pPIC9K-rBSA plasmid was digested and linearised by SacI restriction enzyme using the conditions in Table 4. The linearised plasmid was then purified using the GeneJET PCR purification kit.

Table 4. Digestion mix used to linearise the pPIC9K-rBSA plasmid using SacI restriction enzyme; recognizes GAGCT^C sites.

Component	Volume (µL)
pPIC9K-rBSA (~200ng/µL)	5
SacI Fast digest	1
ddH_2O	12
Fast digest Buffer	2

The electrocompetent cells along with 1 µg of linearised pPIC9K-rBSA were transferred to a pre-chilled electroporation cuvette and incubated on ice for 5 minutes. The moisture was wiped off the cuvette and pulsed at 2000 V/200 Ω/25 µF, followed by the immediate addition of 1mL of ice cold 1M sorbitol to the cuvette for recovery. The cells were transferred to a sterile 1.5 mL Eppendorf tube and incubated at 30^{o}C for 1 hour with no shaking. After 1-hour 500 µL of YPD was added to 500 µL of recovered cells and incubated overnight at room temperature to acquire G418 antibiotic resistance. The cells were pelleted at 3000 x g for 3 minutes and resuspended in 250 µL of water. 50 µL of cells was plated onto increasing concentration of G418 YPD-agar plates 0.25, 0.5, 1.0, 2.0, 4.0 mg/mL G418 and incubated at 30^{o}C for 4-5 days dependent on antibiotic concentrations. Colonies from the highest antibiotic concentration were transferred to 5 mL YPD medium and starter cultures were generated overnight at 30^{o}C, of which 500 µL was used to generate glycerol (15%) stocks. 10 µL of each starter culture was used to streak onto YNBD plates for His^{+} selection to eliminate any spontaneous G418 colonies.

2.1.4. Colony PCR of successful transformants

Successful colonies that showed both the highest antibiotic resistance and His^+ phenotype were used for colony PCR, this was conducted to check for the insertion of the pPIC9K-rBSA cassette at the chromosomal AOX1 promoter. In a 1.5 mL Eppendorf tube, 200 µL of liquid starter culture was spun down at 14,000 rpm for 1 minute. The pellet was resuspended in 100 µL of 200 mM LiOAc + 1% SDS buffer and incubated at 70^oC for 5 minutes. 300 µL of 100% ethanol was added and vortexed for 10 seconds. The DNA was spun down at 13,000 rpm for 3 minutes and the supernatant was discarded carefully without disrupting the white pellet. The pellet was washed once with 500 µL of 70% ethanol and spun down at 13,000 rpm for 1 minute. The ethanol was removed without disrupting the pellet and dissolved in 100 µL RNA free ddH_2O, then spun at 13,000 rpm for 1 minute. 2 µL of the supernatant was used for PCR using the PCR mix in Table 6.

Table 5: The 5' and 3' AOX1, and the Alpha secretion signal primers

5' AOX1	GACTGGTTCCAATTGACAAGC
3' AOX1	GCAAATGGCATTCTGACATCC
Alpha secretion signal	TACTATTGCCAGCATTGCTGC

Table 6: The components used to generate the master mix for colony PCR samples.

Components	Volume (µL)
OneTaq® 2X Master Mix	10
10µM 5' AOX1 Primer	0.5
10µM 3' AOX1 Primer	0.5
ddH_2O	7
DNA	2

In the case of a Mut^+ His^+ phenotype, two bands should appear once the PCR product is run on a 0.8% agarose gel at 120V for 30 minutes. One band corresponding to the chromosomal AOX1 promoter at 2.2 kb and another band corresponding to the rBSA insert sequence plus the 492 bp PCR fragment generated by the parent plasmid at 2.34 kb. Successful transformants that observed both bands were used for subsequent protein expression.

2.1.5. Expression of rBSA in *P. pastoris*

A successful transformant from the highest concentration of antibiotics was streaked onto YPD-Agar containing 4.0 mg/mL G418 and incubated at 30^{o}C for 3 days. One colony was transferred per 25 mL of BMGY medium in a falcon tube and incubated at 30^{o}C, 220 rpm overnight. The cells were pelleted at 1500 x g for 5 minutes, resuspended in 5 mL of BMMY medium and transferred into a 2 L flask containing 500 mL of BMMY medium. The flasks were covered in a layer of sterile gauze and incubated at 28^{o}C, 200 rpm for four days; 2% methanol was supplemented into the medium every 24 hours to maintain induction of the AOX1 promoter and protein expression. A 1 mL sample was taken every 24 hours to be used for the SDS-page gel.

2.1.6. Purification of Avi-rBSA via his-tag nickel affinity chromatography (on AKTA Pure system)

After four days, the cells were centrifuged at 7000 rpm for 15 minutes and the supernatant was further centrifuged in batches at 15,000 rpm for 2 minutes. The supernatant was then filtered and stored at 4^{o}C until purification. Two 5 mL HisTrap columns used in series were connected to an AKTA Pure system and equilibrated using 5 column volumes of wash buffer (PBS + 20 mM imidazole). The supernatant containing the expression rBSA protein was loaded and applied to the column, then washed using 20 column volumes of wash buffer. The protein was eluted from the column using elution buffer (PBS + 500 mM imidazole), the elution fractions were

pooled and stored at 4°C. The column was regenerated with three column volumes of ddH_2O, followed by three column volumes of 1 M NaCl + 0.1 M NaOH, five column volumes of ddH_2O and finally stored in 20% EtOH. SDS samples were taken at every step and a SDS gel was run at 220V for 30 minutes to verify protein purification. The excess salts and imidazole were removed from the buffer using a dialysis step through 14K MWCO dialysis tubing. 5 L of PBS was prepared in a container and the protein solution was pipetted into the dialysis tubing, tied from both ends and allowed to dialyse overnight. The rBSA protein was stored at -80°C in 5% glycerol for long term storage or used immediately for biotinylation.

2.1.7. *In vitro* biotinylation of Avi-rBSA

If the Avi-tagged rBSA protein was thawed from long term storage, the 5% glycerol was removed prior to biotinylation using a PD10 desalting column and eluted using 3.5 mL of PBS buffer. The protein was further concentrated using a 30k MWCO concentrator to reach the 40 μM threshold required for optimal biotinylation. The O/D_{280} was measured for Avi-rBSA using a Quartz cuvette at 280nm in PBS buffer, then protein molarity was calculated using the absorbance value using Beer Lambert's law (equation 2.1).

Equation 2.1: $A = \varepsilon cL$

Where A represents the absorbance value at 280nm, ε the extinction coefficient of the protein ($M^{-1}cm^{-1}$), c the molar concentration of protein (M) and L the optical path length (cm).

In general, it is widely accepted that 1 µg/mL of BirA is capable of biotinylating 1 µM of Avi-tagged substrates[451,452]. The biotinylation experiment was setup in a sterile 15 mL Falcon tube using filtered reagents using the conditions in Table 7.

Table 7: The components used for the invitro biotinylation of Avi-BSA.

Components	**Final concentration**
Avi-Tagged protein in PBS	175 µM
rBirA	3 µM
Magnesium Chloride	10 mM
ATP	10 mM
D-Biotin	0.3 mM

The biotinylation mix was incubated at 30^{o}C, 100 rpm for 1 hour. Amylose resin was washed with PBS three times by centrifugation and 100 µL of 50% amylose resin slurry was added to the mix and rocked for 30 minutes at room temperature. The mix was centrifuged at 14,000 rpm for 2 minutes and the supernatant was transferred to a 15 mL Falcon tube. 2 mL of sample was run once more through a PD10 desalting column to remove excess salts and biotin and eluted into 3.5 mL PBS. The sample was concentrated once more using a 30k MWCO and the protein molarity was measured using a Quartz cuvette at 280 nm in PBS.

2.1.8. Testing for biotinylation of bt-rBSA

Three methods were used to measure the extent of biotinylation. As a quantitative method, the Pierce Biotin Quantitation Kit was used to quantify the amount of biotin molecules per molecule of protein; with a bt-HRP protein used as control. As a qualitative method, 5 µL of 10 µM bt-rBSA was added to 10 µL of 2x SDS buffer, the sample was heated at 95^{o}C for 5 minutes and allowed to cool to room temperature. 5 µL of 1 mg/mL streptavidin was added and incubated for 10 minutes at room temperature. The sample was run on an SDS-page gel at 220V for 30 minutes and the bands were observed for an increase in molecular weight. A secondary qualitative method, emulsions were generated with the bt-rBSA protein, functionalised with 50 µg/mL FITC-Streptavidin and imaged at 488nm to verify streptavidin binding.

2.1.9. Circular Dichroism

The Bt-rBSA protein was concentrated to a concentration of roughly 150 µM using a 30 kDa MWCO PES concentrator (Vivaspin) run at 4000xg and subsequently 1 mL of protein was loaded onto a S200 10/300 SEC column (Cytvia), preequilibrated with 5 mM phosphate buffer (IPO_4) pH 7.4, the flow rate was set to 0.25 mL/min and run overnight. This was step was completed to exchange the buffer from PBS into IPO_4 – a buffer that will not strongly absorb in the UV wavelength range of 180-300nm. The CD machine was purged with nitrogen gas. The temperature was set to 20^{o}C. The photomultiplier voltage was measured at 300nm with a sample chamber containing IPO_4 buffer. 300 µL of 5 µM protein was transferred into a cuvette and loaded into a CD machine (with a pathlength of 0.1 cm) and a wavelength scan protocol was conducted between the 180-300nm range. The raw data output was in millidegrees (m^o) and converted to molar ellipticity ([θ]) via equation 2.2 to account for the concentration of the protein.

$$\textbf{Equation 2.2: } [\boldsymbol{\theta}] = \frac{\boldsymbol{m^o * M}}{\boldsymbol{10 * L * C}}$$

Where [θ] represents the molar ellipticity (deg*cm^2/dmol), m^o represents millidegrees (m^o), M represents the average molecular weight of the protein (g/mol), L represents the path length (cm), and C represents the concentration of protein (g/L).

2.1.10. Mass spectroscopy

0.5 mg/mL samples were kept in 500µL PBS buffer and sent for Mass Spectroscopy; MALDI-TOF analysis run by Dr. Roberto Buccafusca lab.

2.1.11. Generating emulsions with bt-rBSA

The high-speed homogenizer and glass containers were ethanol sprayed then UV sterilised for 15 minutes inside a tissue culture hood. 2 mL of filtered 1mg/mL bt-rBSA protein solution was added to 1mL of filtered Novec-7500 oil inside the glass container. The homogenizer head was lowered into the solution and spun at 15,000 rpm for 2 minutes. The emulsions were left to recover for 5 minutes then transferred using a 3% BSA coated pipette tip into a 3% BSA coated 1 mL Falcon tube. 100 µL of emulsions was transferred to a 3% BSA coated sterile 1.5 mL Eppendorf tube and washed six times with PBS. 100 µL of 100 µg/mL of FITC-Streptavidin (50 µg/mL) was added to the emulsions and incubated at room temperature for 15 minutes. The emulsions were washed six times with PBS and imaged under fluorescent microscope at 488nm.

2.1.12. Interfacial shear rheology

All interfacial shear rheological measurements were carried out on a Discovery Hybrid Rheometer (DHR-3) from TA Instruments. The diamond-shaped Du Noüy Ring (DDR) geometry has a radius of 10 mm and is made of platinum-iridium with a thickness of 0.36 mm. 4 mL of Novec-7500 fluorinated oil was pipetted into the circular double walled trough. Using Axial force monitoring the ring was positioned at the surface of the fluorinated oil interface, a further 180 µm was subtracted from the

contact point to position the medial plane of the ring at the interface. The trough was then filled with 4 mL of PBS solution to fully cover the oil subphase. A time sweep with a constant frequency of 0.1 Hz, a temperature of 25ºC and a displacement of $1.0x10^{-3}$ rad was run for a total of 12,000 s. After 900 s, a solution of bt-rBSA was injected into the aqueous phase at a final concentration of 1mg/mL and left to self-assemble at the interface for 1 hour. After 1 hour a frequency sweep with a displacement of 1.0 10^{-3} rad was carried out, followed by a series of stress relaxation experiments ranging from 0-1% stress. The measurement was paused and the aqueous phase was then washed with 30 mL of PBS using the Elve-flow system at 1 mL/min flowrate for 30 minutes. The interface was given a further 5 minutes to recover and then a solution of Streptavidin was injected into the aqueous phase at a final concentration of 100 µg/mL. Time and frequency sweeps were repeated, followed by stress relaxation experiments and ultimately an amplitude sweep at a frequency of 0.1 Hz.

2.2. Expression and purification of rBSA in *E. coli*

2.2.1. Plasmid cloning and design

The BSA protein sequence used for this experiment was the 3v03 *Bos taurus* sequence. The pOPIN expression vector suite was utilised for this project (kindly gifted by Dr. Rose Protein Facility lab), this contains a wide variety of pre-set vectors that contain different expression tags. The three most commonly used were selected: the GST, MBP and SUMO tags. The subsequent vectors were designed manually using the SnapGene software and ordered via the ThermoFisher GeneArt services. The codons were optimised using this service to the *E. coli* host codons to ensure the highest

reliability in expression. The inserts were then ordered synthesised in a ThermoFisher standard pEX-A2 vector containing the Amp® ampicillin resistance gene.

1 µL of pEX-A2-rBSA vector was transformed into 50 µL of JM109 bacterial cells via standard heat shock at 42ºC and plated onto 100 µg/mL ampicillin LB plates overnight at 37ºC. One colony was picked, transferred into 5mL of 100µg/mL ampicillin LB media and incubated overnight at 37ºC, 220 rpm. 2 mL of the resulting starter culture was centrifuged at 14k rpm and the pellet was mini-prepped using a QIAGEN QIAprep miniprep kit with a final elution volume of 50 µL. pEX-A2-BSA and the three POPIN vectors were digested separately with HindIII and KpnI restriction enzymes at 37ºC for 15 minutes using the digestion master mix in Table 8.

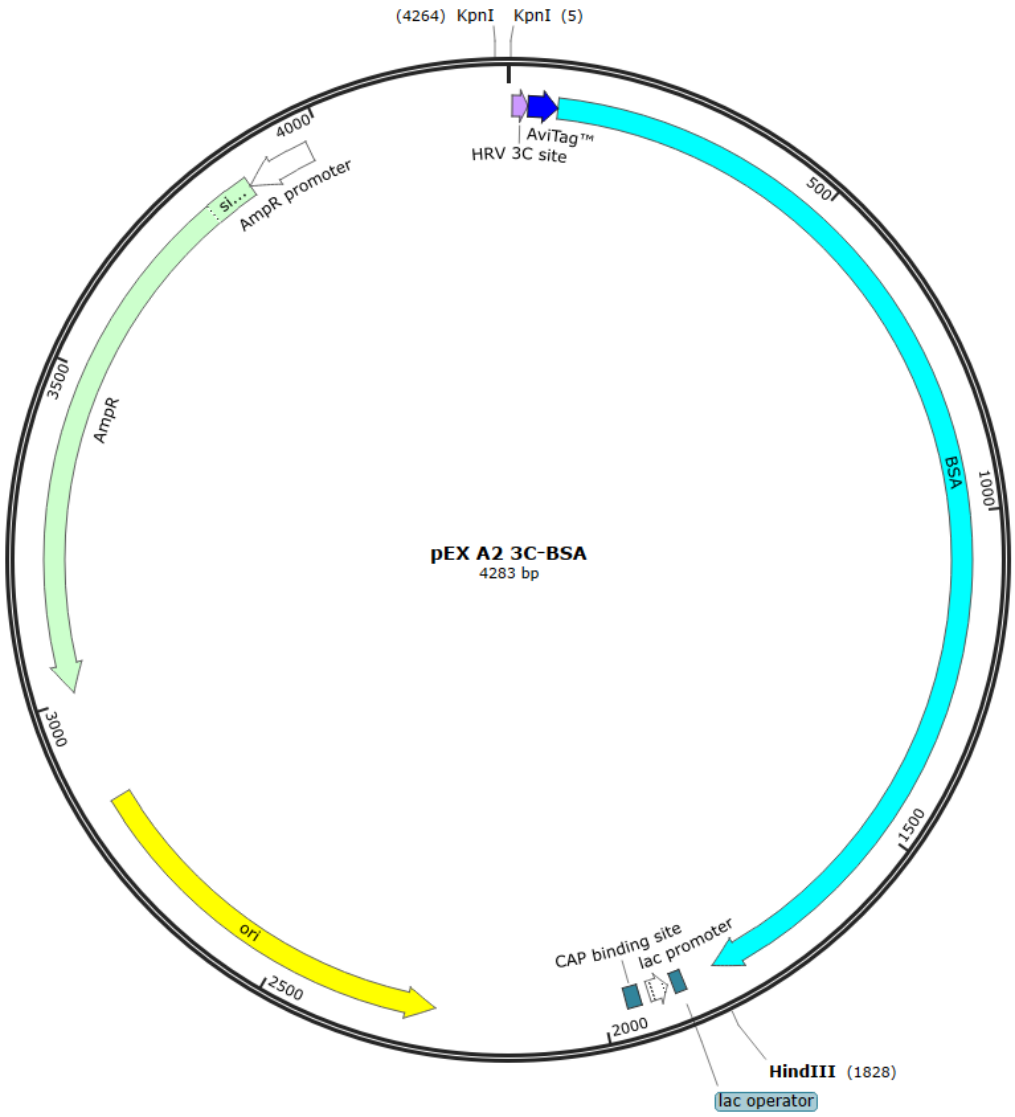

Figure 16: A schematic depicting the pEX-A2-Avi-rBSA plasmid constructed using the SnapGene software[453]. Purple = HRV 3C cleavage site. Dark Blue = AviTag. Cyan = rBSA sequence 3v03, ThermoFisher Optimised. Green = AmpR, Ampicillin resistance gene.

Table 8: Digestion master mix for the digestion of pEX-A2-BSA and the pOPIN plasmids. 10 µL of each plasmid was digested using the master mix in separate tubes. Total reaction volume was 50 µL.

	pOPIN-S3C	pOPIN-J	pOPIN-M	pEXA2-BSA
10x FD Green buffer	5 µL	5 µL	5 µL	5 µL
HindIII endonuclease	3 µL	3 µL	3 µL	3 µL
KpnI endonuclease	3 µL	3 µL	3 µL	3 µL
ddH_2O	29 µL	29 µL	29 µL	29 µL

20 µL of the digested plasmids were run on a 1% agarose gel for 30 minutes at 120V, 5 µL of DNA ladder was also added into the first lane. The BSA insert (1820 bp) and pOPIN vector (~8000 bp) were purified out of 1% agarose gel using a GeneJET gel extraction kit with a final elution volume of 50 µL. 4.5 µL of digested BSA was independently mixed with 0.5 µL of each digested pOPIN vector and 5 µL of Instant sticky end master mix.

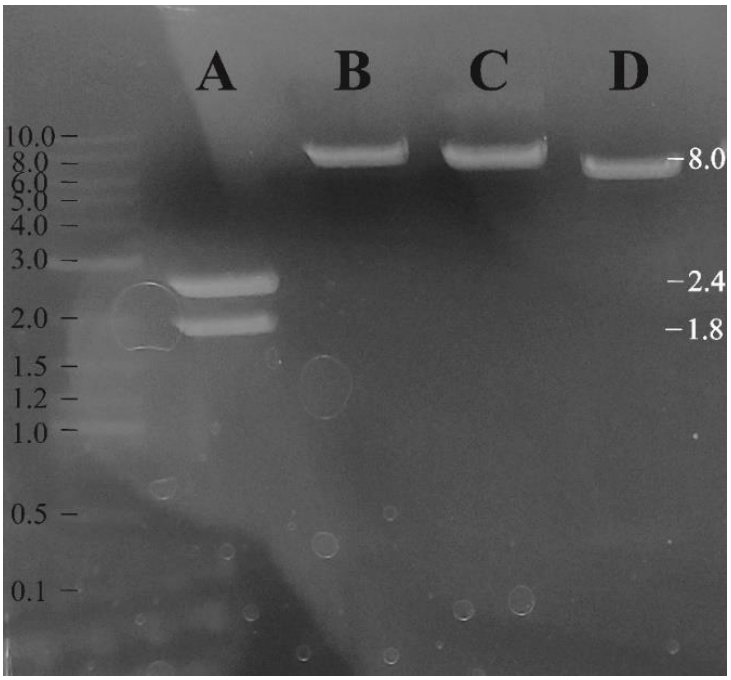

Figure 17: Digestion of cloning plasmids using HindIII and KpnI run on a 1% agarose gel, 120V for 30 minutes. A) pEX-A2-BSA plasmid digest. B) pOPIN-M plasmid digest. C) pOPIN-J Plasmid digest. D) pOPIN-S3C plasmid digest. Avi-BSA insert runs at roughly 1.8kbp. DNA ladder is in kbp (kilobase pairs).

5 µL of the resultant ligations were transformed into DH5α *E. coli* (high chemical competency) cells using the standard heat shock procedure and 200µL of the transformation was plated onto a 100 µg/mL ampicillin LB plate and incubated overnight at 37^{o}C. Six colonies were picked from the plates to form 5 mL starter cultures and subsequently 2mL of culture was miniprepped. For storage of colonies to be analysed, 500 µL of each starter culture was mixed with 500 µL of 30% Glycerol, vortexed, snap frozen with liquid nitrogen then stored at -80^{o}C. Analytical digests run at 37^{o}C for 15 minutes using the digestion mix below (Table 9) were setup for the miniprepped plasmids and run on 1% agarose gels at 120V for 30 minutes.

Table 9: Digestion master mix for the analytical digest of miniprepped pOPIN-BSA plasmids. 3 µL of each plasmid was digested in a separate digestion master mix in separate tubes. Total reaction volume was 10 µL.

	pOPIN-S3C-BSA	pOPIN-J-BSA	pOPIN-M-BSA
10x FD Green buffer	1 µL	1 µL	1 µL
HindIII endonuclease	0.5 µL	0.5 µL	0.5 µL
KpnI endonuclease	0.5 µL	0.5 µL	0.5 µL
ddH_2O	5 µL	5 µL	5 µL

The gel was observed for the generation of two bands, one for the empty pOPIN plasmid (~8000 bp) and another for the rBSA insert (~1820 bp).

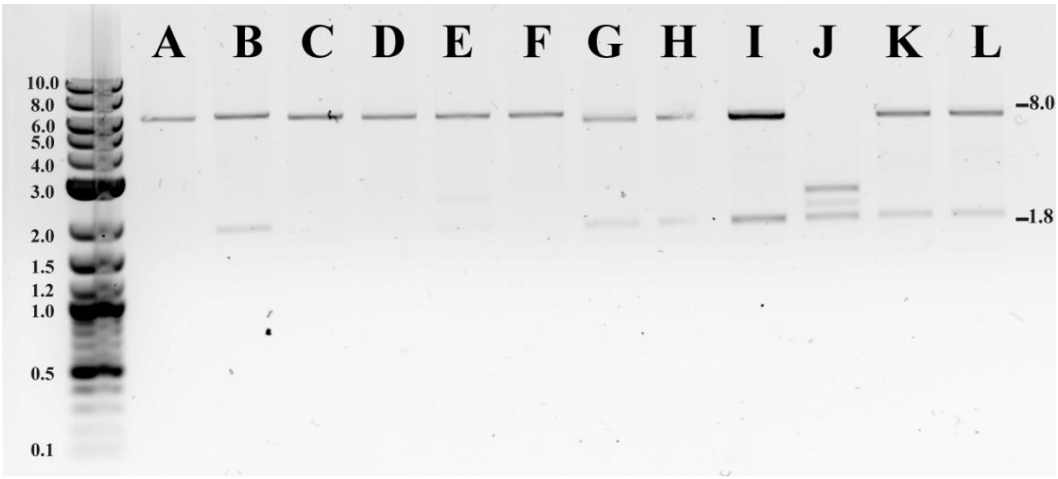

Figure 18: Analytical digest of pOPIN-S3C-BSA and pOPIN-J-BSA miniprepped colonies on a 1% agarose gel, 120V for 30 minutes. Plasmids were digested using HindIII and KpnI restriction enzymes. A-F) pOPIN-J-BSA digests. G-L) pOPIN-S3C-BSA digests. Avi-BSA insert runs at roughly 1.8kbp. DNA ladder is in kbp.

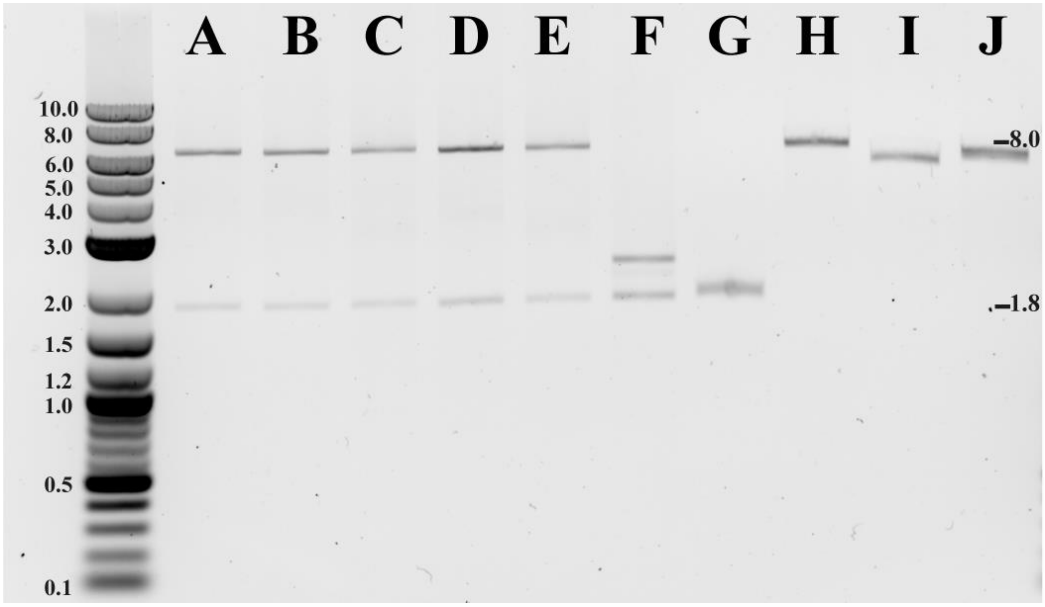

Figure 19: Analytical digest of pOPIN-M-BSA miniprepped colonies on a 1% agarose gel, 120V for 30 minutes. Plasmids were digested using HindIII and KpnI restriction enzymes. A-G) pOPIN-M-BSA digests. H) pOPIN-M backbone vector digest. I) pOPIN-S3C backbone vector digest. J) pOPIN-J backbone vector digest. Avi-BSA insert runs at roughly 1.8 kbp. DNA ladder is in kbp.

10 µL of successful plasmids were sent off for sequencing to further verify the sequence along with 10 µM 5' T7 forward primer. A successful transformant from each plasmid was streaked onto a 100 µg/mL ampicillin LB plate and incubated at 37ºC overnight. Colonies were picked and transferred into 50 mL 100 µg/mL ampicillin LB media and incubated overnight at 37ºC. The cultures were midi-prepped using the QIAGEN plasmid plus midi prep kit. Plasmids were stored at -20ºC until required.

2.2.2. Transformation into *E. coli*

1µL of pOPIN-M-BSA and pOPIN-S3C-BSA vectors was added to 30 µL of SHuffle® T7 Express *E. coli* Competent cells (NEB Biolabs). Each sample was incubated on ice for 5 minutes, then heat shocked at 42ºC using a preheated water bath, then instantly placed on ice for 30 minutes to recover. 200 µL of LB media was added to each sample then incubated at 37ºC for 1 hour, 200 rpm. All the volumes were plated onto separate 100 µg/mL ampicillin LB plates overnight at 37ºC.

2.2.3. Small scale expression of rBSA in *E. coli*

The Avi-BSA protein expression was trialled in *E. coli* with a small-scale expression at varying temperatures. Furthermore, the best expression conditions for MBP-BSA and S3C-BSA proteins were further scaled up to 1 L cultures.

Table 10. Tabulated expression conditions for each of the pOPIN-BSA vectors used in SHuffle *E. coli* cells.

Vector/Strain:	Expression condition:
pOPIN-M-BSA / SHuffle (Small scale)	Overnight expression at 16ºC, 30ºC and 37ºC
pOPIN-S3C-BSA / SHuffle (Small scale)	Overnight expression at 16ºC, 30ºC and 37ºC
pOPIN-M-BSA / SHuffle (1 L scale)	Overnight expression at 16ºC
pOPIN-S3C-BSA / SHuffle (1 L scale)	Overnight expression at 16ºC

Smaller scale expression tests, in 15 mL SHuffle® T7 Express *E. coli* cultures, were carried out at the start to determine which condition would result in the best expression of recombinantly tagged BSA protein.

A single colony was picked for each vector and transferred to 5mL of LB containing 100 µg/mL Ampicillin, then incubated overnight at 37ºC. 150 µL of starter culture was transferred into separate 50 mL Falcon tube containing 15 mL of LB and 100

µg/mL Ampicillin. Cultures were incubated at 37ºC until O/D_{600} = ~0.6. Each condition (Table 10) was induced with 15 µL of 1 M IPTG at a final concentration of 1mM, and incubated at 16ºC, 30ºC and 37ºC overnight respectively. Cultures were pelleted at 4000 rpm for 10 minutes, the supernatant discarded and the pellet resuspended in binding buffer (25 mM Tris-Cl pH 8.0 + 200 mM NaCl + 20 mM Imidazole). The cells were lysed using sonication at 100% power, 30 second pulse for four minutes. Lysate samples were taken. Lysed cells were then centrifuged at 14,000 rpm for 10 minutes; the supernatant was collected and the pellet resuspended in 200 µL of binding buffer. The supernatant was incubated with 500 µL of pre-washed HisPur™ Ni-NTA Resin for 1 hour at 4ºC, then added to a PD10 holding cylinder, washed six times with binding buffer and eluted in 1 mL of elution buffer (25 mM Tris-Cl pH 8.0 + 500 mM NaCl + 500 mM Imidazole). Samples were mixed with 2x SDS dye, boiled at 95ºC for five minutes then run on a SDS page gel with Tris-glycine SDS running buffer at 230v for 20 minutes. Gels were stained with Instant Blue and imaged under a transilluminator.

2.2.4. Large scale expression of rBSA in *E. coli*

The MBP-rBSA and S3C-rBSA conditions were chosen to be scaled up to 1 L in SHuffle® T7 Express *E. coli* Competent cells. A single colony was picked from their respective ampicillin plates and transferred to 10 mL of LB containing 100 µg/mL Ampicillin, then incubated overnight at 37ºC. 10 mL of starter culture was used to inoculate 1 L of LB containing 100 µg/mL Ampicillin and incubated at 37ºC until O/D_{600} = 0.6. The temperature was reduced to 16ºC and cultures were induced

overnight by adding 1000 µL of 1 M IPTG at a final concentration of 1 mM. Cells were harvested by centrifugation at 4000 rpm for 15 minutes and the supernatant was discarded. The pellet was resuspended in 20 mL of binding buffer (25 mM Tris-Cl pH 8.0 + 500 mM NaCl + 10 mM Imidazole) and sonicated at 100% power, 30 second pulse for six minutes. Lysed cells were then centrifuged at 30,000 x g for 20 minutes at 4^{o}C using a Beckman JA-30.50Ti Fixed-Angle Titanium Rotor. The supernatant was collected in a 50 mL Falcon tube and the pellets were resuspended in 5 mL of binding buffer. The supernatant was incubated with 2 mL of pre-washed HisPur™ Ni-NTA Resin (Thermo Fisher Scientific) for 1 hour at 4^{o}C, then centrifuged for 10 seconds at 1000 rpm and the supernatant was discarded. The resin was resuspended in 10mL of wash buffer (25 mM Tris-Cl pH 8.0 + 500 mM NaCl + 10 mM Imidazole) and transferred to a PD10 holding cylinder. The buffer was allowed to drip through by gravity, then washed six column volumes with wash buffer.

To elute the protein from the resin, 10 mL of elution buffer (25 mM Tris-Cl pH 8.0 + 500 mM NaCl + 500 mM Imidazole) was added into the column and collected into 2 mL fractions. Elution fractions were pooled and a final concentration of 10% glycerol added then snap-frozen in liquid nitrogen and stored at -80^{o}C. Samples were mixed with 2x SDS dye, boiled at 95^{o}C for five minutes then run on a SDS page gel with Tris-glycine SDS running buffer at 230V for 20 minutes. Gels were stained with Instant Blue and imaged under a transilluminator. PD10 columns were regenerated by washing once with column regeneration buffer (1 M NaCl + 0.1 M NaOH), once with water and then filled to half with 20% ethanol; stored in 4^{o}C.

2.3. Expression and purification of rBirA in *E. coli*

2.3.1. Plasmid design and cloning

The BirA protein sequence used for this experiment was the P06709 *E. coli* sequence. The pOPIN expression vector suite was utilised for rBirA just as it was used for *the E. coli* expression of rBSA. The subsequent vectors were designed manually using the SnapGene software and ordered via the ThermoFisher GeneArt services. The codons were optimised using this service to the *E. coli* host codons to ensure the highest reliability in expression. The inserts were then ordered synthesised in a ThermoFisher standard pEX-A2 vector containing the Amp® ampicillin resistance gene.

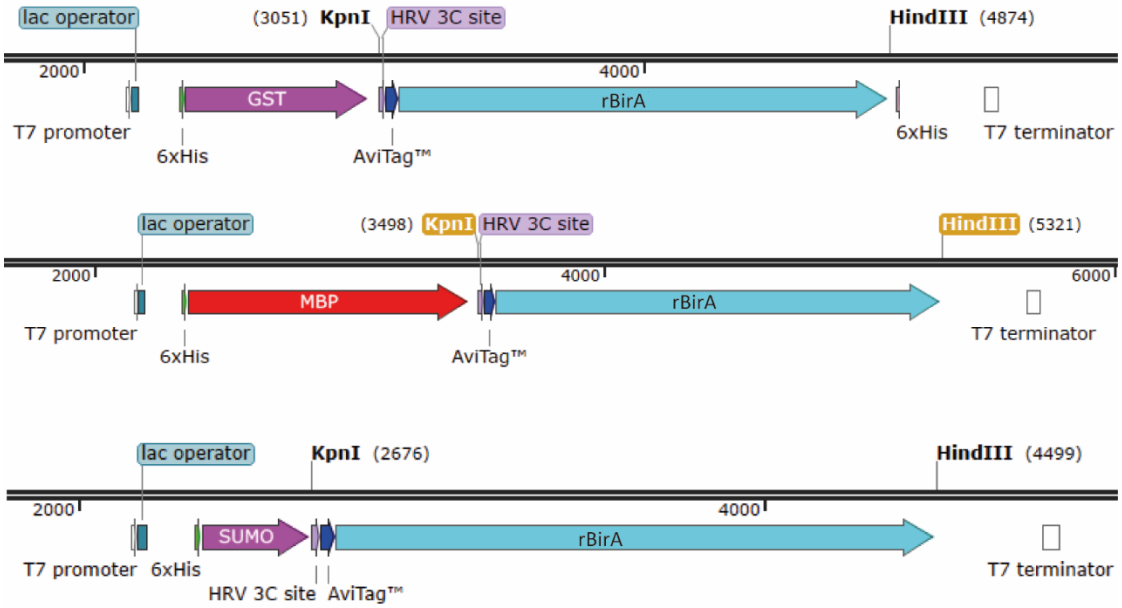

Figure 20: A schematic depicting the various pOPIN vector main components within the T7 promoter and terminator region. The vectors pOPIN-J-BirA, pOPIN-M-BirA vector and pOPIN-S3C-BirA respectively. Constructed using the SnapGene software[453].

1 µL of pEX-A2-rBirA vector was transformed into 50 µL of JM109 bacterial cells via standard heat shock at 42°C and plated onto 100 µg/mL ampicillin LB plates overnight at 37°C. One colony was picked, transferred into 5 mL of 100 µg/mL ampicillin LB media and incubated overnight at 37°C, 220 rpm. 2 mL of the resulting starter culture was centrifuged at 14k rpm and the pellet was mini-prepped using a QIAGEN QIAprep miniprep kit with a final elution volume of 50 µL. pEX-A2-rBirA and the three POPIN vectors were digested separately with HindIII and KpnI restriction enzymes at 37°C for 15 minutes using the digestion master mix in Table 11.

Table 11: Digestion master mix for the digestion of pEX-A2-BirA and the pOPIN plasmids. 10 µL of each plasmid was digested using the master mix in separate tubes. Total reaction volume was 50 µL.

	pOPIN-S3C	pOPIN-J	pOPIN-M	pEXA2-BirA
10x FD Green buffer	5 µL	5 µL	5 µL	5 µL
HindIII endonuclease	3 µL	3 µL	3 µL	3 µL
KpnI endonuclease	3 µL	3 µL	3 µL	3 µL
ddH_2O	29 µL	29 µL	29 µL	29 µL

20 µL of the digested plasmids were run on a 1% agarose gel for 30 minutes at 120V, 5 µL of DNA ladder was also added into the first lane. The rBirA insert (997 bp) and pOPIN vector (~8000 bp) were purified out of 1% agarose gel using a GeneJET gel extraction kit with a final elution volume of 50 µL.

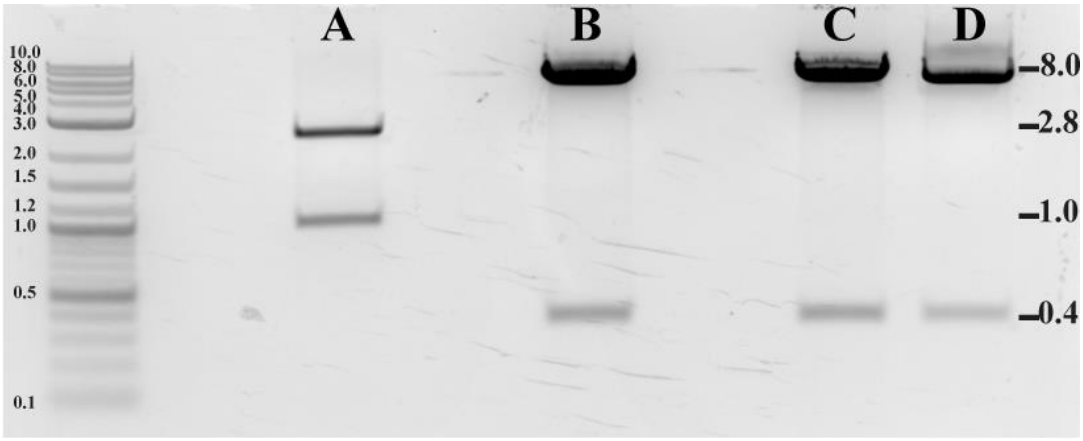

Figure 21: Digestion of cloning plasmids using HindIII and KpnI run on a 1% agarose gel, 120V for 30 minutes. A) pEX-A2-rBirA plasmid digest. B) pOPIN-M plasmid digest. C) pOPIN-J Plasmid digest. D) pOPIN-S3C plasmid digest. DNA ladder is in kbp.

Table 12: Analytical digest mixes for rBirA and the three pOPIN vectors. The "d" prefix indicates that the plasmids were digested with HindIII and KpnI.

Component	S3C plasmid	M plasmid	J plasmid
dpOPIN-S3C	0.5 µL	-	-
dpOPIN-J	-	0.5 µL	-
dpOPIN-M	-	-	0.5 µL
drBirA	4.5 µL	4.5 µL	4.5 µL
Instant sticky end (mm)	5 µL	5 µL	5 µL

4.5 µL of digested rBirA was independently mixed with 0.5 µL of each digested pOPIN vector and 5 µL of Instant sticky end master mix (mm) (Table 12). 5 µL of the resultant ligations were transformed into DH5α *E. coli* (high competency) cells using the standard heat shock procedure and 200 µL of the transformation was plated onto a 100 µg/mL ampicillin LB plate and incubated overnight at 37^{o}C. Six colonies were picked from the plates to form 5 mL starter cultures and subsequently 2 mL of culture was miniprepped. For temporary storage of the colonies to be analysed, 500 µL of

each starter culture was mixed with 500 µL of 30% Glycerol, vortexed, snap frozen with liquid nitrogen then stored at -80^{o}C. Analytical digests run at 37^{o}C for 15 minutes using the digestion mix in Table 13 were setup for the miniprepped plasmids and run on 1% agarose gels at 120V for 30 minutes.

Table 13: Digestion master mix for the analytical digest of miniprepped pOPIN-BirA plasmids. 3 µL of each plasmid was digested in a separate digestion master mix in separate tubes. Total reaction volume was 10 µL.

	pOPIN-S3C-BirA	pOPIN-J-BirA	pOPIN-M-BirA
10x FD Green buffer	1 µL	1 µL	1 µL
HindIII endonuclease	0.5 µL	0.5 µL	0.5 µL
KpnI endonuclease	0.5 µL	0.5 µL	0.5 µL
ddH_2O	5 µL	5 µL	5 µL

The gel was observed for the generation of two bands, one for the empty pOPIN plasmid (~8000 bp) and another for the rBirA insert (997 bp). 10 µL of successful plasmids were sent off for sequencing to further verify the sequence along with 10 µM 5' T7 forward primer. A successful transformant from each plasmid was streaked onto a 100 µg/mL ampicillin LB plate and incubated at 37^{o}C overnight. Colonies were picked and transferred into 50 mL 100 µg/mL ampicillin LB media and incubated overnight at 37^{o}C. The cultures were midi-prepped using the QIAGEN plasmid plus midi prep kit. Plasmids were stored at -20^{o}C until required.

2.3.2. Transformation into *E. coli*

1 µL of each pOPIN vector was added to a separate 30 µL of Rosetta (DE3) *E. coli* cell line and SHuffle® T7 Express *E. coli* Competent cells. Each sample was incubated on ice for 5 minutes, then heat shocked at 42ºC using a preheated water bath, then instantly placed on ice for 30 minutes to recover. 200 µL of LB media was added to each sample then incubated at 37ºC for 1 hour, 200 rpm. All the volumes were plated onto separate 100 µg/mL ampicillin LB plates overnight at 37ºC. The next day, 10 colonies were picked from the Agar plates and transferred into 20 mL LB with a final concentration of 100 µg/mL ampicillin, then incubated overnight at 37ºC, 200 rpm. The next day, 10 mL of starter culture was used to inoculate 1 L of fresh LB media with a final concentration of 100 µg/mL ampicillin. The separate cultures were incubated at 16ºC, 220 rpm overnight.

2.3.3. Small scale expression trials of rBirA in *E. coli*

Smaller scale expression trials in 15mL Rosetta (DE3) *E. coli* cultures were conducted at the start to determine which condition would result in the best expression of recombinantly tagged BSA protein. A single colony was picked for each vector and transferred to 5 mL of LB containing 100 µg/mL Ampicillin, then incubated overnight at 37ºC. 150 µL of starter culture was transferred into separate 50mL Falcon tube containing 15 mL of LB and 100 µg/mL Ampicillin. Cultures were incubated at 37ºC until O/D_{600} = ~0.6. Each tube was induced with 15 µL of 1 M IPTG at a final concentration of 1mM, and incubated at 16ºC overnight, 220 rpm. Cultures were

pelleted at 4000 rpm for 10 minutes, the supernatant discarded and the pellet resuspended in binding buffer (25 mM Tris-Cl pH 8.0 + 200 mM NaCl + 20 mM Imidazole). The cells were lysed using sonication at 100% power, 30 second pulse for four minutes. Lysed cells were then centrifuged at 14,000 rpm for 10 minutes; the supernatant was collected and the pellet resuspended in 200 µL of binding buffer. The supernatant was incubated with 500 µL of pre-washed HisPur™ Ni-NTA Resin for 1 hour at 4°C, then added to a PD10 holding cylinder, washed six times with binding buffer and eluted in 1mL of elution buffer (25 mM Tris-Cl pH 8.0 + 500 mM NaCl + 500 mM Imidazole). Samples were mixed with 2x SDS dye, boiled at 95°C for five minutes then run on a SDS page gel with Tris-glycine SDS running buffer at 230V for 20 minutes. Gels were stained with Instant Blue and imaged under a transilluminator. PD10 columns were regenerated by washing once with column regeneration buffer (1M NaCl + 0.1 M NaOH), once with water and then filled to half with 20% ethanol; stored at 4°C.

2.3.4. Large scale expression of rBirA in E. coli

The MBP-rBirA condition was chosen to be scaled up to 1 L in SHuffle® T7 Express *E. coli* Competent cells. A single colony was picked from the ampicillin plate and transferred to 10 mL of LB containing 100 µg/mL Ampicillin, then incubated overnight at 37°C. 10 mL of starter culture was used to inoculate 1 L of LB containing 100 µg/mL Ampicillin and incubated at 37°C until O/D_{600} = 0.6. The temperature was reduced to 16°C and cultures were induced overnight by adding 1000 µL of 1 M IPTG at a final concentration of 1 mM. Cells were harvested by centrifugation at 4000 rpm

for 15 minutes and the supernatant was discarded. The pellet was resuspended in 20 mL of binding buffer (PBS + 10 mM Imidazole) and sonicated at 100% power, 30 second pulse for six minutes. Lysed cells were then centrifuged at 30,000 x g for 20 minutes at 4^{o}C using a Beckman JA-30.50Ti Fixed-Angle Titanium Rotor. The supernatant was collected in a 50 mL Falcon tube and the pellets were resuspended in 5 mL water. The supernatant was incubated with 2 mL of pre-washed HisPur™ Ni-NTA Resin (Thermo Fisher Scientific) for 1 hour at 4^{o}C, then centrifuged for 10 seconds at 1000 rpm and the supernatant was discarded. The resin was resuspended in 10 mL of wash buffer (PBS + 10 mM Imidazole) and transferred to a PD10 holding cylinder. The buffer was allowed to drip through by gravity, then washed six column volumes with wash buffer.

To elute the protein from the resin, 10 mL of elution buffer (PBS + 500 mM Imidazole) was added into the column and collected into 2 mL fractions. Elution fractions were pooled and a final concentration of 10% glycerol added then snap-frozen in liquid nitrogen and stored at -80^{o}C. Samples were mixed with 2x SDS dye, boiled at 95^{o}C for five minutes then run on a SDS page gel with Tris-glycine SDS running buffer at 230V for 20 minutes. Gels were stained with Instant Blue and imaged under a transilluminator. PD10 columns were regenerated by washing once with column regeneration buffer (1 M NaCl + 0.1 M NaOH), once with water and then filled to half with 20% ethanol; stored at 4^{o}C.

2.4. Biophysics of protein nanosheets

The fluorinated surfactant 2,3,4,5,6-Perfluoro benzoyl chloride, PBS, Trichloro (1H,1H,2H,2H-perfluorooctyl) silane (97%) and the 1H,1H,2H,2H-Perfluorodecanethiol (97%) were purchased from Sigma Aldrich Co. The fluorinated oil (Novec-7500; 3M) is from ACOTA. The SPR-Au chips were obtained from Ssens. Fibrinogen and Thrombin from bovine plasma were purchased from Sigma-Aldrich. Human Bone Marrow Derived Mesenchymal Stem Cells and relevant media were purchased from PromoCell. Thin Glass slides (25x60 mm) from VWR. Sticky-slide 8 well plates from Ibidi. Human Plasma Fibronectin Purified Protein purchased Merck Millipore.

2.4.1. Interfacial shear rheology

All interfacial shear rheological measurements were carried out on a Discovery Hybrid Rheometer (DHR-3) from TA Instruments. The diamond-shaped Du Noüy Ring (DDR) geometry has a radius of 10mm and is made of platinum-iridium with a thickness of 0.36 mm.

4mL of Novec-7500 fluorinated oil was pipetted into the circular double walled trough. Using Axial force monitoring the ring was positioned at the surface of the fluorinated oil interface, a further 200 μm was subtracted from the contact point to position the medial plane of the ring at the interface.

The trough was then filled with 4 mL of PBS solution to fully cover the oil subphase. A time sweep with a constant frequency of 0.1 Hz, a temperature of 25^{o}C and a displacement of 1.0x10^{-3} rad was run for a total of 12,000 seconds. After 900 seconds, a solution of fibrinogen was injected into the aqueous phase at a final concentration of 1 mg/mL and left to self-assemble at the interface for 30 minutes. The aqueous phase was then washed with 30 mL of PBS using the Elve-flow system at 1 mL/min flowrate for 30 minutes and a further 5 minutes to recover. Next, a solution of thrombin at varying concentrations ranging from 0.25-1.0 U/mL was injected into the aqueous phase. After the completion of the time sweep, frequency sweeps (with a displacement of 1.0x10^{-3} rad) and stress relaxation experiments were conducted followed by an amplitude sweep at a frequency of 0.1 Hz. For stress growth experiments the amplitude sweep was replaced by a stress/strain protocol with a velocity of 0.05 rad/s for 3600s at 25^{o}C.

2.4.2. Surface plasmon resonance

All SPR measurements were carried out on a BIACORE X from Biacore AB. Gold coated SPR chips measuring 10x12 mm in size were plasma oxidised for five minutes using the Henniker Plasma HPT-200 machine. Then treated in a 5% methanolic solution of 1H,1H,2H,2H-Perfluorodecanethiol overnight at room temperature; this generated a fluorinated monolayer which serves as a model to mimic the fluorinated Novec-7500 oil. The chips were then washed once with water and dried in air prior to mounting.

The maintenance sensor chip cassette was placed into the sensor chip port and docked onto the Integrated μ-Fluidic Cartridge (IFC) flow block. The system was then primed with ethanol and the maintenance chip removed. The sample sensor chip was then mounted onto a plastic support frame, docked and primed once with PBS. Once primed the signal was allowed to stabilise to a stable baseline. 50 μL of 1mg/mL Fibrinogen protein solution (in PBS) was then loaded into the IFC sample loop with a micropipette at a flow rate of 10 μL/min.

Once injection had finished, the surface of the sample chip was washed with PBS for 10 minutes at a flow rate of 1 0μL/min and then Thrombin (in PBS) was injected with a volume of 50 μL at a flow rate of 10 μL/min. Another washing step was conducted to wash off excess Thrombin and data collection was allowed to continue for another 10 minutes.

2.4.3. Scanning electron microscopy (SEM)

Using a diamond pen, silicon wafers were generated with an approximate area of 1 cm^2, then washed with ethanol and air dried to remove any residues.

The wafers were transferred into a 24 well plate and emulsions generated in ddH_2O (to reduce any salt crystal formations) were deposited onto the surface of the wafers and left to dry for three days. Sample wafers were docked onto an aluminium stub using conductive double-sided tape and coated with gold using a vacuum coater at a thickness of ~6nm. Samples were collected at a voltage of 5 kV, 3 spot size, an aperture of 6 and a working distance of 10 mm at magnifications between 3000-12000x.

2.4.4. Transmission electron microscopy (TEM)

All samples were prepared using the KbnLayer software-controlled robot arm in a 30 mL glass vial (diameter 30 mm).

One carbon lacey grid was mounted onto the robot arm clip as such only the outer edge was in contact with the clip. 4 mL of fluorinated oil was pipetted into the glass vial. The grid was then lowered slowly until full submersion under the oil subphase. The vial was then filled with 3 mL of PBS to fully cover the oil sub-phase. After 15 minutes, Fibrinogen solution was injected into the aqueous phase at a final concentration of 1 mg/mL and left to self-assemble at the interface for one hour.

The aqueous phase was then washed with ddH_2O using the Elve-flow system at 1mL/min flowrate for 30 minutes. The interface was given 10 minutes to recover and then treated with varying concentrations of Thrombin for 30 minutes. The robotic arm was then lifted at a rate of 0.5 mm/min until the grid was completely immersed in the aqueous phase. Grids were allowed to dry in a 24 well plate for 7 days.

All samples were imaged using the JEOL-1230 TEM at a voltage of 80 kV, spot size 1 and a beam current of 67 µA at magnifications between 1000-100,000x.

2.4.5. Fluorinated pinned droplets for cell culture

Isopropanol washed thin glass slides (25 x 60 mm) were plasma oxidised at 100% power for 10 minutes using the Henniker Plasma HPT-200 machine. The slides were then treated in a 5% methanolic solution of Trichloro (1H,1H,2H,2H-perfluorooctyl) silane for 1 hour at room temperature. The fluorinated glass slides were washed once with methanol and dried with nitrogen gas. The slides were mounted onto Ibidi sticky-slide 8 well plates and sterilised promptly with 70% ethanol. The wells were washed once with sterile dPBS and filled with 600 µL of dPBS. 6 µL of filtered Novec-7500 oil was then pipetted with a circular motion onto the surface of each well.

300 µL of dPBS was removed from each well and replaced with 300 µL of filtered 2 mg/mL Fibrinogen solution, this was allowed to incubate for 30 minutes at 37^{o}C. The wells were then washed five times with dPBS to remove excess fibrinogen in solution, and treated with varying concentrations of a 100 U/mL Thrombin stock solution for 30 minutes at 37^{o}C. After 30 minutes, 25 µg/mL Fibronectin was then added into each well and incubated for 1 hour at RT. The wells were washed once with dPBS and twice with MSC medium and left to recover at 37^{o}C for 3 hours.

MSCs were seeded onto the pinned droplets at a cell density of 6k per well.

2.4.6. Fluorinated flat interface for cell culture

A 24 well plate was plasma oxidised at 100% power for 5 minutes using the Henniker Plasma HPT-200 machine. Two solutions were prepared. Per well to be treated, 300 µL of methanol was mixed with either 12 µL of Triethylamine or 12 µL of Trichloro (1H,1H,2H,2H-perfluorooctyl) silane. 300 µL of each solution was added per well, sealed immediately with parafilm and left to be treated overnight at RT.

The solution was then aspirated, and washed promptly with 70% ethanol and three times with sterile dPBS. The wells were aspirated until dry and 500 µL of Novec-7500 oil was added per well and then 2 mL of dPBS. The plates were incubated for 20 minutes at 37ºC CO_2 incubator. Fibrinogen stock solution (100 mg/mL) was added to a final concentration of 1 mg/mL and incubated for 1 hour. The wells were then washed with dPBS six times to remove excess fibrinogen in solution, and treated with thrombin for 30 minutes. Fibronectin at a final concentration of 25 µg/mL was added and incubated for a further 1 hour. The wells were then washed twice with dPBS and then MSC media.

MSCs were seeded onto flat interfaces at a cell density of 5k per well.

2.4.7. Generating emulsions for cell culture

A 5 mL solution of 3% BSA was used to coat a sterile 50 mL Falcon tube, the solution was discarded. 20 mL of 1mg/mL filtered Fibrinogen solution was added to 10mL of filtered Novec-7500 oil into the coated Falcon tube. The solutions were mixed via ten inversions then vortexed at 3000 rpm for 30 seconds. The emulsions were allowed to settle then washed six times with dPBS. 2 mL of the emulsions was transferred into four sterile 15 mL Falcon tubes coated with 3% BSA and the aqueous volume was made up to 4 mL. Each tube was treated with a specific concentration of 100 U/mL sterile thrombin stock solution and rotated for 30 minutes at room temperature. After 30 minutes, a final concentration of 25 µg/mL sterile Fibronectin was added into each Falcon tube and rotated for 1 hour at room temperature. The aqueous solution was washed six times with dPBS. Using a cut 1000 µL pipette tip coated with 3% BSA 100 µL of emulsions was transferred into wells of a 25 µg/mL poly(L-lysine)-graft-polyethylene glycol (PLL-g-PEG, SuSoS) coated 48 well plate. 400 µL of MSC medium was added to each well and 60k MSCs were seeded into each well.

For the Cyquant assay, a separate plate was made for each condition. Once the time point was reached the media was aspirated from the wells and the plate was stored in -80^{o}C.

To evaluate the stability of emulsions, the samples were prepared as described above and stored at room temperature within glass vials. The emulsions were observed visually for coalescence or the maintenance of emulsion integrity after several weeks and months.

2.4.8. Statistical analysis

All experiments were carried out in experimental triplicates, and quantitative results were presented as mean values with their corresponding standard errors [454]. Statistical analysis was conducted using the OriginPro 9 programme, triplicated means for each condition were inputted into the programme and a One-way ANOVA with a post-hoc Tukey test was run to calculate the whether a statistically significant difference was observed between each condition. A One-way ANOVA with Tukey test was chosen as it helps determine if there are statistically significant difference between the means of three or more groups, this was particularly useful when comparing multiple different conditions. If there was a statistically significant difference between two different conditions the P-value would equate to less than 0.05. If the $P < 0.05$, < 0.01, and < 0.001 a '*, ** and ***' respectively was used to indicate the extent of significance, and if $P > 0.05$ a 'n.s.' was used to indicate no significant difference between the two conditions measured. Furthermore, standard errors were shown on figures to depict the precision of means when multiple conditions were being compared. A flow diagram of the steps taken to measure a statistically significant difference between different conditions can be seen in Figure 22.

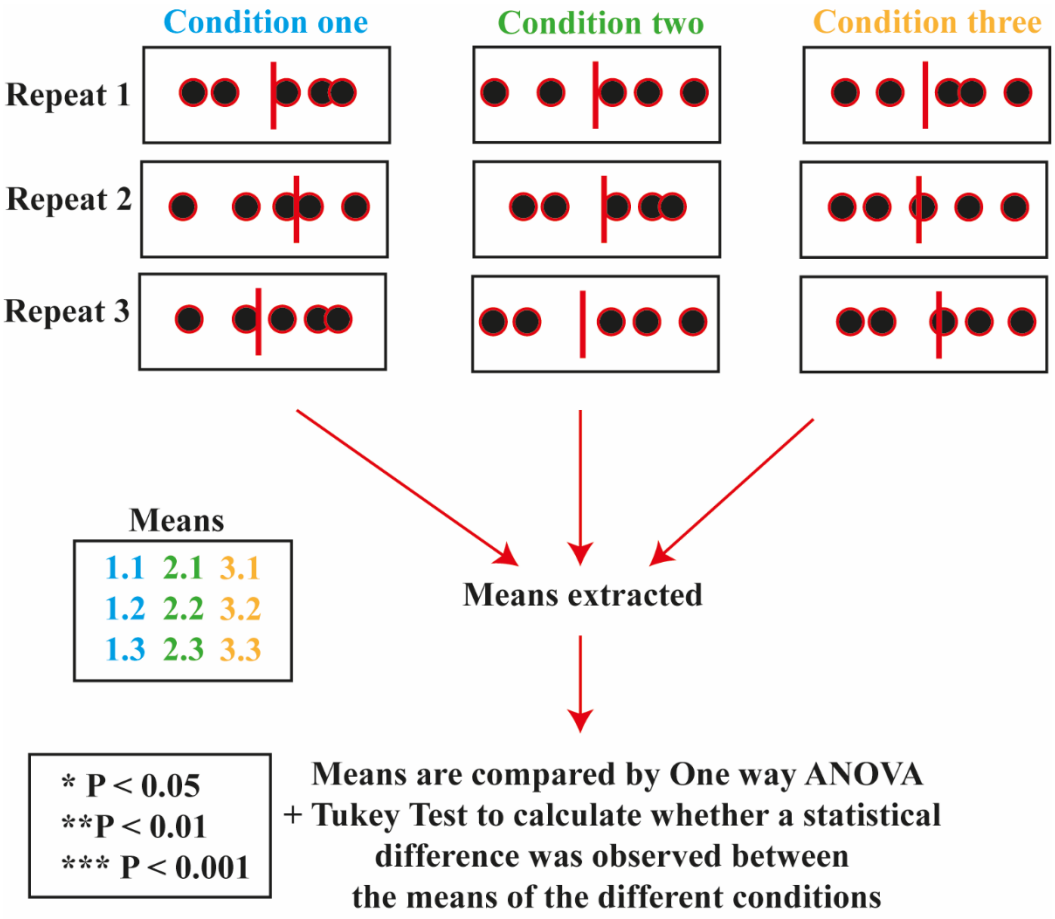

Figure 22: Flow diagram representing the steps taken to measure statistically significant differences. The triplicated means were extracted from each condition and fed into OriginPro software, after which a One-Way ANOVA was run with a Post-hoc Tukey test to calculate whether a statistically significant difference was observed between each condition.

2.4.9. CyQUANT™ assay

Cell densities of emulsions were measured using the CyQUANT™ assay. Once the time points were reached (Day 1, 3 and 7) the well plates were removed from the incubator and the media was aspirated as much as possible without disturbing the emulsions. The plates were stored at -80^{o}C until all the triplicate samples were obtained, after which the samples were thawed at room temperature to induce cell lysis and the resulting suspensions were incubated with the CyQUANT™ kit solutions (attempted to account for dilution) and the protocol provided by the manufacturer was followed. The resulting solutions were transferred into a 96-well plate and the fluorescent intensity was measured using a fluorescence microplate reader at 480nm excitation and 520nm emission. A standard curve was generated using a known cell density of 400k MSC cells (obtained from TPC culture) and this was used to convert the resulting absorbances into cell densities [350].

2.4.10. Hoechst staining

2 μL of Hoechst 33342 (5 mg/mL stock solution) was added to flat interfaces post fixation with 4% PFA, for 30 minutes before fluorescent imaging.

2.4.11. Nuclei count on Pin droplets

Cell counting was conducted by inputting the resultant fluorescent images of pin droplets into ImageJ, filtering by the 408 DAPI channel and applying thresholding followed by water-shedding, nuclei number was obtained by measuring the number of particles in the window.

2.5. Organoid formation

2.5.1. Preparing Matrigel coated plates for hIPSCs cultures

5700 μL of DMEM/F-12 was mixed with 300 μL of thawed Corning® Matrigel® (GFR) Basement Membrane Matrix. 1000 μL of the mix was then pipetted into three wells of two separate 6 well Falcon plates, for a total of six coated wells, swirled to ensure full coverage and incubated at 37^{o}C for 1 hour or until needed; coated plates should not be stored for more than a week.

2.5.2. Preparing hIPSCs for cell culture

Table 14: Media used for the thawing, passaging and maintenance of hIPSCs.

Medium	**Component**	**Volumes**
E8 Flex complete	Essential 8 Flex Basal Medium	24.5 mL
	Essential 8 Flex Supplement	500 μL
E8 Seeding	E8 flex complete	9990 μL
(Per aliquot)	10mM Rock inhibitor (Y-27632)	10 μL (10 μM)
Cell detachment solution	0.5M EDTA (pH 8.0)	1 μL
(Per well)	dPBS	999 μL
Matrigel solution	DMEM/F12	5700 μL
(Per 6 wells)	Matrigel® (GFR)	300 μL

Cultures of hIPSCs were cultured in standard incubator conditions of 5% CO_2 at 37°C.

Any handling or transferring of cells was conducted using a 5ml stripette at low settings to avoid breaking the cell clusters.

10 mL of rock-E8 medium (10 mM Y-27632, final concentration 10 μM) was prepared fresh before thawing and wrapped in foil.

One DMEM/F12-Matrigel coated well was washed once 1 mL of dPBS and replaced with 3 mL of rock-E8 medium.

An aliquot of hIPSCs was removed from the liquid nitrogen cell bank (-80°C) and partially thawed in a 37°C water bath. The cells were transferred using a 5 mL stripette to 5 mL of rock-E8 medium and centrifuged at 300xg for 2 minutes. The supernatant was discarded and the cell pellet was resuspended in 2 mL of rock-E8 medium. The cells were transferred to 3 mL of rock-E8 medium in a Matrigel (GFR) coated wells and incubated at 37°C.

The cells were observed under the microscope to verify that clusters of cells (roughly a few cells per cluster) were present before incubation.

2.5.3. Maintaining and passaging hIPSCs cultures

Cultures of hIPSCs were cultured in standard incubator conditions of 5% CO_2 at 37°C. After 24 hours post-thawing, the rock-E8 media was removed and replaced with 4 mL of complete E8 Flex medium. The media was exchanged every 2 days until cultures reached approximately 80-90% confluency.

Areas of spontaneous differentiation were removed before the passaging process – the media was removed and 1 mL of dPBS was gently pipetted directly onto the affected area to detach the differentiated cells.

Cell detachment solution for passaging was prepared in a 1.5 mL Eppendorf tube by mixing 1 μL of 0.5M EDTA (pH 8.0) with 1 mL of dPBS.

Existing media was removed from the well and replaced with 1ml of cell detachment solution and incubated at 37ºC for 3.5 minutes (if cells were between 90-100%, incubation time was increased to 4 minutes). The solution was slowly pipetted up and down 3-4 times using a 5 mL stripette onto the cells to break up the culture. The cells were then transferred into a sterile 15 mL Falcon tube and centrifuged at 300 x g for 2 minutes.

A fresh Matrigel plate was prepared by removing the existing DMEM/F12-Matrigel solution out of the three wells, washing once with dPBS and replacing with 3 mL of complete E8 Flex medium.

The supernatant was removed carefully using a 1 mL pipette to not disrupt the cell pellet and resuspended into 3ml of complete E8 Flex medium. The cell suspension was evenly distributed between the three wells and incubated at 37ºC for 3-4 days; the cells were observed under the microscope to verify that clusters of cells were present before incubation.

The medium was exchanged every 2 days until 80-90% confluency was obtained, then the passaging cycle was repeated. hIPSCs were used until a cell passage number of roughly 13 or until cells begun to proliferate at a slower rate (taking more than 4-5 days to reach 80% confluency).

2.5.4. Generating Embryoid Bodies

Table 15: Media used for the generation of 30 Embryoid bodies, days -5 to 0.

Medium	Component	Volumes
EB formation	STEMdiff™ Cerebral Organoid Basal Medium 1	8 mL
	STEMdiff™ Cerebral Organoid Supplement A	2 mL
EB seeding	EB formation medium	6994 µL
	10mM Rock inhibitor (Y-27632)	7 µL (10 µM)
Dissociation	Gentle Cell Dissociation Reagent	1 mL

The EB seeding medium was prepared from the EB formation medium and the formation medium was stored at 4^{o}C.

Once the hIPSCs maintenance culture reached a confluency of 80-90%, the media was removed from one well and washed once with dPBS. 1 mL of Gentle dissociation medium was added into the well and incubated at 37^{o}C for 7.5 minutes. The cells were broken gently using a 5ml stripette at low setting 4-5 times and transferred to a sterile 15 mL Falcon tube. 2 mL of EB seeding medium was added to the cells and centrifuged at 300 x g for 2 minutes. The supernatant was removed carefully not disrupting the pellet and resuspended in 1 mL of EB seeding medium. 10 µL was transferred to a haemocytometer and the average cell number/mL was quantified.

The cells were resuspended into 3 mL of EB seeding medium with a final cell density of 90,000 cells/mL. 100µL of cell suspension was added into each well of a sterile 96

well ultra-low attachment (ULA) plate – final cell density per well of 9000 cells. The plate was spun at 700 rpm for 30 seconds, RT to pull the cells into the centre of each well.

The plate was incubated at 37ºC without disruption for the first 24 hours. At day -3, 100 µL of EB formation medium was pipetted gently into each well and incubated for another 2 days (5 days total).

2.5.5. Generating Cerebral organoids

Table 16: Media used for the generation of 30 cerebral organoids, days 0 to 9.

Medium	Component	Volumes
Expansion	STEMdiff™ Cerebral Organoid Basal Medium 2	5,700 µL
	STEMdiff™ Cerebral Organoid Supplement C	60 µL
	STEMdiff™ Cerebral Organoid Supplement D	120 µL
	Matrigel for culture (2% Final)	120 µL
Maturation	STEMdiff™ Cerebral Organoid Basal Medium 2	5,760 µL
	STEMdiff™ Cerebral Organoid Supplement E	120 µL
	Matrigel for culture (2% Final)	120 µL

At day 0, the EBs were induced to the cerebral lineage. Using a 1000 µL pipette tip, the formation media was carefully removed from each well, leaving behind the EB in the well (roughly 4-5 wells per tip). 200 µL of EB induction medium was then pipetted onto the walls of each well with minimal disruption of the EB. The plate was incubated for another 2 days at 37ºC.

At day 2, the EB expansion medium was prepared and the thawed Matrigel was added fresh immediately before starting. Using a 1000 μL pipette tip, the induction media was removed from each well, leaving behind the EB in the well (roughly 4-5 wells per tip). 200 μL of EB expansion medium was then pipetted into each well with minimal disruption of the EB. The plate was further incubated for 3 days.

At day 5, the EB maturation medium was prepared and the thawed Matrigel was added fresh immediately before starting. Using a 1000 μL pipette tip, the expansion media was removed from each well, leaving behind the organoid in the well (roughly 4-5 wells per tip). 200 μL of EB expansion medium was then pipetted into each well with minimal disruption of the EB. The plate was further incubated for 4 days.

If the organoid formation was required to go past 9 days, the maturation step was completed in a 6 well ULA plate filled with 3 mL of EB maturation medium. A 1000 μL pipette tip was coated with sterile 3% BSA and each organoid was transferred into the 6 well ULA plates – with a maximum of 15 organoids per well (with minimal medium transferred from the 96 well plate).

2.5.6 Exploring Media composition breakdown

In this sub-section a breakdown of the composition of the media used to generate both embryoid bodies and cerebral organoids is explored. The components found in the following tables were compiled from the STEMdiff Cerebral organoid kit[455] documentation and the protocols by Lancaster et al[105,110]. It is to be noted that the media used in the differentiation protocols is all commercial and this is simply a breakdown of the reagents.

Table 17: Media component breakdown for maintenance of hIPSCs

E8 Flex Basal Medium	• DMEM/F12 – Basal Medium containing essential nutrients, amino acids and vitamins • Insulin – Supports cell metabolism • Transferrin – Provides Iron for cell proliferation and growth • Fatty Acids – Supports cell membrane and structure • Vitamin C – Antioxidant properties • FGF – Growth Factor to maintain pluripotency • TGFβ Inhibitor – Helps to maintain pluripotency • L-Glutamine – Critical components for cell metabolism • HEPES buffer – Stabilises the pH of the medium between 6-8-8.2 • Phenol red – pH indicator, changes to yellow when acidic
E8 Flex Supplement	• FGF2 – Growth factor for maintaining pluripotency • Insulin • Vitamin C • Thiazovivin – ROCK inhibitor, helps to maintain pluripotency • Y27632 – another compound similar to Thiazovivin

Table 18: Media component breakdown for maintenance of embryoid bodies (Days -5 – 0)

EB formation medium	• DMEM/F12 • KOSR – Serum free replacement that reduces variability in batches and provides the growth factors for maintaining pluripotency • FBS – supports cell growth, anti-apoptotic factors, buffering capacity and contains fibronectin for cell attachment • Glutamax – Source of L-glutamine, useful for cell metabolism and protein synthesis, prevents build-up of ammonia • MEM-NEAA – Non essential amino acid mix, nutrient supplement • β -mercaptoethanol – reducing agent, reduces reactive oxygen species formed from cellular processes • bFGF2 – maintains pluripotency, prevents spontaneous differentiation

Table 19: Media component breakdown for neural induction (Days 0 – 2)

Neural induction medium	• DMEM/F12 • Glutamax • MEM-NEAA supplement • Heparin - inhibits bFGF2, promotes the differentiation into neural lineages • N2 supplement – includes vitamins and amino acids critical for metabolic processes in neural cells, e.g. insulin, transferrin, progesterone, putrescine, biotin and fibronectin

Table 20: Media component breakdown for neural epithelial bud expansion (Days 3 – 5)

Neural expansion medium	• DMEM/F12
	• MEM-NEAA supplement
	• N2 supplement
	• B27 – mix of growth factors and hormones that facilitate differentiation into neural cells (Glia cells)
	• Penicillin – reduces risk of bacterial contamination.
	• Neurobasal medium
	  o Salts – maintain osmotic pressure (NaCl, KCl, $CaCl_2$, $MgSO_4$)
	  o Both essential and non-essential Amino acids
	  o Vitamins – important for enzymatic reactions and cellular processes Biotin, Folic acid, Riboflavin
	  o HEPES buffer

Table 21: Media component breakdown for neural maturation (Days 5 - 9+)

Neural maturation medium	• DMEM/F12 • MEM-NEAA supplement • N2 supplement • B27 – mix of growth factors and hormones that facilitate differentiation into neural cells (Glia cells) • Penicillin – reduces risk of bacterial contamination • Neurobasal medium • Vitamin A (Retinoic acid) – promotes neural progenitor cell differentiation, neurogenesis and gliogenesis o Binds to nuclear retinoic acid receptor to form heterodimer that activates transcription factors linked to neuronal differentiation and maturation

2.6. Generating bioactive Microdroplets using Bt-rBSA

Recombinant Avi-rBSA was expressed and purified from *P. pastoris*. The Avi-rBSA protein was in-vitro biotinylated by recombinantly expressed rBirA. The protein concentration was diluted using PBS to a final working concentration of 1 mg/mL.

The high-speed homogenizer and round bottom glass containers were ethanol sprayed then UV sterilised for 15 minutes inside a tissue culture hood.

2 mL of filtered 1 mg/mL bt-rBSA protein solution was added to 1 mL of filtered Novec-7500 oil inside the glass container. The homogenizer head was lowered into the solution and spun at 15,000 rpm for 2 minutes. The emulsions were left to recover for 5 minutes then transferred using a 3% BSA coated pipette tip into a 3% BSA coated 15 mL Falcon tube.

100 µL of emulsions was transferred to a 3% BSA coated sterile 1.5 mL Eppendorf tube and washed six times with PBS. Optimisation of the functionalisation cascade was conducted to ensure efficient usage of resources and reduce costs. The final concentrations used for functionalisation were the following: 50 µg/mL FITC-Streptavidin, 100 µg/mL Bt-ProteinG, 25 µg/mL Fc-tagged E-Cadherin and 25 µg/mL Fc-tagged N-Cadherin.

The PBS was removed from the emulsions and 100 µL of 50 µg/mL of FITC-Streptavidin was added and incubated at room temperature for 15 minutes. The emulsions were washed six times with PBS and imaged under fluorescent microscope at 488nm to verify fluorescence. The PBS was exchanged with 100 µL of 100 µg/mL

bt-ProteinG and incubated at RT for 15 minutes. The emulsions were washed six times with PBS and the PBS was exchanged with a sterile 25 µg/mL Fc-tagged N-cadherin or E-Cadherin solution, then incubated for 1 hour at 4^{o}C. The emulsions were washed six times with PBS and 1 mL of dPBS was added to a 15 mL Eppendorf tube.

The RGD peptide used to couple to NB-BSA was the FITC (488) GCGG-RGD peptide. 4 mL of 1 mg/mL NB-BSA was mixed with 20 µL of 100 mg/mL GCGG-RGD peptide (final concentration 0.5 mg/mL) and 2 µL of 0.0088 M LAP in a small petri dish. The lid was closed and irradiated with UV light at 20 mW for 10 minutes.

2 mL of filtered 1 mg/mL RGD-BSA protein solution was added to 1 mL of filtered Novec-7500 oil inside the glass container. The homogenizer head was lowered into the solution and spun at 15,000 rpm for 2 minutes. The emulsions were left to recover for 5 minutes then transferred using a 3% BSA coated pipette tip into a 3% BSA coated Eppendorf tube.

100 µL of emulsions was transferred to a 3% BSA coated sterile 1.5 mL Eppendorf tube and washed six times with PBS, with a final volume of 1 mL dPBS.

2.6.1. Integration of bioactive microdroplets into cerebral organoids

Functionalised microdroplets were mixed with single cell hIPSCs at day -5 of EB formation.

Once the hIPSCs were seeded at a seeding density of 4500 cells/well and centrifuged to create a cell mass in the centre of the well, a 1000 µL pipette tip coated with 3% BSA was used to partially resuspend the emulsions in the dPBS and using a 10 µL pipette tip coated with 3% BSA, 1 µL of emulsions was transferred directly on top of the cell masses in each well.

The organoids were grown as per usual protocol used previously.

2.6.2. Cryosectioning cerebral organoids

At day 9 of Organoid formation, the organoids were fixed using 4% PFA for 15 minutes and washed six times with PBS. The organoid was placed within the central region of a mould containing Optimal cutting temperature (OCT) compound, and snap frozen using a hexadecane ice bath. The blocks were stored at -80^{o}C until required.

The blocks were cryosectioned using a bright cryostat at -10^{o}C ambient temperature and -20^{o}C sample temperature, using a slice thickness of 25 µm. Slices were placed onto frost microscope slides and stored at -20^{o}C until required.

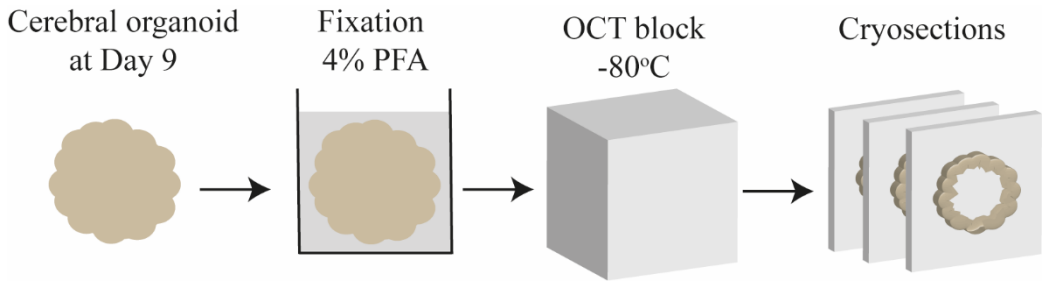

Figure 23: Diagram representing the steps taken to generate cryosectioned slices of Day 9 cerebral organoids. The organoids were fixed with 4% PFA then placed in OCT blocks that were snap frozen and mounted onto the cryostat to generate sections with a thickness of 25 µm.

2.6.3. Immunostaining cerebral organoids sections on slides

Slides containing cryosectioned organoid slices were thawed from -80^{o}C, the excess moisture was wiped from the slides. Using a hydrophobic marker, a square was marked multiple times around the slices; with a tight seal ensured.

50 µL of 4% PFA was pipetted into the seal directly on top of the slices and incubated for 15 minutes at RT. The slices were washed three times with PBS and exchanged with 50 µL of 0.25% Triton-X and incubated for 15 minutes at RT. The slices were washed three times with PBS and blocked with 3% BSA for 30 minutes and incubated with primary antibodies for 1 hour at 4^{o}C. The slices were washed three times with PBS and incubated with secondary antibodies, Actin-555 and DAPI-408 for 1 hour at RT.

The slices were washed three times with PBS and the PBS was replaced with a small drop of Fluoromount-G™ Mounting Medium – carefully not forming bubbles. A circular thin glass slip was placed on top of each slice and left to set for 30 minutes.

Slides were imaged on Nikon CSU-W1 SoRa Spinning Disk Confocal microscope.

Primary antibodies:

Cellsignal: E-Cadherin (4A2) Mouse mAb (14472). Rndsystems: N-Cadherin Antibody (AF6426). BioLegend: Alexa Fluor® 488 anti-Tubulin β3 Antibody (801203). Sigma Aldrich: Anti-Fibronectin antibody (F3648), Anti-YAP1 (C-terminal) antibody (Y4770). Invitrogen: Rhodamine phalloidin (R415), DAPI (D1306), SOX2 Polyclonal Antibody (PA1-094). ThermoFisher: ZO-1 Monoclonal Antibody Alexa Fluor™ 488 (ZO1-1A12), ZO-1 Monoclonal Antibody (ZO1-1A12), Alexa Fluor™ 594, PAX6 Polyclonal Antibody (42-6600), Ki-67 Monoclonal antibody (RM-9106-S0). Abcam: Anti-Integrin alpha 6 antibody [GoH3] (ab105669), Recombinant Anti-Vinculin antibody [EPR8185] (ab129002), Anti-Laminin 5 antibody (ab14509), Recombinant Anti-Collagen I antibody [EPR7785] (ab138492), Anti-FOXG1 antibody (ab18259).

Secondary antibodies:

Invitrogen: anti-Rabbit IgG Alexa Fluor™ 647 (A-31573), anti-Mouse IgG Alexa Fluor™ 647 (A-31571), anti-Rabbit IgG Alexa Fluor™ 488 (a-11008), anti-Sheep IgG Alexa Fluor™ 555 (a21436), anti-Mouse IgG Alexa Fluor™ 647 (a31571), anti-Rabbit IgG Alexa Fluor™ 594 (a11012), anti-Mouse IgG Alexa Fluor™ 488 (a-11029), anti-Mouse IgG Alexa Fluor™ 555 (a31570), anti-Rabbit IgG Alexa Fluor™ 647 (a-31573), anti-Mouse IgG Alexa Fluor™ 594 (a21203).

2.6.4. Immunostaining cerebral organoids directly

Fixing was completed by the transfer of the EBs/organoids into a 3% BSA coated 96 well plate. Each time point was fixed using 4% PFA treatment for 20 minutes at RT, followed by washing with PBS and treatment with 0.25% Triton-x for 15 minutes at RT, followed by PBS washing.

The organoids were washed six times with PBS and blocked with 3% BSA for 30 minutes and incubated with primary antibodies for 1 hour at 4^{o}C. The organoids were washed six times with PBS and incubated with secondary antibodies, Actin-555 and DAPI-408 for 1 hour at RT. The organoids were washed six times with PBS and transferred using a 3% BSA coated 1000 µL pipette tip into a PBS filled Ibidi µ-Slide 8 Well Chamber coated in 3% BSA.

2.6.5. Quantification of rosettes

Three sections from three individual organoids from each condition (N-cad, E-Cad, E/N Cad, RGD and no droplets) that were cryosectioned in section 2.6.3 were stained using the ZO-1 fluorescent antibody to highlight tight junctions formed at the apical region of rosettes. The quantity, perimeter and area of the rosettes was measured and averaged using the ImageJ software.

A max intensity z-projection was generated of the ZO-1 channel; this was converted into an 8-bit image (greyscale). The contrast was enhanced by 0.3% using the Enhance contrast option, and the threshold was adjusted using the OTSU thresholding technique to selectively threshold the rosettes. This generated a binary image of the rosettes (Figure 24). The binary image was further processed using the Binary -> close -> dilate -> fill holes to allow easier detection of rosettes using the analyse particles option; this would generate a particle map of the rosettes and outputting various details of each rosette observed in the particle map such as area, frequency and perimeter.

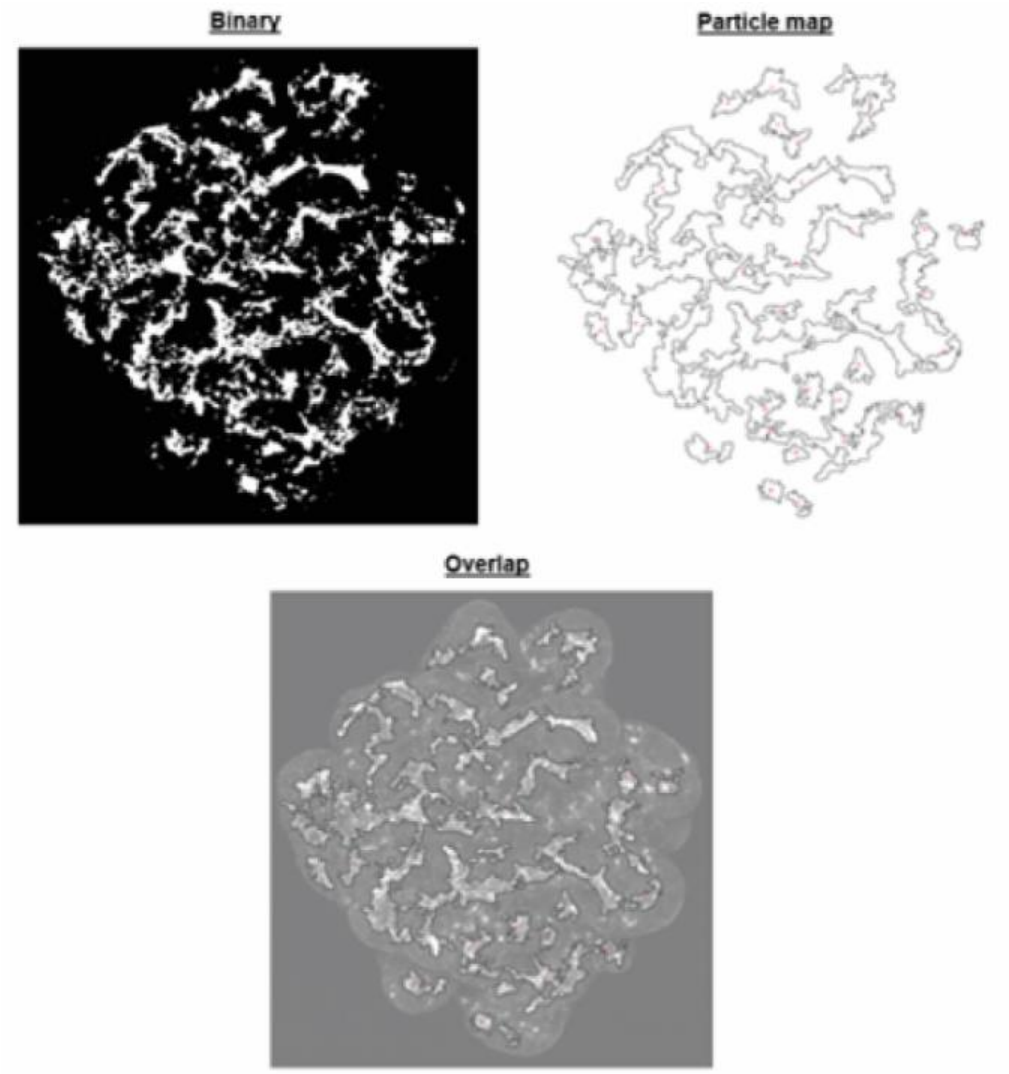

Figure 24: Quantification of rosettes in ImageJ. Schematic depicting an example of the binary map generated from thresholding, followed by the particle map generated from particle analysis and finally the overlay of the particle map onto the original fluorescent image.

3. Expression and purification of rBSA

3.1. Structural alignments of BSA vs HSA

The BSA protein was chosen as the target for our recombinant expression study due to its high utilisation in the food industry[456], high stability, and for our downstream applications including the ability to form and stabilise emulsions[457]. Unfortunately, only recombinant expression protocols for the human variant of the Serum Albumin HSA protein were found in the literature and these were conducted using the *P. pastoris* expression host [458–460]. Therefore, essential bioinformatics on BSA was conducted to explore whether the homology (percentage identity and structural homology) of BSA and HSA was sufficient enough to allow the replacement of HSA with BSA for the expression of our protein.

We first explored the conservation of residues between the two species to identify the similarities in the amino acid sequences. The amino acid sequences chosen for HSA and BSA were 1AO6 and 3V03 respectively and were ran simultaneously in the online alignment tool PRALINE[461]. From the alignment data, it was identified that the percentage sequence identity between HSA and BSA was roughly 76% (Figure 25), this meant that the BSA (PDB: 3V03) sequence used identically matched 76% of the HSA (PDB: 1AO6) amino acid sequence.

When comparing the tertiary structures, the 24% difference in amino acids was found to not impact the structures in a significant way to create a visible difference seen in Figure 25, with both structures composed of mainly α-helices and no β-sheets.

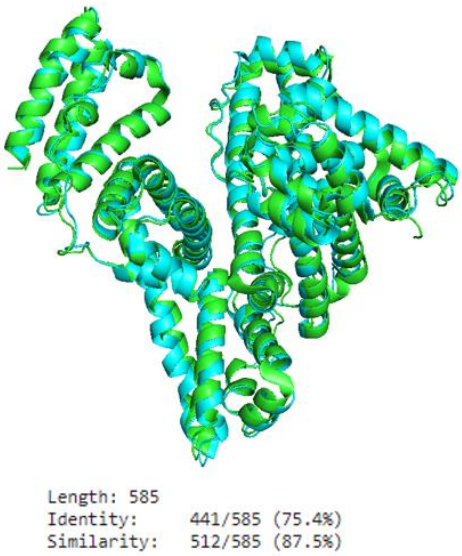

Figure 25: Pymol representation of BSA (PDB: 3V03) and HSA (PDB: 1AO6) superimposed using the Pymol alignment tool. The sequence alignment was completed using EMBL-EBI (EMBOSS Needle tool) (66-18) stating the percentage sequence identity similarity between BSA and HSA.

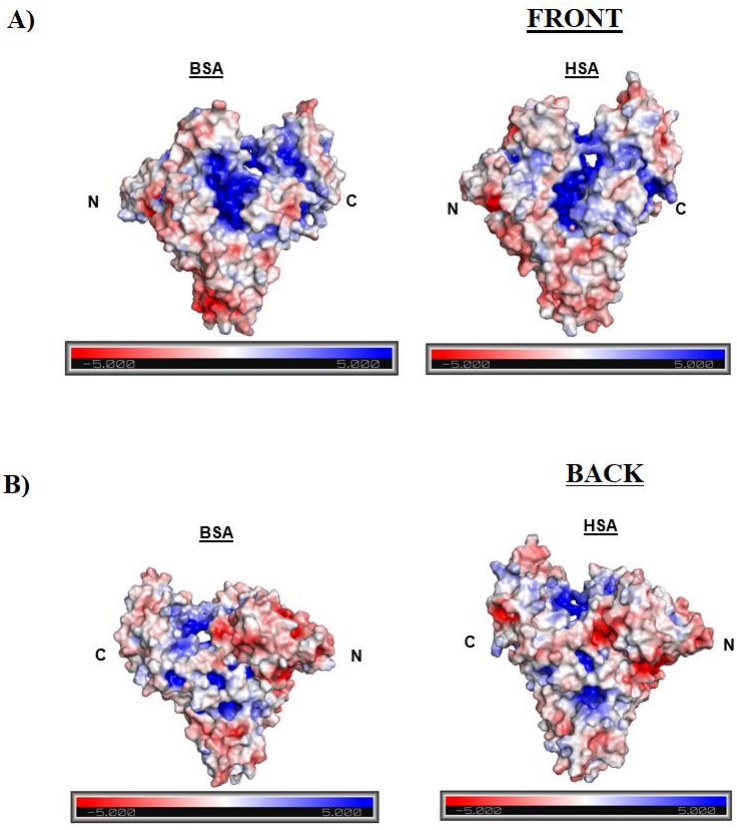

Figure 26: Pymol APBS Electrostatics surface charge simulation (pH 7.0) for the albumin proteins BSA and HSA. A) Front side of the protein. B) Back side of the protein. Red (-5) depicts regions of negatively charged residues and Blue (+5) depicts regions of positively charged residues.

Furthermore, both proteins exhibited a similar surface charge distribution with a negatively charged (red) surface and a positively charged (blue) crevices (Figure 26).

In the literature it is established that there is a significant degree of similarity existing between the sequences and structures of HSA and its counterparts derived from bovine (BSA), equine (ESA), leporine (LSA) and canine (CSA)[19–21]. This allows the HSA to be substituted with BSA for cell culture practices and other biotechnological applications[23].

Given the close resemblance between HSA and BSA, the protocols used in the literature to recombinantly express HSA in Pichia pastoris had good potential to be utilised for the expression of our scaffold BSA protein.

3.2. Addressing the location of Avi-tag

The aim of this project was to generate a recombinant scaffold protein containing a biotinylated bioactive component with specificity. The Avi-tag was selected as our target tag to be introduced at a terminal end of the BSA protein, this creates a specific site for biotinylation carried out by the bacterial Biotin ligase enzyme (BirA), which biotinylates a specific lysine within the 13 amino acid tag. However, the location of the tag was very important due to many factors. The first factor is that the tag must be accessible to other secondary components, such that it is on the surface and not blocked by other structures, hence the tag was placed on the terminal end of BSA. The second factor is the selection of which terminal end to place the tag, the location of the tag was selected to avoid being presented close to the hydrophobic oil phase due to the unfolding mechanisms that occur at this interface and as it could result in the burying of the tag and inability to bind specifically.

Therefore, research into the location of the tag was carried out to increase the probability of successful accessibility. The first step was to identify which face of the protein had the highest probability of interacting and adsorbing to the hydrophobic oil interface and unfold. In the literature and simulation studies, a general consensus is that at strong hydrophobic surfaces such as graphite[462,463], BSA molecules adsorb and unfold at the C-terminal end of the protein. Furthermore, the N-terminal end of BSA was shown in coarse grain Molecular dynamics (MD)[462] simulations to still be immersed in the bulk aqueous phase and the tertiary structure of this section did not unfold. However, this research was carried out at a solid interface rather than a fluid oil, as is the case in the system we proposed to develop. Although no study of BSA

adsorption at liquid-liquid interfaces could be found in the literature, the model studies on solid interface adsorption were considered sufficient for the selection of the N terminus as insertion site for our tag and associated protein design. However, further research could be carried out on the structure of BSA to further establish which terminal end has the highest probability of interacting with the hydrophobic oil phase.

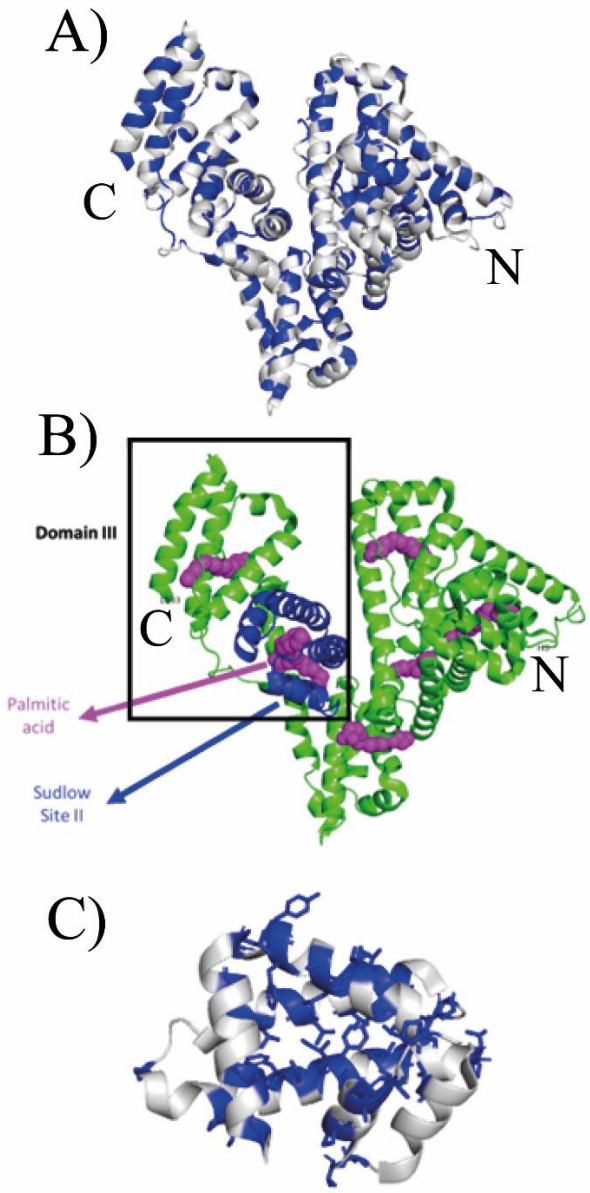

Figure 27: Hydrophobic residues of HSA and its relevant Sudlow sites. A) 3V03 crystal structure of HSA, with hydrophobic residues coloured in blue. B) 1E7H crystal structure[464] of HSA coupled with palmitic acid. C) Sudlow site II of Domain III of HSA with the hydrophobic residues highlighted. Figures were generated in the Pymol software[465].

To investigate the likely mechanism of BSA adsorption at oil interfaces further, the position of hydrophobic residues was examined (Figure 27A). Hydrophobic residues decorated the structure of this protein relatively homogenously, with multiple hydrophobic patches clearly oriented within the core of the protein.

In fact, HSA was reported to display multiple fatty acid binding sites[466] existing within the sub domains. The Sudlow Site II (Figure 27B) found in the Sub domain IIIA was found to be the most important domain for Fatty acid binding[466] and was found to also contain largely hydrophobic residues forming a hydrophobic patch in the region.

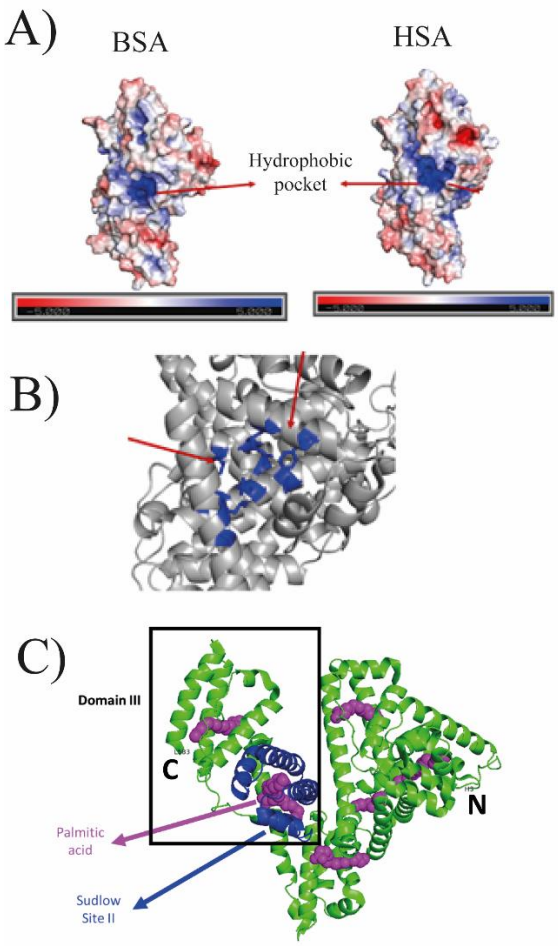

Figure 28: The hydrophobic pocket found in both HSA and BSA. A) Pymol APBS Electrostatics surface charge simulation (pH 7.0) focused on the hydrophobic pocket in BSA and HSA proteins B) Blue residues correspond to hydrophobic residues found in the hydrophobic pocket of BSA and HSA. C) HSA complexed with Palmitic acid (PDB: 1E7H) in Pink are the Fatty acids and highlighted in blue is the Sudlow site II (Hydrophobic pocket).

This hydrophobic patch was also found to be present in BSA and the hydrophobic residues also correlated to the hydrophobic residues present in the Sudlow Site II in HSA (Figure 28C).

C, hydrophobic residues such as Valine, Alanine, Proline and Leucine were found to line the hydrophobic patch highlighted in blue. Hence, we proposed that this strong hydrophobic patch found in the C-terminal region of BSA would drive the adsorption of the C-terminal towards the hydrophobic oil phase; this would leave the N-terminal region less affected by hydrophobic forces and potentially facing outwards towards the aqueous phase. Therefore, the N-terminal region of BSA was selected for introduction of the Avi-tag.

3.3. Selection of expression hosts

The *P. pastoris* recombinant expression system was selected as the main host for our protein expression due to several important factors. We required the protein for downstream experiments to be produced at large quantities without the need for large fermenters or large volumes of media. The BSA protein required post translational modifications such as disulphide bonds that are essential for its secondary, tertiary structures and folding. Furthermore, we required a simple yet effective method to reliably produce our protein without the need for multiple purification steps to process our protein. Finally, it was also ideal to find a cost-efficient method to produce our protein without the need for expensive reagents and media. The scalability of the technique makes this a very attractive method to produce large amounts of a modified protein.

Overall, the *P. pastoris* expression system was the most suitable system for our experiment due to its cost-effectiveness and the ability to produce a high yield of correctly folded mammalian proteins. Moreover, expression of Avi-BSA was also attempted in *E. coli* expression hosts such as the Rosetta (DE3) and the SHuffle® T7 Express *E. coli* competent cells. The Rosetta (DE3) strain is a commonly used bacterial strain derived from the BL21 (DE3) strain, these carry the T7 RNA polymerase gene within the chromosomal DNA that is controlled by the strong expression inducing lacUV5 promoter[467]. Additionally, the Rosetta strain carries mutations that allow the bacterium to express genes encoding rare codon tRNAs, this aids in the expression of proteins that contain rare codons and the ability to improve codon bias[468,469]. This strain was used for preliminary small scale expression trials due to the cost-effective nature of the strain, after which the more expensive SHuffle® T7 Express *E. coli* competent cells were used. After delving deeper into the secondary and tertiary structure of 3v03 BSA, it was found that the secondary structure required 17 essential disulphide bonds to generate the correct structure seen in Figure 1.

Given this outcome, the SHuffle® T7 Express *E. coli* competent cells were adopted for further larger scale expression trials in *E. coli*. These cells are derived from the K12 strain and carry mutations in the genes that encode disulphide bond formations and the export machinery[61]. Just like the Rosetta (DE3) cells they also carry the T7 RNA polymerase gene that allows for tight regulation of gene expression by the T7 promoter, induced by IPTG. These mutations promote the formation of disulphide bonds by generating a more oxidising environment within the cytoplasm of the bacterial cells[61].

3.4. Selection of expression plasmids for yeast expression

A *P. pastoris* compatible vector must also be selected, as yeast expression requires the integration of the plasmid DNA into the chromosomal DNA[470]. There were a range of different plasmid variants to select from. However, the main difference between the different plasmids was the ability to either carry out intracellular or secreted expression of the target protein. For example, the two main candidates were the pPIC3.5K vector (Figure 29A) for intracellular expression or the pPIC9K vector (Figure 29B) for secreted expression.

The main difference between the two plasmids in Figure 29 is the addition of the alpha-secretion signal, this is a 19 amino acid pre sequence followed by a 67-residue pro sequence and contains a Kex2 endopeptidase processing site[471,472]. This signal is processed in three steps, starting with the pre-sequence removal in the endoplasmic reticulum (ER), followed by the cleavage of the pro leader-sequence by Kex2, and finally the rapid cleavage of the Glutamate-Alanine repeats in the Golgi [472,473]. For our project the pPIC9K vector was selected for our expression to reduce the number of purification steps post expression. Since the protein will be secreted into the media, lysis of the cells to harvest the protein is not required, this will reduce the likelihood of damaging the protein during purification. The final plasmid construction can be seen in Figure 30A.

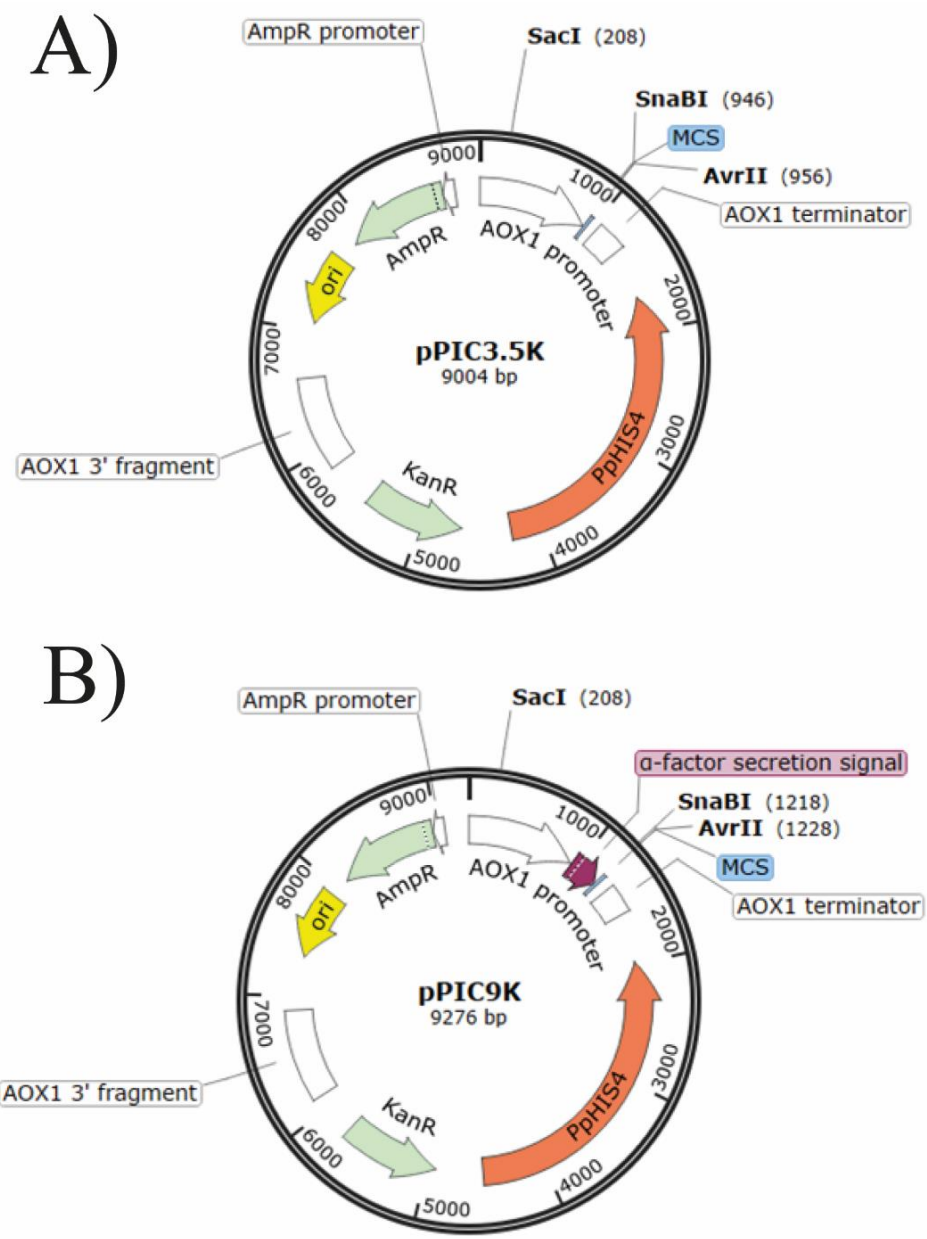

Figure 29: *P. pastoris* expression vectors. A) Schematic showing the pPIC3.5K plasmid constructed using the SnapGene software[453]. Light green: KanR = Geneticin (G418) resistance, AmpR = Ampicillin resistance. White = AOX1 promoter and fragments. Orange: The PpHIS4 fragment to promote growth on histidine deficient media (His+ phenotype). Light blue: Multiple cloning site, contains multiple restriction enzyme sites. Highlighted are the restriction enzyme cleavage sites AvrII and SnaBI and the linearising enzyme SacI. **B) Schematic showing the pPIC9K plasmid constructed using the SnapGene1 software.** Light green: KanR = Geneticin (G418) resistance, AmpR = Ampicillin resistance. White = AOX1 promoter and fragments. Orange: The PpHIS4 fragment to promote growth on histidine deficient media (His+ phenotype). Light blue: Multiple cloning site, contains multiple restriction enzyme sites. Purple: Alpha-factor secretion signal. Highlighted are the restriction enzyme cleavage sites AvrII and SnaBI and the linearising enzyme SacI.

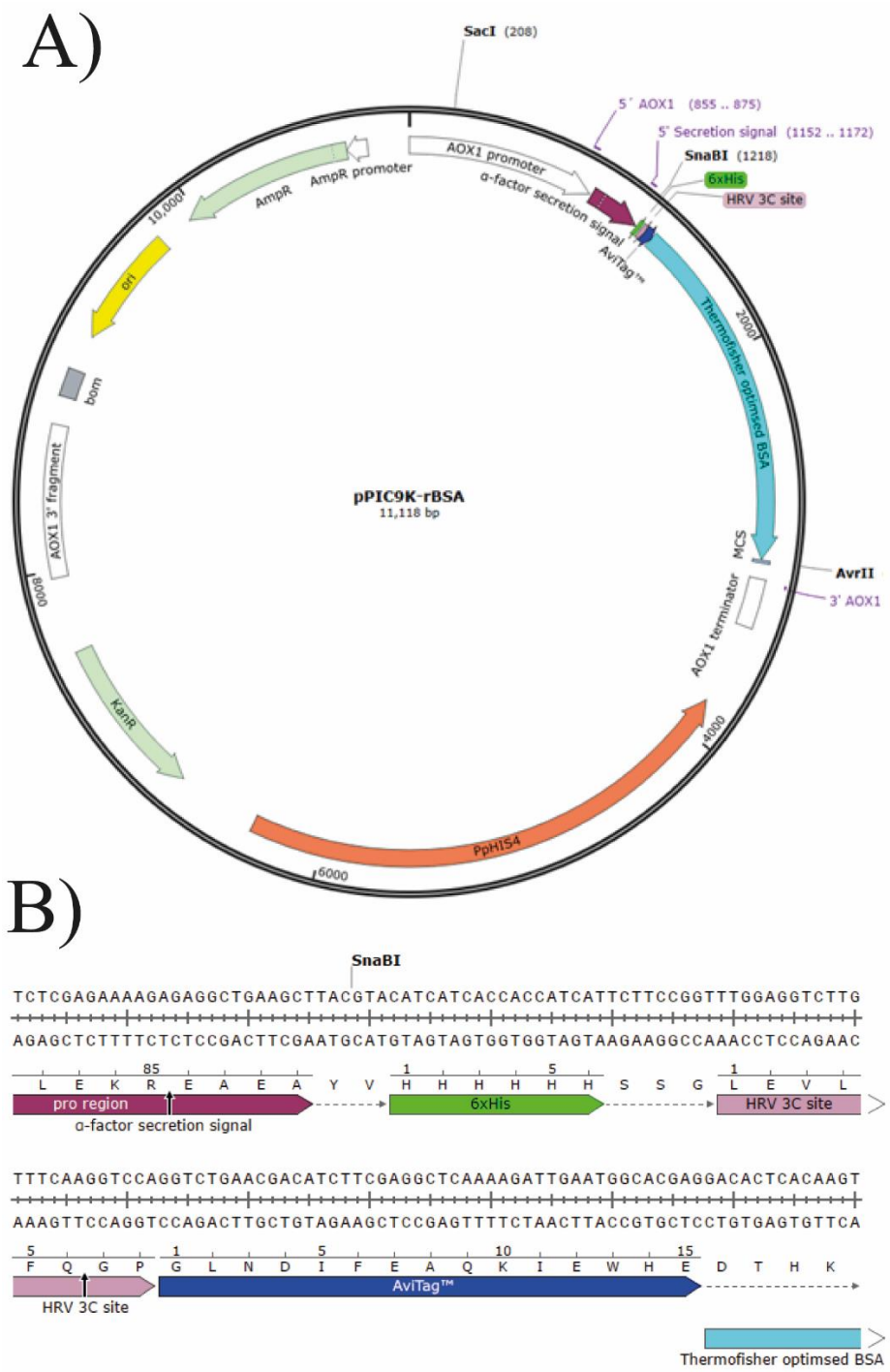

Figure 30: Final *P. pastoris* expression vector for Avi-rBSA. A) Schematic showing the pPIC9K-Avi-rBSA plasmid constructed using the SnapGene software[453]. Light green: KanR = Geneticin (G418) resistance, AmpR = Ampicillin resistance. Cyan = Avi-rBSA insert optimised using the ThermoFisher GeneArt service [474]. Maroon: Alpha-factor secretion signal. White = AOX1 promoter and fragments. Green = 6x His-Tag. Blue = Avi-Tag. Pink = HRV 3C cleavage site. Highlighted are the restriction enzyme cleavage sites AvrII and SnaBI. B) **Magnified schematic showing the detailed N-terminal region of the pPIC9K-Avi-rBSA sequence constructed using the SnapGene software[453].** Cyan = Avi-rBSA insert optimised using the ThermoFisher GeneArt service [474]. Maroon: Alpha-factor secretion signal. White = AOX1 promoter. Green = 6x His-Tag. Pink = Avi-Tag. Light Pink = HRV 3C cleavage site.

3.5. Sequence optimisation for expression in yeast

As we are using a protein sequence found in Bovine species, the DNA sequence must be optimised to promote the correct codon usage in the *P. pastoris* host. Gene optimisation services offered by Eurofins Genomics was used on the BSA (3V03) gene to optimise the codon usage for expression in *P. pastoris.* This optimisation is essential as it reduces the frequency of rare codons encoding the amino acids: Glycine, Isoleucine, Threonine, Leucine and Arginine. This is summarised in Table 22.

Table 22: Rare codon analysis results obtained from running the unoptimized and optimised BSA sequence through *Genscript rare codon analysis tool[475].

Factor	Before Optimisation	After Optimisation	Ideal Values*[475]
CAI	0.53	0.77	0.8-1.0
GC content	51.7%	42.9%	30-70%
Rare codon frequency	16%	2%	< 30%

It is also very important to control the Guanine/Cytosine (GC) content in the DNA sequence for several reasons. The residues Guanine and Cytosine form a much stronger and stable triple bond compared to the Thiamine and Adenine double bond within the DNA double helix. This requires more energy for the helicase to cleave, bind and allow the binding of the transcription machinery to the promoter regions[476]. Furthermore, studies have indicated that a higher GC content can be linked to the formation of secondary structures within the DNA, such as hair pin loops which can interrupt the progression of RNA polymerases or ribosomes[477,478]. However, in some instances GC-rich genes can be beneficial as shown in the promoter regions of some bacterial genes. These serve as binding sites for RNA polymerases and transcription

factors[479]. In addition, the higher the Codon adaptation index (CAI) the higher the probability that the protein is expressed successfully in the expression host organism. In our case the 24% increase to 77% likelihood of expression is very good.

3.6. Selection of linearising enzyme

Table 23: The different enzymes that can be used to linearised the pPIC9K plasmid, to allow the insertion into the *P. pastoris* genome.

Restriction enzyme	Integration event	Phenotype
SalI	Insertion at the His4 locus	His^+ Mut^+
SacI	Insertion at the 5' AOX1 promoter region	His^+ Mut^+

Both SalI and SacI were selected as the enzymes for linearising the plasmid DNA, as they will allow the insertion of the linear DNA into the His4 locus or the 5' region of the AOX1 promoter gene respectively[480]. this will produce the His^+ and Mut^+ GS115 phenotype in the GS115 Pichia strain. Two different phenotypic classes of His^+ strains can be generated, the Mut^+ or the Mut^S depending on the strain used. If the KM71 strain is used, SacI and SalI will produce the His^+ Mut^S phenotype this causes a mutation in the primary AOX1 promoter allowing the slower secondary AOX2 promoter to take control of expression and a slower growth in methanol medium; these slower conditions could favour the expression of certain proteins[480]. However, if the GS115 strain is used, SacI and SalI will produce the His^+ Mut^+ phenotype which

utilises the AOX1 promoter for expression by methanol induction; these conditions are much faster and can provide a higher yield in a shorter time scale[480]. Utilising SalI in the transformation of pPIC9K-BSA into GS115 was found to be inefficient when compared to SacI. Hence, the use of SacI was trialled with much more success, consequently yielding a higher frequency of transformants of Histidine deficient and G418 antibiotic plates (Figure 31B).

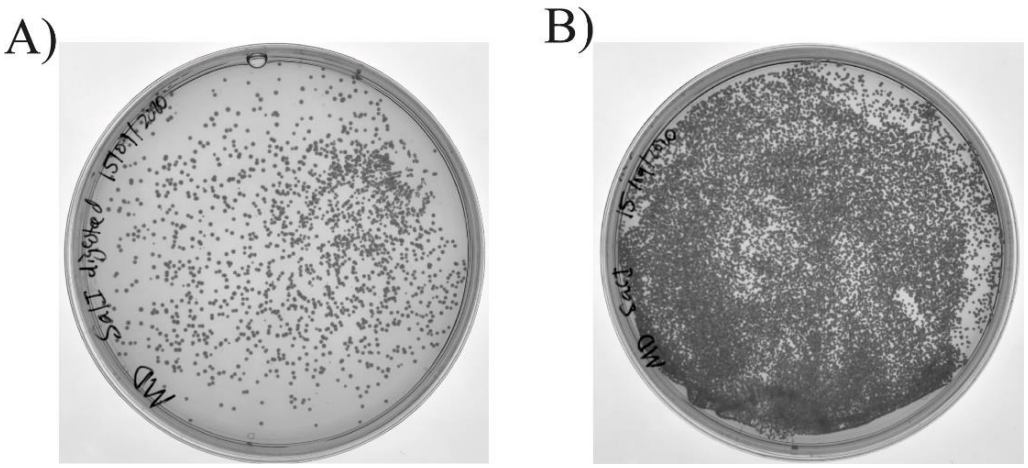

Figure 31: The growth of GS115 Pichia pastoris on MD medium (His$^+$) transformed with pPIC9K-BSA linearised with either SalI or SacI enzymes. A) SalI linearised colonies. B) SacI linearised colonies.

The effect of linearising enzyme on transformation efficiency was also studied by Wu et al [72], they also found that utilising SacI over SalI significantly increased the number of transformants obtained by 28 folds; this correlated quite well with our data as seen in Figure 31.

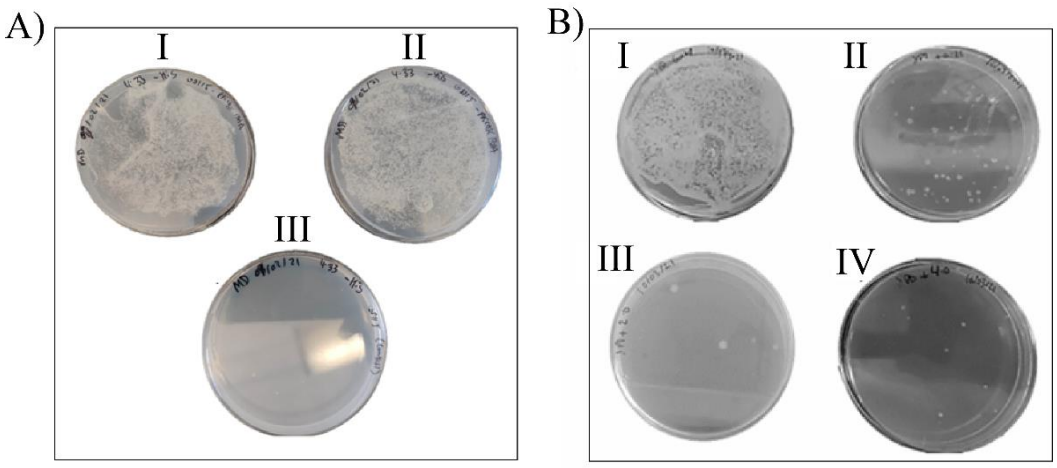

Figure 32: Primary and secondary selection of transformed GS115 *P. pastoris* cells. A) Primary selection of electroporated GS115 *P. pastoris* transformed with pPIC9K-BSA (linearised with SacI) and plated onto Minimal Dextrose + Yeast synthetic drop-out supplement (Histidine deficient). I-II) Electroporated GS115 cells. III) Negative control (GS115 – not transformed). two days incubation at 30ºC. **B) Secondary selection of GS115 *P. pastoris* transformed with pPIC9K-BSA, pooled from MD Histidine selection plates and plated onto YPD with increasing concentrations of G418**. I) Negative control – no antibiotics. II) YPD + 250 μg/mL G418. III) YPD + 2000 μg/mL G418. IV) YPD + 4000 μg/mL G418. Incubated at 30ºC for four days.

It has been documented that the pPIC9K plasmid has the ability to integrate multiple copies of itself into the chromosomal DNA of Pichia pastoris[481]. A high copy number colony will contain multiple insertions of the pPIC9K-BSA plasmid. The growth of the GS115 cells on an increasing concentration of G418 can indicate how many copies of the recombinant plasmid the yeast cells inserted into its genome[481]. If growth occurs on a higher concentration of G418 this will signify a high copy number. A single copy of the pPIC9K plasmid into the GS115 genome will allow the growth on 0.25 mg/mL G418, up to 4 mg/mL with 7-12 copies of the plasmid integrated[481]. This trend was also seen within our studies, as seen in Figure 32B with a decrease in the number of colonies observed as the concentration of antibiotics increased. Direct selection of GS115 *P. pastoris* on YPD plates containing a concentration of G418 antibiotic is not possible as it takes 24 hours for antibiotic resistance to be taken up[482]. Hence selection on His^+ plates must be completed first.

Table 24: General information about high copy number transformants compiled from Invitrogen[481].

Concentration of G418 (mg/mL)	Number of colonies (per plate)	Copy number	Days to grow
1	10-20	2-3	2-3
2	2-5	5-7	3
4	1-10 (per 5 plates)	7-12	4-5

3.7. Optimisation of transformation protocol

Table 25: The various protocols attempted for the transformation of pPIC9K-BSA into GS115 *P. pastoris*.

#	Name	Concentration of DNA attempted (µg)	Electroporation values attempted	Selection plates
1	Eppendorf[483]	0.2, 0.5, 1.0	25 µF, 200 Ω, 1.0 kV 25 µF, 200 Ω, 1.5 kV	YPD + G418 / MD
2	EasySelect[484]	0.5, 1.0	25 µF, 200 Ω, 1.0 kV 25 µF, 200 Ω, 1.5 kV	YPD + G418 / MD
3	High efficiency (DTT + LiOAc[72])	0.01, 0.5, 1.0	25 µF, 200 Ω, 1.0 kV 25 µF, 200 Ω, 1.5 kV	YPD + G418 / MD
4	Simplified protocol (HEPES-NaOH + DTT[485])	0.5, 1.0	25 µF, 200 Ω, 1.0 kV 25 µF, 200 Ω, 1.5 kV	YPD + G418 / MD
5	Present protocol	1.0, 10.0	25 µF, 200 Ω, 1.5 kV	YPD + G418 / MD

The transformation of pPIC9K-BSA into GS115 *P. pastoris* consisted of four steps, the linearisation of the plasmid, the production of electrocompetent cells, the electroporation and the incubation onto selection plates. Each of these steps can accommodate some sort of optimisation to obtain a higher transformation yield.

The standard electroporation protocol originally designed by Becker et al [486], Eppendorf[483], EasySelect[484] and high efficiency[72] protocols all required the processing of large batches of culture medium ranging from 100 mL to 500 mL. This gave rise to multiple issues whilst preparing electrocompetent cells, the first being the increased risk of contaminations occurring during the transfer steps from a large amount of glassware. Furthermore, the processing of such bulk volumes led to a long and tedious process requiring multiple centrifuge cycles. However, compared to the simplified protocol[485], a patch of 4 cm^2 of yeast cells was sufficient to produce successful transformations, thus removing the need to process such bulk cultures as the cells were resuspended in only 1mL of buffer in a 1.5 mL Eppendorf tube.

The standard method to produce electrocompetent cells highlighted by the Becker et al [486], Eppendorf[483] and EasySelect[484] protocols is to wash the cells with ice-cold water and 1M sorbitol. However, recent studies have shown higher success rates with different chemical treatments. The high efficiency protocol[72] uses a pre-treatment process with the combination of LiAc + DTT, this was shown to increase the transformation efficiency by 150 folds. The authors highlighted that pre-treatment with LiAc alone did not have any significant difference. On the other hand, treatment with DTT alone was found to increase transformation efficiency by 20 folds; this was also found to be the case with the pre-treatment of *S. Pombe* with DTT [487]. Moreover, the simplified protocol[485] utilises the pre-treatment of *P. pastoris* with HEPES + DTT and was found to also significantly increase transformation efficiencies compared to

cells without any pre-treatment. The effect of the electroporation conditions: voltage (kV), capacitance (μF) and resistance (Ω) were previously studied by Wu et al[72] and found that the best conditions for electroporation were: 25 μF, 200 Ω, 1.5 kV; with the highest amount of transformants obtained using these conditions. Hence, why this condition was utilised for further transformations.

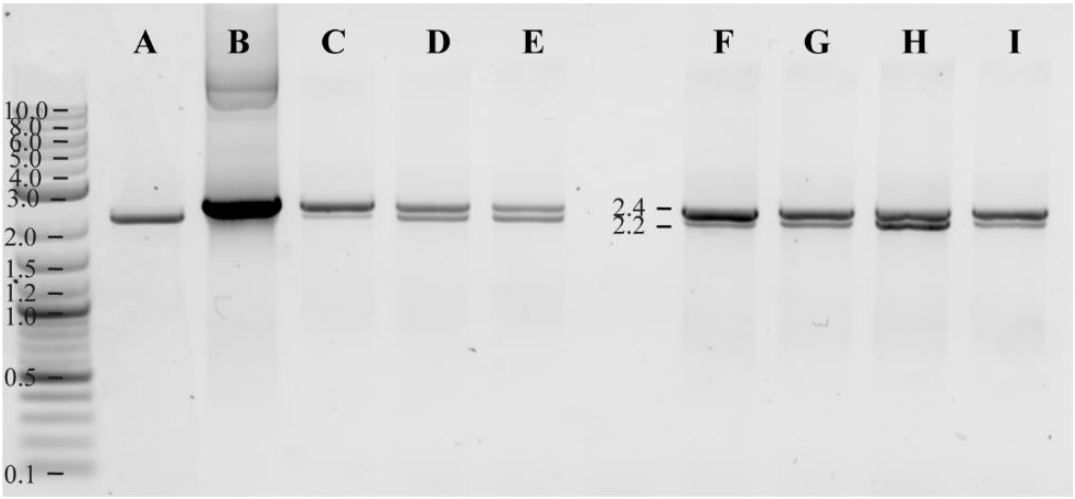

Figure 33: PCR run of Histidine deficient (His$^+$) GS115 Pichia pastoris transformants isolated chromosomal DNA, run on a 0.8% agarose gel. Primers: 5' AOX1 + 3' AOX1. Positive transformants exhibit two bands, one corresponding to the AOX1 promoter in the Pichia pastoris genome (2.2 kbp) and a second for the inserted recombinant BSA sequence (2.45 kbp). Example of a positive transformant = Lane D. Lanes B-I were run with both AOX1 5' and 3' primers. A) pPIC9K plasmid. B) pPIC9K-Avi-BSA. C-I) His+ colonies isolated from histidine deficient media. DNA ladder is in kbp.

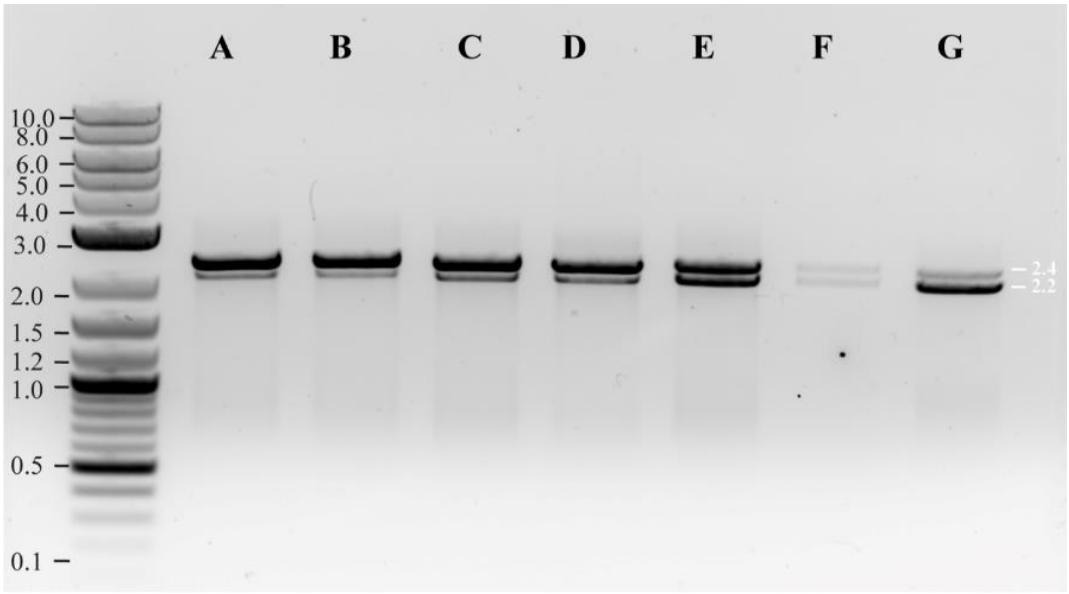

Figure 34: PCR run of isolated chromosomal DNA for GS115 Pichia pastoris transformants that were plated onto varying concentrations of G418 post His^{+} selection, run on a 0.8% agarose gel. Primers: 5' AOX1 + 3' AOX1. Positive transformants exhibit two bands, one corresponding to the AOX1 promoter in the Pichia pastoris genome (2.2 kbp) and a second for the inserted recombinant BSA sequence (2.45 kbp). A-B) 4.0 mg/mL G418 isolated colonies. C-D) 2.0 mg/mL G418 isolated colonies. E) 1.0 mg/mL G418 isolated colonies. F) 0.5 mg/mL G418 isolated colonies. G) 0.25 mg/mL G418 isolated colonies. DNA ladder is in kbp.

Unfortunately, the following protocols tested (1-3) were unsuccessful in producing any transformants that were positive for both the AOX1 promoter and the Avi-BSA insert, post colony PCR. However, they assisted in understanding the technique behind electroporation of yeast and the fundamentals behind it.

The simplified protocol[485] alongside SacI linearisation of 10 µg of plasmid DNA was found to produce the highest yield of positive transformants post electroporation, plated onto histidine deficient MD agar and G418 plates (Figure 34A-B). Positive transformants were found on plates containing up to 4 mg/mL G418 antibiotics, this indicated that up to 12 copies of the plasmid was integrated within the chromosomal DNA of the *P. pastoris* GS115 cells; this was a great outcome for the project as this will translate to a higher protein production capability.

3.8. Optimisation of expression and purification of Avi-BSA in yeast

The protocol developed by Zhu et al[458] for the expression of Human serum albumin was used as the foundation for the expression of Avi-BSA. The authors highlighted that their protocol had reached a highest yield of 1.6 g/L in a shake flask; this was beneficial for our study as we required a yield of at least 1 g/L for downstream experiments. Thankfully the study by Zhu et al[458] trialled various supplementation optimisations to increased their final yield in a shake flask. They found that the addition of 0.5% casamino acids increased the yield by 11% without increasing cell growth[458]; casamino acids. Furthermore, the cell growth was not affected by the addition of other amino acid supplementation such as Ala, Lys, Leu and Glu but increased the final yield by up to 20%[458]. Additionally, in their study they first used the standard final methanol concentration of 0.5% then increased to 1%.

In the literature, Minning et al[488] demonstrated that the methanol concentration was the most important factor to obtain a high protein yield in *P. pastoris*. However, it was found that excessive methanol concentration can lead to an overdose, caused by the accumulation of formaldehyde which is the first product of methanol breakdown[489]. In their study they found that the addition of 1% methanol every 12 hours at 28^{o}C was the most optimal for HSA expression. Moreover, they also studied the effect of temperature and pH on the yield of protein. They found that 28^{o}C was the optimal temperature to balance cell growth and protein production, any lower or higher than this would significantly impact the HSA production. This correlated well with our results, it was determined by the SDS gels that expression at 30^{o}C for 4 days (Figure 35D) showed a much fainter band than expression at 28^{o}C for 4 days (Figure 36D).

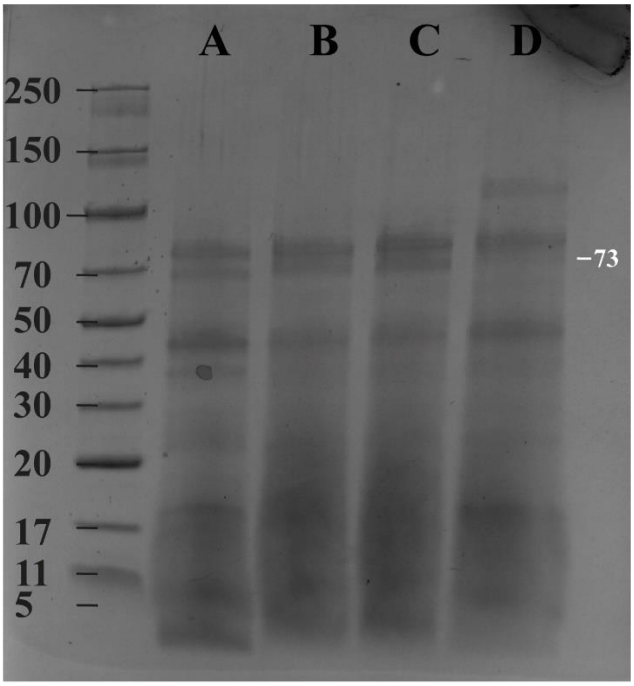

Figure 35: 4-20% SDS page gel (instant blue staining) depicting the small scale recombinant expression of Avi-rBSA in *P. pastoris;* induced with 2% methanol for 4 days at 30ºC. A-D) Samples collected from a four-day expression corresponding to day 1-4. rBSA protein runs at approximately 73 kDa. Protein ladder is in kDa.

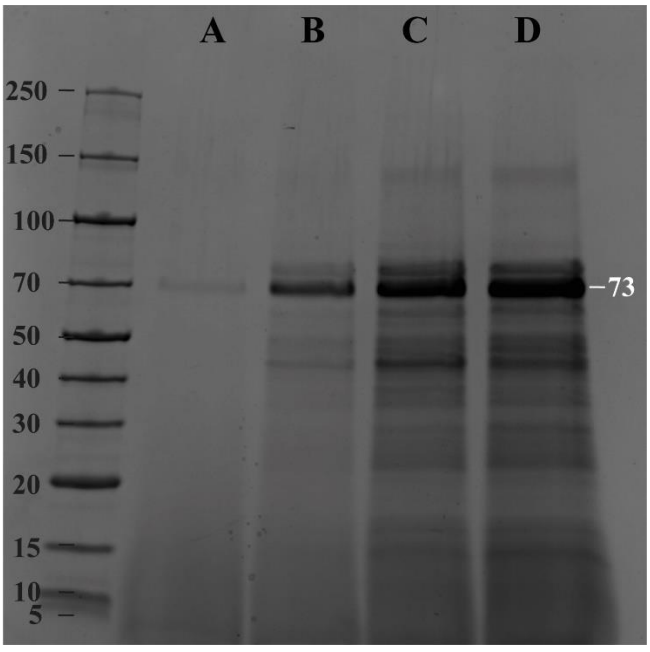

Figure 36: 4-20% SDS page gel (instant blue staining) depicting the small-scale recombinant expression of Avi-rBSA in *P. pastoris;* induced with 2% methanol for 4 days at 28ºC. A-D) Samples collected from a four-day expression corresponding to day 1-4 respectively. rBSA protein runs at approximately 73 kDa. Protein ladder is in kDa.

The pH was also found to play a big role in the final yield, Zhu et al trialled pHs ranging from 4.0 to 8.0[458]; it was identified that *P. pastoris* was capable of growth and protein production at all the pH conditions. However, the most optimal conditions were 6.0 and 5.5[458]. With all these optimisations taken into account we utilised the following conditions for our first expressions: 1% methanol every 24 hours at 28ºC at pH 5.5-6.0, supplemented with a complete amino acid powder (minus histidine) and 0.5% casamino acids. From a volume of 2 L culture medium split into four flasks, post purification and concentration using a concentrator a protein yield of up to 4.35mg/mL with a total of 78.8 mg purified in a final volume of 18 mL (Figure 37).

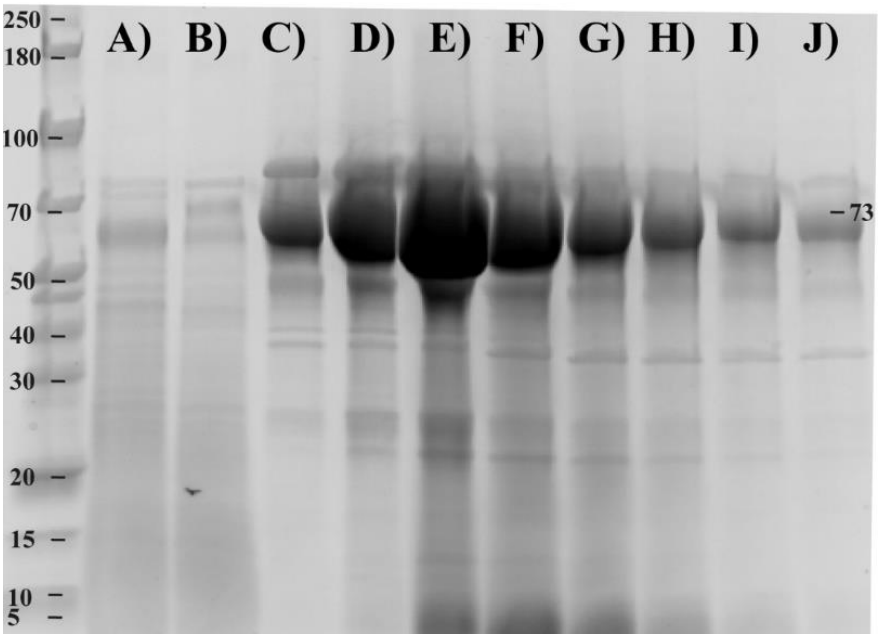

Figure 37: 4-20% SDS page gel (instant blue staining) depicting the large scale (2L) recombinant expression and purification of Avi-rBSA in *P. pastoris* (with the addition of amino acids, 0.5% casamino acids and pH 6.0); induced with 2% methanol for 4 days at 28ºC.

Purification via his tag nickel affinity chromatography, column washing using PBS + 20mM Imidazole, followed by elution using two in tandem HisTrap columns with PBS + 500 mM Imidazole. A) Sample collected after 4-day expression with 1% methanol at 28ºC. B) Flow through. C-J) Elution fractions. Protein ladder is in kDa.

This was a sufficient yield enough for downstream *in vitro* biotinylation by rBirA and relevant downstream experiments, however the yield was significantly improved by increasing the methanol concentration to 2% and further running the flow through once more through two in tandem HisTrap HP Prepacked Columns. After increasing the concentration of methanol to 2% and running two cycles of purification the yield was increased to 16.85mg/mL and a total of 135mg (post concentration in a final volume of 8 mL) of Avi-BSA purified from a 2 L culture (Figure 38A). Additionally, a High-performance liquid chromatography (HPLC) SEC run was completed to verify the oligomeric state of the recombinant Avi-rBSA protein. The SEC chart in Figure 38B depicts a single homogenous peak between fractions 11-14, this suggested that the BSA protein was expressed in a monomeric state, this was in line with the literature stating that the protein naturally occurs as a monomer[490].

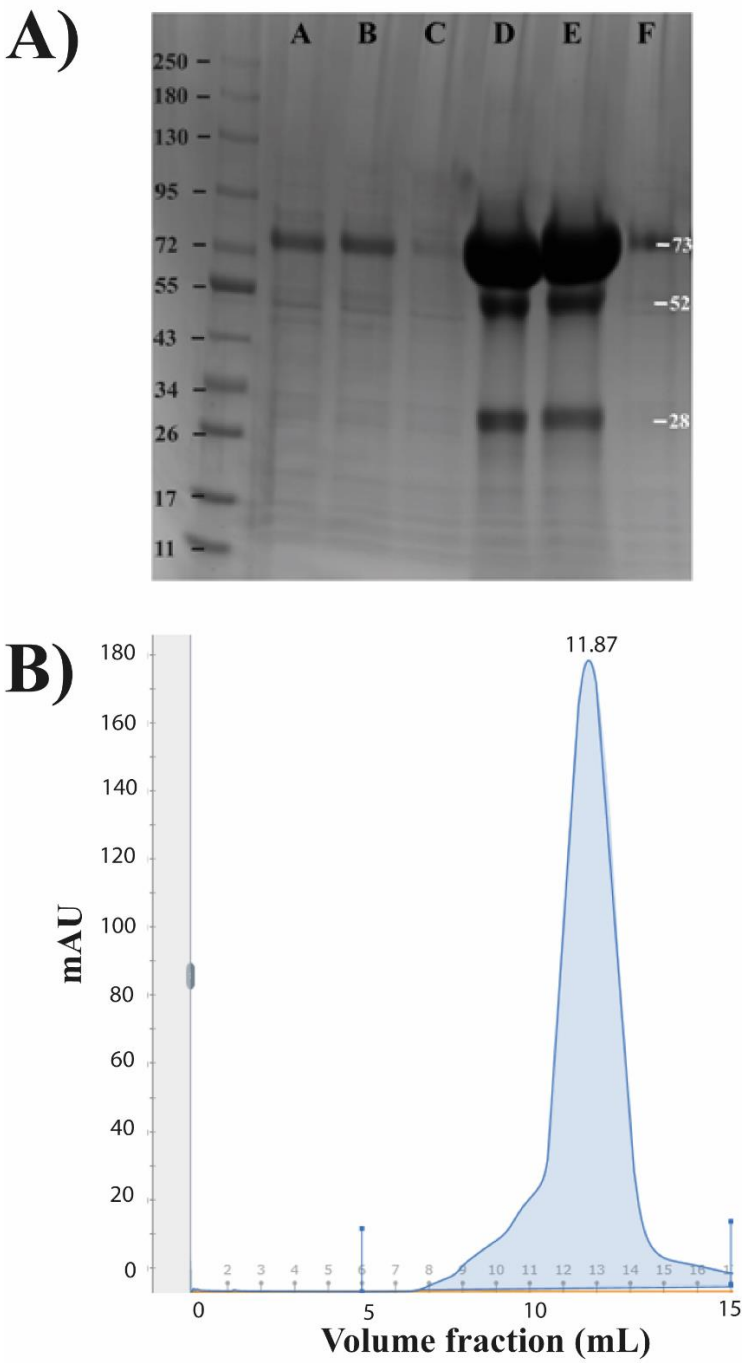

Figure 38: A) 4-20% SDS page gel (instant blue staining) depicting the recombinant expression and purification of Avi-rBSA in *P. pastoris;* induced with 2% methanol for 4 days at 28ºC. Purification his tag nickel affinity chromatography, column washing using PBS + 20mM Imidazole, followed by elution using two in tandem HisTrap columns with PBS + 500 mM Imidazole. A) Sample collected after 4-day expression with 2% methanol at 28ºC. B) Loading fraction. C) Wash fraction. D-E) Elution fractions 11-17. F) Flow Through fraction. Protein ladder is in kDa. **B) HPLC graph of Avi-rBSA purified via S200 10/300 SEC column at a flow rate of 0.25 mL/min. The void volume equated to ~7 mL; the purified protein observed a single homogenous peak indicating the protein was in the monomeric state.**

The tertiary structure for our recombinantly expressed Avi-BSA protein was predicted through the protein structure prediction software Alpha Fold 2, this was conducted to see whether the addition of the extra residues on the N-terminal region could potentially affect the structure of BSA. From Figure 39A, the tertiary structure still retained its typical heart shaped configuration with the new N-terminal attachment of the Avi and His-tag not affecting the overall integrity of the protein. From the Alpha Fold 2 PLDTT scored prediction (Figure 39C) the BSA core structure was to be expected a very high predicted accuracy as the structure is already available in databases online. However, the PLDTT scored prediction for the extra domain added in (Figure 39B) had a very low predicted accuracy, this is to be expected as this is a new sequence that has been attached to the N-terminal region of BSA, therefore the tertiary structure and orientation of this domain as presented in Figure 39A can only be used for visualisation purposes.

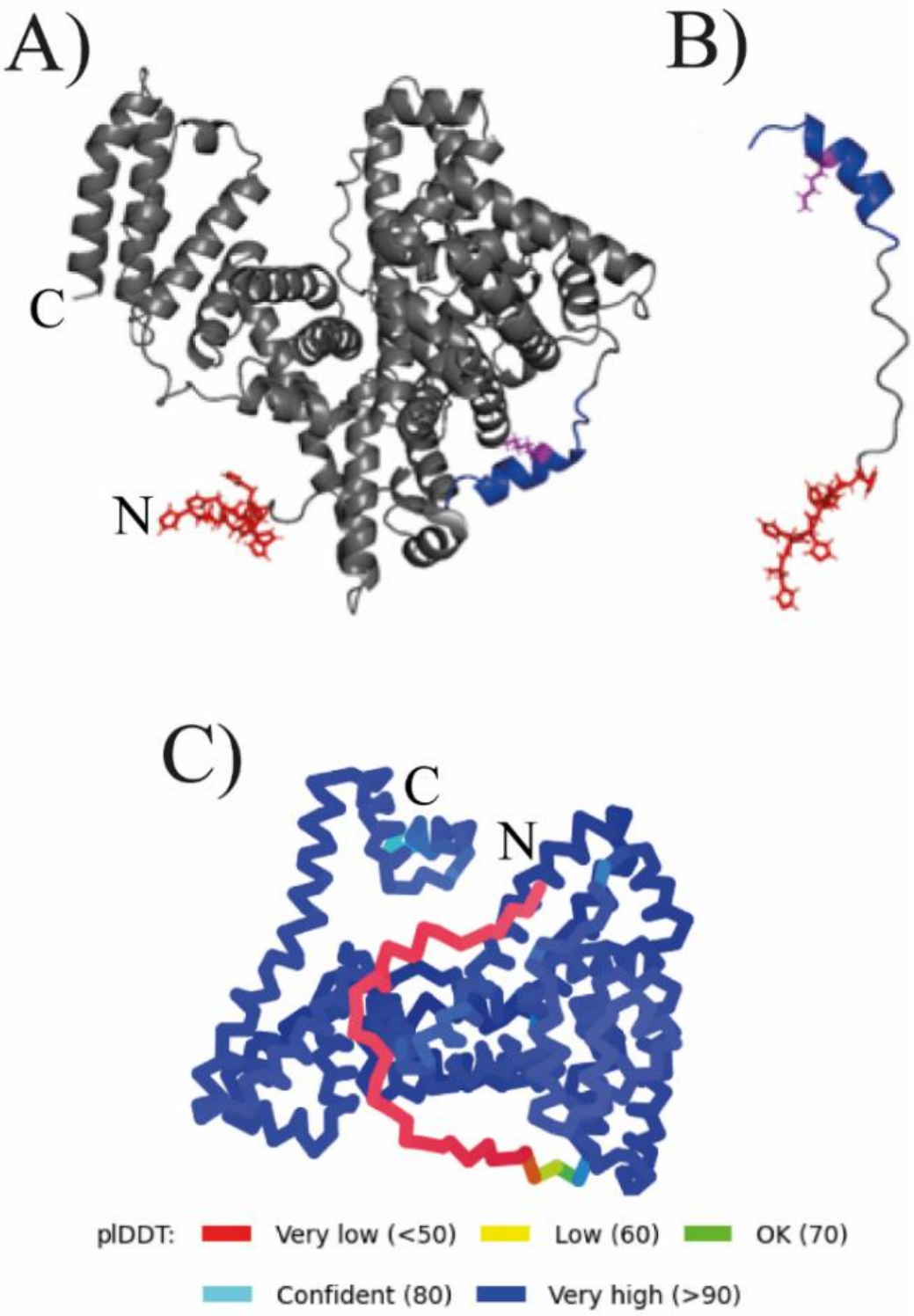

Figure 39: Alpha Fold 2 predictions on Avi-rBSA structure. A) Pymol representation of the predicted secondary structure for Avi-rBSA generated by Alpha Fold 2[491], N- and C- terminal regions highlighted. B) Pymol representation of the N-terminal region of Avi-rBSA, containing the 6x Histidine-tag (red), Avi-Tag (blue) and highlight in pink the lysine residue within the Avi-tag which is biotinylated by rBirA enzyme. C) Alpha fold 2 representation of the predicted Avi-rBSA coloured with the PLDTT score, the higher the value the higher the accuracy of the predicted residue.

3.9. Post expression processing of Avi-rBSA

In terms of optimising purification and processing of the expressed Avi-BSA protein, the original purification buffer utilised for purification contained 25 mM Tris-Cl pH 8.0, with 500 mM NaCl and 500 mM imidazole. This is the standard purification buffer for his-tagged nickel purification. However, downstream experiments required the protein to be in PBS, therefore buffer exchanges were required in PD10 desalting columns. This could have been done through the process of dialysis, however the PD10 columns are much more time efficient, saving at least a day in the process. Hence, a PBS based elution buffer containing 500 mM imidazole was trialled and found to not impair purifications. This saved the extra step of buffer exchange and only required simple dialysis to remove the excess salts and imidazole.

Once the protein was in the correct buffer, the Avi-tag was biotinylated *in vitro* by recombinantly expressed BirA (refer to sections 2.1.7 and 2.3). This enzyme was also recombinantly expressed in our labs to reduce the cost as the enzyme was expensive to use at larger scales. It was important for us to generate a sufficient amount of Avi-tagged protein that is clean of any salts as it is known that salts can affect the enzyme activity and reduce the success of biotinylation[492–494]. The optimal concentration of Avi-tagged protein is above the 40 μM threshold, below this the reaction will become inefficient[492]; it was also recommended that 2.5 μg of BirA was used per 10nmol of protein[494]. The level of biotinylation was quantitively measured using the Pierce biotin quantitation kit with the positive control being Biotinylated Horse Radish Peroxidase (Bt-HRP) protein, this has two biotins per protein molecule. Using this kit, we

managed to achieve a level of biotinylation between 0.9-1.0 biotin per molecule of Avi-BSA.

Furthermore, the biotinylation was also characterised qualitatively, via two separate methods. The first was a streptavidin gel-shift assay adapted from Fairhead et al[493], this involved the binding of the now biotinylated rBSA (Bt-BSA) protein to saturated streptavidin and observing a shift in molecular weight on an SDS gel. This method is time efficient and is based on the ability of streptavidin to retain its tetrameric biotin binding within the denaturing conditions of SDS buffer. This is true as long as the gel temperature does not get too warm[493,495]. We can see from the gel in Figure 40 in lanes L-M the Bt-BSA protein shifts from 73 kDa to 110 kDa, with the excess native streptavidin at 158 kDa.

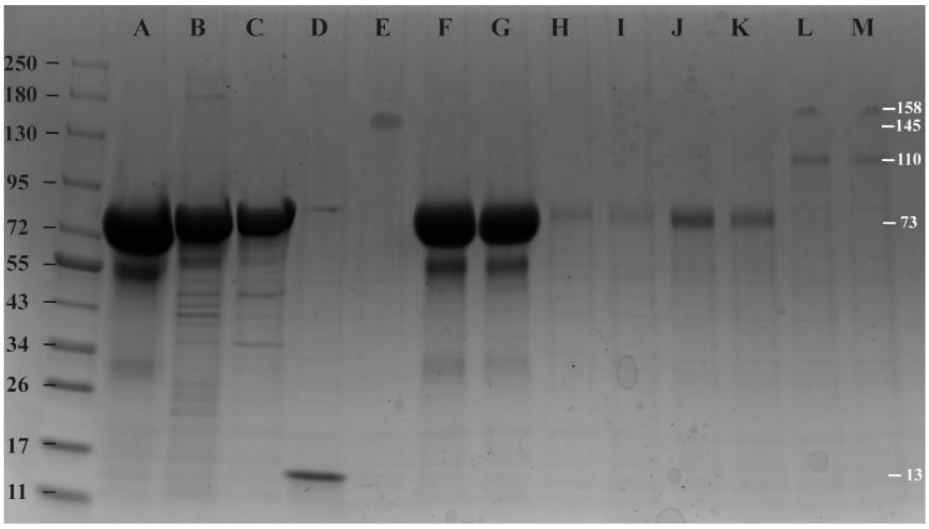

Figure 40: 4-20% SDS page gel (instant blue staining) depicting the successful invitro biotinylation of 45 µM recombinantly expressed Avi-BSA using 3 µM rBirA and 0.3 mM D-Biotin. 6xHis-Avi-BSA runs at approximately 71 kDa. MBP-rBirA runs at approximately 78 kDa. Native Streptavidin runs at 150 kDa. Streptavinated-rBSA runs at approximately 110 kDa. A) 45 µM Avi-rBSA. B-C) MBP-rBirA 3 µM. D) 1 mg/mL Streptavidin boiled at 95ºC. E) 1 mg/mL Streptavidin native. F-G) Bt-Avi-rBSA. H-I) Bt-Avi-rBSA post PD10 column fractions. J-K) Bt-Avi-rBSA post 30K MWCO concentrator fractions. L-M) Bt-Avi-rBSA with the addition of 1mg/mL native Streptavidin. Protein ladder is in kDa.

The second qualitative method used was to form Novec-7500 oil emulsions using the Bt-BSA protein at 1 mg/mL, then binding fluorescent streptavidin at 50 µg/mL to the surface of these emulsions and imaging under fluorescent microscope (Figure 41).

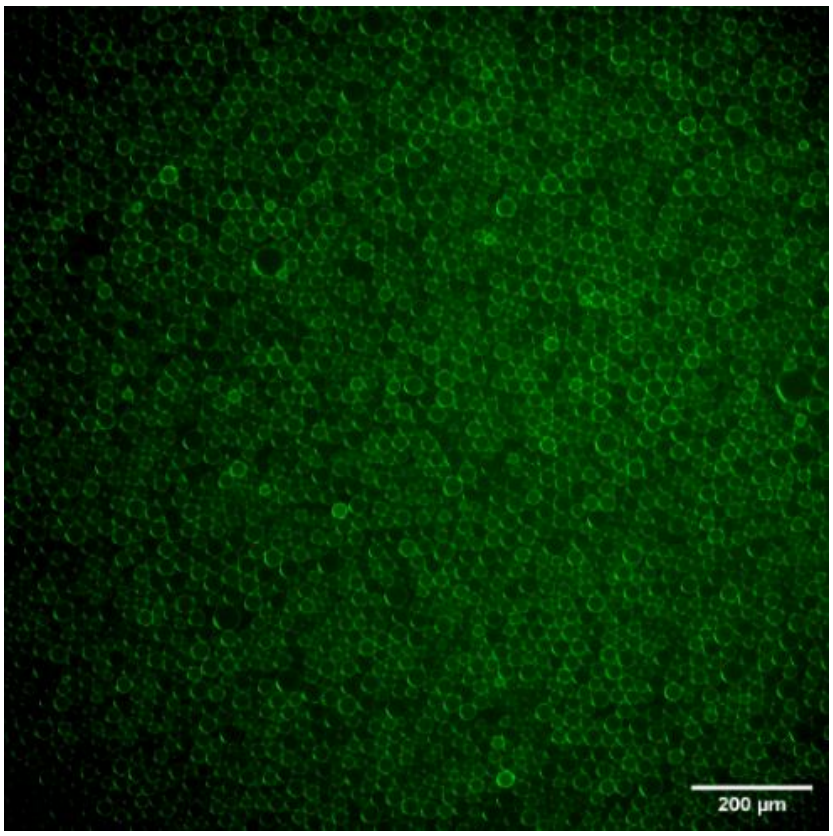

Figure 41: Fluorescent imaging of 1 mg/mL Bt-Avi-BSA emulsions coated with 50 µg/mL 488-Streptavidin.

3.10. Protein structural characterisation

3.10.1. Circular dichroism

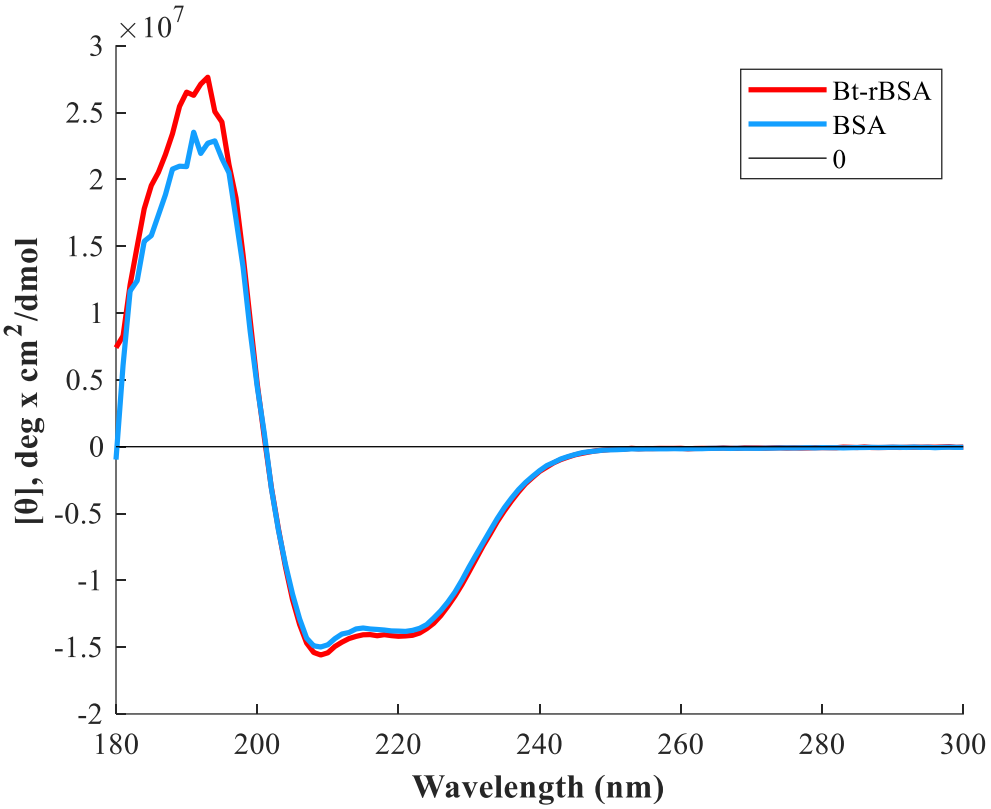

Figure 42: Circular dichroism spectrum of commercial BSA and Bt- rBSA at 20ºC, pH 7.4 (path length of 0.1 cm). Protein concentrations were standardised to 5 µM per sample in 5 mM iPO_4 phosphate buffer and triplicated with the mean Molar ellipticity (deg.cm^2/dmol) plotted.

The secondary structure of Bt-BSA was confirmed by circular dichroism and compared against commercial BSA. From Figure 42 we can see that the Bt-BSA follows a similar spectrum as the commercial BSA, with a peak at 190nm and two negative peaks at 208 and 222nm which indicated a typical alpha helical structure; this correlated with the crystal 3v03 structure (Figure 27A) and the predicted structure (Figure 39A). There was a slight difference in amplitude at the 190nm peak between

BSA and Bt-rBSA this could be due to the difference in molecular weight between the two proteins. The introduction of the Avi and His-tags onto the N-terminal region of Bt-BSA increases the molecular weight by approximately 4059 Da, this could potentially change the reading of the CD spectrum when the protein is measured holistically, the literature also suggests that a reduction in the molecular weight can diminish the peak intensity of the CD spectrum[496], this was similarly seen in our CD spectra.

3.10.2. Mass spectroscopy

The molecular weight of a biotin molecule is 244 Da[497], hence the shift in molecular weight is too small to identify without sensitive equipment. Therefore, mass spectroscopy was run on the recombinantly expressed rBSA samples to quantitatively measure the shift in molecular weight from the biotinylation of Avi-rBSA. From Figures 43-44 we can see that the average molecular weight of commercial BSA measured 67010 Da which was in line with the literature and was shifted by approximately 531 Da once the Avi-tag was introduced. Unexpectedly, the shift was lower than expected as the extra tags added onto the N-terminal region should of equated to roughly 4000 Da bringing the molecular weight to roughly 71200 Da. Furthermore, once the Avi-rBSA was biotinylated an increase of 550 Da in the average molecular weight was measured increasing the molecular weight to 68091 Da, this is roughly 306 Da over the molecular weight of a single biotin molecule of 244 Da. This increase could be linked to the addition of a N-terminal biotin molecule, however the error bars of Bt-rBSA were quite large when compared to the Avi-rBSA, thus the accuracy of the reading was not favourable. Moreover, one can theorise that the

variability in the molecular weight of the recombinant protein could be due to a minor N linked-glycosylation that occurs with the *P. pastoris* expression system during protein synthesis, however in the literature it is thought that the average molecular weight of an N-linked glycosylation is roughly between 1.4-2.7 kDa and in some cases of major glycosylation it can be between 3.6-4.5 kDa[498]. With the numbers obtained it is less likely to be the case of glycosylation occurring as the shifts observed were too small.

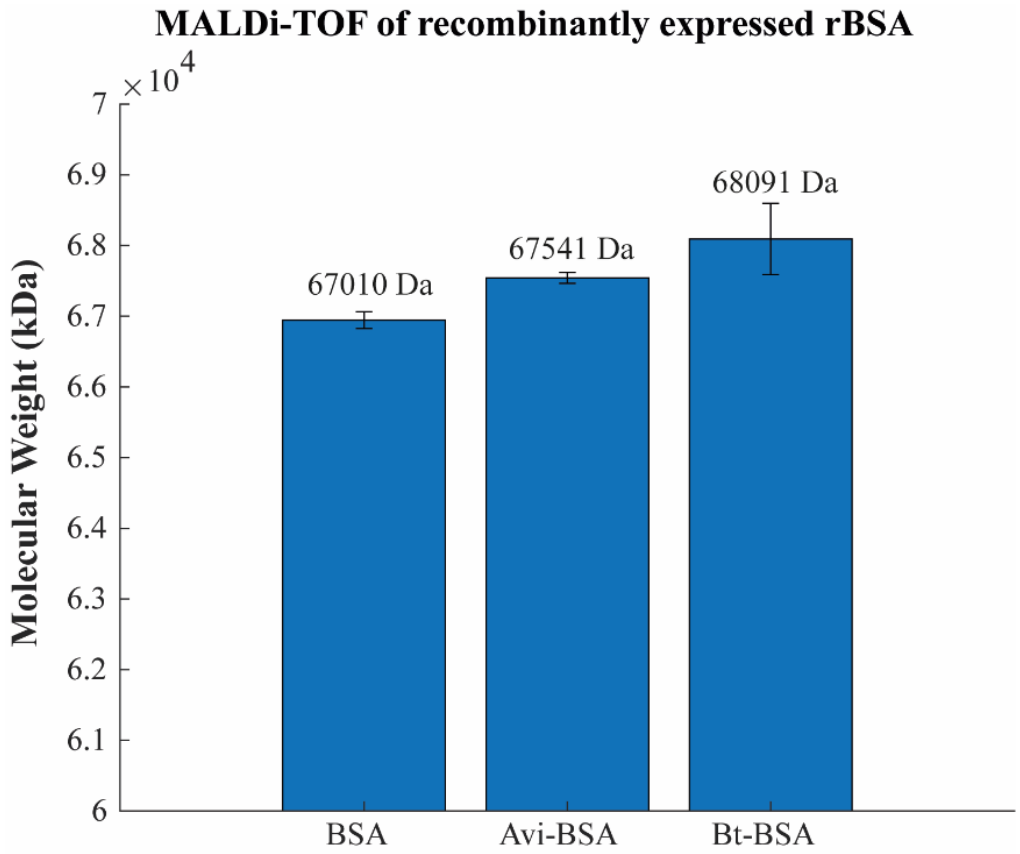

Figure 43: Comparison of the average molecular weight of commercial BSA and recombinantly expressed Avi-BSA and Bt-rBSA. The molecular weights BSA, Avi-BSA and Bt-BSA were 67010, 67541 and 68091 Da respectively. Each condition was triplicated and the mean intensities were plotted. The standard errors were depicted as error bars of three repeats per condition.

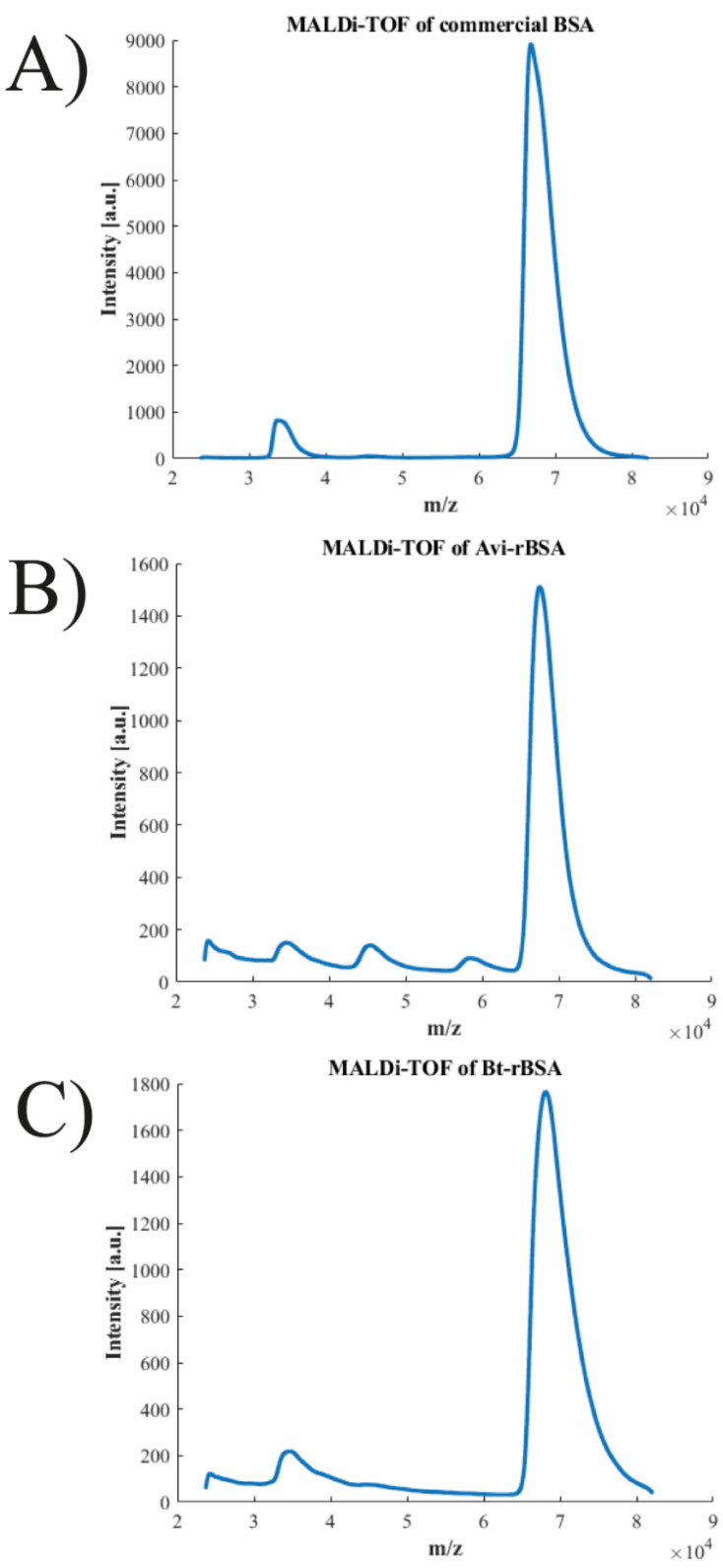

Figure 44: Mass spectroscopy of recombinantly expressed BSA to qualitatively measure the shift in molecular weight of Avi-BSA post-biotinylation with BirA. Each condition was triplicated, and the mean intensities were plotted. Samples were prepared in PBS at a final concentration of 0.5mg/mL**.** A) Commercial BSA. B) Avi-rBSA. C) Bt-rBSA. The molecular weights BSA, Avi-BSA and Bt-BSA were 67010, 67541 and 68091 Da respectively.

3.10.3. Interfacial rheology

Finally, the interfacial mechanics of the oil/PBS interfaces formed by the Bt-BSA was also studied and compared to commercial BSA (Figure 45). After equilibration of Novec-7500/PBS interfaces in the absence of proteins, protein solutions (final concentration in the trough of 1 mg/mL) were injected and the evolution of the interfacial shear moduli was monitored. Here we can see the Bt-BSA reaching roughly the same storage modulus as commercial BSA, this indicated that the network formed at the interface exhibited similar interfacial mechanics and stiffness.

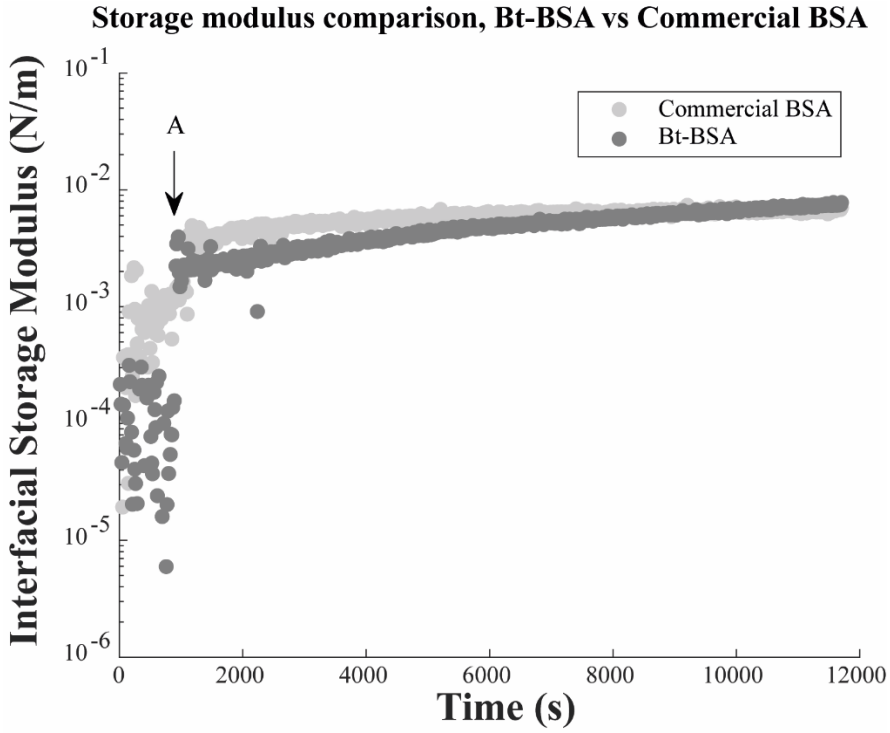

Figure 45: Evolution of the interfacial storage moduli of 1mg/mL commercial BSA and Bt-BSA (1 mg/mL) at the Novec-7500 oil/water interface; measured by interfacial shear rheology. A) Injection of Bt-BSA into the aqueous phase at 900s. The experiment was run once for each condition.

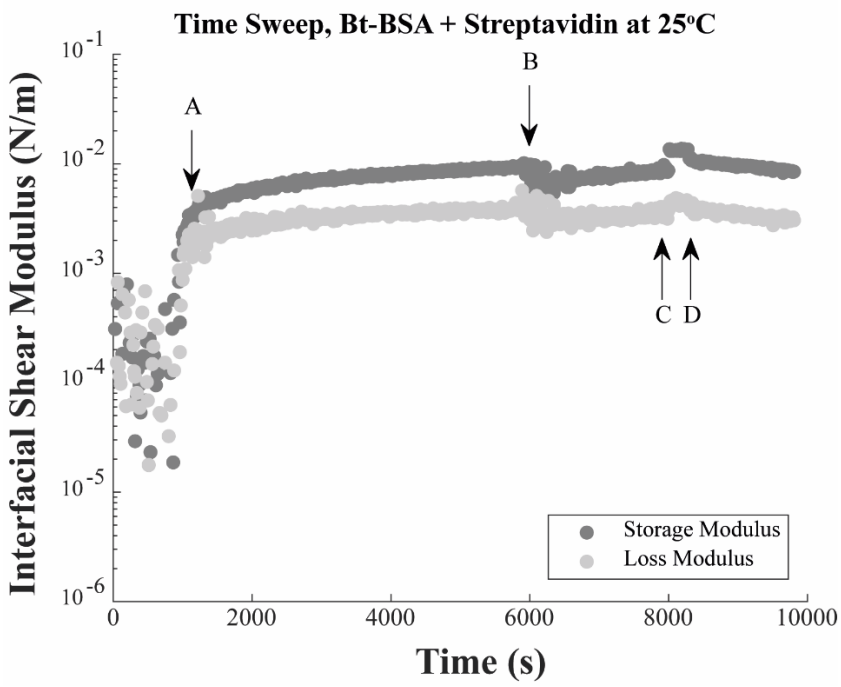

Figure 46: Evolution of the interfacial shear moduli of Bt-BSA at the Novec-7500 oil/water interface. A) Injection of 1mg/mL Bt-BSA protein into the aqueous phase at 900s. B) Washing of the excess protein using 30 mL PBS and Elve Flow system. C) 5 minutes recovery of the nanosheet. D) Introduction of 100 µg/mL streptavidin. The experiment was run once for each condition.

With the addition of streptavidin to the Bt-BSA network (Figure 46) we found a slight decrease in the interfacial shear moduli, indicating a softening of the interface.

3.11. Expression of rBSA in *E. coli*

Whilst experimenting with *P. pastoris* and learning the principles behind expression in yeast, the expression of Avi-rBSA in *E. coli* was attempted. This was completed to test whether the Avi-rBSA protein was able to be produced in analogous system such as the bacterial expression system. The Rosetta BL21 *E. coli* expression strain was chosen as the first host for bacterial expression due to its capabilities to utilise rare codon tRNAs that are commonly used in eukaryotic proteins that are rarely used in *E. coli*[499], and since rBSA is a eukaryotic protein, it was theorised that it would aid in its expression. All three solubility tags were attempted in Rosetta; however, the system was not sufficient to produce any soluble protein, the protein was found to be aggregating in the insoluble pellet. It was thought that the conditions that Rosetta was providing was not enough to promote correct folding, hence the disulphide bonds that are present in BSA were targeted in hopes of promoting correct folding. Thus, the SHuffle® T7 Express *E. coli* strain was incorporated due to its ability of oxidative folding in the bacterial cytoplasm, this promotes the formation of disulphide bonds[500] which the BSA protein is rich in. The SHuffle strain lacks the trxB reductase gene which promotes the expression of Trx1 protein in the cytoplasm, this protein catalyses the formation of disulphide bonds within the cytoplasm under oxidative conditions[500]. Additionally, the strain also is engineered to express DsbC in the cytoplasm which further isomerises mis-oxidised proteins back to their native states[500].

First trials were conducted at a small scale to establish the optimal temperatures to be used, in Figure 47-48 the 16^{o}C condition was found to produce the highest amount of soluble protein, this was indicated by a darker band present in the elution fractions for

S3C-rBSA and MBP-rBSA at their relative molecular weights. It is to be noted that the GST-tag on the GST-rBSA was not sufficient to generate soluble protein in SHuffle, hence was not continued. Using these conditions, the expression conditions were scaled up into 1 L cultures to identify which of the two tags would perform best to promote the expression of rBSA protein in soluble cytoplasm. In Figure 49, it was evident that the MBP-tag generated much higher amount of Avi-rBSA indicated by the darker and thicker bands present in lanes L-N compared to the fainter band S3C-tag in lane F.

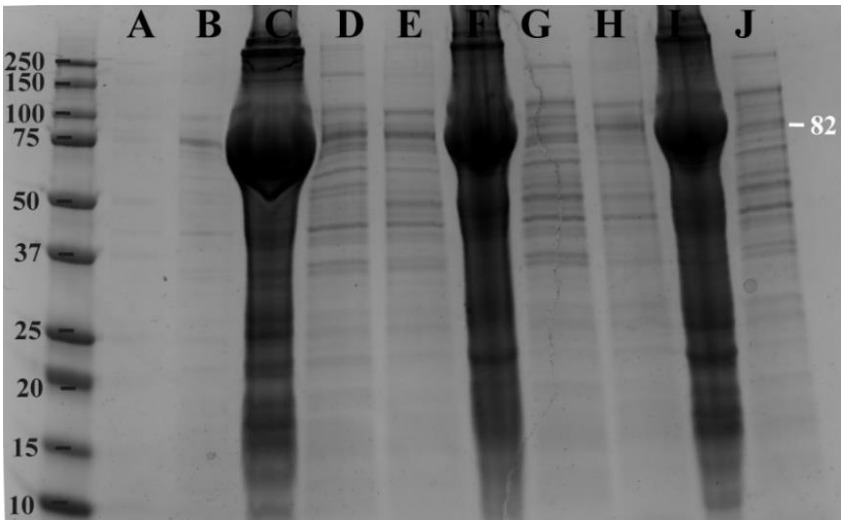

Figure 47: 4-20% SDS page gel (instant blue staining) depicting the small-scale recombinant expression and purification of S3C-rBSA. Expression at 16ºC (B-D), 30ºC (E-G) and 37ºC (H-J) overnight, 1mM IPTG induction SHuffle® T7 Express *E. coli* cultures. A) Pre-induction fraction. B) Post induction fraction. C) Pellet fraction. D) Supernatant fraction. E) Post induction fraction. F) Pellet fraction. G) Supernatant fraction. H) Post induction fraction. I) Pellet fraction. J) Supernatant fraction. Approximate size of S3C-BSA = 82 kDa. Protein ladder is in kDa.

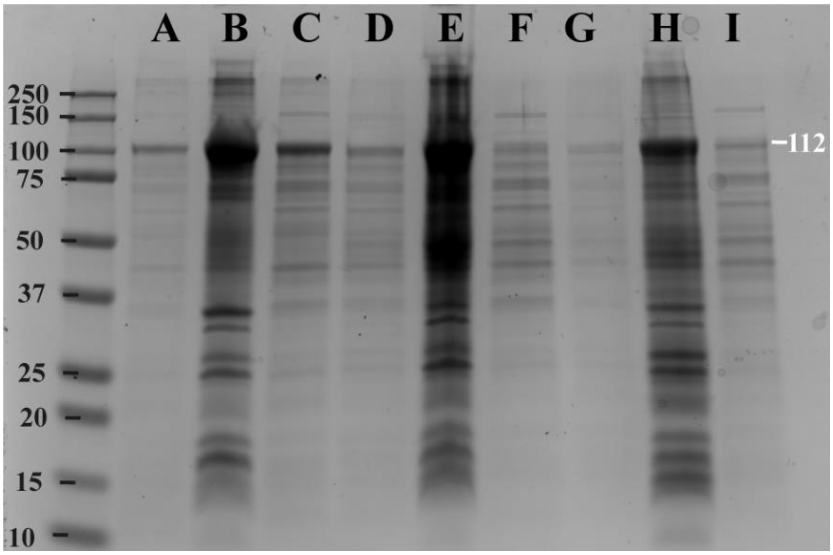

Figure 48: 4-20% SDS page gel (instant blue staining) depicting the small-scale recombinant expression and purification of MBP-rBSA. Expression at 16ºC (B-D), 30ºC (E-G) and 37ºC (H-J) overnight, 1mM IPTG induction SHuffle® T7 Express *E. coli* cultures. A) Pre-induction fraction. B) Post induction fraction. C) Pellet fraction. D) Supernatant fraction. E) Post induction fraction. F) Pellet fraction. G) Supernatant fraction. H) Post induction fraction. I) Pellet fraction. J) Supernatant fraction. Approximate size of MBP-BSA = 112 kDa. Protein ladder is in kDa.

It was concluded that the Avi-rBSA protein is also capable of being expressed in *E. coli*, however the system was not utilised for further studies for multiple reasons. The first being that the *P. pastoris* system was the main goal of the project and we were able to produce Avi-rBSA in *P. pastoris* at the levels required for downstream experiments. Second, the MBP-tagged Avi-rBSA was the most effective tag out of the three for bacterial expression, however the tag is roughly 43 kDa in size, this adds significant bulk and hinderance to the target protein compared to the much smaller his-tag which could potentially hinder downstream applications of bt-BSA. Thus, it is necessary to cleave the MBP-tag off the Avi-rBSA N-terminus, this will require extra purification steps leading to reduction in yields and increase to costs as the 3C protease is extremely expensive, rendering the system unviable for scaled industrial use.

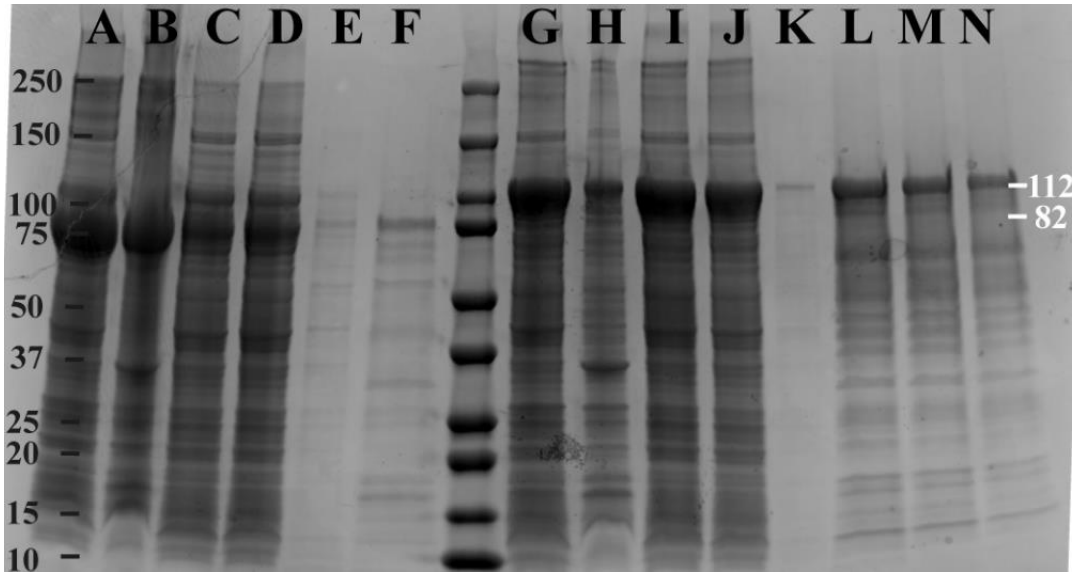

Figure 49: 4-20% SDS page gel (instant blue staining) depicting the recombinant expression and purification of rBSA from 1 L cultures, induced with 1 mM IPTG at 16ºC, 220rpm overnight in SHuffle® T7 Express *E. coli* cultures. Purification via 1 mL elution fractions using 2 mL of HisPur Ni-NTA Resin and elution buffer (PBS + 500 mM Imidazole + 500 mM NaCl). A-F = S3C-BSA expression and purification. A) Cell lysate fraction. B) Cell pellet fraction. C) Supernatant fraction post cell lysis via sonication. D) Nickel NTA resin fraction containing the S3C-tagged rBSA. E) Flow-through fraction post resin incubation. F) Elution fractions collected containing purified S3C-rBSA. G-N = MBP-BSA expression and purification. G) Cell lysate fraction. H) Cell pellet fraction. I) Supernatant fraction post cell lysis via sonication. J) Nickel NTA resin fraction containing the MBP-tagged rBSA. K) Flow-through fraction post resin incubation. L-N) Elution fractions collected containing purified MBP-rBSA. Protein ladder is in kDa.

4. Bioactive microdroplet technology for organoid biology

4.1. Microdroplets as a force sensor in cerebral organoids – outline of the system

The protocol used for the generation of cerebral organoids was adapted from the pioneering study by Lancaster et al[105], in which she reported that different brain regions can be formed within a single organoid by adjusting the media compositions, to direct human iPSCs towards neuroectodermal lineages. These budding organoids form neuroepithelial buds that protrude from the initial embryoid body and can be further matured indefinitely within spinning bioreactors [105]. Previous reports had indicated significant changes in cell shape occurring during early stages of differentiation and rosette development, suggesting the occurrence of significant cell-to-cell forces within these budding structures[92,105,110,168,171]. Therefore, we initially proposed that microdroplets displaying cadherin ligands could allow proving forces generated during these events. Such approach could allow addressing issues with the majority of micromanipulator force measuring techniques such as indenters and microplates, which only have access to the forces on the surfaces of cellular structures [293,294]. To solve this, we proposed to adapt the protocols by Campas et al[243,246,299,301] to use functionalised droplet-based force sensors to measure internal forces generated by the differentiating human iPSCs within the developing cerebral organoids. Thus, the recombinant Bt-rBSA protein expressed in the previous chapter was used to generate

microdroplets at physiological cell sizes (20-30 µm). Furthermore, droplet composed of fluorocarbons generally should stay below 600 µm to prevent the deformation by gravity and above 10 µm to avoid internalisation by cells [292]. The rBSA protein was designed to specifically orientate the biotin located at the N-terminal region of rBSA towards the aqueous phase post adsorption onto the Novec-7500 oil (seen in Figure 50). This proposal worked as it was predicted in Molecular dynamic simulations[462] that the C-terminal domain of BSA, has a higher probability to adsorb at hydrophobic interfaces due to the hydrophobic pockets located at this terminal end; this led to the unfolding of the C-terminal end leaving the N-terminal facing towards the aqueous phase. As previously discussed, the method was verified to work by the addition of 488-tagged Streptavidin to the microdroplets, followed by imaging under a fluorescent microscope (Figure 41). The non-covalent biotin-streptavidin complex was chosen as the primary functionalisation due to its simple click mechanism and very high binding affinity with a dissociation constant of 10^{-14} mol/L[501], making it very relevant to study mechanical forces generated by cells as the bond must be strong enough to withstand the shear and stress generated by cells at the surface of the droplets.

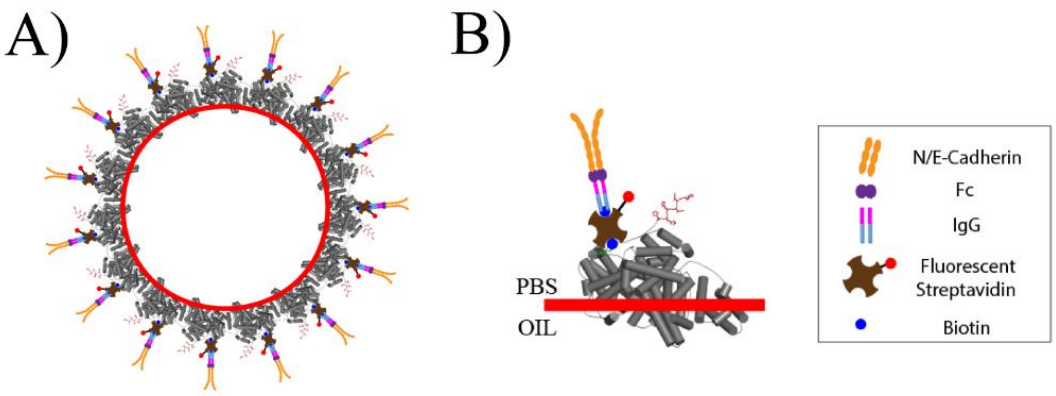

Figure 50: Example of the functionalisation cascade of Bt-BSA. A) Schematic of a functionalised microdroplet with Bt-BSA and bioactive components. B) Schematic of the functionalisation components used to generate Cadherin based-bioactive microdroplets.

4.2. Design of bioactive droplets and optimisation of the functionalisation strategy

Once the successful binding of streptavidin was confirmed on the droplets as seen in Figure 41, the next step was to select bioactive ligands to introduce on the surface of the droplets. This was an important decision as we wanted the droplets to interact with cells within the core of organoids, to allow the cells to deform the droplets and allow the quantification of forces generated using the protocol reported by Campas et al[246,299]. Cadherins were the first target as they are known to play an important role in spontaneous sorting and patterning within embryos. The localisation of Cadherins within complex tissues is explained by the differential adhesive affinity hypothesis that was proposed by Steinberg in 1962-1963 [178,179]. The hypothesis stated that the less adhesive cells (expressing less Cadherins at their surface) will sort towards the periphery and more adhesive cells (expressing more Cadherins at their surface) will be enveloped and sort towards the centre of the cell mass; this provided the lowest free energy state [179]. Hence, the most ideal interaction between our droplets and the cerebral organoids would be for our Cadherin functionalised droplets to interact with the central adhesive cells and undergo a degree of deformation. The Campas group used oil droplets coated with biotinylated mouse E-cadherin antibodies to measure the mechanical stresses in mammary epithelial cell aggregates [243]. Additionally, studies in early mouse embryos demonstrated that E-cadherin and N-cadherin were particularly abundant and underpinned cell-cell adhesion[502], thus these two cadherin types were selected for further experimentations. Protein-G is an immunoglobulin (IgG) binding protein isolated from streptococci that has the ability to bind antibodies from several

species such as human, bovine, rabbit, mouse and goat at a much higher affinity than the staphylococcal Protein-A[503]. To introduce the proposed bioactivity onto the droplets, biotinylated Protein-G was bound to the streptavidin to allow the capture of antibodies such as the relevant Fc-tagged cadherins (as seen in Figure 50). The binding of Protein-G was verified qualitatively by the binding of secondary Alexa Fluor antibodies and viewed under a fluorescent microscope. In Figure 52C, we found that the Alexa Fluor-594 secondary antibody was lining the surface of the droplets indicated by the positive fluorescence. The negative control in Figure 52A verified that no unspecific binding of secondary antibodies was occurring to the surface-bound streptavidin or the surface of the droplets; indicated by the lack of fluorescence in the 594 range. The binding of the commercial Cadherins to Protein-G was verified by SPR, the shift in response units observed after the addition of each component in Figure 51 confirmed the success of the functionalisation cascade.

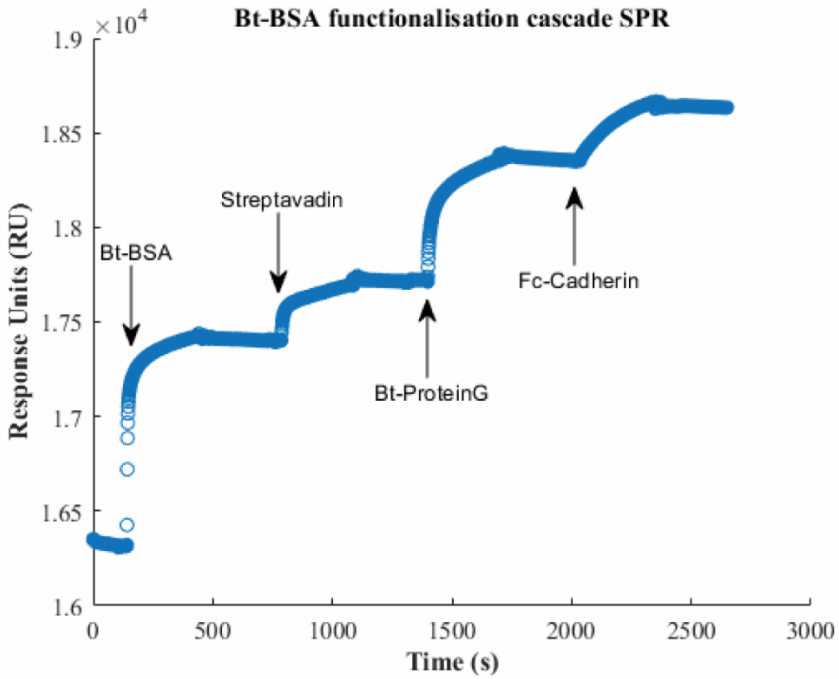

Figure 51: SPR measurements of the functionalisation cascade, injection of 1 mg/mL recombinant Bt-rBSA, followed by 50 µg/mL Streptavidin, 100 µg/mL Bt-ProteinG and 25 µg/mL Fc-tagged E-Cadherin. The experiment was repeated three times and the mean SPR value was plotted.

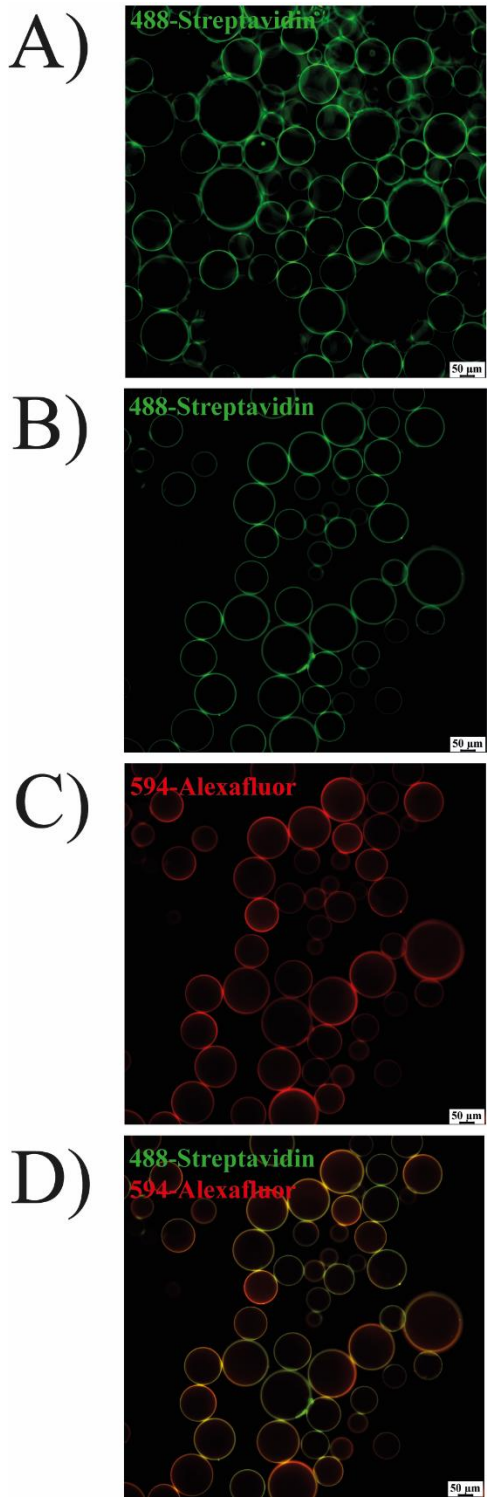

Figure 52: Testing the functionalisation of Bt-BSA Novec-7500 emulsions. A) Negative control, imaged in the 488 and 594 range. Bt-BSA + 488-Streptavidin + 594 Alexa Fluor secondary antibody. **B)** Sample of interest, imaged in the 488 range. Bt-BSA + 488-Streptavidin + Bt-Protein-G + 594 Alexa Fluor secondary antibody. **C)** Sample of interest, imaged in the 594 range. Bt-BSA + 488-Streptavidin + Bt-Protein-G + 594 Alexa Fluor secondary antibody. **D)** Sample of interest, imaged in the 488 and 594 range. Bt-BSA + 488-Streptavidin + Bt-Protein-G + 594 Alexa Fluor secondary antibody. Images captured at 20x magnification.

To optimise the concentrations of each component and increase the cost-effectiveness of the system, fluorescent microscopy was used to measure the fluorescent intensities after varying the concentrations. From the data depicted in Figures 53A-C, the optimal concentrations for each functionalisation were chosen: 100% of Bt-BSA was used to form emulsions, 50 µg/mL FITC-Streptavidin was chosen as the full surface of the emulsion was required to be functionalised to maximise the chance of interactions with the cells and that the graph had not reached the plateau yet. 100 µg/mL Bt-ProteinG was chosen as the difference between 100-500 µg/mL was not as significant as 50-100 µg/mL, thus saving costs due to the expensive cost of Bt-ProteinG. Finally, 25 µg/mL of Fc-tagged E-Cadherin and Fc-tagged N-Cadherin was deemed to be sufficient concentration to line the surface of the emulsions based off the significant increase in response observed in the SPR (Figure 51), thus the cadherins should be presented at a sufficient level on the surface of the droplets to promote interactions with the cells.

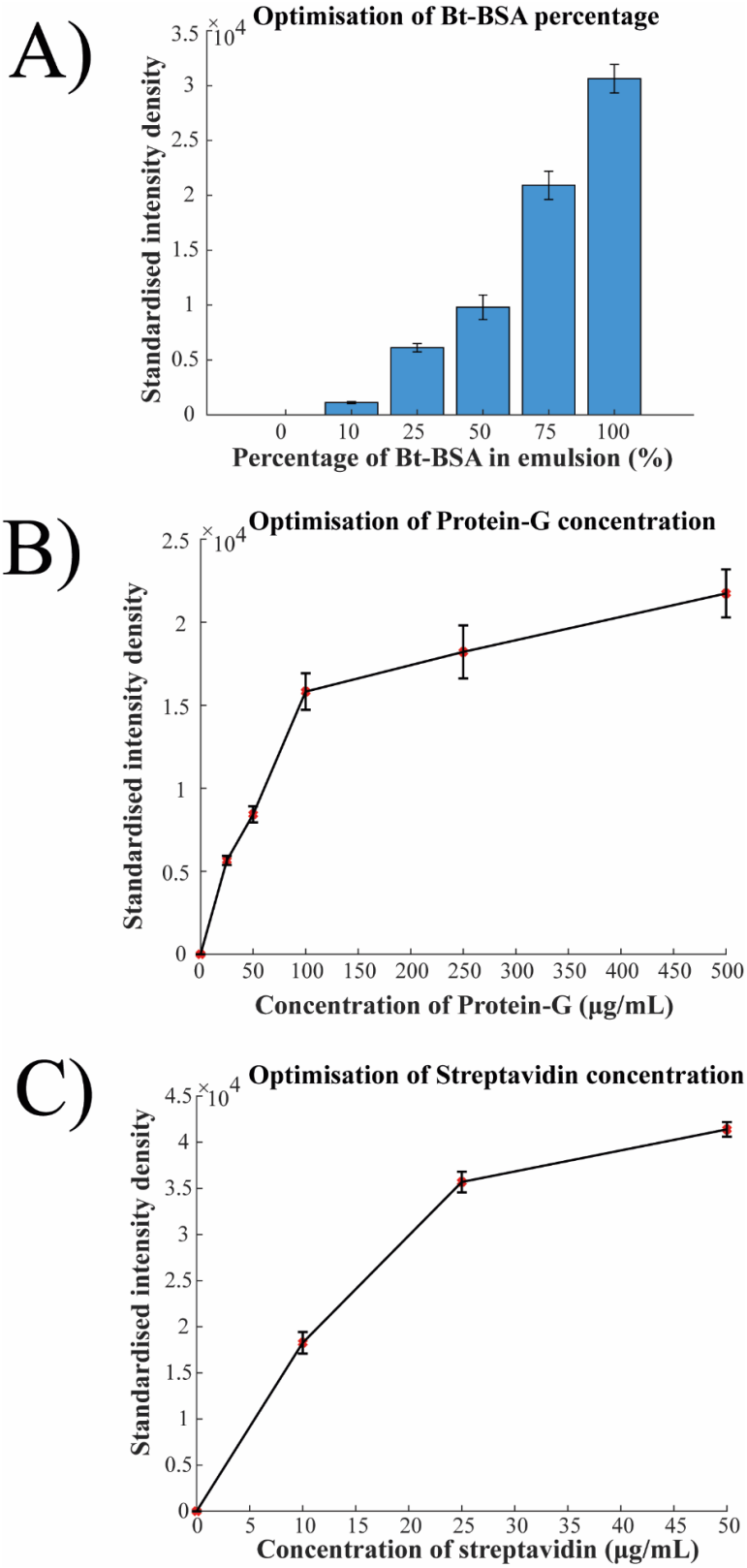

Figure 53: Optimisations of the concentrations of the functionalisation cascade components. Optimisation of the concentration of A) Bt-BSA. B) FTIC-Streptavidin. C) Bt-ProteinG. Each condition studied was triplicated and the mean was plotted. The standard errors were depicted as error bars of three repeats per condition studied.

4.3. Generating cerebral organoids and culture conditions optimisations

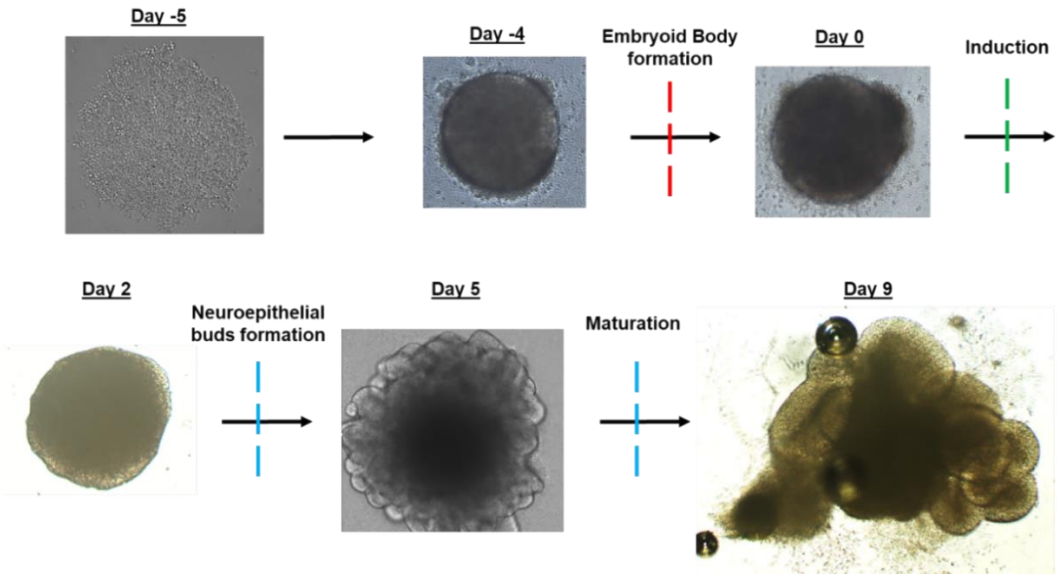

Figure 54: Schematic of the formation of cerebral organoids from hIPSCs from day -5 to day 9. All images were taken on a brightfield microscope at the relevant timepoints.

Once the functionalisation of the droplets was confirmed and the functionalisation strategy was optimised, the next step was to culture and differentiate EBs into cerebral organoids as seen in Figure 54. Due to the novel nature and complexity of the system many attempts were conducted to perfect the EB formation and differentiation process in the lab to increase replicability and accuracy. The protocol available from Lancaster et al[105] suggested that the cerebral organoids at day 2 are required to be embedded into Matrigel to promote neuroepithelial buds to form, however they observed higher rates of necrotic core formations; this is a result of the high cell proliferation and densities during differentiation and the difficulty of diffusion of nutrients and oxygen into the

core due to the surrounding scaffold [91]. Furthermore, due to the crude nature of the Matrigel embedding process we found that the recovery rate of EBs after this step was very low, resulting in at least half of the EBs being lost or damaged. To solve this, we found a method named serum-free floating culture of embryoid body-like aggregates (SFEBq) [146,504], this was adapted by the Sloan lab [161] to generate brain organoids without the need of embedding into an ECM matrix; instead, they supplemented a final concentration of 2% Matrigel into the differentiation medium. With this in mind, we utilised this supplementation technique for our downstream organoid experiments and found great success with the generation of multiple 96 well plates filled with single EBs at a time; this increased the time efficiency of the technique and increased the final yield significantly. This was nicely demonstrated in the timelapse in Figure 55, with the expansion and formation of neuroepithelial buds from days 3-5 without the need of the embedding process. These organoids continued to develop and mature into day 5 and day 9 (Figure 56) cerebral organoids with the characteristic rosette formations, illustrated by the ZO-1 staining of tight junctions in Figure 56.

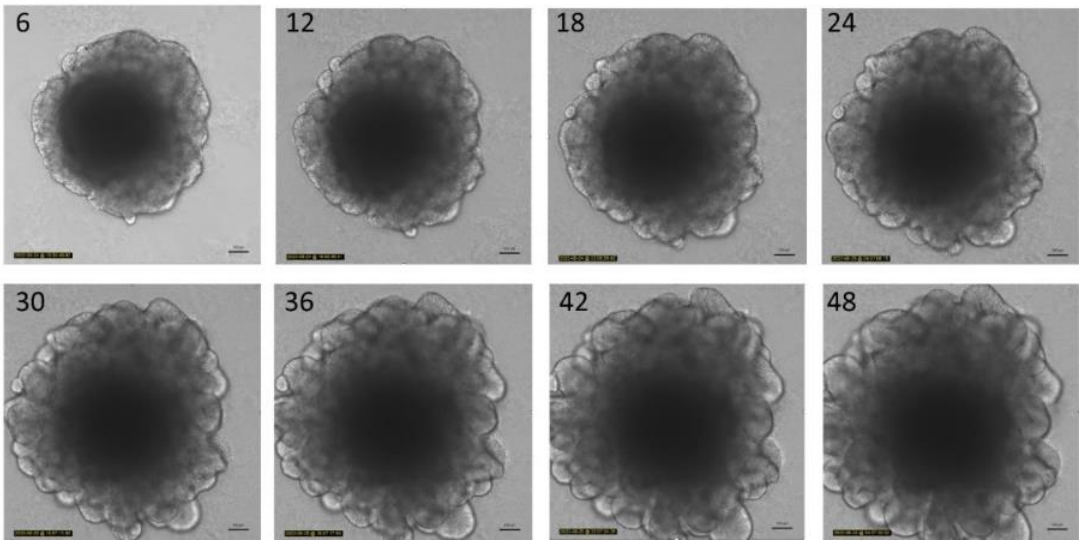

Figure 55: Snapshots of the timelapse of the expansion of neural epithelial buds from days 3-5 using 9000 cells/well initial seeding density. All images at 10x Magnification.

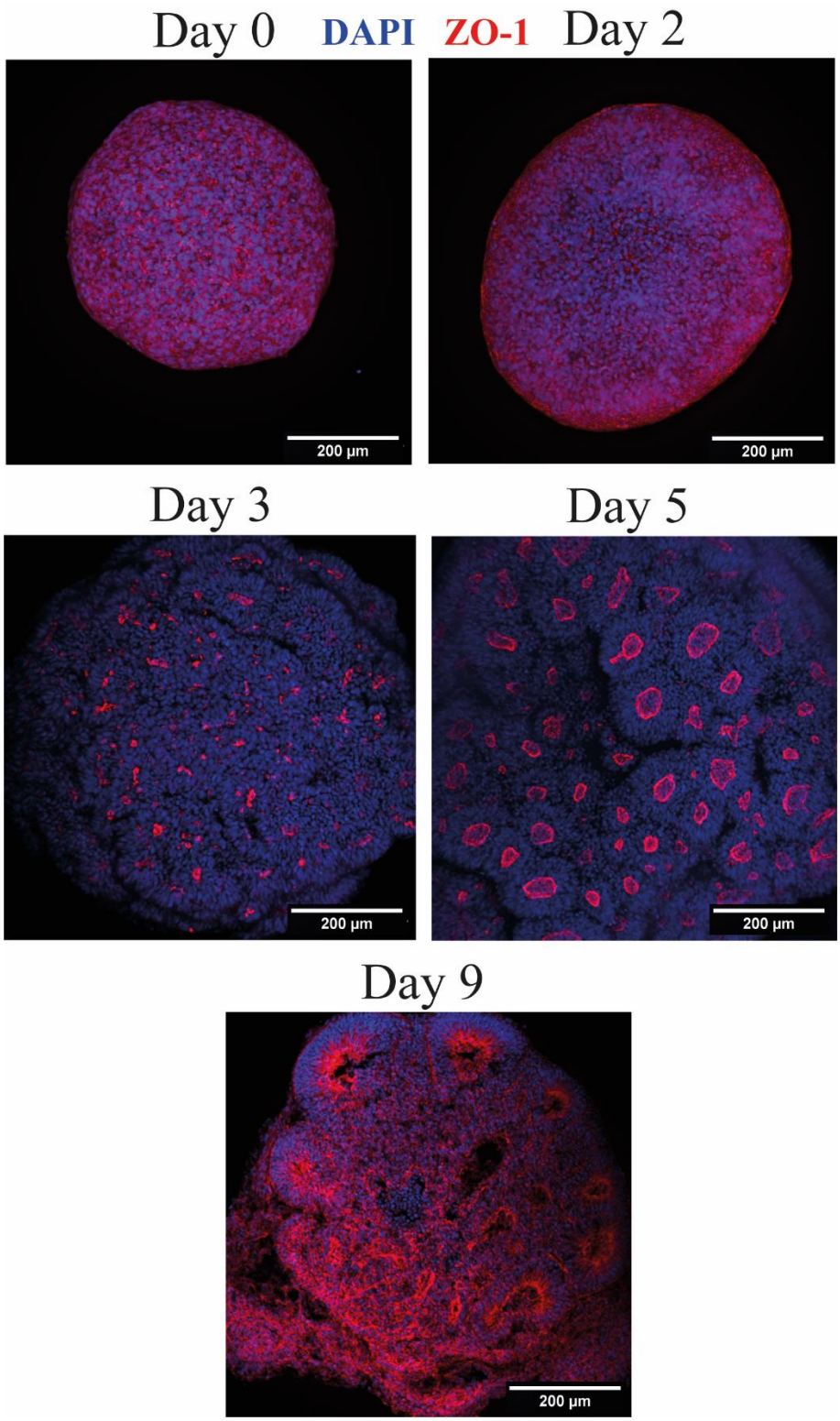

Figure 56: The normal development of rosettes in cerebral organoids at the time points: Day 0, 2, 3, 5 and 9. Stained with Blue = DAPI (1:1000) and Red = ZO-1 (1:200). Day 0 represents the embryoid body. Day 2 represents the embryoid body induced to cerebral lineage. Day 3 represents the early differentiation of cerebral organoids, the beginning of rosette formations. Day 5 represents the expansion of rosettes and neural bud formation. Day 9 (Cryosectioned) represents the maturation of rosettes. All images at 20x magnification.

4.4. Characterisation of mechanical forces in cerebral organoids

The goal of this section was to explore markers associated with cerebral organoid differentiation and potential mechanotransduction events in late day 9 organoids. Due to the extensive cell density within these mature organoids, confocal microscopy was not sufficient to penetrate deep within the centre of the organoids; this rendered the cores uncharacterizable through fluorescent microscopy. Thus, the organoids were snap frozen in OCT (Optimal cutting temperature compound) blocks and cryosectioned using a bright cryostat at -10^{o}C. In the literature, the Lancaster lab utilised gelatin/sucrose treatment to generate cryostat blocks for cryosectioning[110]. However, the same protocol was attempted in our lab, but was found to be inefficient and time consuming if a high number of cerebral organoids was required to be sectioned. Hence, OCT blocks were generated in a very small fraction of the time and produced very clean sections as seen later. The specific cryosectioning temperature was recommended by the cryostat lab manager due to the soft nature of organoids; this formed excellent 25-30 µm slices that were later used for immunostaining.

It had been recognised that morphogenic changes during brain development involves the cellular shape remodelling and movement that exert mechanical forces on the surrounding ECM and neighbouring cells [505]. Furthermore, in both immature [506] and adult [507] neurons the transduction of these mechanical forces into intracellular biochemical pathways is known to be modulated by the process of mechanotransduction, and this has been linked to the maturation and differentiation of these neurons [505]. Mechanical tensions are transmitted between neighbouring cells in the brain via transmembrane receptors such as cadherins and integrins [508].

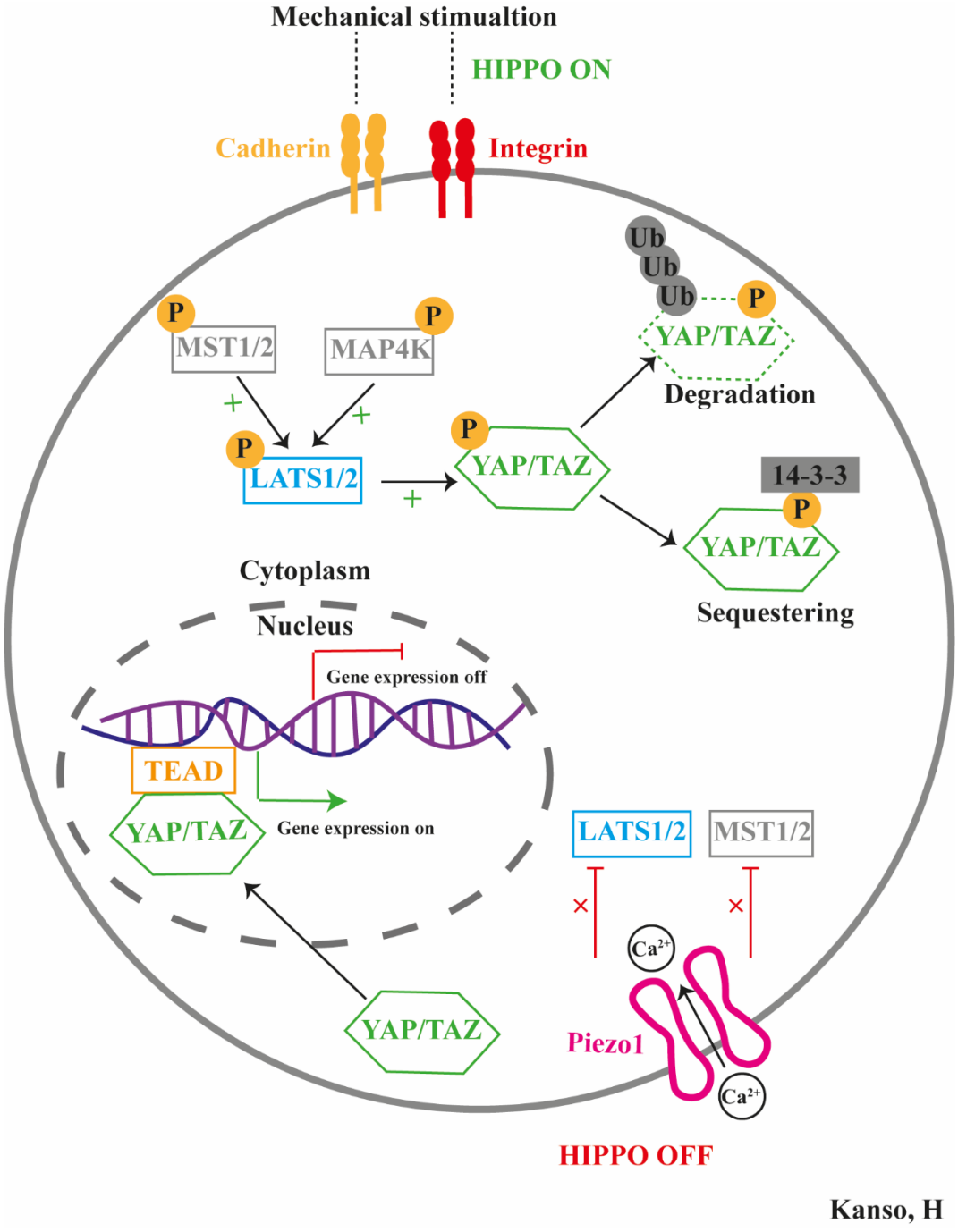

Figure 57: Biomechanical Hippo signalling pathway. HIPPO ON: Mechanical stimulation sensed by mechanosensitive receptors such as Integrins and Cadherins leads to the phosphorylation of MST1/2 and MAP4K proteins, these phosphorylate LATS1/2 which leads to the phosphorylation of YAP/TAZ, this targets YAP1 for either degradation and sequestering. Therefore, preventing YAP1 from entering the nucleus and inhibits the binding of TEAD to the DNA inhibiting gene expression. HIPPO OFF: Piezo1 ion channel is activated and leads to an uptake of Calcium ions, this inhibits the phosphorylation of YAP1 allowing it to translocate into the nucleus, promoting the binding of TEAD to the DNA and activating gene expression. Figure reproduced from Minyang Fu et al[509].

Additionally, a family of mechanically-gated Piezo ion channels have also been observed to transduce mechanical forces in developing neurons in the brain [510–512]. The activation of Piezo1 calcium ion channel promotes the nuclear shuttling of the mechanosensitive transcription factor YAP1[513], which deactivates the Hippo-Yap/Taz pathway [514]. YAP1 is known for it's cytoplasmic-nuclear translocation in response to dynamic mechanical stimuli in the environment; this has been linked to the modulation of cellular behaviour including cells in the brain[515]. Specifically, the nuclear localisation of unphosphorylated YAP1 promotes the proliferation of neural stem cells and inhibits neuronal differentiation, whereas the translocation of phosphorylated YAP1 into the cytoplasm targets the transcription factor leads proteasomal degradation [516] and promotes neuronal differentiation[517,518]. Alongside this, YAP/TAZ activation also increases global transcription of proliferative genes in the developing brain [519]. Thus, characterising this mechanosensitive protein at different timepoints of EB-cerebral organoid formation could provide an insight into maturation state of our cerebral organoids.

The YAP1 protein was quantified by measuring the fluorescent intensity of the protein within the nuclei and outside within the cytoplasm at different timepoints (Figure 58). In the early EB stage (Day 0) YAP1 was found to mainly localise in the nuclei of cells, however once the medium was changed to promote neuronal induction the ratio of cytoplasmic to nuclear YAP1 began to increase. There was a significant difference between the mature Day 9 cells and early neuronal induced Day 5 cells, with the translocation of YAP1 from the nucleus to the cytoplasm of cells; this data supported the literature that suggested the translocation of YAP1 into the cytoplasm promoted neuronal differentiation [517,518], hence the increase of cytoplasmic YAP1 at the more mature timepoint.

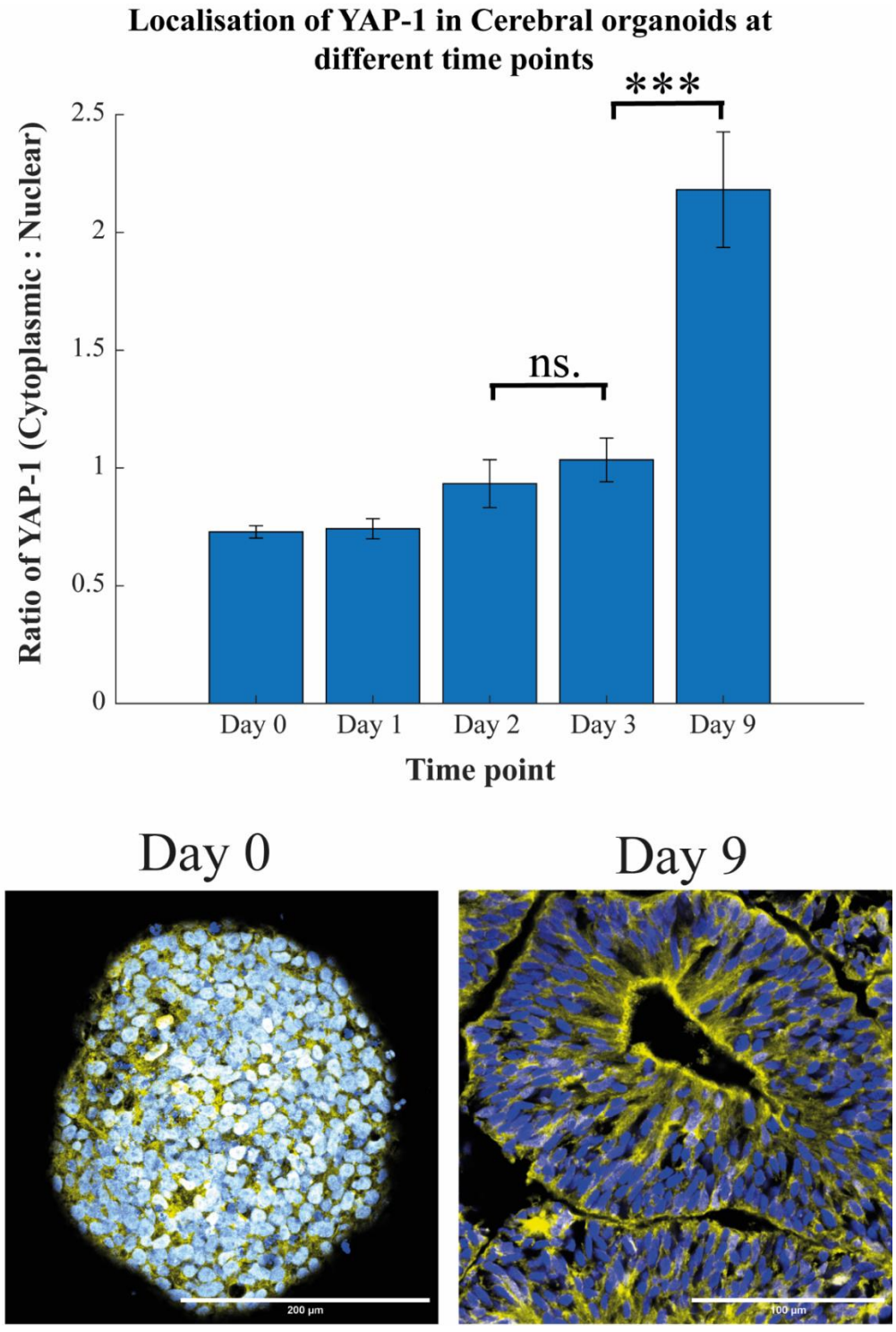

Figure 58: Quantification of the mean ratio of cytoplasmic to nuclear YAP-1 protein in cerebral organoids at days 0, 1, 2, 3 and 9. Representative images for Days 0 (20x magnification) and 9 (63x magnification), stained for YAP-1 protein. Three embryoid bodies/organoids per condition were studied and the standard errors were depicted as error bars of each triplicated data point. Significance was determined by *P < 0.05, **P < 0.01, ***P < 0.001 and n.s. nonsignificant. Blue = DAPI (1:1000). Yellow = YAP1 (1:200).

4.5. Integration of functionalised droplets into Embryoid bodies (Days 0-2)

The next step was to optimise the integration of the droplets into the organoids, many variations were attempted to optimise the uptake of droplets. The original technique used by Campas was to use microinjections to inject droplets into developed embryonic tissues [246,299]. However, this method is relatively invasive and may result in the disruption of both organoids and microdroplets formed, whereas meticulous handling of the EBs would prevent damage. Therefore, we opted to use a simpler approach to mix the cells and droplets together and let them co-aggregate. The first method attempted was to add the droplets into the wells first then pipette the human iPSCs on top, this method didn't work too well and led to a very small amount of Cadherin functionalised droplets being taken up by the forming EBs, this was most likely caused by the cells forming a layer on top of the droplets; thus, the droplets were not incorporated into the 3D cell aggregate. However, once the droplets were pipetted directly on top of the layer of iPSCs, the droplet uptake was significantly improved. An example of this method is shown in Figure 59. Furthermore, timelapse snapshots of the uptake of the droplets using this method is depicted in Figure 60, it was found that in the presence of our functionalised droplets the EBs still managed to form into their characteristic spherical shape after 24 hours. Various types of droplet functionalisation were tested on the surface of the droplets to promote uptake, including E-Cadherin, N-cadherin, a combination of E/N-Cadherin and the Arginylglycylaspartic acid (RGD) peptide (to investigate whether engagement of integrin ligands could promote incorporation). The number of droplets that were

retained by the EB after five days was quantified in Figure 61, with E-Cadherin promoting the highest retention of droplets, followed by the mix of E/N-Cadherin, then N-Cadherin and finally RGD. This correlates very well with the literature as E-Cadherin is known to play an essential role in cell-cell adhesion in EB formation and other metazoan cohesive tissues[189,520,521], whereas N-Cadherin is only upregulated once EBs have been induced into the neuronal lineages and committed to cerebral organoid formation[105,522]. Hence, this could explain why E-Cadherin functionalised droplets were retained more readily than N-Cadherin. Interestingly, the addition of E-Cadherin to the surface of N-Cadherin droplets increased the retention of droplets, however it was not as high as E-Cadherin alone. Moreover, if we delve deeper within the core of the EBs we found that the N-Cadherin droplets were situated more at the surface of the EBs instead of being retained within the core (Figure 62). This is quite different for E-Cadherin and E/N-Cadherin droplets with a significant number of droplets found to be retained within the core of the EB after seven days of culture (Figure 62 and 63). This was promising data as it was required for the droplets to be retained for the duration of EB formation, to allow us to study further their interactions with cerebral organoids. Additionally, droplets functionalised with RGD had the lowest uptake out of the functionalisations shown in Figure 63. However, from the microscopy images in Figures 62 and 63 the RGD droplets were found to be incorporated more within the core of the EB than the N-Cadherin droplets. This is also interesting as it shows that integrins can also be utilised to position the droplets into the core of developing EBs. Nevertheless, regardless of the droplet functionalisation the EBs when compared to the controls developed in a similar fashion and with some slight protrusions caused probably by nonhomogeneous distribution of droplets leading to aggregation in regions of the EBs.

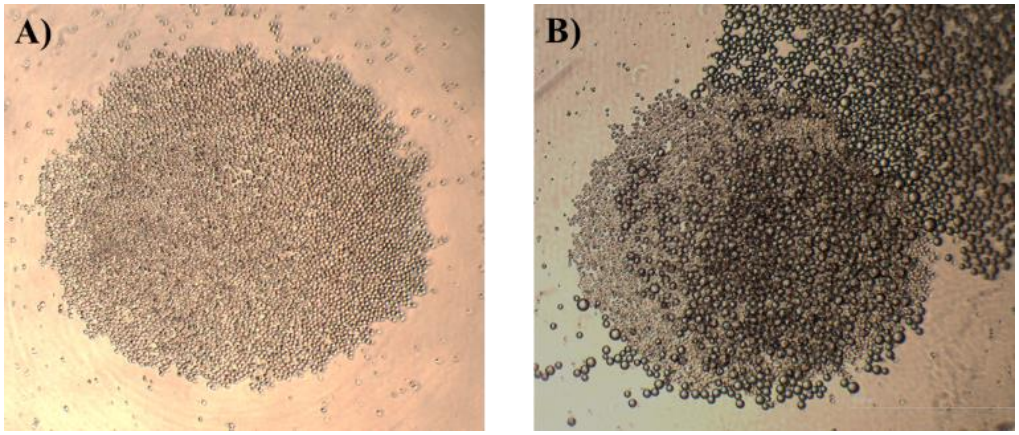

Figure 59: Example of droplet seeding with hIPSCs at day -5. A) Seeding of hIPSCs at a seeding density of 4500 cells/well in a 96 well round bottom ULA plate, day -5 (10x magnification).. B) Seeding of hIPSCs at a seeding density of 4500 cells/well with E/N Cadherin functionalised droplets, in a 96 well round bottom ULA plate, day -5 (10x magnification).

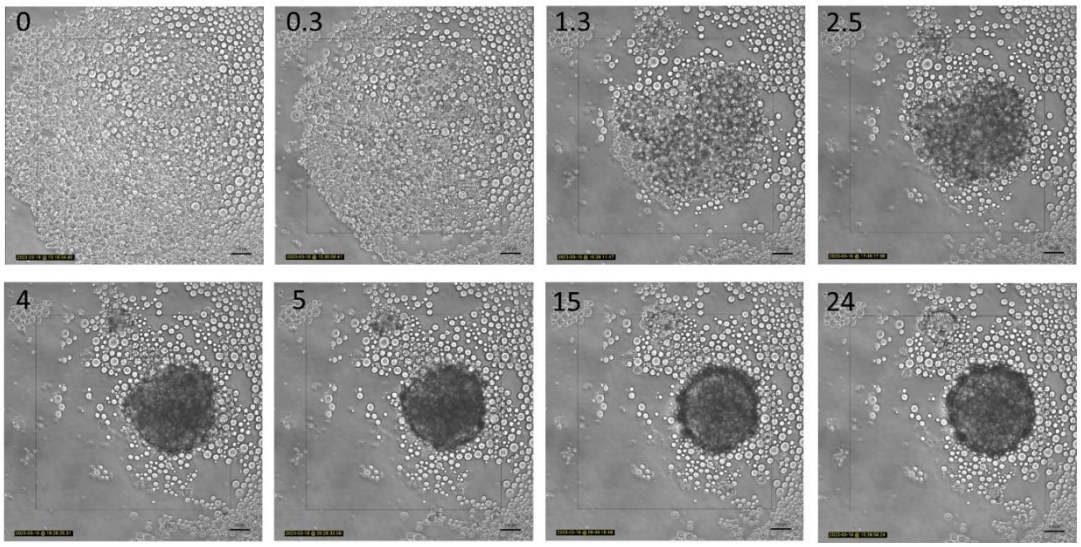

Figure 60: Snapshots of the 24-hour timelapse of EB formation mixed with E/N ACs. The EB forms after 24 hours (10x magnification).

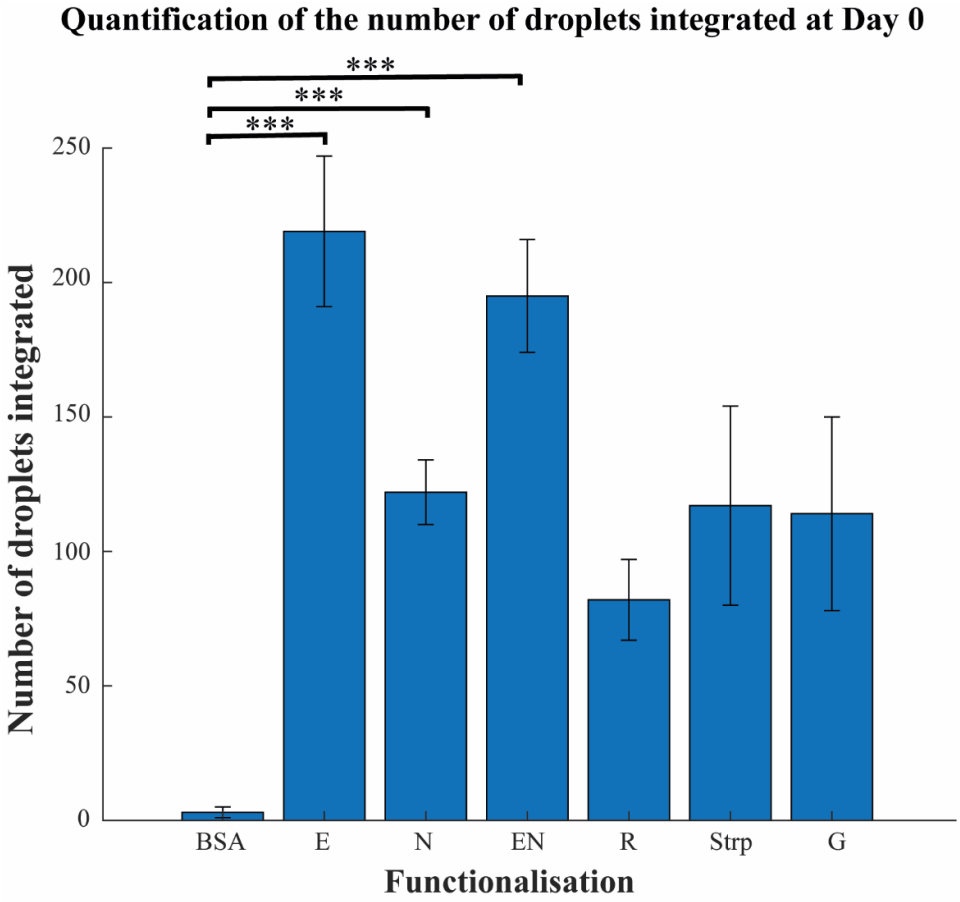

Figure 61: Three embryoid bodies per condition were studied and the mean number of droplets taken up by EBs after 5 days of incubation (day 0) was quantified using ImageJ software. Droplet functionalisation: BSA = commercial BSA. E = E-Cadherin. N = N-Cadherin. EN = E+N-Cadherin. R = RGD. Strp = Streptavidin alone. G = Streptavidin + ProteinG. Standard errors were depicted as error bars of triplicated data points. Significance was determined by *P < 0.05, **P < 0.01, ***P < 0.001 and n.s. nonsignificant.

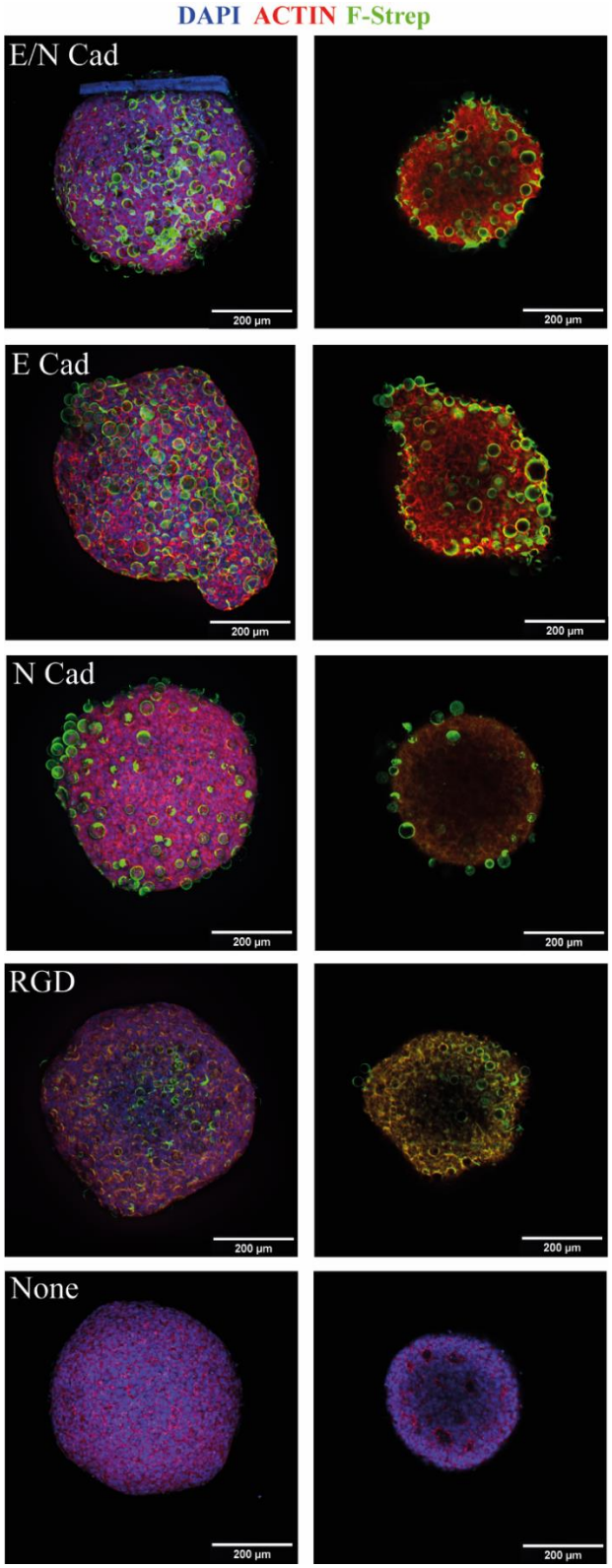

Figure 62: Day 0 Embryoid bodies mixed with droplets with varying functionalisation. Stained using Blue = DAPI (1:1000), Red = Phalloidin (1:500) and Green = pre-conjugated 488-Streptavidin bound to the Bt-BSA protein. Left image = Max Z-projection. Right image = one slice of the Z-stack in the centre of the EB depicting droplet integration within the organoid. All images at 20x Magnification.

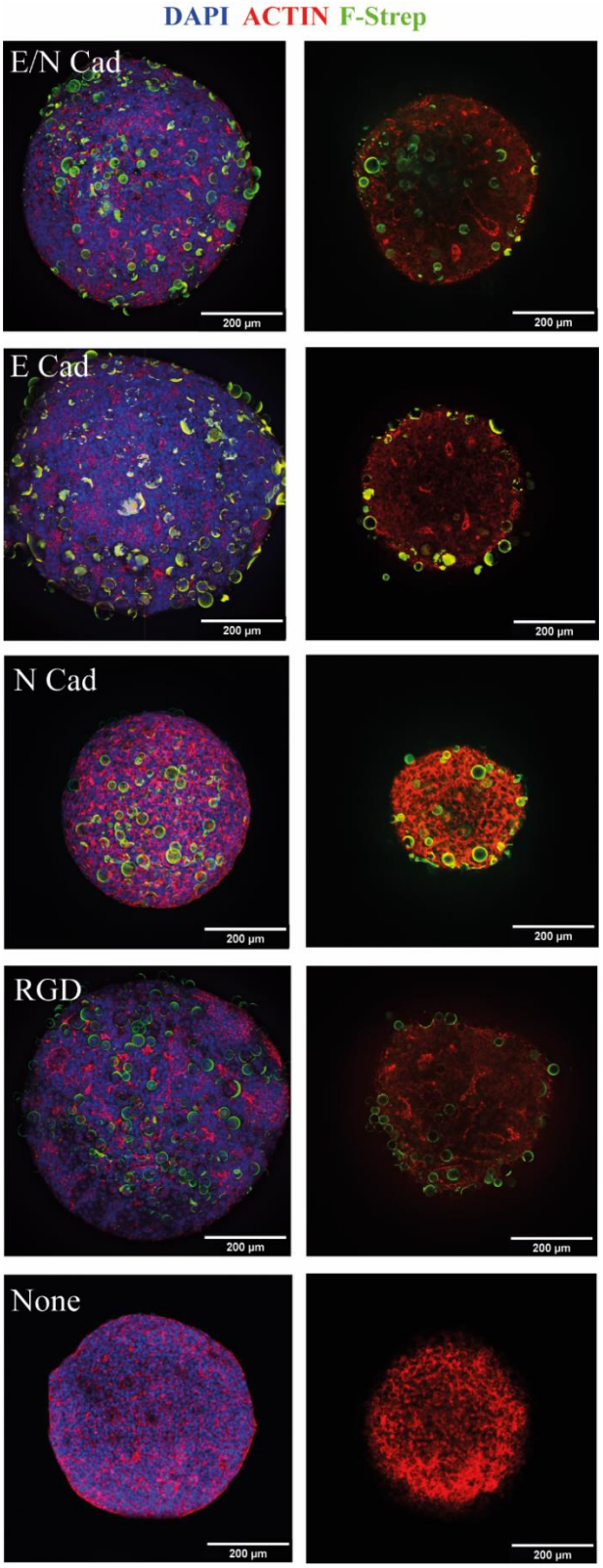

Figure 63: Day 2 Embryoid bodies mixed with droplets with varying functionalisation. Stained using Blue = DAPI (1:1000), Red = Phalloidin (1:500) and Green = pre-conjugated 488-Streptavidin bound to the Bt-BSA protein. Left image = Max Z-projection. Right image = one slice of the Z-stack in the centre of the EB depicting droplet integration within the organoid. All images at 20x Magnification.

The initial seeding density suggested by the Lancaster lab of 9000 cells/well was adjusted to 4500 cells/well (50%) as we also found that halving the cell density promoted a better uptake of droplets. We hypothesised that this could be caused by the decrease in the pressure within the core of the EB. This may have increased the probability of droplet interactions with the central highly adhesive cells, instead of being expelled by the developing pressures. Additionally, the literature has shown that starting with a smaller cell density increased the surface area to volume ratio, generated smaller neuroepithelial buds, and decreased the number of cells with non-neuroectodermal identity (Mesoderm/Endoderm); this increased reproducibility of neuronal induction, thus reducing the variability within batches[171]. Fluorescent microscopy was used with ZO-1 staining to monitor the effect of cell density on the final rosette phenotype, images were taken at day 5 after neuronal differentiation. From Figure 64 it was evident that the starting cell density affected the final size of the EB after five days of culture, decreasing the size as the cell density decreased.

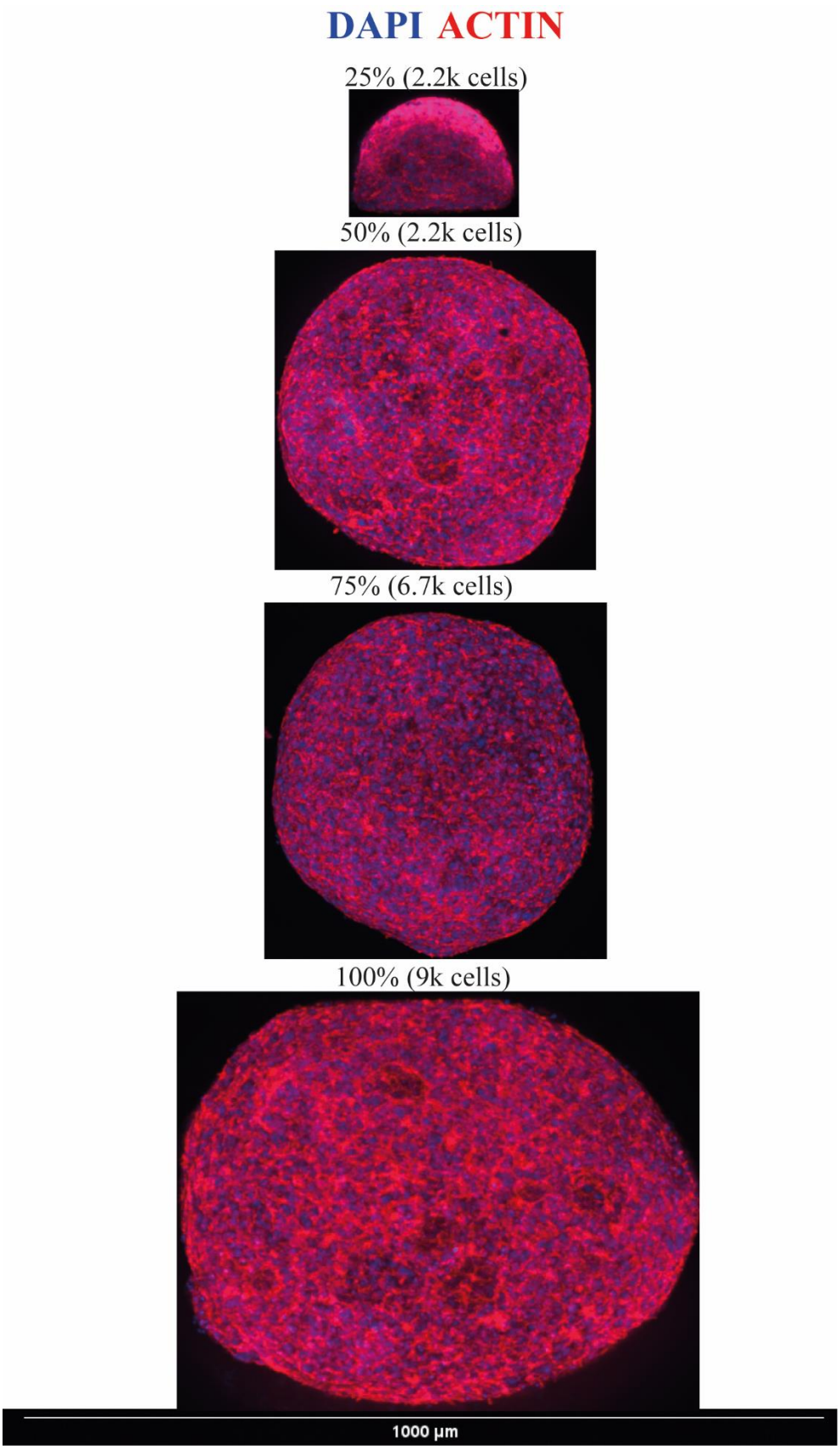

Figure 64: The effect of initial cell seeding density on the size of EBs at day 0. Blue = DAPI (1:1000) and Red = Phalloidin (1:500).

4.6. Impact of bioactive microdroplets onto cerebral organoid development

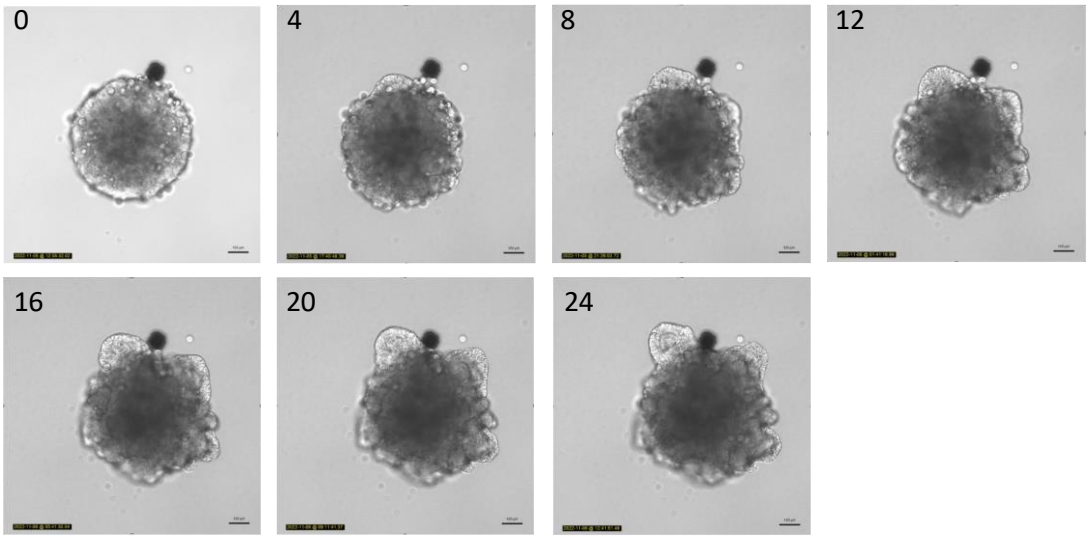

Figure 65: Snapshots of the 24-hour timelapse of early cerebral organoid formation between days 2-3, mixed with E/N functionalised droplets. Early neural epithelial buds begin to expand and form. All images at 10x magnification.

The addition of Cadherin functionalised droplets to the EBs did not hinder neuroepithelial bud expansion as seen in the Figure 65 timelapse snapshots, the neuroepithelial buds-initiated expansion the same as EBs without any droplets (Figure 55) and expanded outwards. However, note the difference in the overall size of the organoids was due to the difference in initial seeding density, as 4500 cells/well was used for experiments with droplets. Unfortunately, most of the droplets maintained their roundness and exhibited very minimal deformations; this was depicted by Figure 66 indicating that all droplet functionalisation did not have a significant impact on the roundness of the droplets in Day 8 organoids. From Figure 67, it was interesting to see that the previously lower retained N-Cadherin droplets underwent a significant change observing much more retention; this is most likely explained by the increase in the N-

Cadherin adherens junctions once neuronal differentiation has been initiated. All the different droplet functionalisations experienced a degree of retention within the core of the organoid. However, the droplets seemed to not localise within the rosette formations rather found around the rosettes depicted by the ZO-1 staining in (Figure 67). A similar trend was also seen in the later time point of day 5 (Figure 68) with droplets localising around rosettes instead of within. However, qualitatively it was observed that less droplets were retained at day 5 compared to day 3, this is most likely explained by the consistent expulsion of the droplets from the core as the developing organoid undergoes a significant outward expansion.

We next quantified the number of rosettes formed and the area they constituted, to examine whether the presence of these droplets within the organoids developed a different phenotype. From Figures 70A-B, the number of rosettes did not vary significantly from the control with no droplets. However, when the area of rosettes was quantified at day 3 (Figure 69A-B), we observed a significant increase in the area of rosettes with the addition of droplets even with the non-functionalised BSA and negative controls; the average areas of the rosettes continued to increase with cerebral organoid development as seen at day 5 in Figure 69B. Hence, the addition of the droplets during neuroepithelial bud formation (irrespective of functionalisation) impacted the rosette's shape and area, leading to a more elongated and larger rosettes. This could be speculated to mean that these rosettes were maturing faster than those formed in the absence of droplets. It was also intriguing to see this phenotype translated to day 9 organoids depicted by the cryosections in Figure 71. The retention of the droplets by day 9 led to interesting phenotypes such as larger rosette lumens in the case of all functionalised droplets. Yet, evidence of a necrotic core usually found within these mature organoids as suggested by Lancaster et al [105] was still produced.

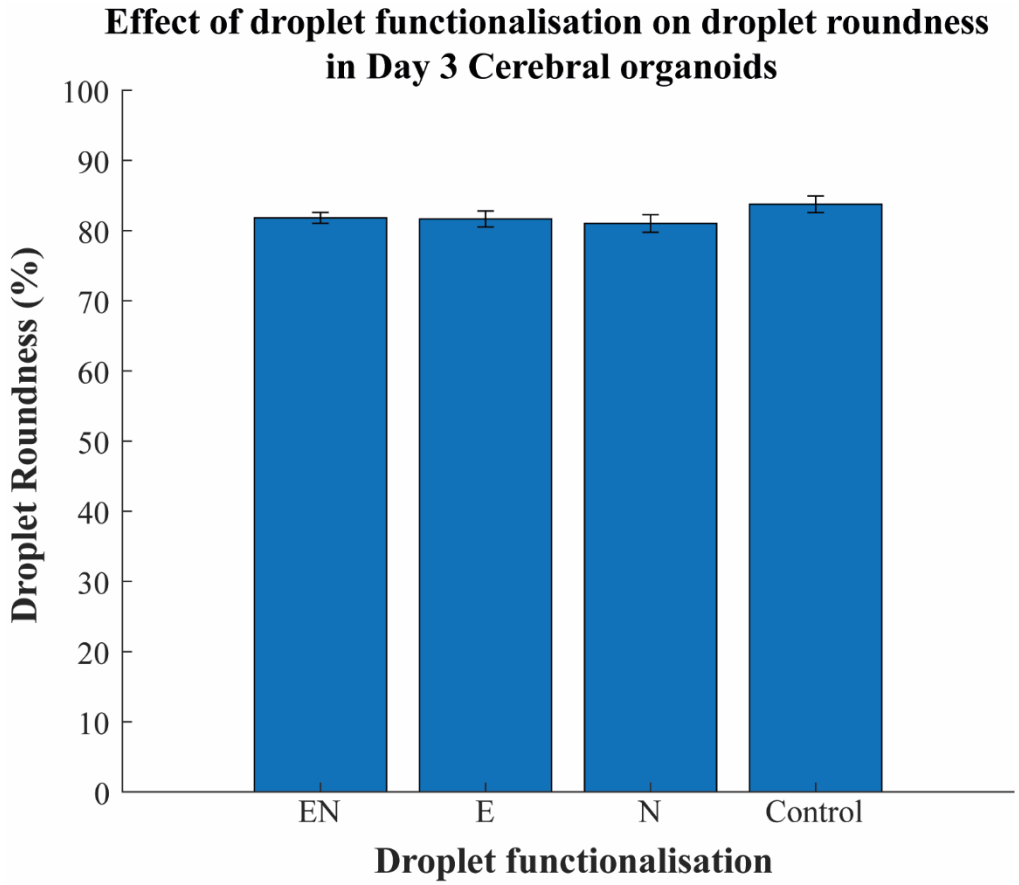

Figure 66: Three organoids were used per condition to study the effect of droplet functionalisation on the mean droplet roundness in Day 8 cerebral organoids. Roundness was calculated using thresholding in ImageJ followed by particle analysis to measure roundness of droplets. Droplet functionalisation: Control = no droplets. E = E-Cadherin. N = N-Cadherin. EN = E+N- Cadherin. The standard error was depicted as error bars per triplicated data point. No statistical significant difference was observed.

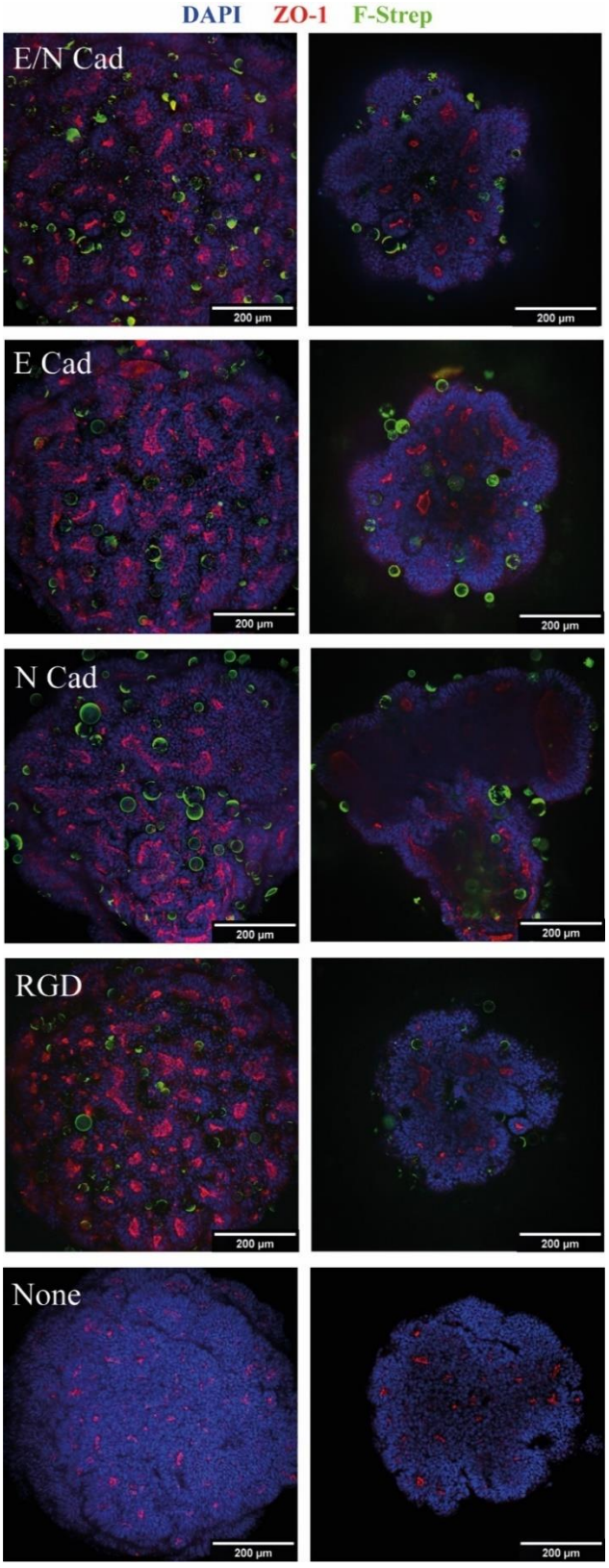

Figure 67: Day 3 cerebral organoids mixed with droplets with varying functionalisation. Stained using Blue = DAPI (1:1000), Red = ZO-1 (1:200) and Green = pre-conjugated 488-Streptavidin bound to the Bt-BSA protein. Left image = Max Z-projection. Right image = one slice of the Z-stack in the centre of the EB depicting droplet integration within the organoid. All images at 20x Magnification.

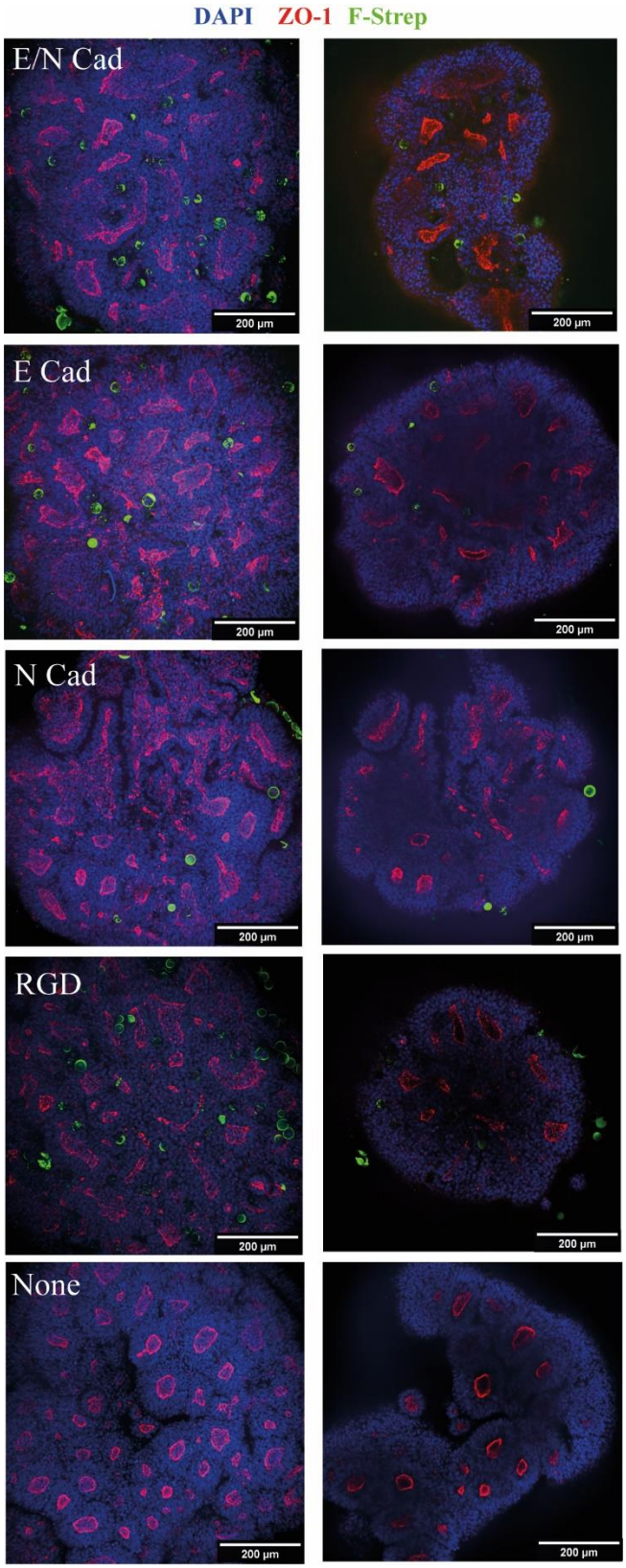

Figure 68: Day 5 cerebral organoids mixed with droplets with varying functionalisation. Stained using DAPI (1:1000), ZO-1 (1:200) and pre-conjugated 488-Streptavidin bound to the Bt-BSA protein. Left image = Max Z-projection. Right image = one slice of the Z-stack in the centre of the EB depicting droplet integration within the organoid. All images at 20x Magnification.

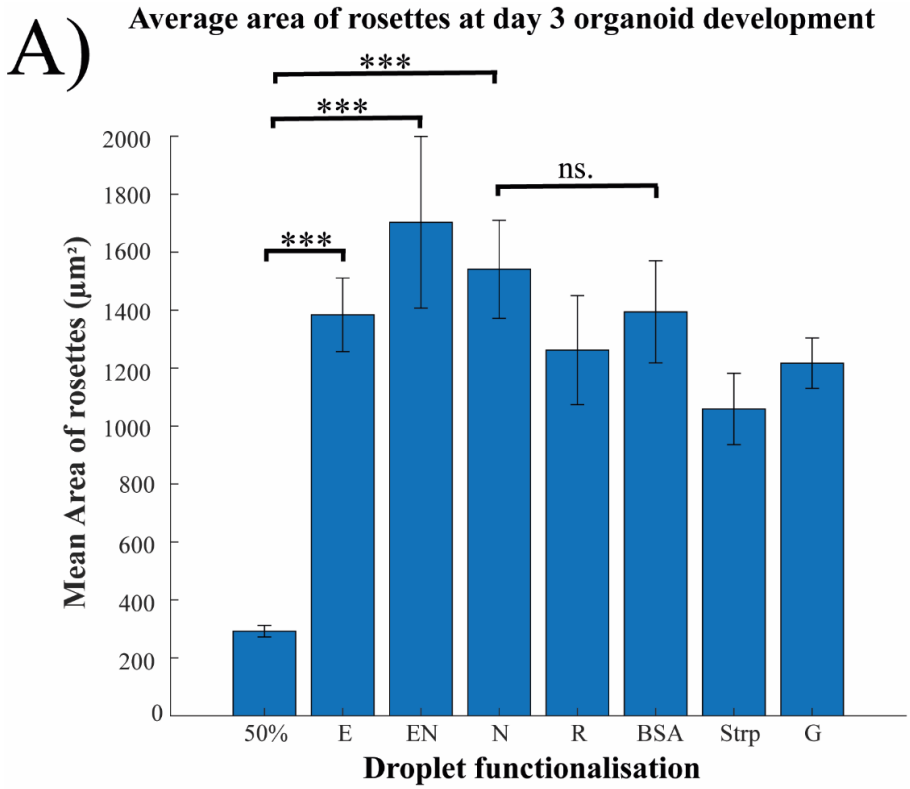

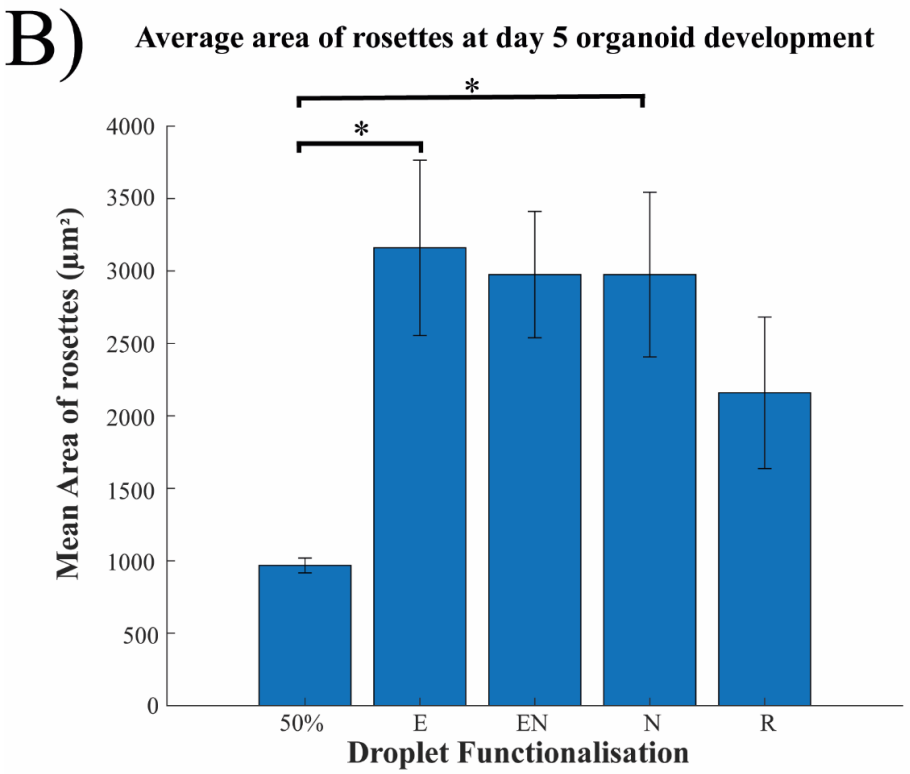

Figure 69: Three organoids per condition were used to quantify the area of rosettes within Cerebral organoids at days 3 and 5 of development. A) Average area of rosettes at day 3. B) Average area of rosettes at day 5. Significance was determined by *P < 0.05, **P < 0.01, ***P < 0.001 and n.s. nonsignificant. 50% = no droplets. BSA = commercial BSA. E = E-Cadherin. N = N-Cadherin. EN = E+N- Cadherin. R = RGD. Strp = Streptavidin alone. G = Streptavidin + ProteinG. The standard error was depicted as error bars per triplicated data point.

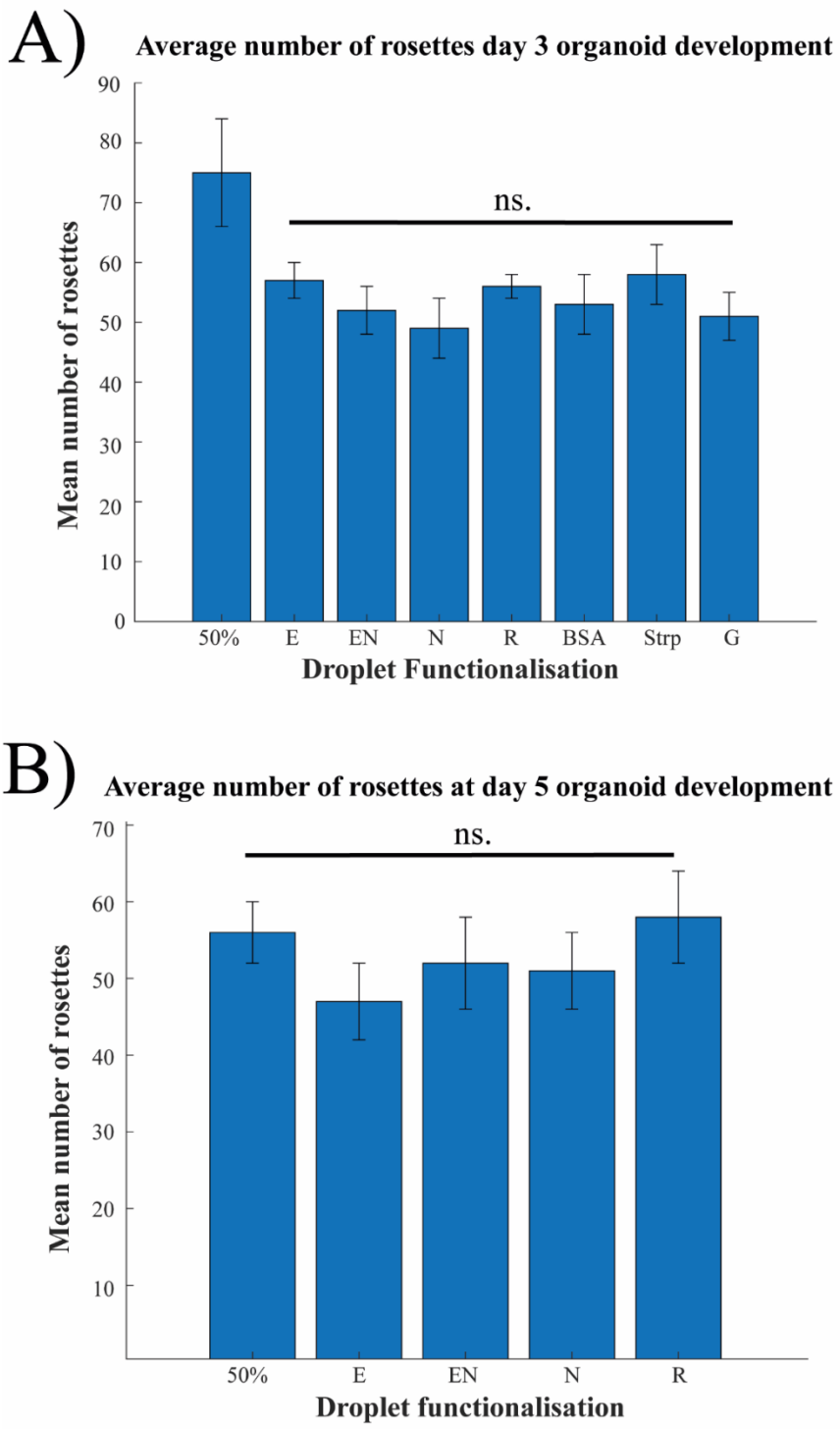

Figure 70: Three organoids per condition were used to quantify the number of rosettes within Cerebral organoids at days 3 and 5 of development. A) Average number of rosettes at day 3. B) Average number of rosettes at day 5. Droplet functionalisation: 50% = no droplets. BSA = commercial BSA. The standard error was depicted as error bars per triplicated data.E = E-Cadherin. N = N-Cadherin. EN = E+N- Cadherin. R = RGD. Strp = Streptavidin alone. G = Streptavidin + ProteinG. Significance was determined by *P < 0.05, **P < 0.01, ***P < 0.001 and n.s. nonsignificant. The standard error was depicted as error bars per triplicated data point. No statistically significant difference was observed.

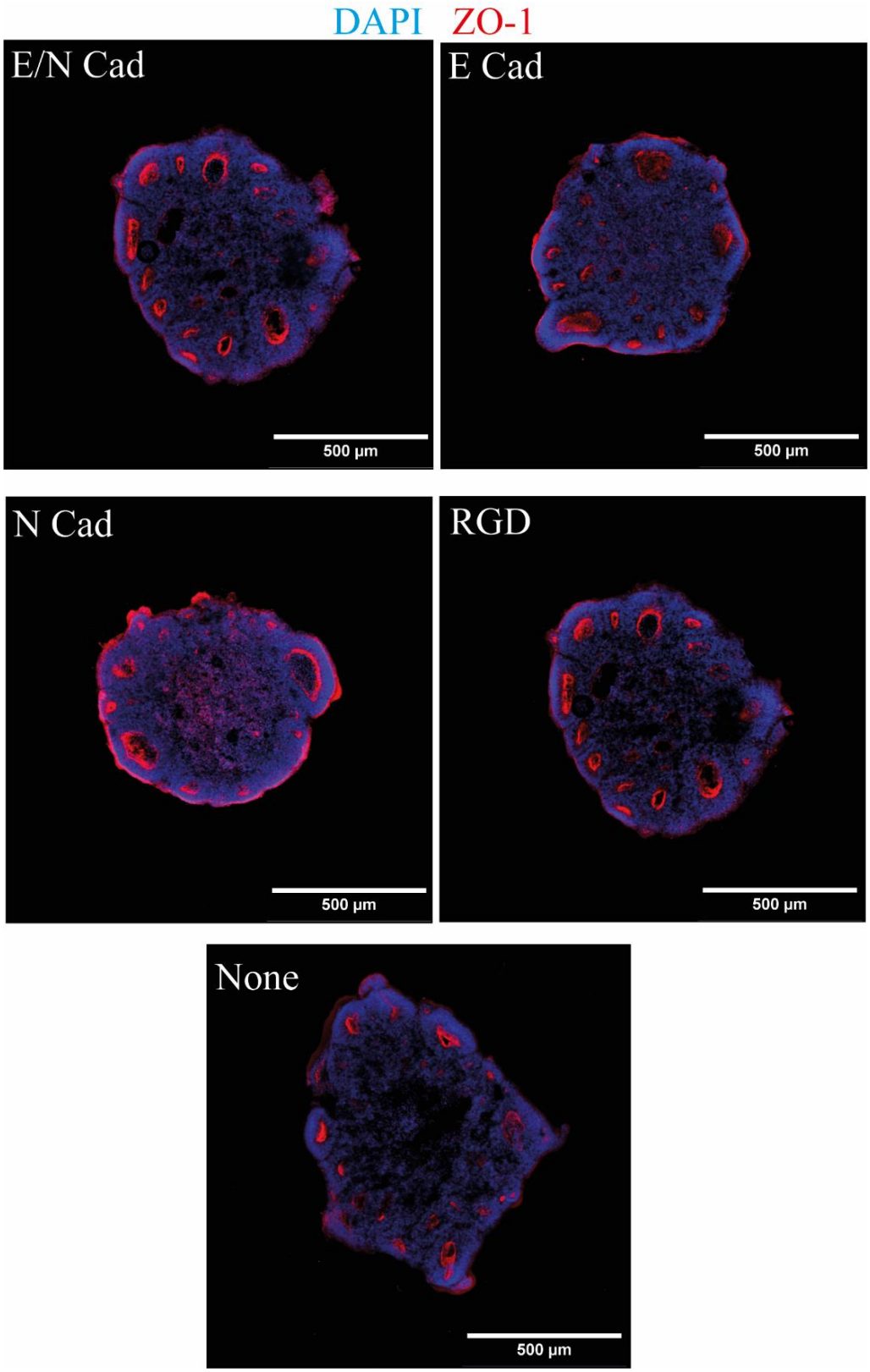

Figure 71: Cryosectioned day 9 mature organoids that were mixed with functionalised droplets (E/N-Cad, E-Cad, N-Cad, RGD and no droplets respectively)**.** Organoids were stained using DAPI (Blue, 1:1000), ZO-1 (Red, 1:200) and the droplets with pre-conjugated 488-Streptavidin bound to the Bt-BSA protein. Max projections of Z-stacks, at a 10x magnification. Droplets are not seen due to the handling process and cryosectioning.

During early neurogenesis, the neuroepithelium found in mammalian brain development expands to generate radial glia (RG)[523], these RGs located at the apical surface divide within the ventricular zone (VZ) to generate intermediate progenitors (IPs)[105]. These IPs then expand to populate the adjacent subventricular zone (SVZ) with more mature neurons migrating towards the basal region of the cortical plate (CP)[105]. This SVZ is further split into two characteristic regions the inner (ISVZ) and outer subventricular zone (OSVZ), and within the OSVZ reside IPs and unique stem cells called outer radial glia cells (oRGs)[105]. These oRGs have long radial fibres that extend to the basal side[524], generate the majority of cortical neurons, lack the apical junctions found in RG cells but retain basal processes[525], hence are a hallmark of neuronal maturation[526,527].

To confirm whether the presence of functionalised droplets was affecting the differentiation process and/or hindering the formation of the neuroectoderm, several markers of cerebral organoid formation were chosen and compared to Day 9 cerebral organoids.

The expression of progenitor marker PAX6 (Figure 73) and neural identity marker SOX2 (Figure 72) indicated a commitment to the neuronal lineages and successful neural induction; this supported the significant upregulation found in the literature[105,110]. Furthermore, the neural maturation marker Neuron-specific class III β-tubulin (Tuj1) (Figure 74) was also found to be expressed and localised around the apical regions of rosettes, this suggested the formation of early oRGs which are a hallmark of cerebral organoid maturation. The apical localisation of Tuj1 in rosettes was also found to follow the localisations found in the literature[105,110].

Additionally, to further confirm the commitment to the cerebral lineages, the FOXG1 marker a hallmark marker of the human forebrain [105,110], was also found to be highly expressed within all the organoids containing all variants of functionalisation (Figure 75). To verify the proliferation of cells within the organoids, the expression of Ki67 (Figure 78) an indicator of cell proliferation and growth was found to be expressed in all variants, interestingly the protein was found mostly around the highly proliferative rosettes, these regions contain high levels of outward growth and expansion, this trend seems to follow the discussions in the literature [105,110].

Cadherin markers were also studied to aid in the investigation of the cellular adhesion between cells and functionalised droplets within cerebral organoids. Cadherins are a group of transmembrane proteins that regulate Calcium (Ca^{2+}) dependent cell adhesion[528–531]. From Figures 76-77, the prevalence of N-Cadherin over E-Cadherin depicted by the higher intensity of N-Cadherin suggested that the organoids present at Day 9 have undergone neuronal progenitor cell differentiation into more mature neurons that fill the SVZ[532]. From a recent study, N-Cadherin was found to accumulate at the apical region of the neural tube[533], this is similar to what we see with the apical localisation of N-Cadherin. The study also suggested that the interaction of N-Cadherin with nectin-2 at the extracellular domain regulated the mechanism of neural tube morphogenesis[531,533]. The difference between the fluorescent intensities of E/N-Cadherins at Day 9 reinforces the claim that once the embryonic ectoderm is induced to neural differentiation the E-Cadherins are replaced by N-Cadherins[531,534]. Literature suggests that E-Cadherin does remain to a certain degree within the overlying ectoderm to maintain architecture, however N-Cadherin becomes the major adherens junction (AJ)[535] similarly, we saw a low fluorescence level for E-Cadherin at the

mature timepoint. These trends were seen for all variations of the droplet functionalisations including the control.

Nevertheless, by compiling all the datasets for these markers we concluded that the integration of these functionalised droplets most likely did not significantly impact the differentiation or lineage commitment towards neuronal ectoderm; which led to healthy development of cerebral organoids that grew in similar nature to organoids without any droplets. We theorised that due to the significant outward expansion of the neural epithelial buds, the droplets were being expulsed out of the organoid without being deformed, this led to us concluding that at the current stage of knowledge of the *in vivo* interactions of these functionalised droplets within cerebral organoids, the droplets cannot be used as droplet-based sensors of mechanics. It is also to be noted that there are some limitations to obtaining definitive conclusions extracted from the immunohistochemistry images as these are only imaged at 10x magnification and the proteins chosen stain relatively small membrane and nuclear proteins. Nevertheless, the accumulation of these proteins into definitive regions can help give a qualitative understanding on the localisations of such markers and a clear commitment of all the different conditions to cerebral organoid lineages.

We can take also take advantage of the success of integration of the E/N Cadherin or RGD based droplets to retain these droplets sufficiently enough to introduce other factors that are involved in regulating neural tube development such as BMP4, Shh, Notch1 and Wnt[536]; leading to the potential use of our droplets as signalling hubs that can introduce ligands to induce signalling pathways within organoids. This would most likely be accomplished by the utilisation of our current functionalisation cascade by the addition of biotinylated or Fc-tagged versions of these proteins. Furthermore, if the *in vivo* mechanics within these organoids was to be continued to be explored

then potential alterations to the interfacial stiffness of our BSA nanosheets can be introduced. For example, introducing different ratios of caseins to form softer droplets which could theoretically increase the likelihood to probe deformations.

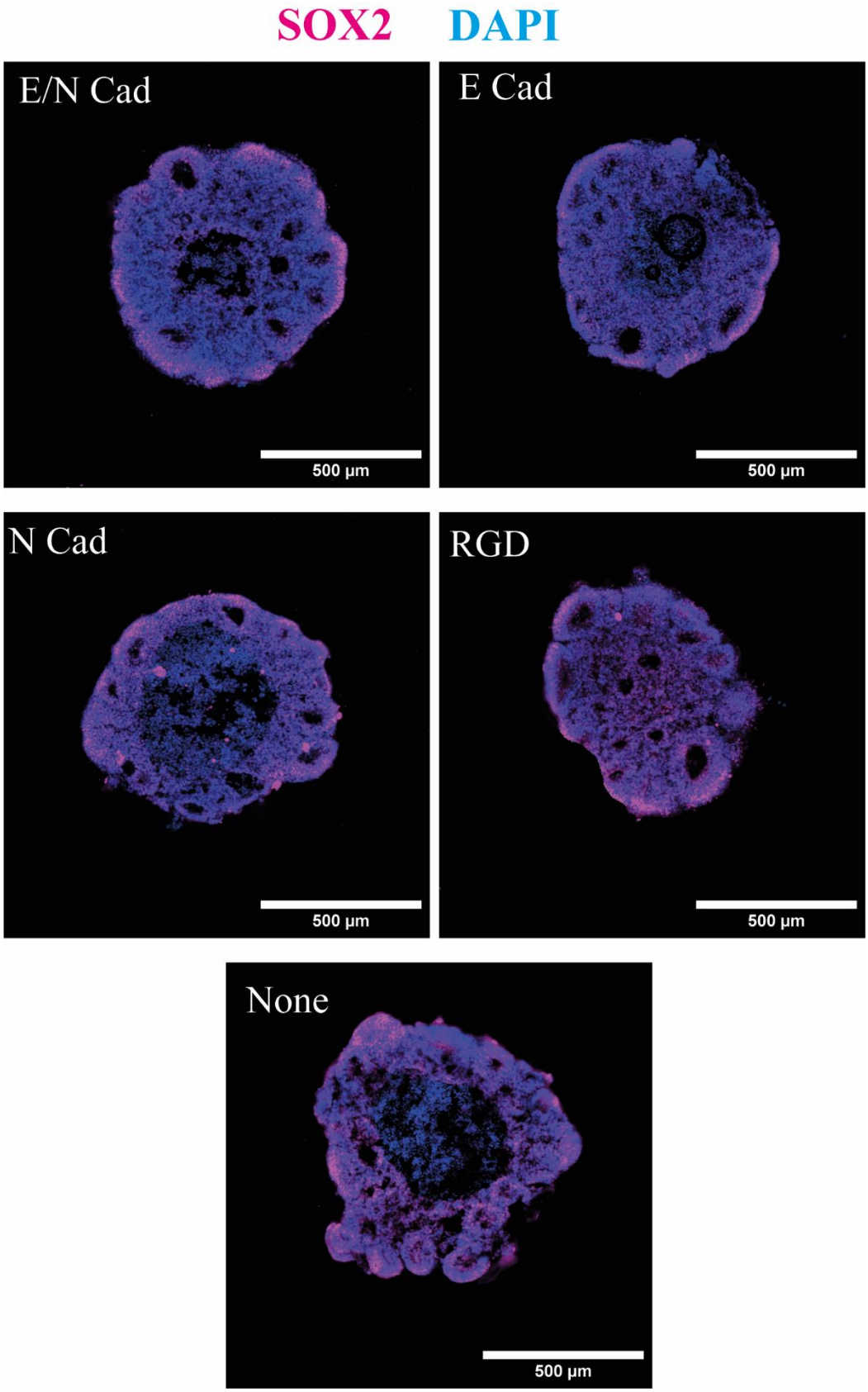

Figure 72: Studying SOX2 (Purple, 1:200) expression in mature day 9 organoids with different types of functionalised droplets (E/N-Cad, E-Cad, N-Cad, RGD and no droplets respectively). All cryosections were imaged at 10x magnification.

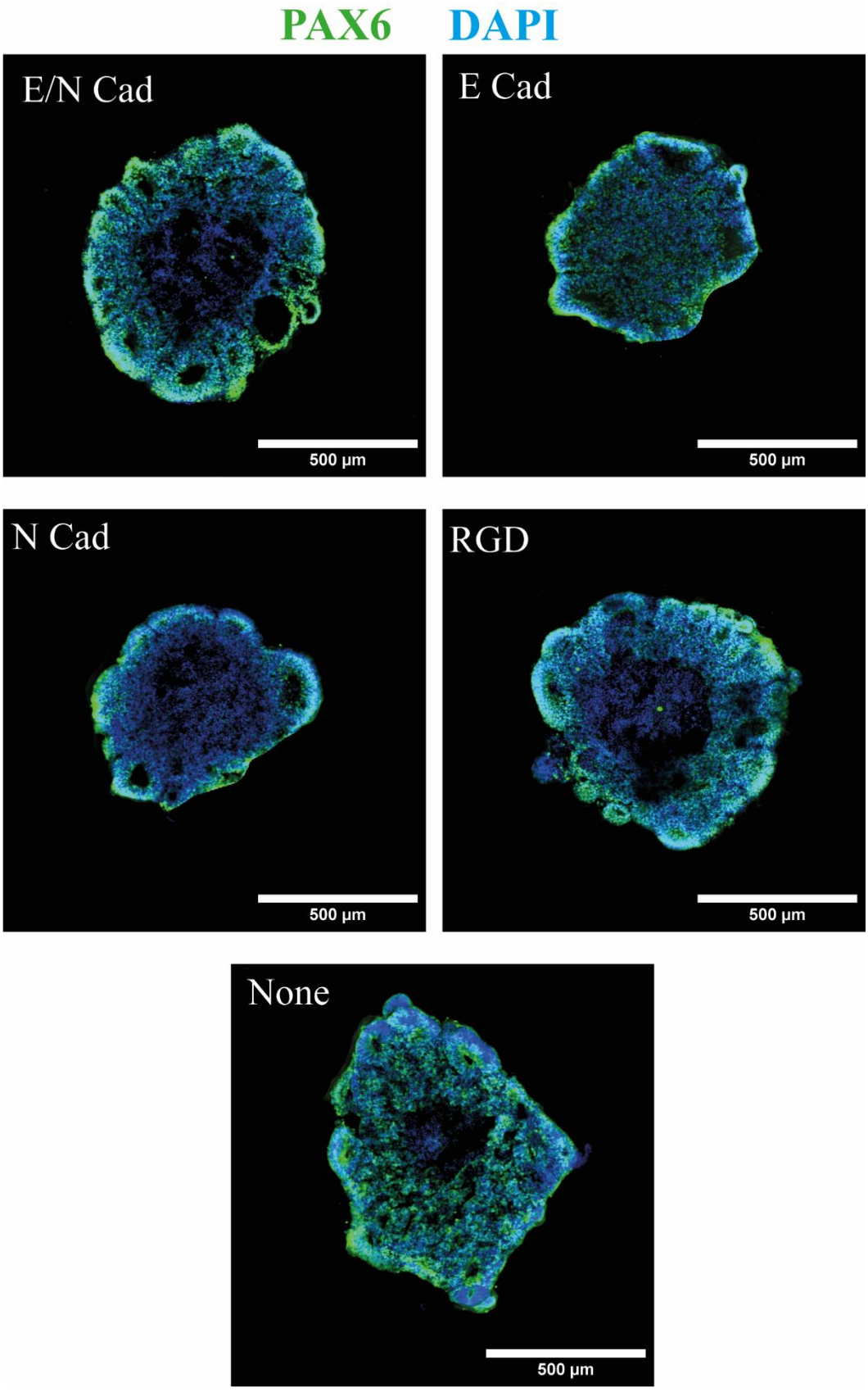

Figure 73: PAX6 (Green, 1:200) expression in mature day 9 organoids with different types of functionalised droplets (E/N-Cad, E-Cad, N-Cad, RGD and no droplets respectively). All cryosections were imaged at 10x magnification.

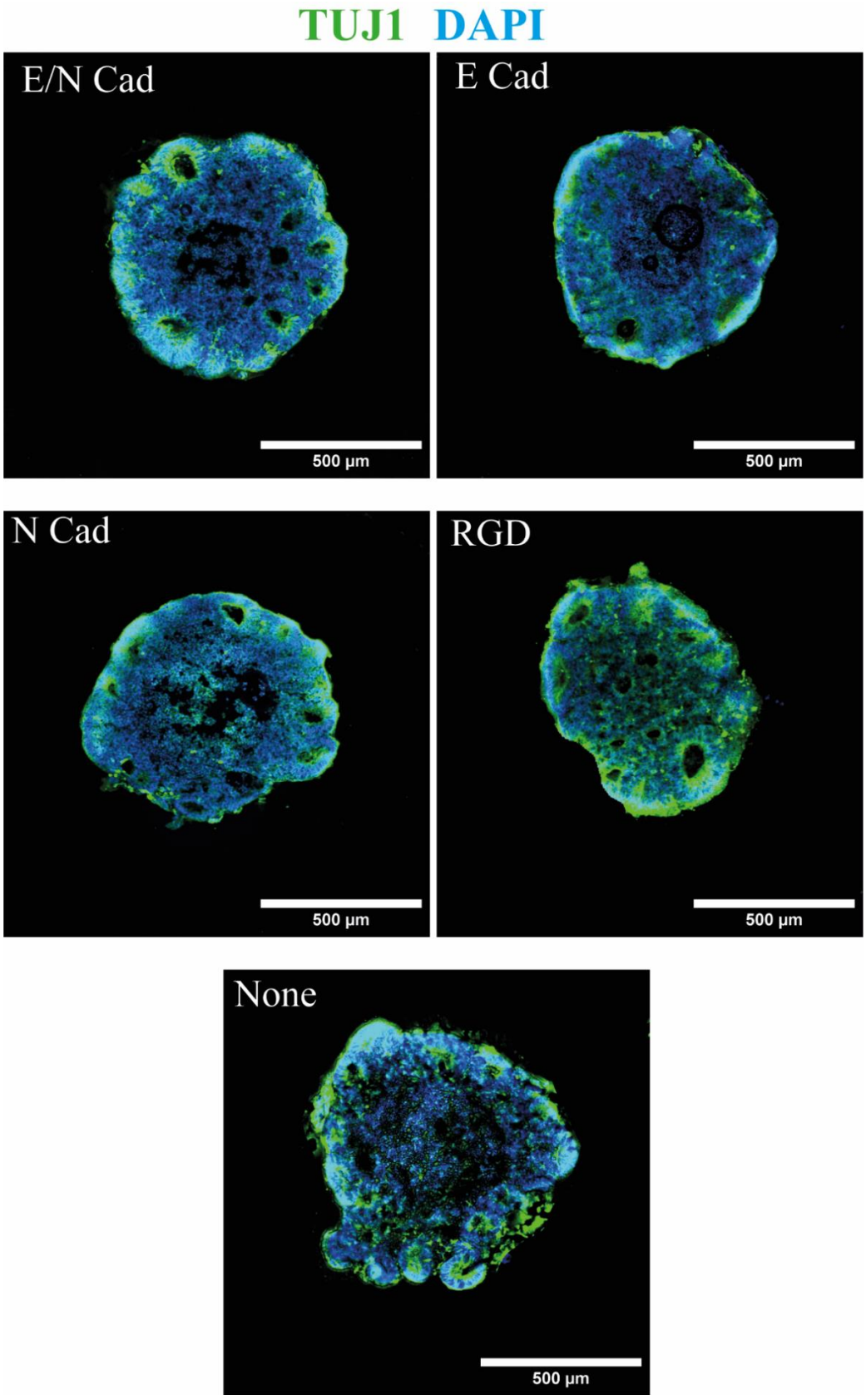

Figure 74: Studying TUJ-1 (Green, 1:200) expression in mature day 9 organoids with different types of functionalised droplets (E/N-Cad, E-Cad, N-Cad, RGD and no droplets respectively). All cryosections were imaged at 10x magnification.

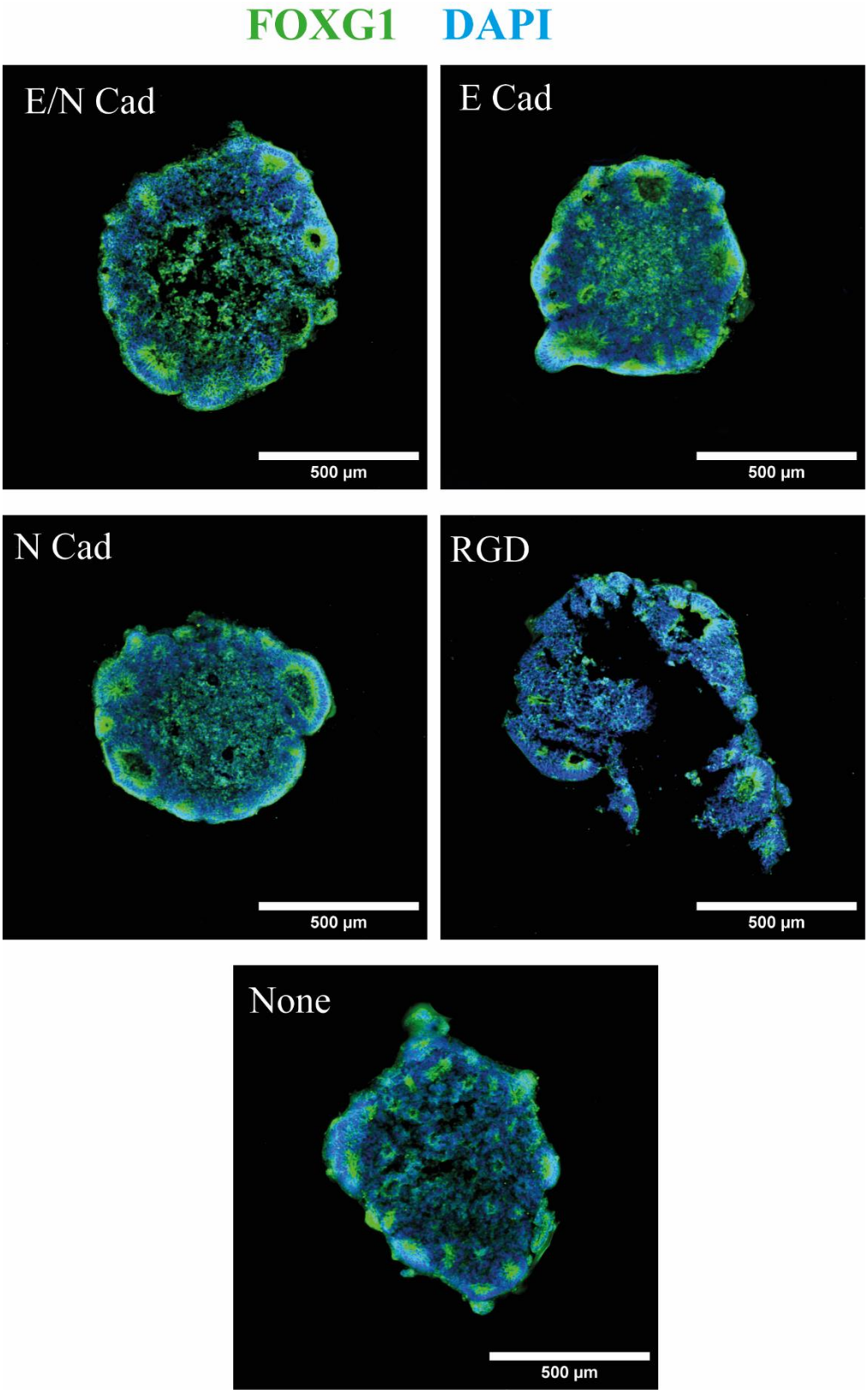

Figure 75: Studying FOXG1 (Green, 1:200) and PAX6 (Green, 1:200) expression in mature day 9 organoids with different types of functionalised droplets (E/N-Cad, E-Cad, N-Cad, RGD and no droplets respectively). All cryosections were imaged at 10x magnification.

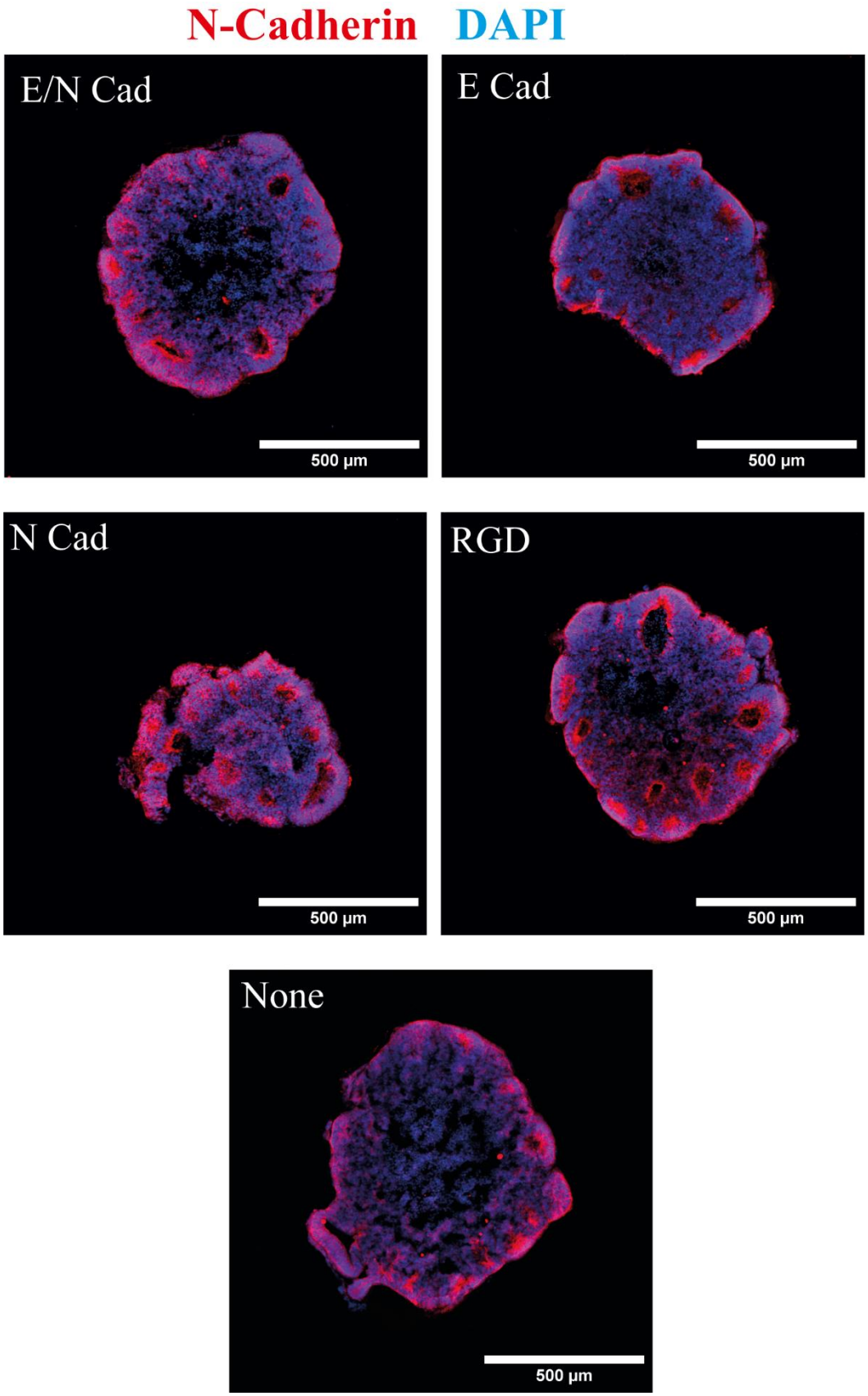

Figure 76: Studying N-Cadherin (Red, 1:200) expression in mature day 9 organoids with different types of functionalised droplets (E/N-Cad, E-Cad, N-Cad, RGD and no droplets respectively). All cryosections were imaged at 10x magnification.

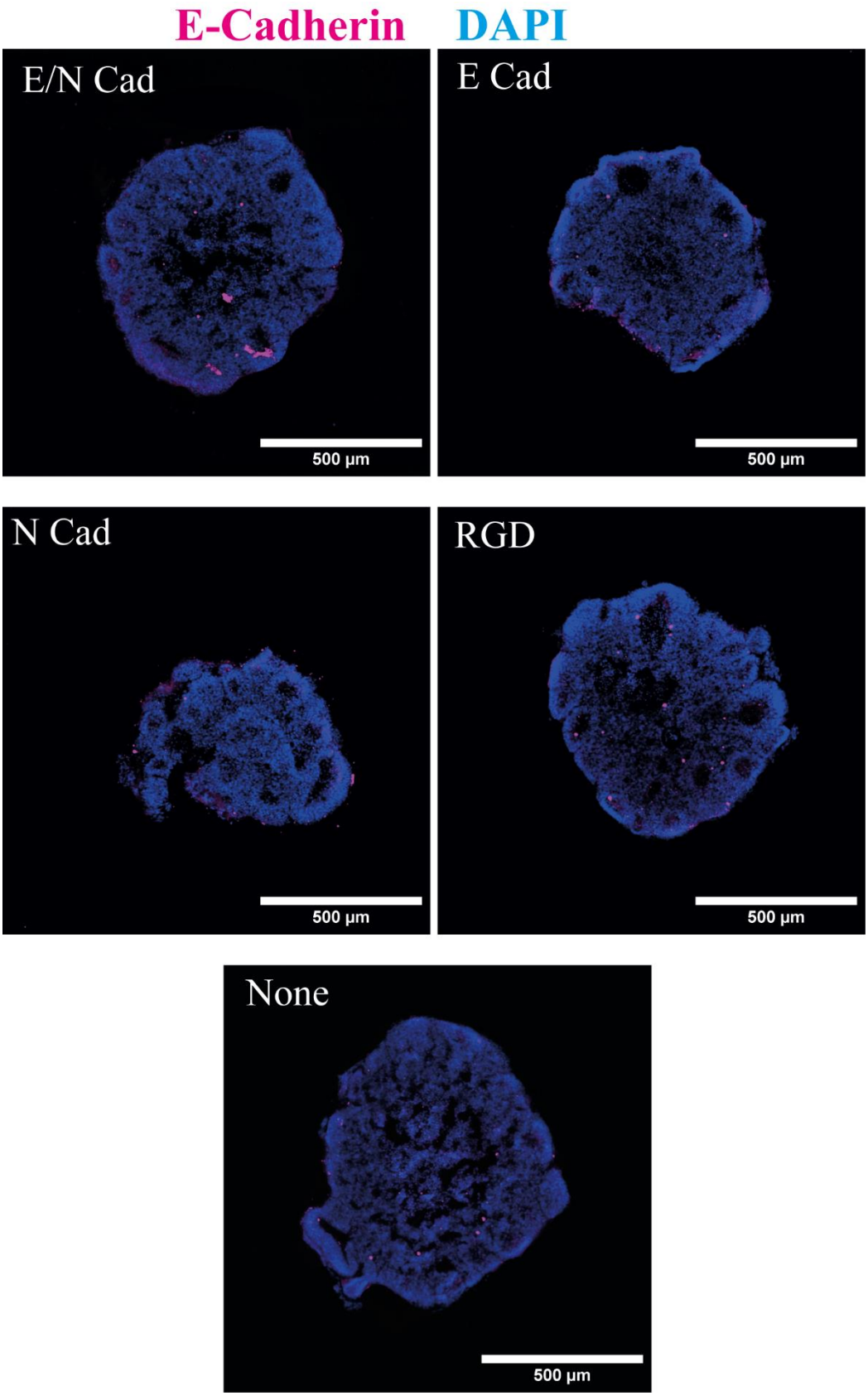

Figure 77: Studying E-Cadherin (Purple, 1:200) expression in mature day 9 organoids with different types of functionalised droplets (E/N-Cad, E-Cad, N-Cad, RGD and no droplets respectively). All cryosections were imaged at 10x magnification.

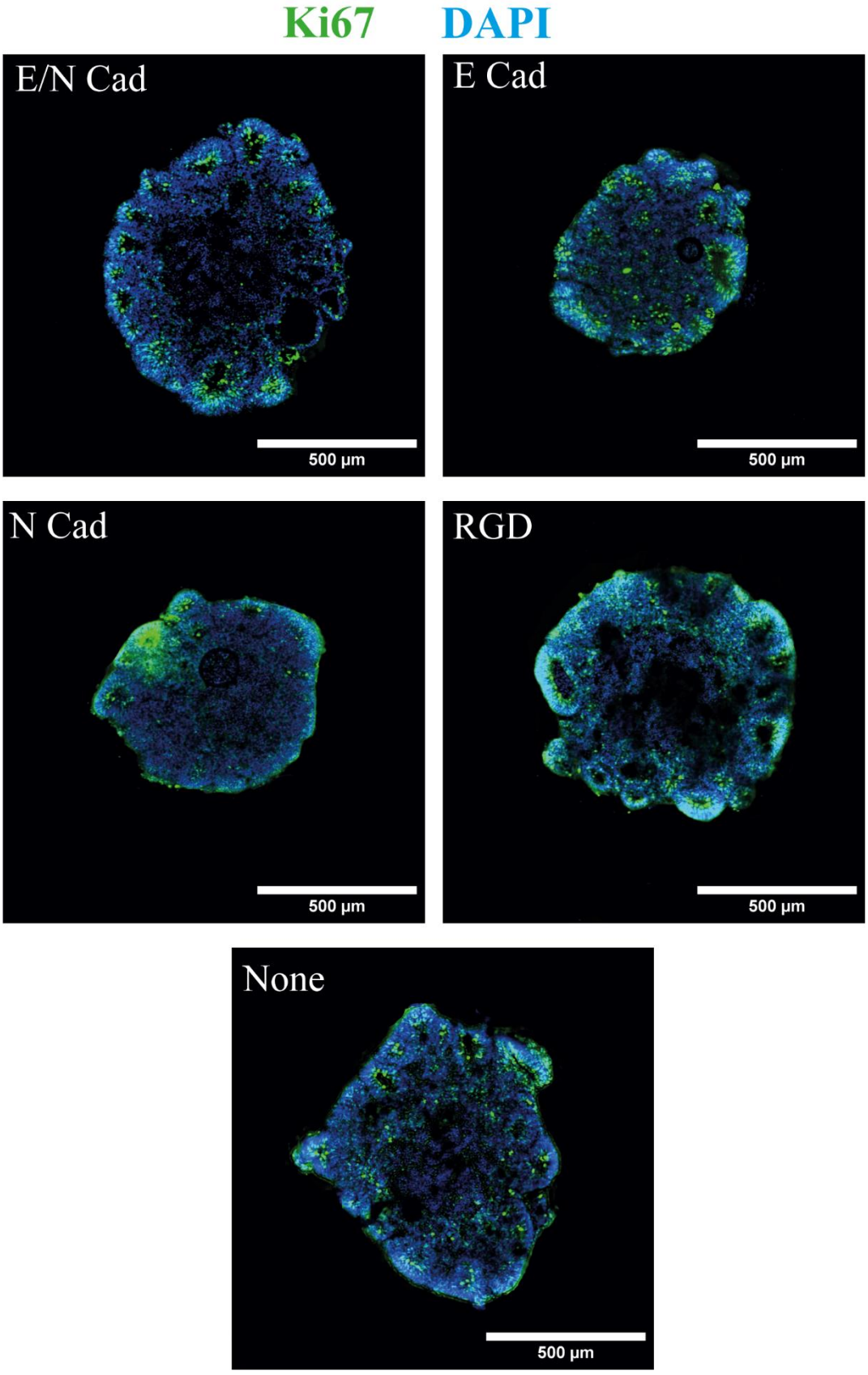

Figure 78: Studying Ki67 (Green, 1:500) expression in mature day 9 organoids with different types of functionalised droplets (E/N-Cad, E-Cad, N-Cad, RGD and no droplets respectively). All cryosections were imaged at 10x magnification.

5. Biophysics of protein nanosheets

In addition to bringing new bioactive elements to nanosheets and microdroplets, the purpose of this chapter was to search for proteins that promoted the direct strengthening of interfacial mechanics of protein nanosheets without the need of a co-surfactant. In this chapter we proposed to explore the assembly of fibrinogen that is known to adsorb to both hydrophobic and hydrophilic surfaces and to study the impact of the addition of thrombin on the liquid-liquid interfacial mechanics.

5.1. Selection of a protein candidate for protein nanosheets

In the literature the cosurfactant PFBC has been used to strengthen BSA, β-lactoglobulin and PLL nanosheets formed at oil-water interfaces and improve their viscoelasticity[353]. Without the treatment of PFBC, the BSA nanosheet was unable to support cell culture, but with the treatment of PFBC the nanosheet was promoted to facilitate the proliferation and spreading of MSCs on the liquid-liquid interface [353]. Unfortunately, PFBC is known to induce cytotoxicity at increased concentrations[537] and due to its fluorinated chemical structure, it will be difficult to translate to industry and downstream clinical applications. Therefore, the goal of this chapter was to find an alternative protein nanosheet that could enhance interfacial mechanics similar to those seen with PFBC treated BSA nanosheets but without the need of a cytotoxic surfactant. At the beginning of the project, a search was conducted to find physiological proteins that change their behaviours once treated with a chemical.

The protein fibrinogen was considered attractive for this project due to its physiological occurrence in humans and the capability to be chemically tuned with thrombin to form fibrin fibres[538]. Fibrinogen is also known to adsorb readily to a range of hydrophobic surfaces (an important issue to prevent unwanted clotting in medical grade surfaces) and can promote the adsorption of ECM proteins underpinning cell adhesion, such as fibronectin[539–541]. With the newly selected protein system, the next step was to explore which concentrations of thrombin to test. A study by Rowe et al explored the influence of thrombin concentration of the mechanical and morphological properties of fibrin hydrogels [542]. They found that increasing the concentration of thrombin decreased the gelation time leading to thinner fibres and a decrease in porosity. In contrast, at lower concentrations this led to much slower gelation times and thicker fibres with larger pores[542]. These thicker fibres exhibited much stronger mechanical properties allowing a higher tolerance to mechanical forces and reaching higher maximum forces at failures. The study utilised 0.001, 0.01, 0.1- and 1-unit thrombin (UT), hence for the study we adopted a middle ground of 0.25, 0.5 and 1.0 UT.

5.2. Interfacial rheology of Fibrinogen nanosheets at the Oil/Water interface

The next step was to investigate the effect of thrombin on the interfacial mechanics of fibrinogen nanosheets at the oil/water interface. Fibrinogen and thrombin were both sourced from Sigma Aldrich and were used alongside Novec-7500 oil to generate the interfaces. Interfacial shear rheology was used to investigate these properties, specifically time sweeps, frequency sweeps, stress relaxations and amplitude sweeps. At the time of writing this thesis, there is currently no data on interfacial shear rheological measurements of fibrinogen treated with thrombin at the oil/water interface, however studies have been conducted using interfacial dilation rheology at the gas-liquid interface[543,544] and adsorption of fibrinogen to oil droplets and solid substrates[539–541], hence the data presented is novel and could only be compared to other protein assemblies previously characterised with interfacial shear rheology at the oil/water interface, such as those formed of BSA. From the time sweep data in Figure 79A the interfacial shear storage moduli of pristine oil/PBS interfaces remained low (10^{-5}-10^{-3} N/m), as expected, and upon the injection of 1 mg/mL fibrinogen into the aqueous phase, self-assembly resulted in the formation of a fibrinogen nanosheet exhibiting an increase of 2 orders of magnitude to roughly 10^{-2} N/m. This trend is comparable to the data observed for BSA without PFBC treatment, also exhibiting a storage modulus of 10^{-2} N/m[353].

Our interfacial rheology set up allowed us to exchange the aqueous phases without disrupting corresponding interfaces, by flowing clean buffer prior to injection of a second protein (in the present case, thrombin). With the addition of 0.5 – 1.0 U/mL T

the interfacial shear storage moduli experienced a slight increase indicating a stiffening of the interfaces. On the other hand, the addition of a lower concentration of 0.25 U/mL T exhibited a slight softening of the interface, but this did not exceed statistical significance range of the storage modulus of untreated fibrinogen nanosheets (Figure 79B).

We next turned our attention to the toughness of resulting interfaces, as our laboratory previously reported that, in addition to interfacial viscoelasticity, interfacial toughness was sensed by adherent cells such as MSCs and that this enabled the maintenance of cultures over prolonged periods of time[454]. When the toughness was calculated through amplitude sweeps the lowest concentration of thrombin 0.25 U/mL T led to the highest increase of toughness (J/m^2) of one order of magnitude (Figure 80). However, the other higher concentrations exhibited an insignificant increase in toughness compared to fibrinogen at roughly 10^{-3} J/m^2. However, the amplitude sweeps were not sufficient to obtain an accurate measurement of the toughness as the measurements were still within the linear viscoelastic regions and did not reach full fracture of the nanosheets. Therefore, a different method was utilised to replace the oscillatory strain approach. A constant strain growth was used to measure the true toughness of the nanosheets as this would enable us to achieve strains at which fracture of the nanosheet could occur, the stress growth experiment was demonstrated in Figure 82A. It was intriguing to delve deeper into stress/strain curves (Figure 82A), at 10^0 DL/L strain the nanosheets began to experience their first small fractures, but this did not result in failure as a constant increase in strain was applied; this suggested a possible rearrangement of the proteins at the interface to accommodate for the higher strains and stresses applied. Yet, all conditions experienced complete fracture at just over 10^1 DL/L strain. Interestingly, when the new toughness values were obtained, the

0.5-1.0 U/mL T conditions also exhibited a significant increase in toughness (Figure 82B) compared to the previously obtained toughness from the amplitude sweeps (Figure 80). The 0.25 U/mL T condition displayed the highest increase in toughness. However, interestingly the 0.5 U/mL T treated nanosheet also reached a similar level of toughness as the 0.25 U/mL T condition. Nevertheless, this was very exciting data as the thrombin concentration had a significant impact on the toughness of fibrinogen nanosheets at the oil/water interface; when compared to other systems in the literature [545] the 0.25 U/mL T condition was exhibiting toughness values on par with one of the toughest materials, MA Silk and almost four times as tough as Kevlar-49, this was astonishing. This strengthening would potentially facilitate the stability of nanosheets and associated proliferation of adherent cells such as MSCs exerting significant forces on these interfaces. Finally, the elasticity of the system was calculated by exponentially fitting the stress relaxation data. The stress relaxation curves (Figure 83A) and the frequency sweeps (Figure 81) indicated that the interfacial storage moduli in all conditions displayed some frequency dependency and affiliated with a viscoelastic response. Additionally, from Figure 83B it was interesting to observe that the untreated fibrinogen nanosheet exhibited an elasticity of roughly 60%, even in the absence of co-surfactants, and with the treatment of 0.25 U/mL T this only reduced this by 10%. However, strangely the increase of thrombin to 0.5 U/mL T only decreased the elasticity by 5%, but further increasing to 1.0 U/mL T led to a significant decrease in elasticity to 33%. Thus, from all the interfacial data the 0.25 U/mL T condition seemed to be the most optimal thrombin concentration out of the studied conditions due to the very significant increase in toughness and insignificant decrease in retention of the elasticity compared to the untreated nanosheet.

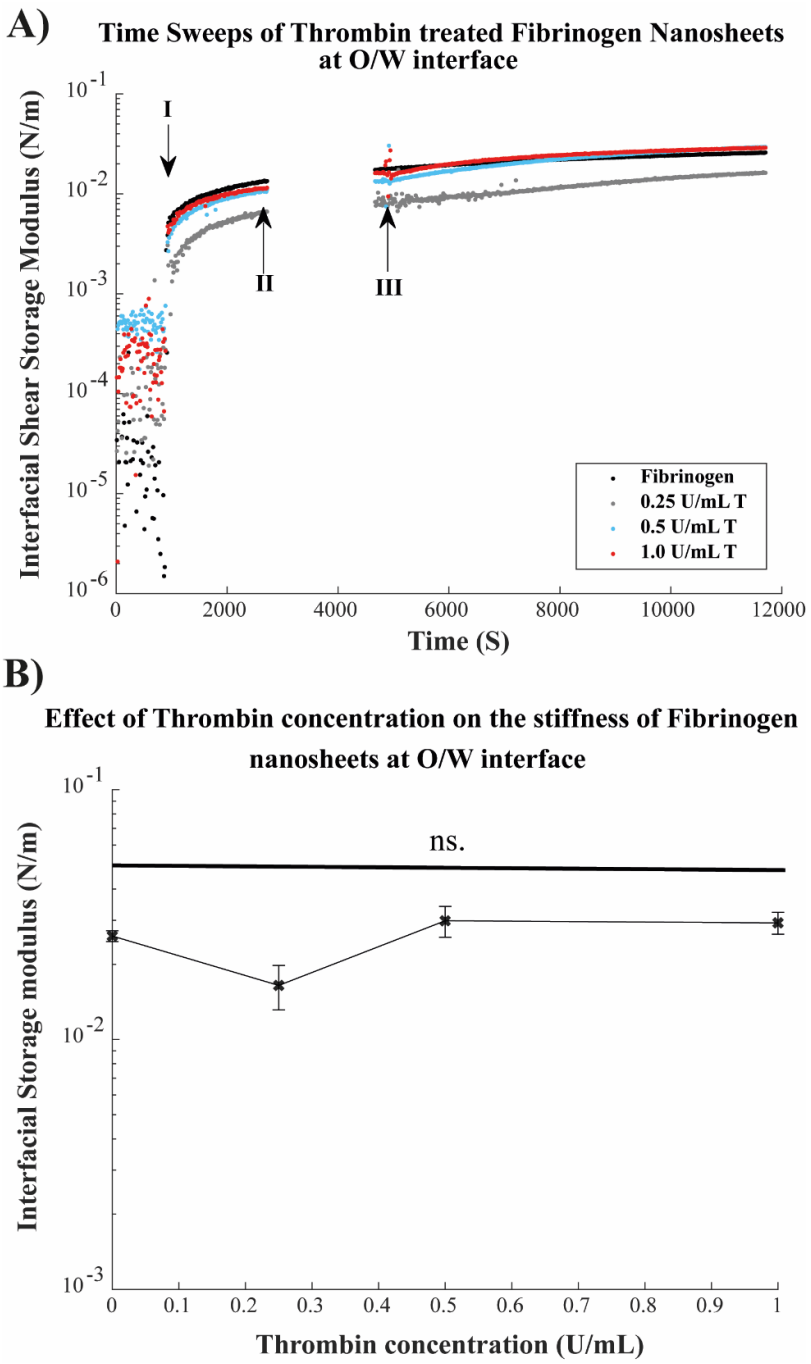

Figure 79: Characterising the interfacial shear storage moduli and stiffness of Fibrinogen treated with varying concentrations of thrombin at the Oil/water interface, three repeats were conducted per thrombin concentration. A) Evolution of the interfacial storage moduli upon formation of fibrinogen nanosheets, followed by washing of the aqueous phase to remove excess fibrinogen and further crosslinking via thrombin treatment (concentrations indicated). I) Injection of 1mg/mL Fibrinogen (final concentration). II) Washing of the aqueous phase with Elve-flow system. III) Injection of various concentrations of thrombin. B) The mean final storage moduli of fibrinogen nanosheets post thrombin treatment. Significance was determined by *P < 0.05, **P < 0.01, ***P < 0.001 and n.s. nonsignificant. The standard error was depicted as error bars per triplicated data point.

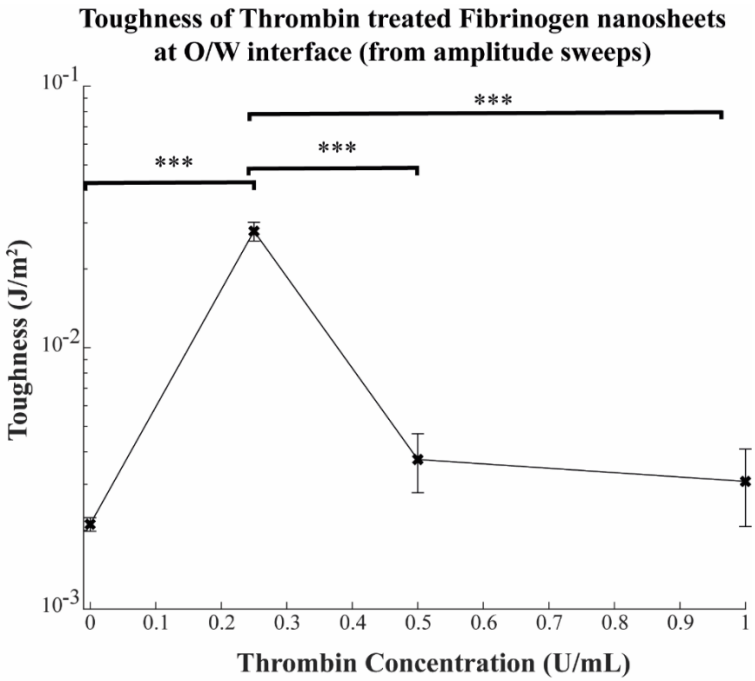

Figure 80: Characterising the mean toughness of Thrombin treated Fibrinogen nanosheets at the oil/water interface through amplitude sweeps, three repeats were conducted per thrombin concentration. Old method - Toughness was obtained through the integration of amplitude sweeps. Significance was determined by *P < 0.05, **P < 0.01, ***P < 0.001 and n.s. nonsignificant. The standard error was depicted as error bars per triplicated data point.

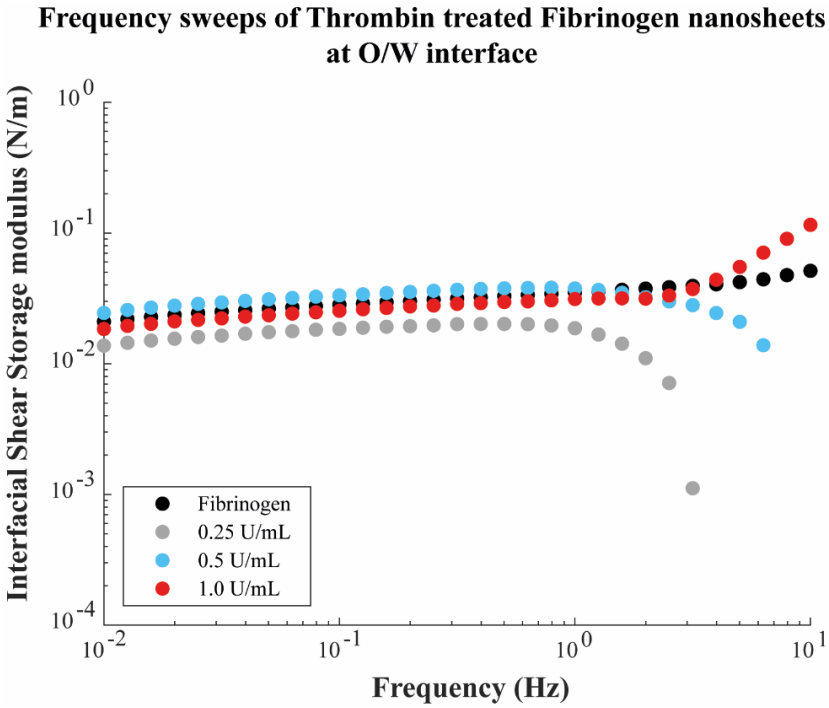

Figure 81: Frequency sweeps of Fibrinogen nanosheets post thrombin treatment at the Oil/water interface. Each thrombin concentration was repeated three times and the average frequency was plotted.

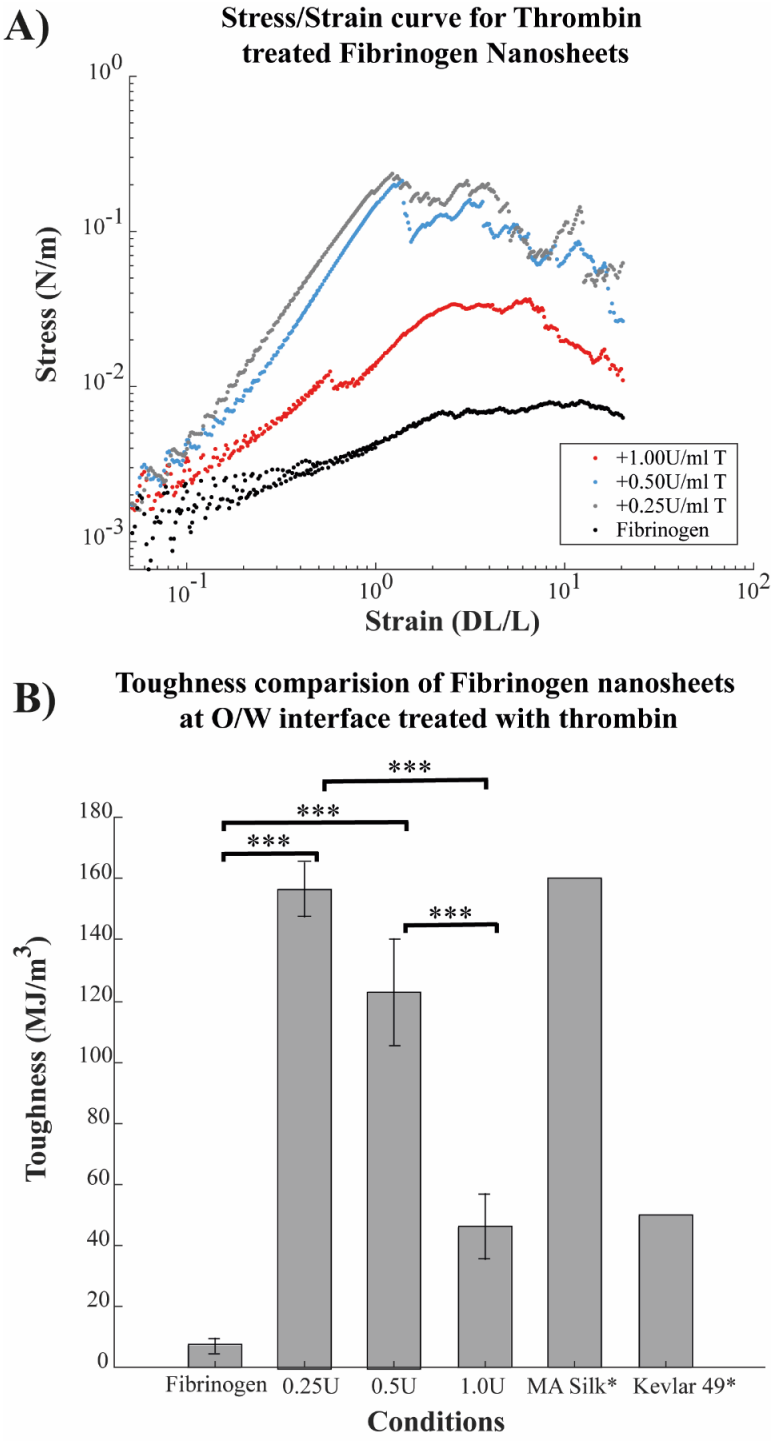

Figure 82: A) Stress/strain curves used to obtain the true toughness of fibrinogen nanosheets treated with varying concentrations of thrombin. B) True toughness of fibrinogen nanosheets post thrombin treatment. *Values obtained from the literature[545]. New method – Toughness (MJ/m^3) was obtained through the integration of the region found in the stress/strain curves (B) followed by correction for nanosheet thickness (10nm) and converted into Mega Joules. Significance was determined by *P < 0.05, **P < 0.01, ***P < 0.001 and n.s. nonsignificant. Each thrombin concentration was repeated three times and the average stress/toughness was plotted. The standard error was depicted as error bars per triplicated data point.

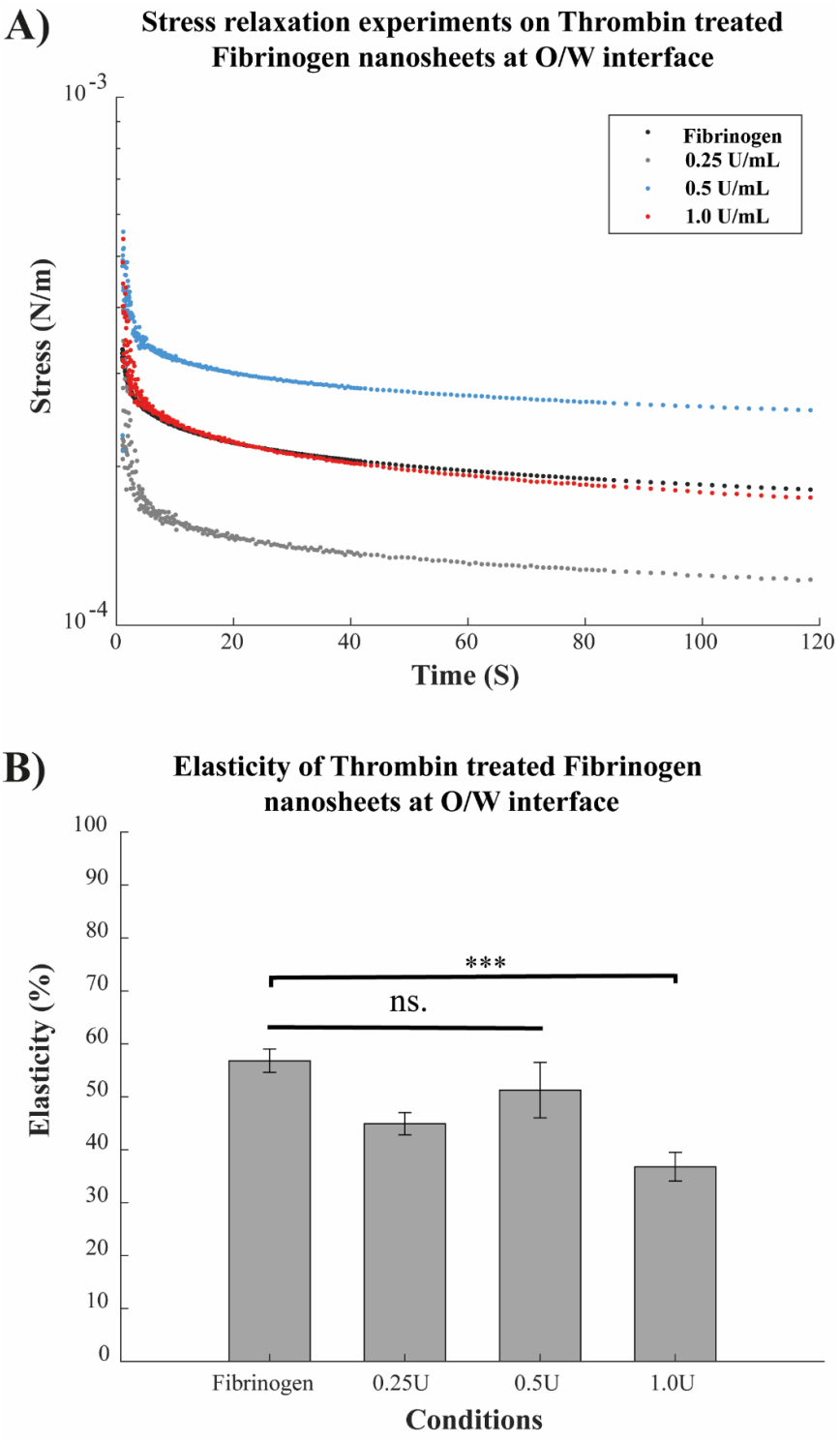

Figure 83: Measuring stress relaxation and elasticity of Thrombin treated Fibrinogen nanosheets at the Oil/water interface. A) Stress relaxation experiments of Fibrinogen nanosheets post thrombin treatment. B) Elasticity of fibrinogen nanosheets post thrombin treatment. Elasticity was obtained through the exponential fitting of stress relaxation data at 1% strain using function ExpDec2. Significance was determined by *P < 0.05, **P < 0.01, ***P < 0.001 and n.s. nonsignificant. Each thrombin concentration was repeated three times and the average stress/elasticity was plotted. The standard error was depicted as error bars per triplicated data point.

5.3. Self-assembly of fibrinogen nanosheets

After characterising the interfacial mechanics of the nanosheets, we moved our attention to examine the structure of the fibrinogen nanosheets formed and the impact of the enzyme crosslinker thrombin on their architecture. It is worth stressing that fibrinogen and thrombin were introduced sequentially and free fibrinogen was completely removed from the system prior to introduction of thrombin, this was conducted to reduce the risk of crosslinking the free fibrinogen instead of the adsorbed protein at the interface. A combination of SEM, TEM and fluorescent microscopy was used to investigate whether fibres are being formed at the interface. From the SEM images (Figure 84) we found that emulsions treated with varying concentrations of thrombin did not exhibit fibre formation at the surface, however folds in the nanosheet could be seen within the centre of the emulsions, these folds result from the drying process of the fibrinogen-stabilised microdroplets in air and evaporation of the oil phase, leaving a "deflated" nanosheet skin. This hypothesis of no fibre formation was further supported by the TEM images in Figure 85, the untreated fibrinogen nanosheet exhibited a homogenous nanosheet that filled the carbon lacey grids with small holes within the nanosheet. Interestingly when thrombin was introduced, all conditions observed a higher frequency of breakages, and we observed much more folding of the nanosheet (supporting the SEM data), this could be due to a rearrangement in the protein nanosheet leading to an outward retraction. Additionally, when we took a higher magnification image of the 0.25 U/mL T it also exhibited a homogenous nanosheet with darker domains. It was interesting to see that no fibres formed at the oil/water interface, despite the fibrinogen/thrombin system readily forming fibres that

leads to gelation in solution when introduced together[542]. Additionally, from the fluorescent microscopy images (Figure 86) fibrinogen was also found to form a homogenous assembly with small breakages at the interfaces depicted by the darker regions. However, with the introduction of thrombin the interface seemed introduce changes in the assembly and at the highest thrombin concentration of 1.0 U/mL T formed higher occurrences of aggregation depicted by the higher fluorescent intensity filaments.

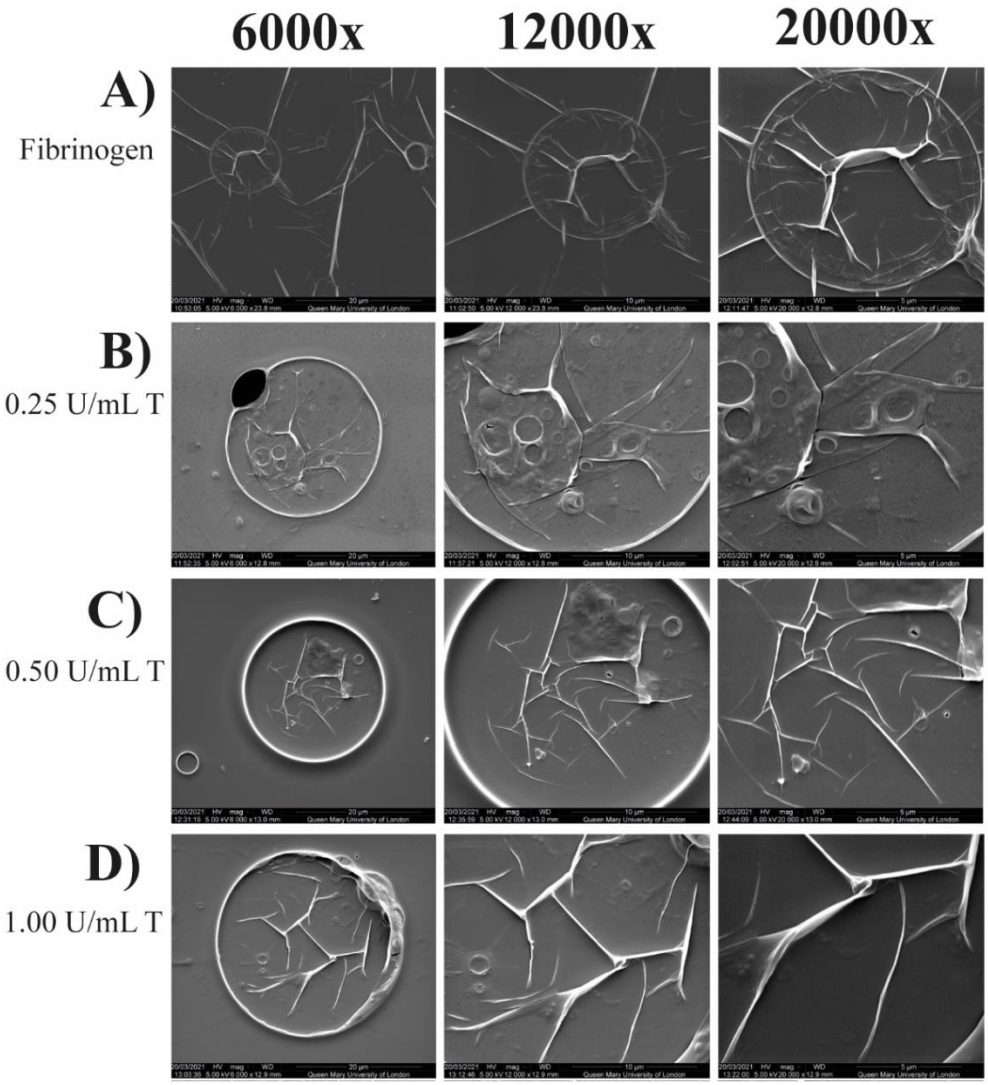

Figure 84: Characterising the self-assembly of Fibrinogen at the Oil//water interface. SEM images of Fibrinogen emulsions treated with varying concentrations of thrombin, at 6000x, 12000x and 20000x magnifications. A-D) Fibrinogen emulsions treated with 0, 0.25, 0.50 and 1.0 U/mL T respectively.

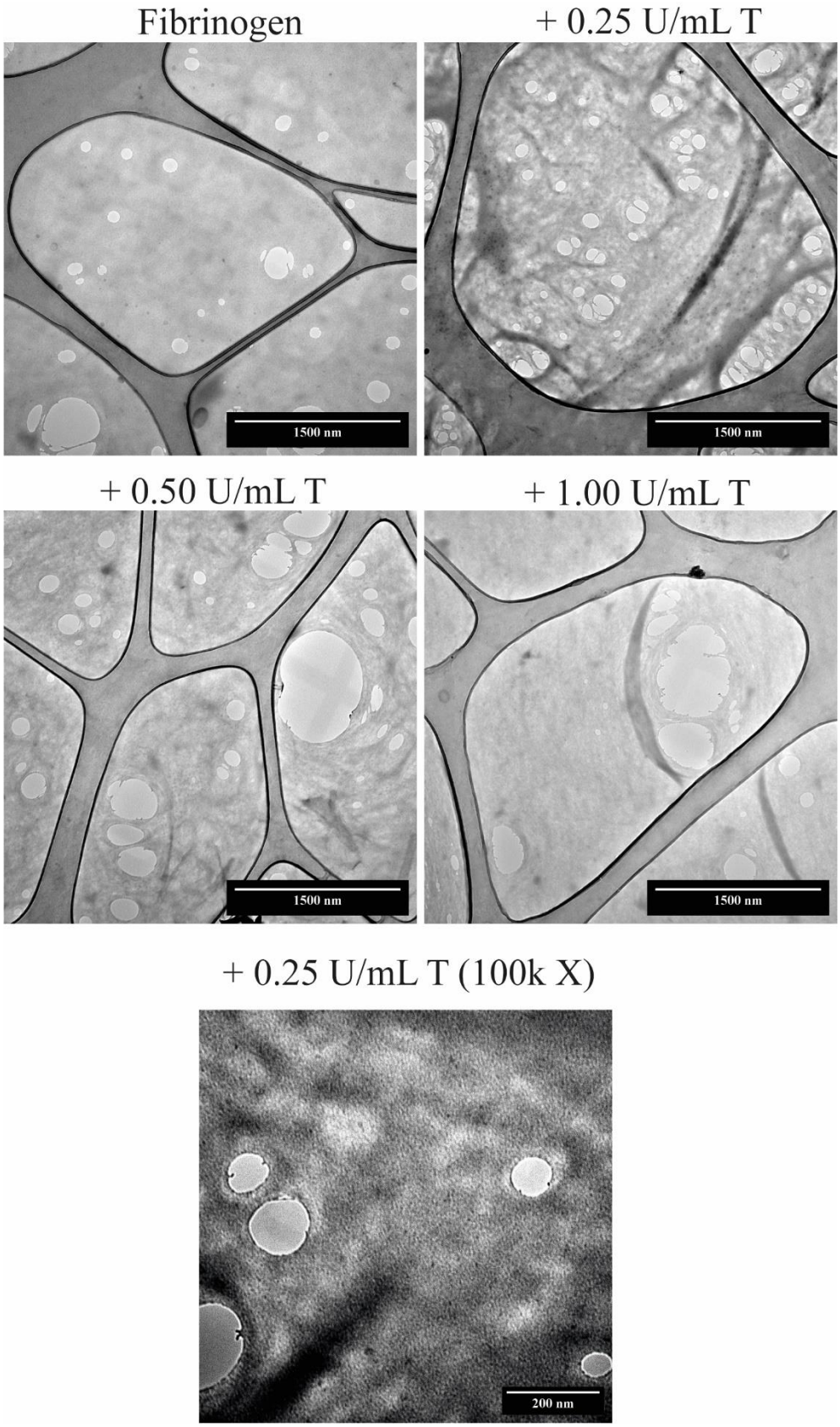

Figure 85: TEM images of Fibrinogen Novec-7500 Oil/Water interfaces prepared on Carbon lacey grids treated with varying concentration of thrombin. Fibrinogen treated with 0, 0.25 and 1.0 U/mL T respectively, at 25,000x magnification and 0.25 U/mL T at 100,000x magnification respectively.

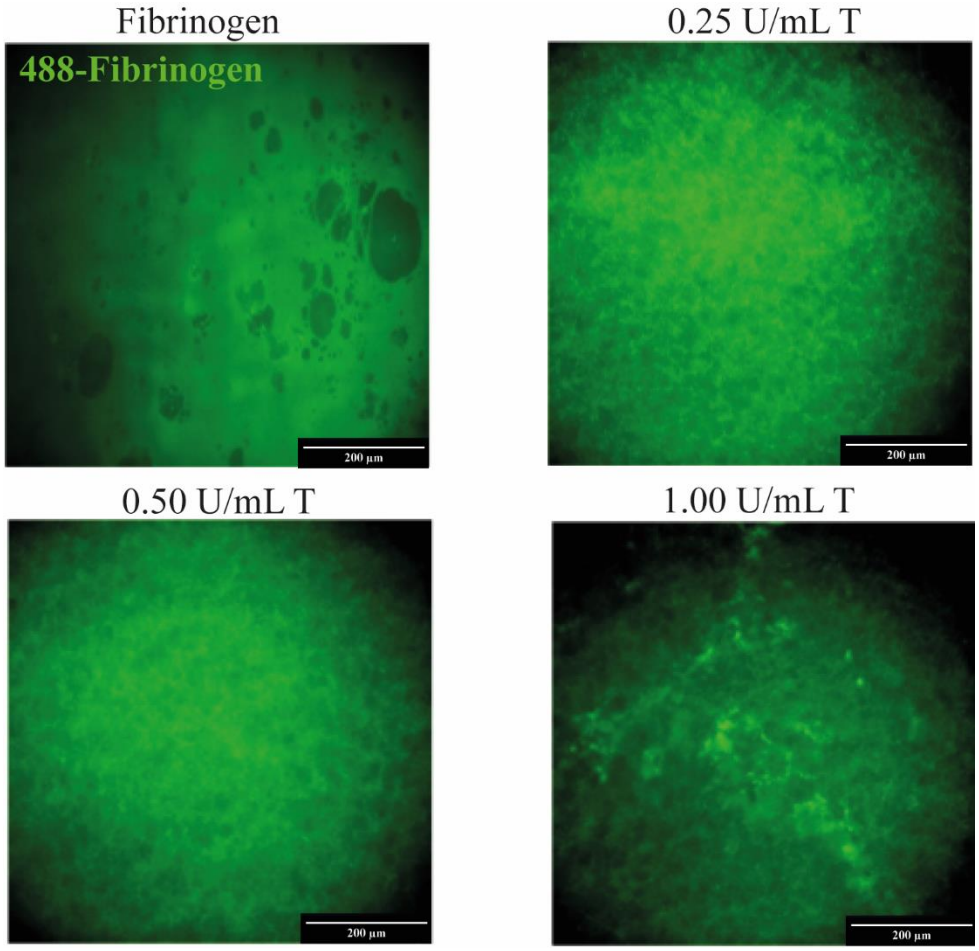

Figure 86: Fluorescent microscopy of 488-Fibrinogen flat interfaces treated with varying concentrations of Thrombin at 20x magnification. Fibrinogen treated with 0, 0.25, 0.50 and 1.0 U/mL T respectively.

5.4. Culture of MSCs on fibrinogen nanosheets

After probing the architecture of the nanosheets, the next step was to explore the capabilities of this new system for application in cell culture. Various types of experiments were implemented to test the system, such as culture of cells on flat interfaces that attempt to mirror the flat 2D culture on tissue culture plastic (TCP), pinned droplets (easier to form and retaining a quasi-2D geometry) and bioemulsions, offering opportunities for 3D culture. MSCs were selected to be used to study these interfaces due to their relevance for tissue engineering and cell therapies, and ability to generate high contractile forces to sense and remodel their extracellular microenvironments[546]; utilising this cell type has allowed us to push the system capabilities to sustain adherent cell cultures. From the flat interface study in Figure 87, MSCs were observed to attach on all thrombin treated fibrinogen nanosheet conditions and proliferate up to day 7 of culture. Furthermore, the 0.25 U/mL T condition appeared to promote adhesion and facilitate cell proliferation at qualitatively similar levels to the TCP control which could be as a result of the increased toughness of the interface seen in the rheological measurements previously. Similarly, all thrombin treated conditions in the pinned droplet approach (Figure 88) provided a stable scaffold that withstood 5 days of MSC culture and facilitated the proliferation of MSCs at a high cell density. Interestingly, the untreated fibrinogen nanosheet provided cell proliferative capacity up until day 3 of cell culture, after which it fractured and recoiled towards the outer edge of the droplet. Despite the 1.0 U/mL T condition having a lower toughness than the lower concentrations of thrombin, it was also capable of sustaining day 5 MSCs cell densities, however some fractures were observed in the nanosheet at

this time point. Furthermore, the pinned droplet data aligns with the rheological toughness data with 0.25-0.5 U/mL T providing the highest form of scaffold stability with no fractures observed at day 5. A holistic example of the 0.25 U/mL T pinned droplet can be seen in Figure 89AI, it was observed that the cells formed a very strong 2D network at very high cell densities covering the entire surface of the pin droplet by five days of culture Figure 89BI.

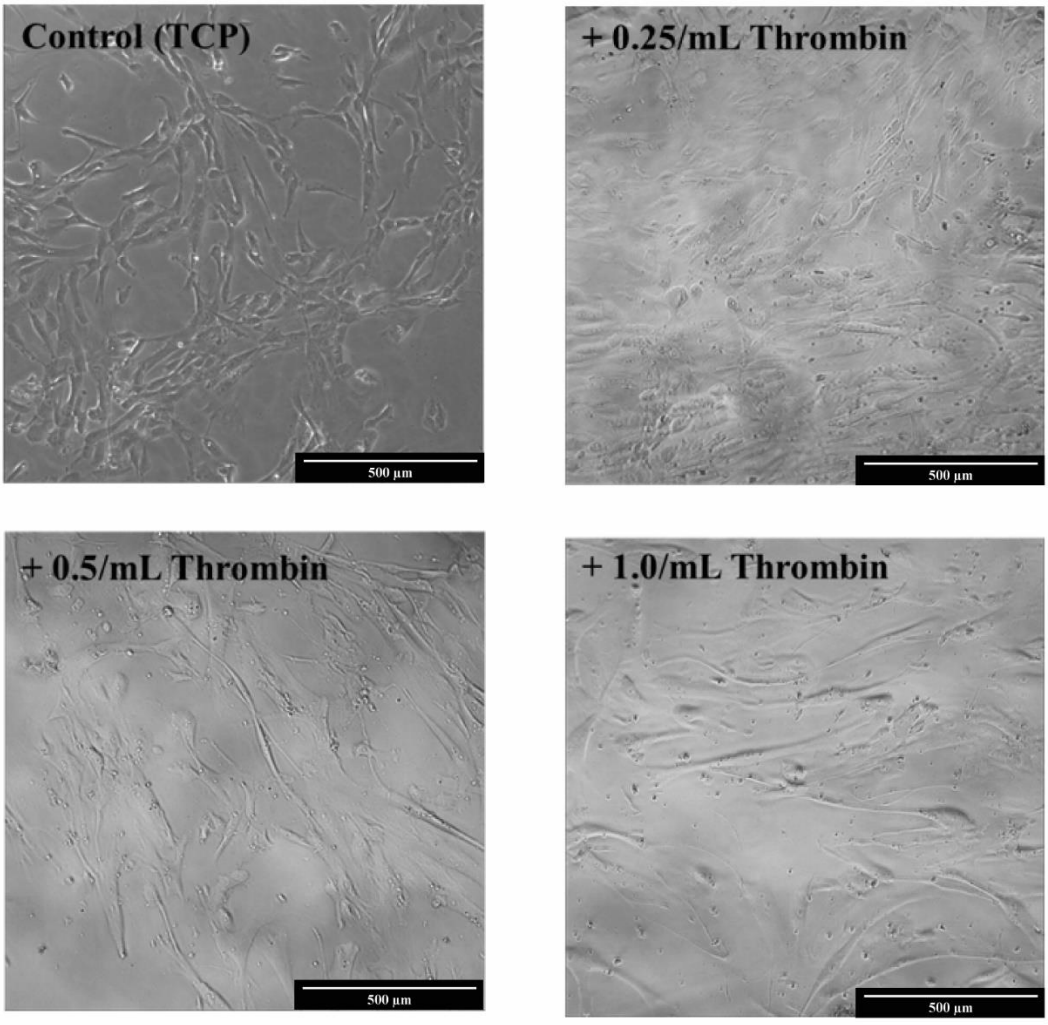

Figure 87: Qualitatively measuring the effect of thrombin on the adhesion of MSCs on fibrinogen nanosheets using 2D flat interfaces. Growth of MSCs on Novec-7500 oil flat interfaces stabilised with Fibrinogen treated with varying concentrations of thrombin 0.25, 0.5 and 1.0 U/mL T respectively in a 24 well plate. Control - MSCs cultured on TCP in a 24 well plate. Brightfield image taken at 10x magnification.

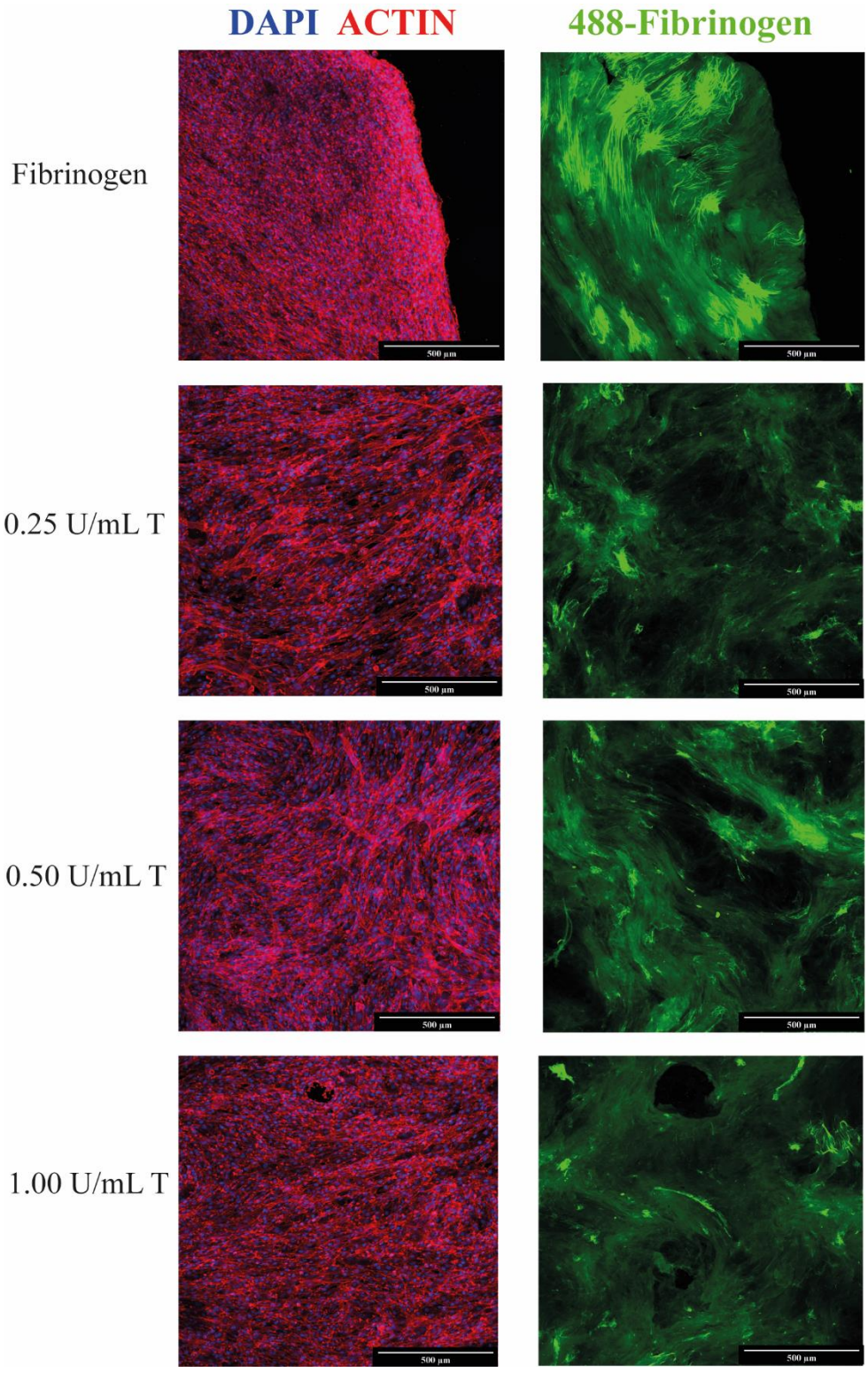

Figure 88: Qualitatively measuring the effect of thrombin on the adhesion of MSCs on fibrinogen nanosheets using Quasi-2d pinned droplets. MSCs growing for 5 days on fibrinogen-stabilised pinned droplet interfaces with varying levels of thrombin crosslinking, and fibronectin adsorption (25µg/mL). Actin (red), DAPI (blue) and 488-Fibrinogen (green) staining. Fibrinogen emulsions treated with 0, 0.25, 0.5 and 1.0 U/mL T respectively. Fluorescent images taken at 10x magnification.

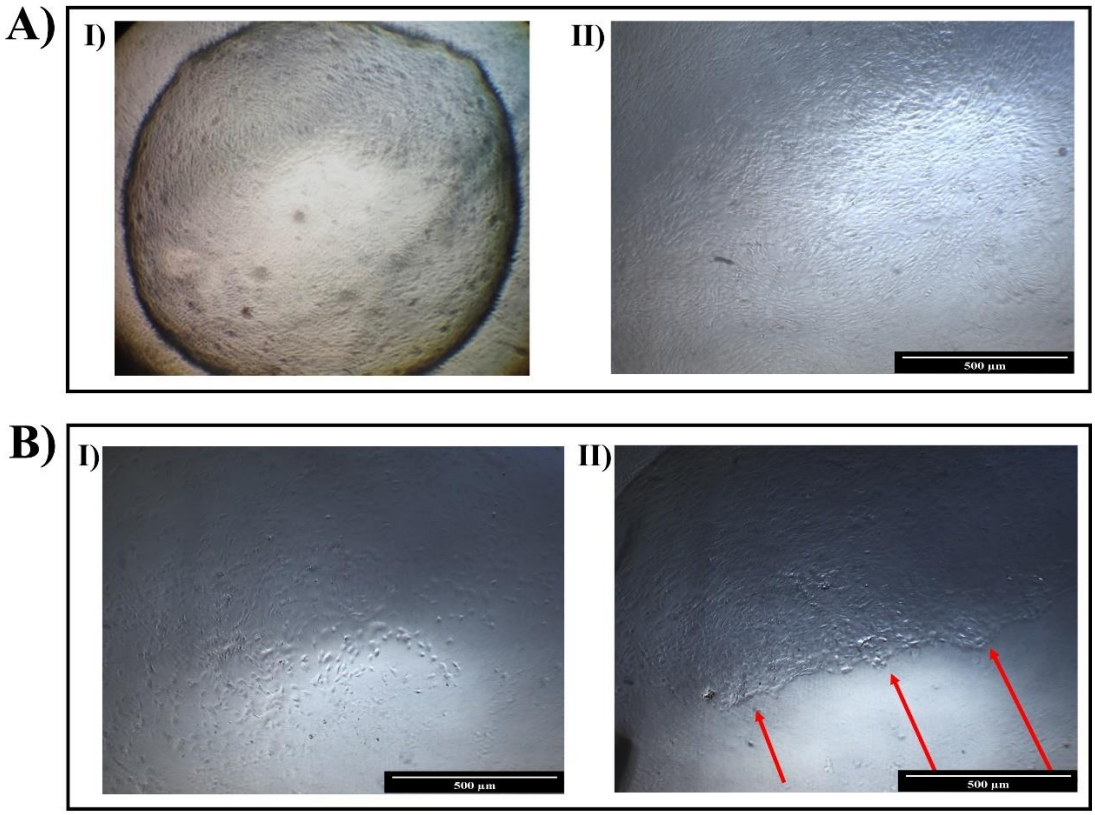

Figure 89: An example of a Novec-7500 pinned droplet treated with 0.25 U/mL T. A) Pinned droplet stabilised with fibrinogen treated with 0.25 U/mL T at day 5. I) Full view, taken by mobile phone. II) 10x view taken by brightfield microscope. B) Pinned droplet stabilised with fibrinogen and no treatment with thrombin. I) Day 2 before nanosheet fracture. II) Day 3 after nanosheet fracture, red arrows indicate the recoil of the nanosheet alongside cells towards the outer edge. Brightfield images taken at 10x magnification.

The number of cells at the centre of each pinned droplet was measured to obtain a quantitative measurement of cell densities at the pinned droplet surface. From Figure 91 it was observed that 0.25 U/mL T condition provided the necessary scaffold to promote the highest cell adhesion and proliferation depicted by possession of the highest cell densities at the surface at 130k cells, this was a 21.6x increase from the initial 6k seeding density with a significant difference when compared to the untreated fibrinogen nanosheets.

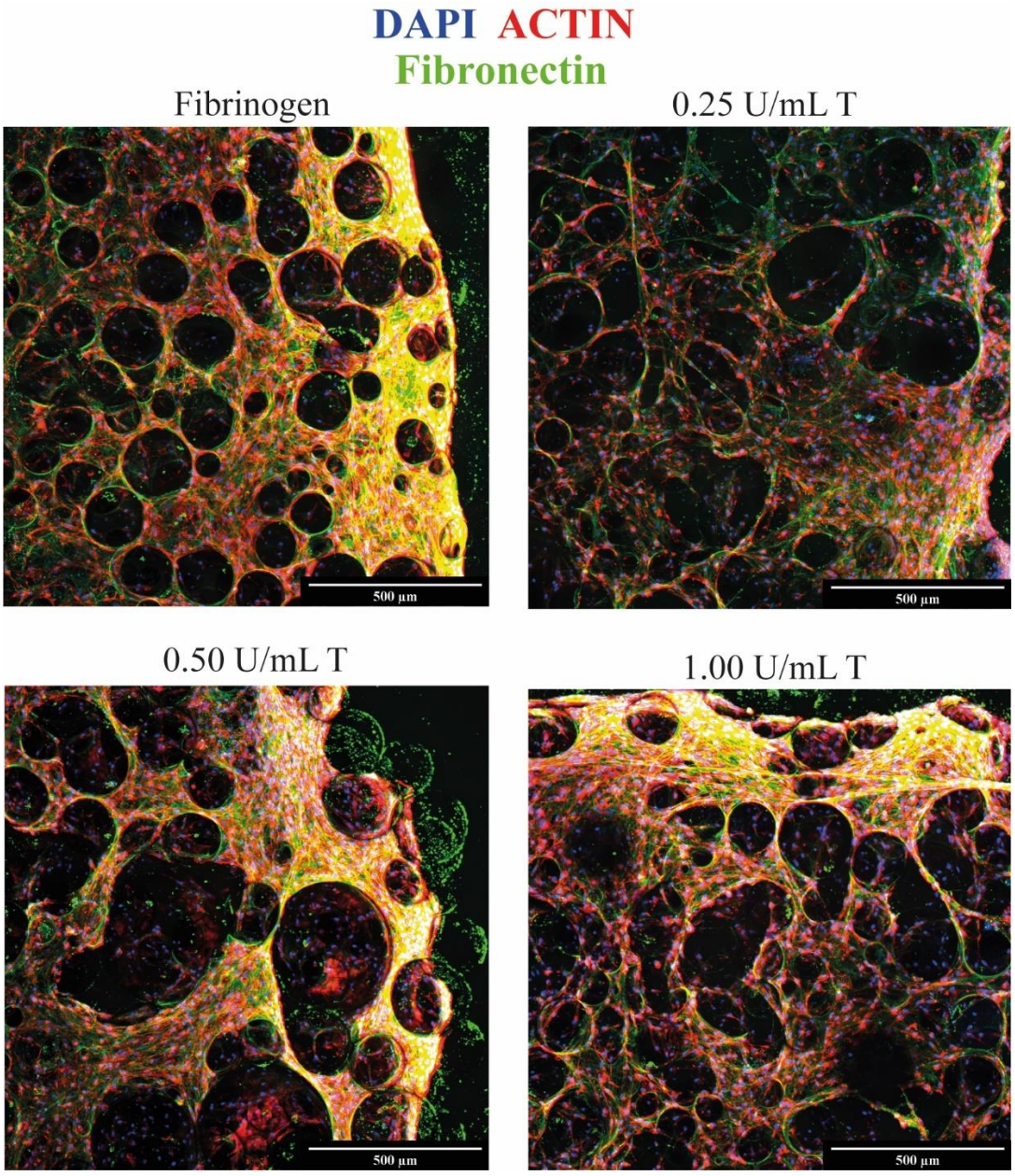

Figure 90: MSCs growing for 7 days on fibrinogen-stabilised Novec 7500 emulsions, with different degrees of thrombin crosslinking and fibronectin adsorption (25 µg/mL). Actin (red), DAPI (blue) and Fibronectin (green) staining. Fibrinogen emulsions treated with 0, 0.25, 0.5 and 1.0 U/mL T respectively. Fluorescent images taken at 10x magnification; Max Z-Projections generated through ImageJ.

The final approach used to study the adherence of cells was the 3D bioemulsions, these emulsions provide a much higher surface area which theoretically provides more area for cells to adhere to and proliferate. From Figure 90 all conditions were capable of sustaining cell adhesion and proliferation and provided a scaffold that lasted the seven

days of culture. It can be seen that the cells were able to adhere and completely surround these emulsions forming 3D networks, with cells penetrating and proliferating deep within the gel-like structure formed by the aggregated emulsion droplets. Cyquant assays were run to quantify the number of cells proliferating in these 3D systems, from Figure 92 all conditions contained roughly the same number of cells by day 7 around 200k cells, which is a 33x increase from the initial 6k cell seeding density. However, it is to be noted that the Cyquant assay is not fully accurate as the nuclei count used for the pinned droplets as residual volumes were still present in the wells caused by the lysis of emulsions and residue media; they couldn't be completely removed without the risk of aspirating the cells, this potentially diluted the samples, thus the number of cells in each well could greater than stated.

It is interesting to note that large colonies formed, and high cell proliferation was observed, irrespective of the interface formulation, when cultured on bioemulsions. This may result from the different geometry and restricted size of each protein nanosheets. We hypothesise that whereas large colonies can generate high forces on 2D or quasi-2D interfaces, as a result of collective contractility, the restricted size and surface of single droplets and the 3D network ultimately formed may not enable similar collective contractility to take place, or at least not directed to the interfaces. As a result, cell proliferation was observed in all conditions, irrespective of the thrombin treatment applied.

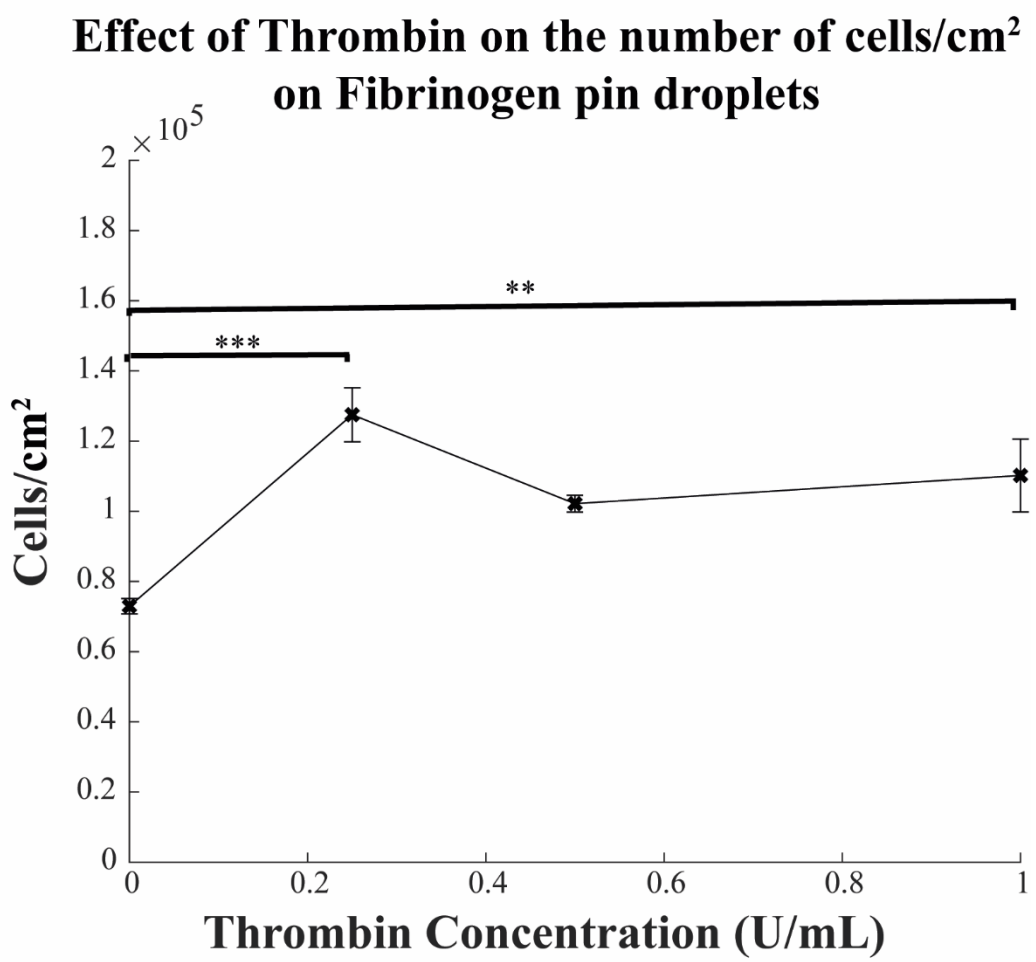

Figure 91: Quantitative analysis of the number of cells proliferating at the quasi-2D fibrinogen scaffolds. Measuring the number of MSCs (cells/cm^2) on Novec-7500 oil pin droplets stabilised with Fibrinogen treated with different degrees of thrombin crosslinking and fibronectin adsorption (25 µg/mL). Significance was determined by *P < 0.05, **P < 0.01, ***P < 0.001 and n.s. nonsignificant. Each thrombin concentration was repeated three times and the average number of cells/cm^2 was plotted. The standard error was depicted as error bars per triplicated data point.

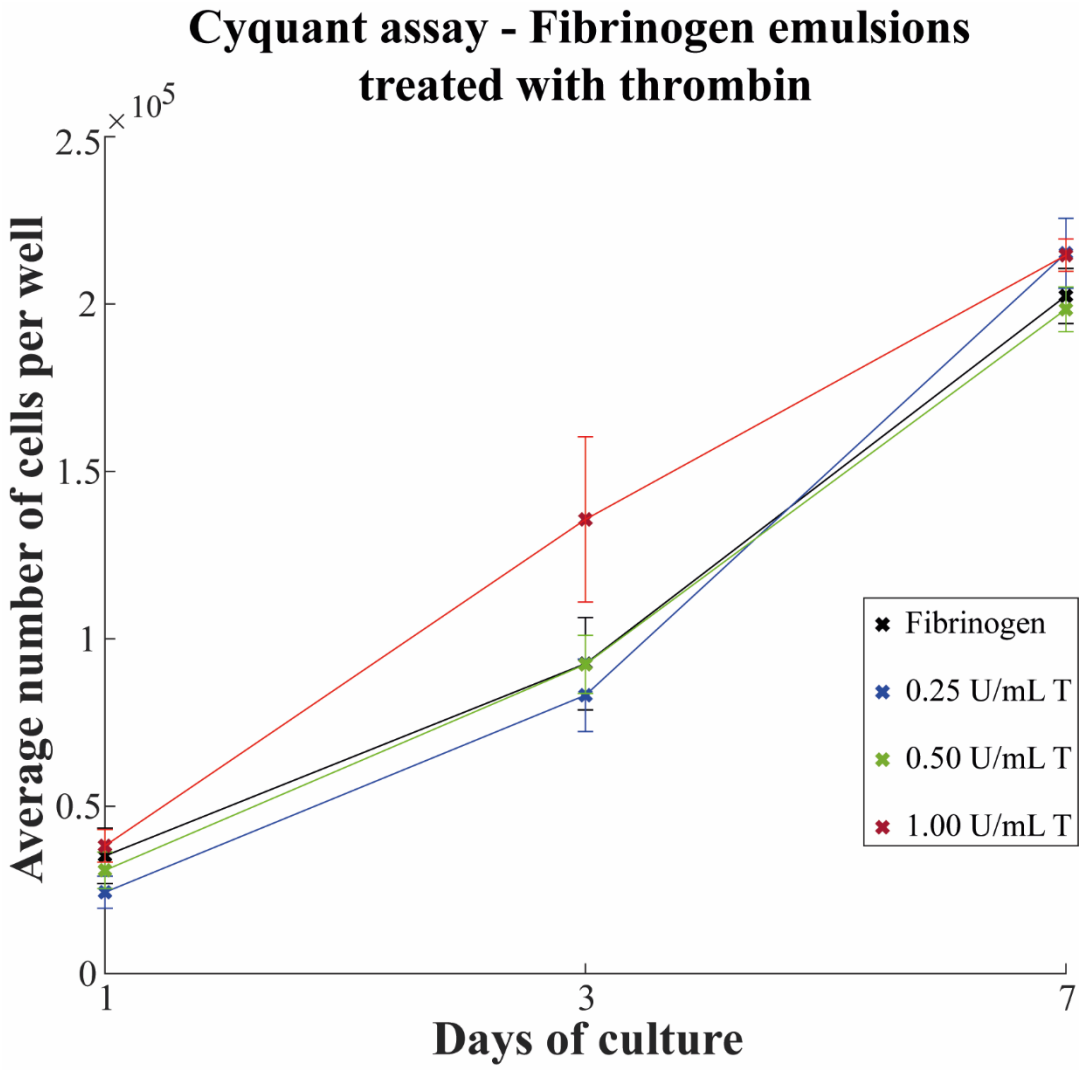

Figure 92: Quantitative analysis of the number of cells proliferating at the 3D fibrinogen scaffolds. Cyquant assay - Measuring the number of MSCs per well on Novec-7500 oil emulsions stabilised with Fibrinogen treated with different degrees of thrombin crosslinking and fibronectin adsorption (25 µg/mL).

6. Conclusions and future work

The aim of this thesis was split into two, the first was to introduce bioactivity to self-assembled protein nanosheets and then apply this technology to potentially study forces and introduce ligands within complex tissues such as cerebral organoids. The Avi-tag initially proposed to be attached to the N-terminus of rBSA was successfully expressed and purified using the *P. pastoris* expression system, and was generated at high levels of 135mg of protein (16.85mg/mL) from 2L shaker flask cultures; the amount of protein produced was sufficient for downstream applications. The *in vitro* biotinylation of Avi-rBSA by rBirA was also completed with minimal loss to final protein yield. The success of the system was signified by the high reproducibility of expression/purification and consistent yield of high levels of biotinylated rBSA protein that was correctly folded and relatively pure. The Bt-rBSA protein exhibited similar interfacial mechanics to commercial BSA and was successfully used to capture bioactive components such as Streptavidin and ProteinG; these opened avenues to introduce infinite types of bioactivities either by using the biotin-streptavidin click chemistry or the ability to capture any Fc-tagged proteins or antibodies through ProteinG. The newly synthesised bioactive protein was used to stabilise Novec-7500 oil droplets that were capable of being stored for at least a year without any detrimental effects to the introduction of bioactivity to the surface of the droplets. These droplets were functionalised with Cadherins and RGD to explore how they will interact with complex tissues such as cerebral organoids and whether they can be used as a force sensor to probe the forces within the organoids. From the results obtained we demonstrated that the addition of Cadherins specifically E-Cadherin promoted the

uptake of these droplets at higher levels in the early stages of embryoid body formation, however it became clear that the introduction of N-Cadherin was also necessary to retain the droplets once the EBs were induced to neural ectoderm. The droplets seemed to not have a negative impact on cerebral organoid formation in terms of lineage commitment depicted by the high level of expression of hallmark markers such as TUJ1, FOXG1, PAX6, SOX2, YAP1 and ZO-1. However, the introduction of the droplets did seem to have an effect on the rosette formations, generating rosettes with larger lumens and greater area; an interesting phenomenon. Unfortunately, the droplets did not deform as expected probably due to the stiff interfacial mechanics of the rBSA nanosheet, thus future work can include the introduction of softer proteins such as beta casein can theoretically soften the interface to hypothetically increase the probability of deformation. Additionally, for the future we can also probe whether it is necessary to use oil droplets to promote uptake of particles into the organoids, rather to use glass nanoparticles hydrophobized (in the range of 20-30 μm) using the same technique used to generate pinned droplets on glass slides. The Bt-rBSA protein would adsorb to these hydrophobic glass nanoparticles and then mixed in a similar fashion; these nanoparticles would be less prone to rupture and maybe resist the expulsion from the organoid, an interesting hypothesis. Nevertheless, the successful incorporation and retention of E/N-Cadherin and RGD functionalised droplets can theoretically be used as a signalling hub to introduce specific ligands within complex tissues, this could induce signalling pathways that could potentially act as nodes to drive differentiation and development.

The second aim was to search for proteins that promoted the direct strengthening of interfacial mechanics of protein nanosheets without the need of a co-surfactant. We proposed to explore this through the assembly of fibrinogen that is known to adsorb

to both hydrophobic and hydrophilic surfaces and to study the impact of the addition of thrombin on the interfacial liquid-liquid mechanics and whether these enhanced nanosheets promoted the adherence and proliferation of highly contractile cells such as Mesenchymal stem cells. The interfacial mechanics of the fibrinogen nanosheet was characterised through interfacial shear rheology and was found to have a similar storage modulus to BSA. However, with the addition of the thrombin enzyme the toughness of the resulting nanosheet was significantly increased with the lowest concentration of 0.25 U/mL T generating a toughness similar to MA Silk one of the toughest materials studied and four times higher than Kevlar-49. However, the opposite trend was seen for the elasticity, which seemed to decrease as the thrombin concentration increased. With this exciting data we pushed to see if these enhanced mechanics could translate to facilitate the adherence of MSCs for prolonged cultures. All conditions including untreated fibrinogen were capable of generating 3D networks as bioemulsions that promoted the adhesion of high number of MSCs for seven days. However, the untreated fibrinogen nanosheet in the 2D pinned droplet format was only capable of sustaining proliferation for three days before fracturing. Nevertheless, all the thrombin treated nanosheets were capable of sustaining high density cultures for five days with small fractures appearing only in the higher concentrations of thrombin conditions. For future work, the system is very attractive from a cell culture point of view as the bioemulsions can be potentially scaled up into spinning flask bioreactors to exponentially increase the yield of cells. Furthermore, the stability and physiological nature of the system could allow this technology to be utilised in the food, cell and therapeutic industry bypassing the need to form recombinantly or remove any cyto-toxic chemicals; this is due to the high availability of human derived fibrinogen and thrombin.

Bibliography

1. Jivan, F. & Alge, D. L. Bio-Orthogonal, Site-Selective Conjugation of Recombinant Proteins to Microporous Annealed Particle Hydrogels for Tissue Engineering. *Adv Ther (Weinh)* **3**, 1900148 (2020).
2. Fisher, S. A., Baker, A. E. G. & Shoichet, M. S. Designing Peptide and Protein Modified Hydrogels: Selecting the Optimal Conjugation Strategy. *Journal of the American Chemical Society* vol. 139 7416–7427 Preprint at https://doi.org/10.1021/jacs.7b00513 (2017).
3. Žilić, S., Barać, M., Pešić, M., Dodig, D. & Ignjatović-Micić, D. Characterization of Proteins from Grain of Different Bread and Durum Wheat Genotypes. *Int J Mol Sci* **12**, 5878 (2011).
4. Abeyrathne, E. D. N. S., Lee, H. Y. & Ahn, D. U. Egg white proteins and their potential use in food processing or as nutraceutical and pharmaceutical agents—A review. *Poult Sci* **92**, 3292–3299 (2013).
5. El-Fakharany, E. M. *et al.* The Use of Human, Bovine, and Camel Milk Albumins in Anticancer Complexes with Oleic Acid. *Protein J* **37**, 203–215 (2018).
6. Kalra, H. *et al.* Comparative proteomics evaluation of plasma exosome isolation techniques and assessment of the stability of exosomes in normal human blood plasma. *Proteomics* **13**, 3354–3364 (2013).
7. Anguizola, J. *et al.* Review: Glycation of human serum albumin. *CLINICA CHIMICA ACTA* **425**, 64–76 (2013).
8. Raoufinia, R. *et al.* Overview of Albumin and Its Purification Methods. *Adv Pharm Bull* **6**, 495–507 (2016).
9. Mishra, V. & Heath, R. J. Structural and Biochemical Features of Human Serum Albumin Essential for Eukaryotic Cell Culture. *Int J Mol Sci* **22**, (2021).
10. Strauss, A. W. *et al.* Conversion of rat pre-proalbumin to proalbumin in vitro by ascites membranes. Demonstration by NH2-TERMINAL SEQUENCE ANALYSIS. *Journal of Biological Chemistry* **253**, 6270–6274 (1978).
11. Brennan, S. O. & Carrell, R. W. A circulating variant of human proalbumin. *Nature* **274**, 908–909 (1978).
12. Nakamura, K. *et al.* Conformational changes in seventeen cystine disulfide bridges of bovine serum albumin proved by Raman spectroscopy. *FEBS Lett* **417**, 375–378 (1997).
13. SUDLOW, G., BIRKETT, D. J. & WADE, D. N. The Characterization of Two Specific Drug Binding Sites on Human Serum Albumin. *Mol Pharmacol* **11**, (1975).
14. HE, X. M. & CARTER, D. C. ATOMIC-STRUCTURE AND CHEMISTRY OF HUMAN SERUM-ALBUMIN (VOL 358, PG 209, 1992). *Nature* **364**, 362 (1993).
15. Murayama, K. & Tomida, M. Heat-induced secondary structure and conformation change of bovine serum albumin investigated by Fourier transform infrared spectroscopy. *Biochemistry* **43**, 11526–11532 (2004).

16. Chen, Z., He, Y., Shi, B. & Yang, D. C. Human serum albumin from recombinant DNA technology: Challenges and strategies. *BIOCHIMICA ET BIOPHYSICA ACTA-GENERAL SUBJECTS* **1830**, 5515–5525 (2013).
17. Lapolla, A. *et al.* Enzymatic digestion and mass spectrometry in the study of advanced glycation end products/peptides. *J Am Soc Mass Spectrom* **15**, 496–509 (2004).
18. Lee, P. & Wu, X. Review: Modifications of Human Serum Albumin and Their Binding Effect. *Curr Pharm Des* **21**, 1862 (2015).
19. Ketrat, S., Japrung, D. & Pongprayoon, P. Exploring how structural and dynamic properties of bovine and canine serum albumins differ from human serum albumin. *J Mol Graph Model* **98**, (2020).
20. Majorek, K. A. *et al.* Structural and immunologic characterization of bovine, horse, and rabbit serum albumins. *Mol Immunol* **52**, 174–182 (2012).
21. Bujacz, A. Structures of bovine, equine and leporine serum albumin. *Acta Crystallogr D Biol Crystallogr* **68**, 1278–1289 (2012).
22. Huang, B. X., Kim, H. Y. & Dass, C. Probing three-dimensional structure of bovine serum albumin by chemical cross-linking and mass spectrometry. *J Am Soc Mass Spectrom* **15**, 1237–1247 (2004).
23. Francis, G. L. Albumin and mammalian cell culture: implications for biotechnology applications. *Cytotechnology* **62**, 1–16 (2010).
24. Fanali, G. *et al.* Human serum albumin: from bench to bedside. *Mol Aspects Med* **33**, 209–290 (2012).
25. Ghuman, J. *et al.* Structural basis of the drug-binding specificity of human serum albumin. *J Mol Biol* **353**, 38–52 (2005).
26. HE, X. M. & CARTER, D. C. ATOMIC-STRUCTURE AND CHEMISTRY OF HUMAN SERUM-ALBUMIN (VOL 358, PG 209, 1992). *Nature* **364**, 362 (1993).
27. Arroyo, V., Garcia-Martinez, R. & Salvatella, X. Human serum albumin, systemic inflammation, and cirrhosis. *J Hepatol* **61**, 396–407 (2014).
28. Bernardi, M., Ricci, C. S. & Zaccherini, G. Role of human albumin in the management of complications of liver cirrhosis. *J Clin Exp Hepatol* **4**, 302–311 (2014).
29. Quinlan, G. J., Martin, G. S. & Evans, T. W. Albumin: Biochemical properties and therapeutic potential. *HEPATOLOGY* **41**, 1211–1219 (2005).
30. Raoufinia, R. *et al.* Overview of Albumin and Its Purification Methods. *Adv Pharm Bull* **6**, 495–507 (2016).
31. He, Y. *et al.* Large-scale production of functional human serum albumin from transgenic rice seeds. *Proc Natl Acad Sci U S A* **108**, 19078–19083 (2011).
32. Tsuchida, E. *et al.* Artificial Oxygen Carriers, Hemoglobin Vesicles and Albumin-Hemes, Based on Bioconjugate Chemistry. *Bioconjug Chem* **20**, 1419–1440 (2009).
33. Cai, C., Zhou, K. Y., Wu, Y. & Wu, L. Y. Enhanced liver targeting of 5-fluorouracil using galactosylated human serum albumin as a carrier molecule. *J Drug Target* **14**, 55–61 (2006).
34. Li, S. J. *et al.* A novel purification procedure for recombinant human serum albumin expressed in Pichia pastoris. *Protein Expr Purif* **149**, 37–42 (2018).

35. Curling, J. M., Berglöf, J., Lindquist, L. -O & Eriksson, S. A chromatographic procedure for the purification of human plasma albumin. *Vox Sang* **33**, 97–107 (1977).
36. Chamberland, M. E., Alter, H. J., Busch, M. P., Nemo, G. & Ricketts, M. Emerging infectious disease issues in blood safety. *Emerg Infect Dis* **7**, 552–553 (2001).
37. Erstad, B. L. Viral infectivity of albumin and plasma protein fraction. *Pharmacotherapy* **16**, 996–1001 (1996).
38. Arber, W. Restriction Endonucleases. *Angewandte Chemie International Edition in English* **17**, 73–79 (1978).
39. *Omics Technologies and Bio-Engineering*. *Omics Technologies and Bio-Engineering* (Elsevier, 2018). doi:10.1016/c2015-0-01634-3.
40. Lin, C. Y. & Liu, J. C. Modular protein domains: An engineering approach toward functional biomaterials. *Current Opinion in Biotechnology* vol. 40 56–63 Preprint at https://doi.org/10.1016/j.copbio.2016.02.011 (2016).
41. Booth, W. T. *et al.* Impact of an N-terminal polyhistidine tag on protein thermal stability. *ACS Omega* **3**, 760–768 (2018).
42. Zhu, W. *et al.* High level expression and purification of recombinant human serum albumin in Pichia pastoris. *Protein Expr Purif* **147**, 61–68 (2018).
43. Abascal, N. C. & Regan, L. The past, present and future of protein-based materials. *Open Biol* **8**, (2018).
44. Sutherland, T. D., Rapson, T. D., Huson, M. G. & Church, J. S. Recombinant Structural Proteins and Their Use in Future Materials. *Subcell Biochem* **82**, 491–526 (2017).
45. SLEEP, D., BELFIELD, G. P. & GOODEY, A. R. THE SECRETION OF HUMAN-SERUM ALBUMIN FROM THE YEAST SACCHAROMYCES-CEREVISIAE USING 5 DIFFERENT LEADER SEQUENCES. *BIO-TECHNOLOGY* **8**, 42–46 (1990).
46. FLEER, R. *et al.* STABLE MULTICOPY VECTORS FOR HIGH-LEVEL SECRETION OF RECOMBINANT HUMAN SERUM-ALBUMIN BY KLUYVEROMYCES YEASTS. *BIO-TECHNOLOGY* **9**, 968–975 (1991).
47. OKABAYASHI, K. *et al.* SECRETORY EXPRESSION OF THE HUMAN SERUM-ALBUMIN GENE IN THE YEAST, SACCHAROMYCES-CEREVISIAE. *J Biochem* **110**, 103–110 (1991).
48. SLEEP, D. *et al.* SACCHAROMYCES-CEREVISIAE STRAINS THAT OVEREXPRESS HETEROLOGOUS PROTEINS. *BIO-TECHNOLOGY* **9**, 183–187 (1991).
49. Sumi, A. *et al.* Purification of recombinant human serum albumin efficient purification using STREAMLINE. *Bioseparation* **8**, 195–200 (1999).
50. Youn, J. K. *et al.* Enhanced Production of Human Serum Albumin by Fed-Batch Culture of Hansenula polymorpha with High-Purity Oxygen. *J Microbiol Biotechnol* **20**, 1534–1538 (2010).
51. He, Y. *et al.* Large-scale production of functional human serum albumin from transgenic rice seeds. *Proc Natl Acad Sci U S A* **108**, 19078–19083 (2011).
52. SIJMONS, P. C. *et al.* PRODUCTION OF CORRECTLY PROCESSED HUMAN SERUM-ALBUMIN IN TRANSGENIC PLANTS. *BIO-TECHNOLOGY* **8**, 217–221 (1990).

53. Farran, I., Sanchez-Serrano, J. J., Medina, J. F., Prieto, J. & Mingo-Castel, A. M. Targeted expression of human serum albumin to potato tubers. *Transgenic Res* **11**, 337–346 (2002).
54. Fernandez-San Millan, A., Mingo-Castel, A., Miller, M. & Daniell, H. A chloroplast transgenic approach to hyper-express and purify Human Serum Albumin, a protein highly susceptible to proteolytic degradation. *Plant Biotechnol J* **1**, 71–79 (2003).
55. Huang, L. F., Liu, Y. K., Lu, C. A., Hsieh, S. L. & Yu, S. M. Production of human serum albumin by sugar starvation induced promoter and rice cell culture. *Transgenic Res* **14**, 569–581 (2005).
56. BARASH, I. *et al.* SYNTHESIS AND SECRETION OF HUMAN SERUM-ALBUMIN BY MAMMARY-GLAND EXPLANTS OF VIRGIN AND LACTATING TRANSGENIC MICE. *Transgenic Res* **2**, 266–276 (1993).
57. Murasugi, A. Secretory expression of human protein in the Yeast Pichia pastoris by controlled fermentor culture. *Recent Pat Biotechnol* **4**, 153–166 (2010).
58. Zhang, Q., Yu, H., Zhang, F. Z. & Shen, Z. C. Expression and purification of recombinant human serum albumin from selectively terminable transgenic rice. *JOURNAL OF ZHEJIANG UNIVERSITY-SCIENCE B* **14**, 867–874 (2013).
59. Fanali, G. *et al.* Human serum albumin: From bench to bedside. *Mol Aspects Med* **33**, 209–290 (2012).
60. LAWN, R. M. *et al.* THE SEQUENCE OF HUMAN-SERUM ALBUMIN CDNA AND ITS EXPRESSION IN ESCHERICHIA-COLI. *Nucleic Acids Res* **9**, 6103–6114 (1981).
61. Lobstein, J. *et al.* SHuffle, a novel Escherichia coli protein expression strain capable of correctly folding disulfide bonded proteins in its cytoplasm. *Microb Cell Fact* **11**, 1–16 (2012).
62. Singh, S. M. & Panda, A. K. Solubilization and refolding of bacterial inclusion body proteins. *J Biosci Bioeng* **99**, 303–310 (2005).
63. Singh, A., Upadhyay, V., Upadhyay, A. K., Singh, S. M. & Panda, A. K. Protein recovery from inclusion bodies of Escherichia coli using mild solubilization process. *Microb Cell Fact* **14**, (2015).
64. Makino, T., Skretas, G. & Georgiou, G. Strain engineering for improved expression of recombinant proteins in bacteria. *Microb Cell Fact* **10**, (2011).
65. Rosano, G. L. & Ceccarelli, E. A. Recombinant protein expression in Escherichia coli: advances and challenges. *Front Microbiol* **5**, (2014).
66. Nguyen, M. T. *et al.* Bacterial overexpression and purification of soluble recombinant human serum albumin using maltose-binding protein and protein disulphide isomerase. *Protein Expr Purif* **167**, 105530 (2020).
67. Picanco-Castro, V., Freitas, M., Bomfim, A. & Russo, E. Patents in therapeutic recombinant protein production using mammalian cells. *Recent Pat Biotechnol* **8**, 165–171 (2014).
68. Chen, Z., He, Y., Shi, B. & Yang, D. C. Human serum albumin from recombinant DNA technology: Challenges and strategies. *BIOCHIMICA ET BIOPHYSICA ACTA-GENERAL SUBJECTS* **1830**, 5515–5525 (2013).

69. Yin, J., Li, G., Ren, X. & Herrler, G. Select what you need: a comparative evaluation of the advantages and limitations of frequently used expression systems for foreign genes. *J Biotechnol* **127**, 335–347 (2007).
70. Zhu, W. *et al.* Medium optimization for high yield production of human serum albumin in Pichia pastoris and its efficient purification. *Protein Expr Purif* **181**, 105831 (2021).
71. Cereghino, G. P. L., Cereghino, J. L., Ilgen, C. & Cregg, J. M. Production of recombinant proteins in fermenter cultures of the yeast Pichia pastoris. *Curr Opin Biotechnol* **13**, 329–332 (2002).
72. Wu, S. & Letchworth, G. J. High efficiency transformation by electroporation of Pichia pastoris pretreated with lithium acetate and dithiothreitol. *Biotechniques* **36**, 152–154 (2004).
73. Karbalaei, M., Rezaee, S. A. & Farsiani, H. Pichia pastoris: A highly successful expression system for optimal synthesis of heterologous proteins. *J Cell Physiol* **235**, 5867 (2020).
74. Brewing Microbiology. *Brewing Microbiology* (1996) doi:10.1007/978-1-4757-4679-2.
75. Kazim, M., Bibi, Z. & Waqas, M. Pichia pastoris expression system: a potential candidate to express protein in industrial and biopharmaceutical domains Hair Cell Regeneration View project Production of protease View project.
76. Wang, X. *et al.* Mit1 transcription factor mediates methanol signaling and regulates the alcohol oxidase 1 (AOX1) promoter in pichia pastoris. *Journal of Biological Chemistry* **291**, 6245–6261 (2016).
77. Vanz, A. L. *et al.* Physiological response of Pichia pastoris GS115 to methanol-induced high level production of the Hepatitis B surface antigen: catabolic adaptation, stress responses, and autophagic processes. *Microb Cell Fact* **11**, (2012).
78. Cámara, E. *et al.* Increased dosage of AOX1 promoter-regulated expression cassettes leads to transcription attenuation of the methanol metabolism in Pichia pastoris. *Sci Rep* **7**, (2017).
79. Pla, I. A. *et al.* Evaluation of Mut(+) and Mut(S) Pichia pastoris phenotypes for high level extracellular scFv expression under feedback control of the methanol concentration. *Biotechnol Prog* **22**, 881–888 (2006).
80. Looser, V. *et al.* Cultivation strategies to enhance productivity of Pichia pastoris: A review. *Biotechnol Adv* **33**, 1177–1193 (2015).
81. Kobayashi, K. *et al.* High-level expression of recombinant human serum albumin from the methylotrophic yeast Pichia pastoris with minimal protease production and activation. *J Biosci Bioeng* **89**, 55–61 (2000).
82. Ohya, T., Ohyama, M. & Kobayashi, K. Optimization of human serum albumin production in methylotrophic yeast Pichia pastoris by repeated fed-batch fermentation. *Biotechnol Bioeng* **90**, 876–887 (2005).
83. Mallem, M. *et al.* Maximizing recombinant human serum albumin production in a Muts Pichia pastoris strain. *Biotechnol Prog* **30**, 1488–1496 (2014).
84. Zhu, W. *et al.* High level expression and purification of recombinant human serum albumin in Pichia pastoris. *Protein Expr Purif* **147**, 59–66 (2018).

85. Guan, B. *et al.* Constitutive Expression of a rhIL-2-HSA Fusion Protein in Pichia pastoris Using Glucose as Carbon Source. *Appl Biochem Biotechnol* **171**, 1792–1804 (2013).
86. Sigar, M., Maity, N. & Mishra, S. Enhancing granulocyte colony-stimulating factor expression in Pichia pastoris through fusion with human serum albumin. *http://dx.doi.org/10.1080/10826068.2016.1252922* **47**, 364–370 (2017).
87. Mallem, M. *et al.* Maximizing recombinant human serum albumin production in a Muts Pichia pastoris strain. *Biotechnol Prog* **30**, 1488–1496 (2014).
88. Kobayashi, K. *et al.* High-level expression of recombinant human serum albumin from the methylotrophic yeast Pichia pastoris with minimal protease production and activation. *J Biosci Bioeng* **89**, 55–61 (2000).
89. Kerry-Williams, S. M., Gilbert, S. C., Evans, L. R. & Ballance, D. J. Disruption of the Saccharomyces cerevisiae YAP3 gene reduces the proteolytic degradation of secreted recombinant human albumin. *YEAST* **14**, 161–169 (1998).
90. Shamir, E. R. & Ewald, A. J. Three-dimensional organotypic culture: experimental models of mammalian biology and disease. *Nat Rev Mol Cell Biol* **15**, 647–664 (2014).
91. Corrò, C., Novellasdemunt, L. & Li, V. S. W. A brief history of organoids. *Am J Physiol Cell Physiol* **319**, C151–C165 (2020).
92. Lancaster, M. A. & Knoblich, J. A. Organogenesis in a dish: Modeling development and disease using organoid technologies. *Science (1979)* **345**, (2014).
93. Fatehullah, A., Tan, S. H. & Barker, N. Organoids as an in vitro model of human development and disease. *Nat Cell Biol* **18**, 246–254 (2016).
94. Rodriguez-Gatica, J. E. *et al.* Imaging three-dimensional brain organoid architecture from meso- to nanoscale across development. *Development* **149**, (2022).
95. Kim, J., Koo, B. K. & Knoblich, J. A. Human organoids: model systems for human biology and medicine. *Nat Rev Mol Cell Biol* **21**, 571–584 (2020).
96. Eiraku, M. *et al.* Self-organizing optic-cup morphogenesis in three-dimensional culture. *Nature* **472**, 51-U73 (2011).
97. Sato, T. *et al.* Single Lgr5 stem cells build crypt-villus structures in vitro without a mesenchymal niche. *Nature* **459**, 262-U147 (2009).
98. Antonica, F. *et al.* Generation of functional thyroid from embryonic stem cells. *Nature* **491**, 66-U170 (2012).
99. Huch, M. *et al.* In vitro expansion of single Lgr5(+) liver stem cells induced by Wnt-driven regeneration. *Nature* **494**, 247–250 (2013).
100. Suga, H. *et al.* Self-formation of functional adenohypophysis in three-dimensional culture. *Nature* **480**, 57-U215 (2011).
101. Koehler, K. R., Mikosz, A. M., Molosh, A. I., Patel, D. & Hashino, E. Generation of inner ear sensory epithelia from pluripotent stem cells in 3D culture. *Nature* **500**, 217-+ (2013).
102. Xia, Y. *et al.* Directed differentiation of human pluripotent cells to ureteric bud kidney progenitor-like cells. *Nat Cell Biol* **15**, 1507-+ (2013).

103. Takasato, M. *et al.* Directing human embryonic stem cell differentiation towards a renal lineage generates a self-organizing kidney. *Nat Cell Biol* **16**, 118-+ (2014).
104. Taguchi, A. *et al.* Redefining the In Vivo Origin of Metanephric Nephron Progenitors Enables Generation of Complex Kidney Structures from Pluripotent Stem Cells. *Cell Stem Cell* **14**, 53–67 (2014).
105. Lancaster, M. A. *et al.* Cerebral organoids model human brain development and microcephaly. *Nature* **501**, 373-+ (2013).
106. Evans, M. Discovering pluripotency: 30 years of mouse embryonic stem cells. *Nat Rev Mol Cell Biol* **12**, 680–686 (2011).
107. Weitzer, G. Embryonic stem cell-derived embryoid bodies: an in vitro model of eutherian pregastrulation development and early gastrulation. *Handb Exp Pharmacol* 21–51 (2006).
108. Xinaris, C., Brizi, V. & Remuzzi, G. Organoid Models and Applications in Biomedical Research. *Nephron* **130**, 191–199 (2015).
109. Hynds, R. E. & Giangreco, A. Concise Review: The Relevance of Human Stem Cell-Derived Organoid Models for Epithelial Translational Medicine. *Stem Cells* **31**, 417–422 (2013).
110. Lancaster, M. A. & Knoblich, J. A. Generation of cerebral organoids from human pluripotent stem cells. *Nat Protoc* **9**, 2329–2340 (2014).
111. Drost, J. *et al.* Sequential cancer mutations in cultured human intestinal stem cells. *Nature* **521**, 43-U329 (2015).
112. Matano, M. *et al.* Modeling colorectal cancer using CRISPR-Cas9-mediated engineering of human intestinal organoids. *Nat Med* **21**, 256-+ (2015).
113. Li, X. N. *et al.* Oncogenic transformation of diverse gastrointestinal tissues in primary organoid culture. *Nat Med* **20**, 769–777 (2014).
114. Velasco, S. *et al.* Individual brain organoids reproducibly form cell diversity of the human cerebral cortex. *Nature* **570**, 523-+ (2019).
115. Dekkers, J. F. *et al.* A functional CFTR assay using primary cystic fibrosis intestinal organoids. *Nat Med* **19**, 939-+ (2013).
116. Huch, M. *et al.* Unlimited in vitro expansion of adult bi-potent pancreas progenitors through the Lgr5/R-spondin axis. *EMBO JOURNAL* **32**, 2708–2721 (2013).
117. Huch, M. *et al.* Long-Term Culture of Genome-Stable Bipotent Stem Cells from Adult Human Liver. *Cell* **160**, 299–312 (2015).
118. Fordham, R. P. *et al.* Transplantation of Expanded Fetal Intestinal Progenitors Contributes to Colon Regeneration after Injury. *Cell Stem Cell* **13**, 734–744 (2013).
119. Yui, S. R. *et al.* Functional engraftment of colon epithelium expanded in vitro from a single adult Lgr5(+) stem cell. *Nat Med* **18**, 618–623 (2012).
120. Fukuda, M. *et al.* Small intestinal stem cell identity is maintained with functional Paneth cells in heterotopically grafted epithelium onto the colon. *Genes Dev* **28**, 1752–1757 (2014).
121. Heins, N. *et al.* Derivation, Characterization, and Differentiation of Human Embryonic Stem Cells. *Stem Cells* **22**, 367–376 (2004).
122. Bartfeld, S. & Clevers, H. Stem cell-derived organoids and their application for medical research and patient treatment. *J Mol Med* **95**, 729–738 (2017).

123. Barker, N. *et al.* Lgr5(+ve) Stem Cells Drive Self-Renewal in the Stomach and Build Long-Lived Gastric Units In Vitro. *Cell Stem Cell* **6**, 25–36 (2010).
124. Stange, D. E. *et al.* Differentiated Troy(+) Chief Cells Act as Reserve Stem Cells to Generate All Lineages of the Stomach Epithelium. *Cell* **155**, 357–368 (2013).
125. Bartfeld, S. *et al.* In Vitro Expansion of Human Gastric Epithelial Stem Cells and Their Responses to Bacterial Infection. *Gastroenterology* **148**, 126-U554 (2015).
126. Boj, S. F. *et al.* Organoid Models of Human and Mouse Ductal Pancreatic Cancer. *Cell* **160**, 324–338 (2015).
127. Greggio, C. *et al.* Artificial three-dimensional niches deconstruct pancreas development in vitro. *DEVELOPMENT* **140**, 4452–4462 (2013).
128. Karthaus, W. R. *et al.* Identification of Multipotent Luminal Progenitor Cells in Human Prostate Organoid Cultures. *Cell* **159**, 163–175 (2014).
129. Chua, C. W. *et al.* Single luminal epithelial progenitors can generate prostate organoids in culture. *Nat Cell Biol* **16**, 951–961 (2014).
130. Sato, T. *et al.* Long-term Expansion of Epithelial Organoids From Human Colon, Adenoma, Adenocarcinoma, and Barrett's Epithelium. *Gastroenterology* **141**, 1762–1772 (2011).
131. DeWard, A. D., Cramer, J. & Lagasse, E. Cellular Heterogeneity in the Mouse Esophagus Implicates the Presence of a Nonquiescent Epithelial Stem Cell Population. *Cell Rep* **9**, 701–711 (2014).
132. Scanu, T. *et al.* Salmonella Manipulation of Host Signaling Pathways Provokes Cellular Transformation Associated with Gallbladder Carcinoma. *Cell Host Microbe* **17**, 763–774 (2015).
133. Lugli, N. *et al.* R-spondin 1 and noggin facilitate expansion of resident stem cells from non-damaged gallbladders. *EMBO Rep* **17**, 769–779 (2016).
134. Ren, W. W. *et al.* Single Lgr5- or Lgr6-expressing taste stem/progenitor cells generate taste bud cells ex vivo. *Proc Natl Acad Sci U S A* **111**, 16401–16406 (2014).
135. Spence, J. R. *et al.* Directed differentiation of human pluripotent stem cells into intestinal tissue in vitro. *Nature* **470**, 105-U120 (2011).
136. Wong, A. P. *et al.* Directed differentiation of human pluripotent stem cells into mature airway epithelia expressing functional CFTR protein. *Nat Biotechnol* **30**, 876-U108 (2012).
137. Dye, B. R. *et al.* In vitro generation of human pluripotent stem cell derived lung organoids. *Elife* **4**, (2015).
138. Huang, S. X. L. *et al.* Efficient generation of lung and airway epithelial cells from human pluripotent stem cells. *Nat Biotechnol* **32**, 84-+ (2014).
139. Takebe, T. *et al.* Vascularized and functional human liver from an iPSC-derived organ bud transplant. *Nature* **499**, 481-+ (2013).
140. Kurmann, A. A. *et al.* Regeneration of Thyroid Function by Transplantation of Differentiated Pluripotent Stem Cells. *Cell Stem Cell* **17**, 527–542 (2015).

141. Longmire, T. A. *et al.* Efficient Derivation of Purified Lung and Thyroid Progenitors from Embryonic Stem Cells. *Cell Stem Cell* **10**, 398–411 (2012).
142. McCracken, K. W. *et al.* Modelling human development and disease in pluripotent stem-cell-derived gastric organoids. *Nature* **516**, 400-+ (2014).
143. Noguchi, T. K. *et al.* Generation of stomach tissue from mouse embryonic stem cells. *Nat Cell Biol* **17**, 984-U62 (2015).
144. Huang, L. *et al.* Ductal pancreatic cancer modeling and drug screening using human pluripotent stem cell- and patient-derived tumor organoids. *Nat Med* **21**, 1364–1371 (2015).
145. Ogawa, M. *et al.* Directed differentiation of cholangiocytes from human pluripotent stem cells. *Nat Biotechnol* **33**, 853-+ (2015).
146. Eiraku, M. *et al.* Self-Organized Formation of Polarized Cortical Tissues from ESCs and Its Active Manipulation by Extrinsic Signals. *Cell Stem Cell* **3**, 519–532 (2008).
147. Nakano, T. *et al.* Self-Formation of Optic Cups and Storable Stratified Neural Retina from Human ESCs. *Cell Stem Cell* **10**, 771–785 (2012).
148. Muguruma, K., Nishiyama, A., Kawakami, H., Hashimoto, K. & Sasai, Y. Self-Organization of Polarized Cerebellar Tissue in 3D Culture of Human Pluripotent Stem Cells. *Cell Rep* **10**, 537–550 (2015).
149. Sakaguchi, H. *et al.* Generation of functional hippocampal neurons from self-organizing human embryonic stem cell-derived dorsomedial telencephalic tissue. *Nat Commun* **6**, (2015).
150. Suga, H. *et al.* Self-formation of functional adenohypophysis in three-dimensional culture. *Nature* **480**, 57-U215 (2011).
151. Camp, J. G. *et al.* Human cerebral organoids recapitulate gene expression programs of fetal neocortex development. *Proc Natl Acad Sci U S A* **112**, 15672–15677 (2015).
152. Su, H. L. *et al.* Generation of cerebellar neuron precursors from embryonic stem cells. *Dev Biol* **290**, 287–296 (2006).
153. Muguruma, K. *et al.* Ontogeny-recapitulating generation and tissue integration of ES cell-derived Purkinje cells. *Nat Neurosci* **13**, 1171–1180 (2010).
154. Danjo, T. *et al.* Subregional Specification of Embryonic Stem Cell-Derived Ventral Telencephalic Tissues by Timed and Combinatory Treatment with Extrinsic Signals. *JOURNAL OF NEUROSCIENCE* **31**, 1919–1933 (2011).
155. Takahashi, K. *et al.* Induction of pluripotent stem cells from adult human fibroblasts by defined factors. *Cell* **131**, 861–872 (2007).
156. Takahashi, K. & Yamanaka, S. Induction of pluripotent stem cells from mouse embryonic and adult fibroblast cultures by defined factors. *Cell* **126**, 663–676 (2006).
157. Yu, J. Y. *et al.* Induced pluripotent stem cell lines derived from human somatic cells. *Science (1979)* **318**, 1917–1920 (2007).
158. Brady, M. V. & Vaccarino, F. M. Role of SHH in Patterning Human Pluripotent Cells towards Ventral Forebrain Fates. *Cells 2021, Vol. 10, Page 914* **10**, 914 (2021).
159. Pasca, S. P., Panagiotakos, G. & Dolmetsch, R. E. Generating Human Neurons In Vitro and Using Them to Understand Neuropsychiatric Disease. in

ANNUAL REVIEW OF NEUROSCIENCE, VOL 37 (ed. Hyman, S. E.) vol. 37 479-+ (2014).
160. Dolmetsch, R. & Geschwind, D. H. The Human Brain in a Dish: The Promise of iPSC-Derived Neurons. *Cell* **145**, 831–834 (2011).
161. Sloan, S. A., Andersen, J., Paşca, A. M., Birey, F. & Paşca, S. P. Generation and assembly of human brain region–specific three-dimensional cultures. *Nature Protocols 2018 13:9* **13**, 2062–2085 (2018).
162. Purves, D. L. J. W. *Principles of neural development*. *(No Title)* (1985).
163. Petros, T. J., Tyson, J. A. & Anderson, S. A. Pluripotent stem cells for the study of CNS development. *Front Mol Neurosci* **4**, (2011).
164. Nasu, M. *et al.* Robust Formation and Maintenance of Continuous Stratified Cortical Neuroepithelium by Laminin-Containing Matrix in Mouse ES Cell Culture. *PLoS One* **7**, (2012).
165. Takahashi, K., Okita, K., Nakagawa, M. & Yamanaka, S. Induction of pluripotent stem cells from fibroblast cultures. *Nat Protoc* **2**, 3081–3089 (2007).
166. Yu, J. Y. *et al.* Induced pluripotent stem cell lines derived from human somatic cells. *Science (1979)* **318**, 1917–1920 (2007).
167. Sasai, Y. Next-Generation Regenerative Medicine: Organogenesis from Stem Cells in 3D Culture. *Cell Stem Cell* **12**, 520–530 (2013).
168. Li, Y. *et al.* Induction of Expansion and Folding in Human Cerebral Organoids. *Cell Stem Cell* **20**, 385-396.e3 (2017).
169. Jo, J. *et al.* Midbrain-like Organoids from Human Pluripotent Stem Cells Contain Functional Dopaminergic and Neuromelanin-Producing Neurons. *Cell Stem Cell* **19**, 248–257 (2016).
170. Pasca, A. M. *et al.* Functional cortical neurons and astrocytes from human pluripotent stem cells in 3D culture. *Nat Methods* **12**, 671-+ (2015).
171. Lancaster, M. A. *et al.* Guided self-organization and cortical plate formation in human brain organoids. *Nat Biotechnol* **35**, 659-+ (2017).
172. Shi, Y., Kirwan, P., Smith, J., Robinson, H. P. C. & Livesey, F. J. Human cerebral cortex development from pluripotent stem cells to functional excitatory synapses. *Nature Neuroscience 2012 15:3* **15**, 477–486 (2012).
173. Gaspard, N. *et al.* An intrinsic mechanism of corticogenesis from embryonic stem cells. *Nature* **455**, 351-U10 (2008).
174. Elkabetz, Y. *et al.* Human ES cell-derived neural rosettes reveal a functionally distinct early neural stem cell stage. *Genes Dev* **22**, 152–165 (2008).
175. Zhang, S. C., Wernig, M., Duncan, I. D., Brustle, O. & Thomson, J. A. In vitro differentiation of transplantable neural precursors from human embryonic stem cells. *Nat Biotechnol* **19**, 1129–1133 (2001).
176. Kadoshima, T. *et al.* Self-organization of axial polarity, inside-out layer pattern, and species-specific progenitor dynamics in human ES cell-derived neocortex. *Proc Natl Acad Sci U S A* **110**, 20284–20289 (2013).
177. Mariani, J. *et al.* Modeling human cortical development in vitro using induced pluripotent stem cells. *Proc Natl Acad Sci U S A* **109**, 12770–12775 (2012).
178. STEINBERG, M. S. On the mechanism of tissue reconstruction by dissociated cells. I. Population kinetics, differential adhesiveness. and the

absence of directed migration. *Proc Natl Acad Sci U S A* **48**, 1577–1582 (1962).
179. STEINBERG, M. S. Reconstruction of tissues by dissociated cells. Some morphogenetic tissue movements and the sorting out of embryonic cells may have a common explanation. *Science* **141**, 401–408 (1963).
180. FUJIMORI, T., MIYATANI, S. & TAKEICHI, M. ECTOPIC EXPRESSION OF N-CADHERIN PERTURBS HISTOGENESIS IN XENOPUS EMBRYOS. *DEVELOPMENT* **110**, 97- (1990).
181. DETRICK, R. J., DICKEY, D. & KINTNER, C. R. THE EFFECTS OF N-CADHERIN MISEXPRESSION ON MORPHOGENESIS IN XENOPUS EMBRYOS. *Neuron* **4**, 493–506 (1990).
182. Alberts Bruce. *Molecular Biology of the Cell*. (2002).
183. Abe, K. & Takeichi, M. EPLIN mediates linkage of the cadherin-catenin complex to F-actin and stabilizes the circumferential actin belt. *Proc Natl Acad Sci U S A* **105**, 13–19 (2008).
184. Taguchi, K., Ishiuchi, T. & Takeichi, M. Mechanosensitive EPLIN-dependent remodeling of adherens junctions regulates epithelial reshaping. *JOURNAL OF CELL BIOLOGY* **194**, 643–656 (2011).
185. Chervin-Petinot, A. *et al.* Epithelial Protein Lost In Neoplasm (EPLIN) Interacts with alpha-Catenin and Actin Filaments in Endothelial Cells and Stabilizes Vascular Capillary Network in Vitro. *JOURNAL OF BIOLOGICAL CHEMISTRY* **287**, 7556–7572 (2012).
186. Rangarajan, E. S. & Izard, T. The Cytoskeletal Protein alpha-Catenin Unfurls upon Binding to Vinculin. *JOURNAL OF BIOLOGICAL CHEMISTRY* **287**, 18492–18499 (2012).
187. Peng, X., Maiers, J. L., Choudhury, D., Craig, S. W. & Demali, K. A. alpha-Catenin Uses a Novel Mechanism to Activate Vinculin. *JOURNAL OF BIOLOGICAL CHEMISTRY* **287**, 7728–7737 (2012).
188. Choi, H. J. *et al.* alpha E-catenin is an autoinhibited molecule that coactivates vinculin. *Proc Natl Acad Sci U S A* **109**, 8576–8581 (2012).
189. Halbleib, J. M. & Nelson, W. J. Cadherins in development: cell adhesion, sorting, and tissue morphogenesis. *Genes Dev* **20**, 3199–3214 (2006).
190. Borghi, N. *et al.* E-cadherin is under constitutive actomyosin-generated tension that is increased at cell-cell contacts upon externally applied stretch. *Proc Natl Acad Sci U S A* **109**, 12568–12573 (2012).
191. Yonemura, S., Wada, Y., Watanabe, T., Nagafuchi, A. & Shibata, M. alpha-Catenin as a tension transducer that induces adherens junction development. *Nat Cell Biol* **12**, 533-U35 (2010).
192. Sackmann, E. How actin/myosin crosstalks guide the adhesion, locomotion and polarization of cells. *BIOCHIMICA ET BIOPHYSICA ACTA-MOLECULAR CELL RESEARCH* **1853**, 3132–3142 (2015).
193. Vicente-Manzanares, M., Ma, X. F., Adelstein, R. S. & Horwitz, A. R. Non-muscle myosin II takes centre stage in cell adhesion and migration. *Nat Rev Mol Cell Biol* **10**, 778–790 (2009).
194. Kasza, K. E. & Zallen, J. A. Dynamics and regulation of contractile actin-myosin networks in morphogenesis. *Curr Opin Cell Biol* **23**, 30–38 (2011).

195. Connelly, J. T. *et al.* Actin and serum response factor transduce physical cues from the microenvironment to regulate epidermal stem cell fate decisions. *Nature Cell Biology 2010 12:7* **12**, 711–718 (2010).
196. Bao, M., Xie, J., Piruska, A. & Huck, W. T. S. 3D microniches reveal the importance of cell size and shape. *Nat Commun* **8**, (2017).
197. Panciera, T., Azzolin, L., Cordenonsi, M. & Piccolo, S. Mechanobiology of YAP and TAZ in physiology and disease. *Nat Rev Mol Cell Biol* **18**, 758–770 (2017).
198. Martino, F., Perestrelo, A. R., Vinarsky, V., Pagliari, S. & Forte, G. Cellular Mechanotransduction: From Tension to Function. *Front Physiol* **9**, (2018).
199. Harris, A. R., Jreij, P. & Fletcher, D. A. Mechanotransduction by the Actin Cytoskeleton: Converting Mechanical Stimuli into Biochemical Signals. in *ANNUAL REVIEW OF BIOPHYSICS, VOL 47* (ed. Dill, K. A.) vol. 47 617–631 (2018).
200. Piccolo, F. M. *et al.* Role of YAP in early ectodermal specification and a Huntington's Disease model of human neurulation. *Elife* **11**, (2022).
201. Indana, D., Agarwal, P., Bhutani, N. & Chaudhuri, O. Viscoelasticity and Adhesion Signaling in Biomaterials Control Human Pluripotent Stem Cell Morphogenesis in 3D Culture. *ADVANCED MATERIALS* **33**, (2021).
202. Buskermolen, A. B. C. *et al.* Entropic Forces Drive Cellular Contact Guidance. *Biophys J* **116**, 1994–2008 (2019).
203. Bruyere, C. *et al.* Actomyosin contractility scales with myoblast elongation and enhances differentiation through YAP nuclear export. *Sci Rep* **9**, (2019).
204. Totaro, A. *et al.* YAP/TAZ link cell mechanics to Notch signalling to control epidermal stem cell fate. *Nat Commun* **8**, (2017).
205. Wang, X. L. *et al.* Discriminating the Independent Influence of Cell Adhesion and Spreading Area on Stem Cell Fate Determination Using Micropatterned Surfaces. *Sci Rep* **6**, (2016).
206. Giraldez, S. *et al.* YAP1 Regulates the Self-organized Fate Patterning of hESCs-Derived Gastruloids. *bioRxiv* 2021.03.12.434631 (2021) doi:10.1101/2021.03.12.434631.
207. Fattah, A. R. A. *et al.* Actuation enhances patterning in human neural tube organoids. *Nat Commun* **12**, (2021).
208. Nikolaev, M. *et al.* Homeostatic mini-intestines through scaffold-guided organoid morphogenesis. *Nature* **585**, 574-+ (2020).
209. Karzbrun, E. *et al.* Human neural tube morphogenesis in vitro by geometric constraints. *Nature* **599**, 268–272 (2021).
210. Gjorevski, N. *et al.* Tissue geometry drives deterministic organoid patterning. *Science (1979)* **375**, 40-+ (2022).
211. ORKIN, R. W. *et al.* MURINE TUMOR PRODUCING A MATRIX OF BASEMENT-MEMBRANE. *JOURNAL OF EXPERIMENTAL MEDICINE* **145**, 204–220 (1977).
212. LI, M. L. *et al.* INFLUENCE OF A RECONSTITUTED BASEMENT-MEMBRANE AND ITS COMPONENTS ON CASEIN GENE-EXPRESSION AND SECRETION IN MOUSE MAMMARY EPITHELIAL-CELLS. *Proc Natl Acad Sci U S A* **84**, 136–140 (1987).

213. Hauser, H., Timmins, N. E. & Nielsen, L. K. Generation of multicellular tumor spheroids by the hanging-drop method. in *Tissue Engineering* vol. 140 141–151 (2007).
214. Sato, T. & Clevers, H. Growing Self-Organizing Mini-Guts from a Single Intestinal Stem Cell: Mechanism and Applications. *Science (1979)* **340**, 1190–1194 (2013).
215. Sasai, Y., Eiraku, M. & Suga, H. In vitro organogenesis in three dimensions: self-organising stem cells. *DEVELOPMENT* **139**, 4111–4121 (2012).
216. Martin, I., Wendt, D. & Heberer, M. The role of bioreactors in tissue engineering. *Trends Biotechnol* **22**, 80–86 (2004).
217. Mammoto, T. & Ingber, D. E. Mechanical control of tissue and organ development. *DEVELOPMENT* **137**, 1407–1420 (2010).
218. Wozniak, M. A. & Chen, C. S. Mechanotransduction in development: a growing role for contractility. *Nat Rev Mol Cell Biol* **10**, 34–43 (2009).
219. Blanchard, G. B. *et al.* Tissue tectonics: morphogenetic strain rates, cell shape change and intercalation. *Nat Methods* **6**, 458-U86 (2009).
220. Butler, L. C. *et al.* Cell shape changes indicate a role for extrinsic tensile forces in Drosophila germ-band extension. *Nat Cell Biol* **11**, 859-U181 (2009).
221. Beloussov, L. V. Mechanically based generative laws of morphogenesis. *Phys Biol* **5**, (2008).
222. Lecuit, T. & Lenne, P. F. Cell surface mechanics and the control of cell shape, tissue patterns and morphogenesis. *Nat Rev Mol Cell Biol* **8**, 633–644 (2007).
223. Ingber, D. E. Mechanical control of tissue growth: Function follows form. *Proc Natl Acad Sci U S A* **102**, 11571–11572 (2005).
224. Shraiman, B. I. Mechanical feedback as a possible regulator of tissue growth. *Proc Natl Acad Sci U S A* **102**, 3318–3323 (2005).
225. Farge, E. Mechanical induction of twist in the Drosophila foregut/stomodeal primordium. *CURRENT BIOLOGY* **13**, 1365–1377 (2003).
226. Desprat, N., Supatto, W., Pouille, P. A., Beaurepaire, E. & Farge, E. Tissue deformation modulates twist expression to determine anterior midgut differentiation in Drosophila embryos. *Dev Cell* **15**, 470–477 (2008).
227. Trepat, X. *et al.* Physical forces during collective cell migration. *Nat Phys* **5**, 426–430 (2009).
228. Tambe, D. T. *et al.* Collective cell guidance by cooperative intercellular forces. *Nat Mater* **10**, 469–475 (2011).
229. Parker, K. K. *et al.* Directional control of lamellipodia extension by constraining cell shape and orienting cell tractional forces. *FASEB JOURNAL* **16**, (2002).
230. Nestor-Bergmann, A., Goddard, G. & Woolner, S. Force and the spindle: Mechanical cues in mitotic spindle orientation. *Semin Cell Dev Biol* **34**, 133–139 (2014).
231. Fink, J. *et al.* External forces control mitotic spindle positioning. *Nat Cell Biol* **13**, 771-U401 (2011).
232. Thery, M., Jimenez-Dalmaroni, A., Racine, V., Bornens, M. & Julicher, F. Experimental and theoretical study of mitotic spindle orientation. *Nature* **447**, 493-U6 (2007).

233. Watt, F. M. & Huck, W. T. S. Role of the extracellular matrix in regulating stem cell fate. *Nat Rev Mol Cell Biol* **14**, 467–473 (2013).
234. Guilak, F. *et al.* Control of Stem Cell Fate by Physical Interactions with the Extracellular Matrix. *Cell Stem Cell* **5**, 17–26 (2009).
235. Discher, D. E., Mooney, D. J. & Zandstra, P. W. Growth Factors, Matrices, and Forces Combine and Control Stem Cells. *Science (1979)* **324**, 1673–1677 (2009).
236. Engler, A. J., Sen, S., Sweeney, H. L. & Discher, D. E. Matrix elasticity directs stem cell lineage specification. *Cell* **126**, 677–689 (2006).
237. McBeath, R., Pirone, D. M., Nelson, C. M., Bhadriraju, K. & Chen, C. S. Cell shape, cytoskeletal tension, and RhoA regulate stem cell lineage commitment. *Dev Cell* **6**, 483–495 (2004).
238. Puliafito, A. *et al.* Collective and single cell behavior in epithelial contact inhibition. *Proc Natl Acad Sci U S A* **109**, 739–744 (2012).
239. Montel, F. *et al.* Stress Clamp Experiments on Multicellular Tumor Spheroids. *Phys Rev Lett* **107**, (2011).
240. Chen, C. S., Mrksich, M., Huang, S., Whitesides, G. M. & Ingber, D. E. Geometric control of cell life and death. *Science (1979)* **276**, 1425–1428 (1997).
241. SINGHVI, R. *et al.* ENGINEERING CELL-SHAPE AND FUNCTION. *Science (1979)* **264**, 696–698 (1994).
242. Nishimura, T., Honda, H. & Takeichi, M. Planar Cell Polarity Links Axes of Spatial Dynamics in Neural-Tube Closure. *Cell* **149**, 1084–1097 (2012).
243. Campas, O. *et al.* Quantifying cell-generated mechanical forces within living embryonic tissues. *Nat Methods* **11**, 183-+ (2014).
244. Rauzi, M. & Lenne, P. F. CORTICAL FORCES IN CELL SHAPE CHANGES AND TISSUE MORPHOGENESIS. in *FORCES AND TENSION IN DEVELOPMENT* (ed. Labouesse, M.) vol. 95 93–144 (2011).
245. Hutson, M. S. *et al.* Forces for morphogenesis investigated with laser microsurgery and quantitative modeling. *Science (1979)* **300**, 145–149 (2003).
246. Campas, O. A toolbox to explore the mechanics of living embryonic tissues. *Semin Cell Dev Biol* **55**, 119–130 (2016).
247. Guillot, C. & Lecuit, T. Mechanics of Epithelial Tissue Homeostasis and Morphogenesis. *Science (1979)* **340**, 1185–1189 (2013).
248. Heisenberg, C. P. & Bellaiche, Y. Forces in Tissue Morphogenesis and Patterning. *Cell* **153**, 948–962 (2013).
249. Lecuit, T., Lenne, P. F. & Munro, E. Force Generation, Transmission, and Integration during Cell and Tissue Morphogenesis. in *ANNUAL REVIEW OF CELL AND DEVELOPMENTAL BIOLOGY, VOL 27* (eds. Schekman, R., Goldstein, L. & Lehmann, R.) vol. 27 157–184 (2011).
250. Keller, R., Shook, D. & Skoglund, P. The forces that shape embryos: physical aspects of convergent extension by cell intercalation. *Phys Biol* **5**, (2008).
251. Montell, D. J. Morphogenetic Cell Movements: Diversity from Modular Mechanical Properties. *Science (1979)* **322**, 1502–1505 (2008).
252. Paluch, E. & Heisenberg, C. P. Biology and Physics of Cell Shape Changes in Development. *CURRENT BIOLOGY* **19**, R790–R799 (2009).

253. Nelson, C. M. & Gleghorn, J. P. Sculpting Organs: Mechanical Regulation of Tissue Development. in *ANNUAL REVIEW OF BIOMEDICAL ENGINEERING, VOL 14* (ed. Yarmush, M. L.) vol. 14 129–154 (2012).
254. Eyckmans, J., Boudou, T., Yu, X. & Chen, C. S. A hitchhiker's guide to mechanobiology. *Dev Cell* **21**, 35–47 (2011).
255. Bachir, A. I., Horwitz, A. R., Nelson, W. J. & Bianchini, J. M. Actin-Based Adhesion Modules Mediate Cell Interactions with the Extracellular Matrix and Neighboring Cells. *Cold Spring Harb Perspect Biol* **9**, (2017).
256. Harunaga, J. S., Doyle, A. D. & Yamada, K. M. Local and global dynamics of the basement membrane during branching morphogenesis require protease activity and actomyosin contractility. *Dev Biol* **394**, 197–205 (2014).
257. Pastor-Pareja, J. C. & Xu, T. Shaping Cells and Organs in Drosophila by Opposing Roles of Fat Body-Secreted Collagen IV and Perlecan. *Dev Cell* **21**, 245–256 (2011).
258. Haigo, S. L. & Bilder, D. Global Tissue Revolutions in a Morphogenetic Movement Controlling Elongation. *Science (1979)* **331**, 1071–1074 (2011).
259. Zaman, M. H. *et al.* Migration of tumor cells in 3D matrices is governed by matrix stiffness along with cell-matrix adhesion and proteolysis. *Proc Natl Acad Sci U S A* **103**, 10889–10894 (2006).
260. Paszek, M. J. *et al.* Tensional homeostasis and the malignant phenotype. *Cancer Cell* **8**, 241–254 (2005).
261. Ingber, D. E. Mechanical control of tissue morphogenesis during embryological development. *INTERNATIONAL JOURNAL OF DEVELOPMENTAL BIOLOGY* **50**, 255–266 (2006).
262. Martin, A. C., Gelbart, M., Fernandez-Gonzalez, R., Kaschube, M. & Wieschaus, E. F. Integration of contractile forces during tissue invagination. *JOURNAL OF CELL BIOLOGY* **188**, 735–749 (2010).
263. Guirao, B. *et al.* Unified quantitative characterization of epithelial tissue development. *Elife* **4**, (2015).
264. Etournay, R. *et al.* Interplay of cell dynamics and epithelial tension during morphogenesis of the Drosophila pupal wing. *Elife* **4**, (2015).
265. Bonnet, I. *et al.* Mechanical state, material properties and continuous description of an epithelial tissue. *J R Soc Interface* **9**, 2614–2623 (2012).
266. Heemskerk, I. & Streichan, S. J. Tissue cartography: compressing bio-image data by dimensional reduction. *Nat Methods* **12**, 1139-+ (2015).
267. Guevorkian, K., Colbert, M. J., Durth, M., Dufour, S. & Brochard-Wyart, F. Aspiration of Biological Viscoelastic Drops. *Phys Rev Lett* **104**, (2010).
268. Marmottant, P. *et al.* The role of fluctuations and stress on the effective viscosity of cell aggregates. *Proc Natl Acad Sci U S A* **106**, 17271–17275 (2009).
269. Schotz, E. M. *et al.* Quantitative differences in tissue surface tension influence zebrafish germ layer positioning. *HFSP J* **2**, 42–56 (2008).
270. Forgacs, G., Foty, R. A., Shafrir, Y. & Steinberg, M. S. Viscoelastic properties of living embryonic tissues: a quantitative study. *Biophys J* **74**, 2227–2234 (1998).
271. FOTY, R. A., FORGACS, G., PFLEGER, C. M. & STEINBERG, M. S. LIQUID PROPERTIES OF EMBRYONIC-TISSUES - MEASUREMENT OF INTERFACIAL-TENSIONS. *Phys Rev Lett* **72**, 2298–2301 (1994).

272. Johansen, P. L., Fenaroli, F., Evensen, L., Griffiths, G. & Koster, G. Optical micromanipulation of nanoparticles and cells inside living zebrafish. *Nat Commun* **7**, (2016).
273. Almonacid, M. *et al.* Active diffusion positions the nucleus in mouse oocytes. *Nat Cell Biol* **17**, 470-+ (2015).
274. Lim, C. T., Zhou, E. H. & Quek, S. T. Mechanical models for living cells - A review. *J Biomech* **39**, 195–216 (2006).
275. Bausch, A. R., Moller, W. & Sackmann, E. Measurement of local viscoelasticity and forces in living cells by magnetic tweezers. *Biophys J* **76**, 573–579 (1999).
276. Bambardekar, K., Clement, R., Blanc, O., Chardes, C. & Lenne, P. F. Direct laser manipulation reveals the mechanics of cell contacts in vivo. *Proc Natl Acad Sci U S A* **112**, 1416–1421 (2015).
277. Wottawah, F. *et al.* Optical rheology of biological cells. *Phys Rev Lett* **94**, (2005).
278. Khalilgharibi, N., Fouchard, J., Recho, P., Charras, G. & Kabla, A. The dynamic mechanical properties of cellularised aggregates. *Curr Opin Cell Biol* **42**, 113–120 (2016).
279. Puech, P. H. *et al.* Measuring cell adhesion forces of primary gastrulating cells from zebrafish using atomic force microscopy. *J Cell Sci* **118**, 4199–4206 (2005).
280. Krieg, M. *et al.* Tensile forces govern germ-layer organization in zebrafish. *Nat Cell Biol* **10**, 429-U122 (2008).
281. Maitre, J. L. & Heisenberg, C. P. The role of adhesion energy in controlling cell-cell contacts. *Curr Opin Cell Biol* **23**, 508–514 (2011).
282. Guevorkian, K., Gonzalez-Rodriguez, D., Carlier, C., Dufour, S. & Brochard-Wyart, F. Mechanosensitive shivering of model tissues under controlled aspiration. *Proc Natl Acad Sci U S A* **108**, 13387–13392 (2011).
283. WANG, N., BUTLER, J. P. & INGBER, D. E. MECHANOTRANSDUCTION ACROSS THE CELL-SURFACE AND THROUGH THE CYTOSKELETON. *Science (1979)* **260**, 1124–1127 (1993).
284. Stabley, D. R., Jurchenko, C., Marshall, S. S. & Salaita, K. S. Visualizing mechanical tension across membrane receptors with a fluorescent sensor. *Nat Methods* **9**, 64-U172 (2012).
285. Grashoff, C. *et al.* Measuring mechanical tension across vinculin reveals regulation of focal adhesion dynamics. *Nature* **466**, 263-U143 (2010).
286. Tan, J. L. *et al.* Cells lying on a bed of microneedles: An approach to isolate mechanical force. *Proc Natl Acad Sci U S A* **100**, 1484–1489 (2003).
287. du Roure, O. *et al.* Force mapping in epithelial cell migration. *Proc Natl Acad Sci U S A* **102**, 2390–2395 (2005).
288. Legant, W. R. *et al.* Measurement of mechanical tractions exerted by cells in three-dimensional matrices. *Nat Methods* **7**, 969-U113 (2010).
289. Gjorevski, N. & Nelson, C. M. Mapping of Mechanical Strains and Stresses around Quiescent Engineered Three-Dimensional Epithelial Tissues. *Biophys J* **103**, 152–162 (2012).
290. HARRIS, A. K., WILD, P. & STOPAK, D. SILICONE-RUBBER SUBSTRATA - NEW WRINKLE IN THE STUDY OF CELL LOCOMOTION. *Science (1979)* **208**, 177–179 (1980).

291. Dembo, M. & Wang, Y. L. Stresses at the cell-to-substrate interface during locomotion of fibroblasts. *Biophys J* **76**, 2307–2316 (1999).
292. Sugimura, K., Lenne, P. F. & Graner, F. Measuring forces and stresses in situ in living tissues. *DEVELOPMENT* **143**, 186–196 (2016).
293. DAVIS, G. S. MIGRATION-DIRECTING LIQUID PROPERTIES OF EMBRYONIC AMPHIBIAN TISSUES. *Am Zool* **24**, 649–655 (1984).
294. Davidson, L. & Keller, R. Measuring mechanical properties of embryos and embryonic tissues. in *CELL MECHANICS* (eds. Wang, Y. L. & Discher, D. E.) vol. 83 425–439 (2007).
295. EVANS, E. & YEUNG, A. APPARENT VISCOSITY AND CORTICAL TENSION OF BLOOD GRANULOCYTES DETERMINED BY MICROPIPET ASPIRATION. *Biophys J* **56**, 151–160 (1989).
296. Tinevez, J. Y. *et al.* Role of cortical tension in bleb growth. *Proc Natl Acad Sci U S A* **106**, 18581–18586 (2009).
297. Rauzi, M., Verant, P., Lecuit, T. & Lenne, P. F. Nature and anisotropy of cortical forces orienting Drosophila tissue morphogenesis. *Nat Cell Biol* **10**, 1401-U57 (2008).
298. Behrndt, M. *et al.* Forces Driving Epithelial Spreading in Zebrafish Gastrulation. *Science (1979)* **338**, 257–260 (2012).
299. Lucio, A. A., Ingber, D. E. & Campas, O. Generation of biocompatible droplets for in vivo and in vitro measurement of cell-generated mechanical stresses. in *BIOPHYSICAL METHODS IN CELL BIOLOGY* (ed. Paluch, E. K.) vol. 125 373–390 (2015).
300. Widom, B. Capillarity and Wetting Phenomena: Drops, Bubbles, Pearls, Waves. *Phys Today* **57**, 66–67 (2004).
301. Serwane, F. *et al.* In vivo quantification of spatially varying mechanical properties in developing tissues. *Nature Methods 2016 14:2* **14**, 181–186 (2016).
302. Seta, L., Baldino, N., Gabriele, D., Lupi, F. R. & Cindio, B. de. Rheology and adsorption behaviour of β-casein and β-lactoglobulin mixed layers at the sunflower oil/water interface. *Colloids Surf A Physicochem Eng Asp* **441**, 669–677 (2014).
303. Schestkowa, H., Drusch, S. & Wagemans, A. M. FTIR analysis of β-lactoglobulin at the oil/water-interface. *Food Chem* **302**, 125349 (2020).
304. Jakoby, M., Wang, H.-Y., Reidt, W., Weisshaar, B. & Bauer, P. *FRU* (*BHLH029*) is required for induction of iron mobilization genes in *Arabidopsis thaliana*. *FEBS Lett* **577**, 528–534 (2004).
305. Lu, J. R., Su, T. J. & Thomas, R. K. Structural conformation of bovine serum albumin layers at the air-water interface studied by neutron reflection. *J Colloid Interface Sci* **213**, 426–437 (1999).
306. Maldonado-Valderrama, J. & Patino, J. M. R. Interfacial rheology of protein-surfactant mixtures. *Current Opinion in Colloid and Interface Science* vol. 15 271–282 Preprint at https://doi.org/10.1016/j.cocis.2009.12.004 (2010).
307. MURRAY, B. S. & DICKINSON, E. Interfacial Rheology and the Dynamic Properties of Adsorbed Films of Food Proteins and Surfactants. *Food Science and Technology International, Tokyo* **2**, 131–145 (1996).
308. Bos, M. A. & Van Vliet, T. Interfacial rheological properties of adsorbed protein layers and surfactants: A review. *Advances in Colloid and*

Interface Science vol. 91 437–471 Preprint at https://doi.org/10.1016/S0001-8686(00)00077-4 (2001).
309. Antony M, S., Jaganathan, M. & Dhathathreyan, A. Relevance of interfacial viscoelasticity in stability and conformation of biomolecular organizates at air/fluid interface. *Advances in Colloid and Interface Science* vol. 234 80–88 Preprint at https://doi.org/10.1016/j.cis.2016.04.002 (2016).
310. Wilde, P., Mackie, A., Husband, F., Gunning, P. & Morris, V. Proteins and emulsifiers at liquid interfaces. *Adv Colloid Interface Sci* **108–109**, 63–71 (2004).
311. Rodríguez Patino, J. M., Carrera Sánchez, C. & Rodríguez Niño, M. R. Implications of interfacial characteristics of food foaming agents in foam formulations. *Advances in Colloid and Interface Science* vol. 140 95–113 Preprint at https://doi.org/10.1016/j.cis.2007.12.007 (2008).
312. Aksenenko, E. V., Kovalchuk, V. I., Fainerman, V. B. & Miller, R. Surface dilational rheology of mixed adsorption layers at liquid interfaces. *Advances in Colloid and Interface Science* vol. 122 57–66 Preprint at https://doi.org/10.1016/j.cis.2006.06.012 (2006).
313. Kotsmar, C. *et al.* Equilibrium and dynamics of adsorption of mixed β-casein/surfactant solutions at the water/hexane interface. *Colloids Surf A Physicochem Eng Asp* **354**, 210–217 (2010).
314. Kotsmar, C. *et al.* Thermodynamics, adsorption kinetics and rheology of mixed protein-surfactant interfacial layers. *Advances in Colloid and Interface Science* vol. 150 41–54 Preprint at https://doi.org/10.1016/j.cis.2009.05.002 (2009).
315. Krägel, J., Derkatch, S. R. & Miller, R. Interfacial shear rheology of protein-surfactant layers. *Advances in Colloid and Interface Science* vol. 144 38–53 Preprint at https://doi.org/10.1016/j.cis.2008.08.010 (2008).
316. Rodríguez Patino, J. M., Rodríguez Niño, M. R. & Carrera Sánchez, C. Physico-chemical properties of surfactant and protein films. *Current Opinion in Colloid and Interface Science* vol. 12 187–195 Preprint at https://doi.org/10.1016/j.cocis.2007.06.003 (2007).
317. Benjamins, J. & Lucassen-Reynders, E. H. Surface dilational rheology of proteins adsorbed at air/water and oil/water interfaces. *Studies in Interface Science* **7**, 341–384 (1998).
318. Dickinson, E. Adsorbed protein layers at fluid interfaces: Interactions, structure and surface rheology. *Colloids and Surfaces B: Biointerfaces* vol. 15 161–176 Preprint at https://doi.org/10.1016/S0927-7765(99)00042-9 (1999).
319. Douillard, R., Daoud, M. & Aguié-Béghin, V. Polymer thermodynamics of adsorbed protein layers. *Current Opinion in Colloid and Interface Science* vol. 8 380–386 Preprint at https://doi.org/10.1016/S1359-0294(03)00097-9 (2003).
320. Damodaran, S. Adsorbed layers formed from mixtures of proteins. *Current Opinion in Colloid and Interface Science* vol. 9 328–339 Preprint at https://doi.org/10.1016/j.cocis.2004.09.008 (2004).
321. KIM, S. H. & KINSELLA, J. E. Surface Activity of Food Proteins: Relationships Between Surface Pressure Development, Viscoelasticity of Interfacial Films and Foam Stability of Bovine Serum Albumin. *J Food Sci* **50**, 1526–1530 (1985).
322. Nakai, S. & Li-Chan, E. Recent Advances in Structure and Function of Food Proteins: Qsar Approach. *Crit Rev Food Sci Nutr* **33**, 477–499 (1993).

323. Corredig, M. & Dalgleish, D. G. Effect of different heat treatments on the strong binding interactions between whey proteins and milk fat globules in whole milk. *Journal of Dairy Research* **63**, 441–449 (1996).
324. Félix, M., Carrera, C., Romero, A., Bengoechea, C. & Guerrero, A. Rheological approaches as a tool for the development and stability behaviour of protein-stabilized emulsions. *Food Hydrocoll* **104**, 105719 (2020).
325. Bengoechea, C., Cordobés, F. & Guerrero, A. Rheology and microstructure of gluten and soya-based o/w emulsions. *Rheol Acta* **46**, 13–21 (2006).
326. Dickinson, E. Proteins at interfaces and in emulsions. Stability, rheology and interactions. *Journal of the Chemical Society - Faraday Transactions* **94**, 1657–1669 (1998).
327. Dickinson, E. Milk protein interfacial layers and the relationship to emulsion stability and rheology. *Colloids and Surfaces B: Biointerfaces* vol. 20 197–210 Preprint at https://doi.org/10.1016/S0927-7765(00)00204-6 (2001).
328. Benjamins, J., Cagna, A. & Lucassen-Reynders, E. H. Viscoelastic properties of triacylglycerol/water interfaces covered by proteins. in *Colloids and Surfaces A: Physicochemical and Engineering Aspects* vol. 114 245–254 (Elsevier Science B.V., 1996).
329. Chrysanthou, A., Bosch-Fortea, M. & Gautrot, J. E. Co-Surfactant-Free Bioactive Protein Nanosheets for the Stabilization of Bioemulsions Enabling Adherent Cell Expansion. *Biomacromolecules* (2023) doi:10.1021/acs.biomac.2c01289.
330. Fang, Y. & Dalgleish, D. G. Conformation of β-lactoglobulin studied by FTIR: Effect of pH, temperature, and adsorption to the oil-water interface. *J Colloid Interface Sci* **196**, 292–298 (1997).
331. Smith, L. J. & Clark, D. C. Measurement of the secondary structure of adsorbed protein by circular dichroism. 1. Measurements of the helix content of adsorbed melittin. *Biochimica et Biophysica Acta (BBA)/Protein Structure and Molecular* **1121**, 111–118 (1992).
332. Kim, J. Systematic approach to characterize the dynamics of protein adsorption on the surface of biomaterials using proteomics. *Colloids and Surfaces B: Biointerfaces* vol. 188 110756 Preprint at https://doi.org/10.1016/j.colsurfb.2019.110756 (2020).
333. Horbett, T. A. & Brash, J. L. Proteins at Interfaces: An Overview. *Proteins at Interfaces II* **602**, 1–23 (1995).
334. Norde, W. & Lyklema, J. Why proteins prefer interfaces. *J Biomater Sci Polym Ed* **2**, 183–202 (1991).
335. Sengupta, T., Razumovsky, L. & Damodaran, S. Energetics of protein-interface interactions and its effect on protein adsorption. *Langmuir* **15**, 6991–7001 (1999).
336. Waugh, D. F., Anthony, L. J. & Ng, H. The interactions of thrombin with borosilicate glass surfaces. *J Biomed Mater Res* **9**, 511–536 (1975).
337. Wilde, P. J. Emulsions and nanoemulsions using dairy ingredients. *Dairy-Derived Ingredients: Food and Nutraceutical Uses* 539–564 (2009) doi:10.1533/9781845697198.3.539.
338. Kinsella, J.E., P.F. Fox, J. J. C. Food Proteins, Applied Science, London. in *Food Proteins, Applied Science, London* 51 (1982).

339. Wierenga, P. A., Meinders, M. B. J., Egmond, M. R., Voragen, F. A. G. J. & De Jongh, H. H. J. Protein Exposed Hydrophobicity Reduces the Kinetic Barrier for Adsorption of Ovalbumin to the Air-Water Interface. *Langmuir* **19**, 8964–8970 (2003).
340. Chrysanthou, A., Kanso, H., Zhong, W., Shang, L. & Gautrot, J. E. Supercharged Protein Nanosheets for Cell Expansion on Bioemulsions. *bioRxiv 2022.06.21.497058* na (2022).
341. Slack, S. M. & Horbett, T. A. Changes in the strength of fibrinogen attachment to solid surfaces: An explanation of the influence of surface chemistry on the Vroman effect. *J Colloid Interface Sci* **133**, 148–165 (1989).
342. Lassen, B. & Malmsten, M. Competitive protein adsorption at plasma polymer surfaces. *J Colloid Interface Sci* **186**, 9–16 (1997).
343. Latour, R. A. Biomaterials: Protein–Surface Interactions. 270–284 (2008) doi:10.1081/E-EBBE2-120041856.
344. Miller, R. *et al.* Dynamics of protein and mixed protein/surfactant adsorption layers at the water/fluid interface. *Adv Colloid Interface Sci* **86**, 39–82 (2000).
345. Mojares, E., Chrysanthou, A. & Gautrot, J. E. Strong Elastic Protein Nanosheets Enable the Culture and Differentiation of Induced Pluripotent Stem Cells on Microdroplets. *bioRxiv* 2023.06.22.546128 (2023) doi:10.1101/2023.06.22.546128.
346. Bellani, C. F. *et al.* Scale-Up Technologies for the Manufacture of Adherent Cells. *Front Nutr* **7**, 575146 (2020).
347. Peng, L. & Gautrot, J. E. Long term expansion profile of mesenchymal stromal cells at protein nanosheet-stabilised bioemulsions for next generation cell culture microcarriers. (2021) doi:10.1016/j.mtbio.2021.100159.
348. Chen, A. K. L., Reuveny, S. & Oh, S. K. W. Application of human mesenchymal and pluripotent stem cell microcarrier cultures in cellular therapy: Achievements and future direction. *Biotechnol Adv* **31**, 1032–1046 (2013).
349. Badenes, S. M., Fernandes, T. G., Rodrigues, C. A. V, Diogo, M. M. & Cabral, J. M. S. Microcarrier-based platforms for in vitro expansion and differentiation of human pluripotent stem cells in bioreactor culture systems. *J Biotechnol* **234**, 71–82 (2016).
350. Peng, L. H. & Gautrot, J. E. Long term expansion profile of mesenchymal stromal cells at protein nanosheet-stabilised bioemulsions for next generation cell culture microcarriers. *Mater Today Bio* **12**, (2021).
351. Li, B. Y. *et al.* Past, present, and future of microcarrier-based tissue engineering. *J Orthop Translat* **3**, 51–57 (2015).
352. Chen, X. Y. *et al.* Recent advances in the use of microcarriers for cell cultures and their ex vivo and in vivo applications. *Biotechnol Lett* **42**, 1–10 (2020).
353. Kong, D. *et al.* Protein Nanosheet Mechanics Controls Cell Adhesion and Expansion on Low-Viscosity Liquids. *Nano Lett* **18**, 1946–1951 (2018).
354. Kong, D., Peng, L., Di Cio, S., Novak, P. & Gautrot, J. E. Stem Cell Expansion and Fate Decision on Liquid Substrates Are Regulated by Self-Assembled Nanosheets. *ACS Nano* **12**, 9206–9213 (2018).

355. Kong, D. *et al.* Impact of the multiscale viscoelasticity of quasi-2D self-assembled protein networks on stem cell expansion at liquid interfaces. *Biomaterials* **284**, 121494 (2022).
356. Leber, J. *et al.* Microcarrier choice and bead-to-bead transfer for human mesenchymal stem cells in serum-containing and chemically defined media. *PROCESS BIOCHEMISTRY* **59**, 255–265 (2017).
357. Rafiq, Q. A., Coopman, K., Nienow, A. W. & Hewitt, C. J. Systematic microcarrier screening and agitated culture conditions improves human mesenchymal stem cell yield in bioreactors. *Biotechnol J* **11**, 473–486 (2016).
358. Petry, F. *et al.* Manufacturing of Human Umbilical Cord Mesenchymal Stromal Cells on Microcarriers in a Dynamic System for Clinical Use. *Stem Cells Int* **2016**, (2016).
359. Frauenschuh, S. *et al.* A microcarrier-based cultivation system for expansion of primary mesenchymal stem cells. *Biotechnol Prog* **23**, 187–193 (2007).
360. Hanga, M. P. *et al.* Expansion of human mesenchymal stem/stromal cells on temporary liquid microcarriers. *JOURNAL OF CHEMICAL TECHNOLOGY AND BIOTECHNOLOGY* **96**, 930–940 (2021).
361. Eibes, G. *et al.* Maximizing the ex vivo expansion of human mesenchymal stem cells using a microcarrier-based stirred culture system. *J Biotechnol* **146**, 194–197 (2010).
362. Yang, H. S., Jeon, O., Bhang, S. H., Lee, S. H. & Kim, B. S. Suspension Culture of Mammalian Cells Using Thermosensitive Microcarrier That Allows Cell Detachment Without Proteolytic Enzyme Treatment. *Cell Transplant* **19**, 1123–1132 (2010).
363. McKee, C. & Chaudhry, G. R. Advances and challenges in stem cell culture. *COLLOIDS AND SURFACES B-BIOINTERFACES* **159**, 62–77 (2017).
364. Rafiq, Q. A., Coopman, K. & Hewitt, C. J. Scale-up of human mesenchymal stem cell culture: current technologies and future challenges. *Curr Opin Chem Eng* **2**, 8–16 (2013).
365. Hervy, M. *et al.* Long Term Expansion of Bone Marrow-Derived hMSCs on Novel Synthetic Microcarriers in Xeno-Free, Defined Conditions. *PLoS One* **9**, (2014).
366. Rafiq, Q. A. *et al.* Qualitative and quantitative demonstration of bead-to-bead transfer with bone marrow-derived human mesenchymal stem cells on microcarriers: Utilising the phenomenon to improve culture performance. *Biochem Eng J* **135**, 11–21 (2018).
367. Panchalingam, K. M., Jung, S., Rosenberg, L. & Behie, L. A. Bioprocessing strategies for the large-scale production of human mesenchymal stem cells: a review. *Stem Cell Res Ther* **6**, (2015).
368. Tamura, A., Kobayashi, J., Yamato, M. & Okano, T. Thermally responsive microcarriers with optimal poly(N-isopropylacrylamide) grafted density for facilitating cell adhesion/detachment in suspension culture. *Acta Biomater* **8**, 3904–3913 (2012).
369. Zhang, J. *et al.* Thermo-responsive microcarriers based on poly(N-isopropylacrylamide). *Eur Polym J* **67**, 346–364 (2015).

370. Dabiri, S. M. H. *et al.* Multifunctional Thermoresponsive Microcarriers for High-Throughput Cell Culture and Enzyme-Free Cell Harvesting. *Small* **17**, 2103192 (2021).
371. Rodrigues, A. L. *et al.* Dissolvable Microcarriers Allow Scalable Expansion And Harvesting Of Human Induced Pluripotent Stem Cells Under Xeno-Free Conditions. *Biotechnol J* **14**, (2019).
372. Tamura, A., Kobayashi, J., Yamato, M. & Okano, T. Temperature-responsive poly(N-isopropylacrylamide)-grafted microcarriers for large-scale non-invasive harvest of anchorage-dependent cells. *Biomaterials* **33**, 3803–3812 (2012).
373. Dickinson, E. & Hong, S. T. Surface Coverage of β-Lactoglobulin at the Oil-Water Interface: Influence of Protein Heat Treatment and Various Emulsifiers. *J Agric Food Chem* **42**, 1602–1606 (1994).
374. Tavassoli, H. *et al.* Large-scale production of stem cells utilizing microcarriers: A biomaterials engineering perspective from academic research to commercialized products. *Biomaterials* **181**, 333–346 (2018).
375. dos Santos, F. F., Andrade, P. Z., da Silva, C. L. & Cabral, J. M. S. Bioreactor design for clinical-grade expansion of stem cells. *Biotechnol J* **8**, 644–654 (2013).
376. Nienow, A. W., Rafiq, Q. A., Coopman, K. & Hewitt, C. J. A potentially scalable method for the harvesting of hMSCs from microcarriers. *Biochem Eng J* **85**, 79–88 (2014).
377. Discher, D. E., Janmey, P. & Wang, Y. L. Tissue cells feel and respond to the stiffness of their substrate. *Science* vol. 310 1139–1143 Preprint at https://doi.org/10.1126/science.1116995 (2005).
378. Giaever, I. & Keese, C. R. *Behavior of Cells at Fluid Interfaces*. *Proc. NatL Acad. Sci. USA* vol. 80 (1983).
379. Keese, C. R. & Giaever, I. Cell growth on liquid microcarriers. *Science (1979)* **219**, 1448–1449 (1983).
380. Minami, K. *et al.* Suppression of Myogenic Differentiation of Mammalian Cells Caused by Fluidity of a Liquid-Liquid Interface. *ACS Appl Mater Interfaces* **9**, 30553–30560 (2017).
381. Kong, D., Nguyen, K. D. Q., Megone, W., Peng, L. & Gautrot, J. E. The culture of HaCaT cells on liquid substrates is mediated by a mechanically strong liquid-liquid interface. *Faraday Discuss* **204**, 367–381 (2017).
382. Kong, D. *et al.* Protein Nanosheet Mechanics Controls Cell Adhesion and Expansion on Low-Viscosity Liquids. *Nano Lett* **18**, 1946–1951 (2018).
383. Kong, D., Peng, L., Cio, S. Di, Novak, P. & Gautrot, J. E. Stem Cell Expansion and Fate Decision on Liquid Substrates Are Regulated by Self-Assembled Nanosheets. (2018) doi:10.1021/acsnano.8b03865.
384. Kong, D. X., Peng, L. H., Di Cio, S., Novak, P. & Gautrot, J. E. Stem Cell Expansion and Fate Decision on Liquid Substrates Are Regulated by Self-Assembled Nanosheets. *ACS Nano* **12**, 9206–9213 (2018).
385. Chu, L. & Robinson, D. K. Industrial choices for protein production by large-scale cell culture. *Current Opinion in Biotechnology* vol. 12 180–187 Preprint at https://doi.org/10.1016/S0958-1669(00)00197-X (2001).
386. Warikoo, V. *et al.* Integrated continuous production of recombinant therapeutic proteins. *Biotechnol Bioeng* **109**, 3018–3029 (2012).
387. Hacker, D. L., De Jesus, M. & Wurm, F. M. 25 years of recombinant proteins from reactor-grown cells - Where do we go from here? *Biotechnology*

Advances vol. 27 1023–1027 Preprint at https://doi.org/10.1016/j.biotechadv.2009.05.008 (2009).
388. Ulrich, T. A., Pardo, E. M. D. & Kumar, S. The Mechanical Rigidity of the Extracellular Matrix Regulates the Structure, Motility, and Proliferation of Glioma Cells. *Cancer Res* **69**, 4167–4174 (2009).
389. Chen, C. S., Mrksich, M., Huang, S., Whitesides, G. M. & Ingber, D. E. Geometric control of cell life and death. *Science (1979)* **276**, 1425–1428 (1997).
390. Dalby, M. J. *et al.* The control of human mesenchymal cell differentiation using nanoscale symmetry and disorder. *Nat Mater* **6**, 997–1003 (2007).
391. Saha, K. *et al.* Substrate Modulus Directs Neural Stem Cell Behavior. *Biophys J* **95**, 4426–4438 (2008).
392. Engler, A. J., Sen, S., Sweeney, H. L. & Discher, D. E. Matrix elasticity directs stem cell lineage specification. *Cell* **126**, 677–689 (2006).
393. Kim, S. N. *et al.* ECM stiffness regulates glial migration in Drosophila and mammalian glioma models. *DEVELOPMENT* **141**, 3233–3242 (2014).
394. Pelham, R. J. & Wang, Y. L. Cell locomotion and focal adhesions are regulated by substrate flexibility. *Proc Natl Acad Sci U S A* **94**, 13661–13665 (1997).
395. Tzvetkova-Chevolleau, T. *et al.* The motility of normal and cancer cells in response to the combined influence of the substrate rigidity and anisotropic microstructure. *Biomaterials* **29**, 1541–1551 (2008).
396. Yeung, T. *et al.* Effects of substrate stiffness on cell morphology, cytoskeletal structure, and adhesion. *Cell Motil Cytoskeleton* **60**, 24–34 (2005).
397. Keese, C. R. & Giaever, I. Cell growth on liquid interfaces: Role of surface active compounds. *Proceedings of the National Academy of Sciences* **80**, 5622–5626 (1983).
398. Keese, C. R. & Giaever, I. Cell Growth on Liquid Microcarriers. *Science (1979)* **219**, 1448–1449 (1983).
399. Kong, D. X. *et al.* Impact of the multiscale viscoelasticity of quasi-2D self-assembled protein networks on stem cell expansion at liquid interfaces. *Biomaterials* **284**, (2022).
400. Gardel, M. L., Schneider, I. C., Aratyn-Schaus, Y. & Waterman, C. M. Mechanical Integration of Actin and Adhesion Dynamics in Cell Migration. in *ANNUAL REVIEW OF CELL AND DEVELOPMENTAL BIOLOGY, VOL 26* (eds. Schekman, R., Goldstein, L. & Lehmann, R.) vol. 26 315–333 (2010).
401. Kong, D. *et al.* Protein Nanosheet Mechanics Controls Cell Adhesion and Expansion on Low-Viscosity Liquids. *Nano Lett* **18**, 1946–1951 (2018).
402. Chrysanthou, A., Kanso, H., Zhong, W., Shang, L. & Gautrot, J. E. Supercharged Protein Nanosheets for Cell Expansion on Bioemulsions. *bioRxiv 2022.06.21.497058* na (2022).
403. Jones, D. L. & Wagers, A. J. No place like home: anatomy and function of the stem cell niche. *Nat Rev Mol Cell Biol* **9**, 11–21 (2008).
404. Dalby, M. J., Gadegaard, N. & Oreffo, R. O. C. Harnessing nanotopography and integrin-matrix interactions to influence stem cell fate. *Nat Mater* **13**, 558–569 (2014).

405. Engler, A. J., Sen, S., Sweeney, H. L. & Discher, D. E. Matrix elasticity directs stem cell lineage specification. *Cell* **126**, 677–689 (2006).
406. Benoit, D. S. W., Schwartz, M. P., Durney, A. R. & Anseth, K. S. Small functional groups for controlled differentiation of hydrogel-encapsulated human mesenchymal stem cells. *Nat Mater* **7**, 816–823 (2008).
407. Dalby, M. J. *et al.* The control of human mesenchymal cell differentiation using nanoscale symmetry and disorder. *Nat Mater* **6**, 997–1003 (2007).
408. McMurray, R. J. *et al.* Nanoscale surfaces for the long-term maintenance of mesenchymal stem cell phenotype and multipotency. *Nat Mater* **10**, 637–644 (2011).
409. Pan, Z. *et al.* Particle-collision and porogen-leaching technique to fabricate polymeric porous scaffolds with microscale roughness of interior surfaces. *CHINESE JOURNAL OF POLYMER SCIENCE* **31**, 737–747 (2013).
410. Wang, P. Y. *et al.* Modulation of Human Mesenchymal Stem Cell Behavior on Ordered Tantalum Nanotopographies Fabricated Using Colloidal Lithography and Glancing Angle Deposition. *ACS Appl Mater Interfaces* **7**, 4979–4989 (2015).
411. Lee, J., Abdeen, A. A., Zhang, D. & Kilian, K. A. Directing stem cell fate on hydrogel substrates by controlling cell geometry, matrix mechanics and adhesion ligand composition. *Biomaterials* **34**, 8140–8148 (2013).
412. Chen, C. S., Mrksich, M., Huang, S., Whitesides, G. M. & Ingber, D. E. Geometric control of cell life and death. *Science (1979)* **276**, 1425–1428 (1997).
413. Wang, X., Li, S. Y., Yan, C., Liu, P. & Ding, J. D. Fabrication of RGD Micro/Nanopattern and Corresponding Study of Stem Cell Differentiation. *Nano Lett* **15**, 1457–1467 (2015).
414. Peng, R., Yao, X. & Ding, J. D. Effect of cell anisotropy on differentiation of stem cells on micropatterned surfaces through the controlled single cell adhesion. *Biomaterials* **32**, 8048–8057 (2011).
415. Yao, X., Peng, R. & Ding, J. D. Effects of aspect ratios of stem cells on lineage commitments with and without induction media. *Biomaterials* **34**, 930–939 (2013).
416. Cao, B., Li, Z. H., Peng, R. & Ding, J. D. Effects of cell-cell contact and oxygen tension on chondrogenic differentiation of stem cells. *Biomaterials* **64**, 21–32 (2015).
417. Peng, R., Yao, X., Cao, B., Tang, J. & Ding, J. D. The effect of culture conditions on the adipogenic and osteogenic inductions of mesenchymal stem cells on micropatterned surfaces. *Biomaterials* **33**, 6008–6019 (2012).
418. Tang, J., Peng, R. & Ding, J. D. The regulation of stem cell differentiation by cell-cell contact on micropatterned material surfaces. *Biomaterials* **31**, 2470–2476 (2010).
419. Frantz, C., Stewart, K. M. & Weaver, V. M. The extracellular matrix at a glance. *Journal of Cell Science* vol. 123 4195–4200 Preprint at https://doi.org/10.1242/jcs.023820 (2010).
420. Di Cio, S. & Gautrot, J. E. Cell sensing of physical properties at the nanoscale: Mechanisms and control of cell adhesion and phenotype. *Acta*

Biomaterialia vol. 30 26–48 Preprint at https://doi.org/10.1016/j.actbio.2015.11.027 (2016).
421. Assoian, R. K. & Klein, E. A. Growth control by intracellular tension and extracellular stiffness. *Trends Cell Biol* **18**, 347–352 (2008).
422. Lee-Thedieck, C., Rauch, N., Fiammengo, R., Klein, G. & Spatz, J. P. Impact of substrate elasticity on human hematopoietic stem and progenitor cell adhesion and motility. *J Cell Sci* **125**, 3765–3775 (2012).
423. Leight, J. L., Wozniak, M. A., Chen, S., Lynch, M. L. & Chen, C. S. Matrix rigidity regulates a switch between TGF-beta 1-induced apoptosis and epithelial-mesenchymal transition. *Mol Biol Cell* **23**, 781–791 (2012).
424. Gilbert, P. M. *et al.* Substrate Elasticity Regulates Skeletal Muscle Stem Cell Self-Renewal in Culture. *Science (1979)* **329**, 1078–1081 (2010).
425. Trappmann, B. *et al.* Extracellular-matrix tethering regulates stem-cell fate. *Nat Mater* **11**, 642–649 (2012).
426. Connelly, J. T. *et al.* Actin and serum response factor transduce physical cues from the microenvironment to regulate epidermal stem cell fate decisions. *Nat Cell Biol* **12**, 711-U177 (2010).
427. Dupont, S. *et al.* Role of YAP/TAZ in mechanotransduction. *Nature* **474**, 179-U212 (2011).
428. Geiger, B., Spatz, J. P. & Bershadsky, A. D. Environmental sensing through focal adhesions. *Nature Reviews Molecular Cell Biology* vol. 10 21–33 Preprint at https://doi.org/10.1038/nrm2593 (2009).
429. Roca-Cusachs, P., Gauthier, N. C., Del Rio, A. & Sheetz, M. P. Clustering of α5β1 integrins determines adhesion strength whereas αvβ3 and talin enable mechanotransduction. *Proc Natl Acad Sci U S A* **106**, 16245–16250 (2009).
430. Galbraith, C. G., Yamada, K. M. & Sheetz, M. P. The relationship between force and focal complex development. *Journal of Cell Biology* **159**, 695–705 (2002).
431. Balaban, N. Q. *et al. Force and focal adhesion assembly: a close relationship studied using elastic micropatterned substrates*. *NATURE CELL BIOLOGY* vol. 3 (2001).
432. Balaban, N. Q. *et al.* Force and focal adhesion assembly: A close relationship studied using elastic micropatterned substrates. *Nat Cell Biol* **3**, 466–472 (2001).
433. Van Hoorn, H. *et al.* The nanoscale architecture of force-bearing focal adhesions. *Nano Lett* **14**, 4257–4262 (2014).
434. Moore, S. W., Roca-Cusachs, P. & Sheetz, M. P. Stretchy proteins on stretchy substrates: The important elements of integrin-mediated rigidity sensing. *Developmental Cell* vol. 19 194–206 Preprint at https://doi.org/10.1016/j.devcel.2010.07.018 (2010).
435. Engler, A. J., Sen, S., Sweeney, H. L. & Discher, D. E. Matrix Elasticity Directs Stem Cell Lineage Specification. *Cell* **126**, 677–689 (2006).
436. Dalby, M. J., Gadegaard, N. & Oreffo, R. O. C. Harnessing nanotopography and integrin-matrix interactions to influence stem cell fate. *Nat Mater* **13**, 558–569 (2014).
437. Chaudhuri, O. *et al.* Hydrogels with tunable stress relaxation regulate stem cell fate and activity. *Nat Mater* **15**, 326–334 (2016).

438. Murphy, W. L., McDevitt, T. C. & Engler, A. J. Materials as stem cell regulators. *Nature Materials* vol. 13 547–557 Preprint at https://doi.org/10.1038/nmat3937 (2014).
439. Wang, Y. & Xia, Y. Bottom-up and top-down approaches to the synthesis of monodispersed spherical colloids of low melting-point metals. *Nano Lett* **4**, 2047–2050 (2004).
440. Geissler, M. & Xia, Y. Patterning: Principles and some new developments. *Advanced Materials* vol. 16 1249–1269 Preprint at https://doi.org/10.1002/adma.200400835 (2004).
441. Yim, E. K. F. *et al.* Nanopattern-induced changes in morphology and motility of smooth muscle cells. *Biomaterials* **26**, 5405–5413 (2005).
442. Murrell, M., Kamm, R. & Matsudaira, P. Substrate Viscosity Enhances Correlation in Epithelial Sheet Movement. *Biophys J* **101**, 297–306 (2011).
443. Discher, D. E., Janmey, P. & Wang, Y. L. Tissue cells feel and respond to the stiffness of their substrate. *Science (1979)* **310**, 1139–1143 (2005).
444. Chaudhuri, O. *et al.* Substrate stress relaxation regulates cell spreading. *Nat Commun* **6**, (2015).
445. Chaudhuri, O. *et al.* Hydrogels with tunable stress relaxation regulate stem cell fate and activity. *Nat Mater* **15**, 326-+ (2016).
446. Attwood, S. J. *et al.* Adhesive ligand tether length affects the size and length of focal adhesions and influences cell spreading and attachment. *Sci Rep* **6**, (2016).
447. Moore, S. W., Roca-Cusachs, P. & Sheetz, M. P. Stretchy Proteins on Stretchy Substrates: The Important Elements of Integrin-Mediated Rigidity Sensing. *Dev Cell* **19**, 194–206 (2010).
448. Khetan, S. *et al.* Degradation-mediated cellular traction directs stem cell fate in covalently crosslinked three-dimensional hydrogels. *Nat Mater* **12**, 458–465 (2013).
449. Huebsch, N. *et al.* Harnessing traction-mediated manipulation of the cell/matrix interface to control stem-cell fate. *Nat Mater* **9**, 518–526 (2010).
450. Jia, X. *et al.* Adaptive Liquid Interfacially Assembled Protein Nanosheets for Guiding Mesenchymal Stem Cell Fate. *Advanced Materials* **32**, 1905942 (2020).
451. Cull, M. G. & Schatz, P. J. [26] Biotinylation of proteins in vivo and in vitro using small peptide tags. *Methods Enzymol* **326**, 430–440 (2000).
452. Cull, M. G. & Schatz, P. J. Biotinylation of proteins in vivo and in vitro using small peptide tags. *Methods Enzymol* **326**, 430–440 (2000).
453. SnapGene | Software for everyday molecular biology. https://www.snapgene.com/.
454. Peng, L. *et al.* Mesenchymal Stem Cells Sense the Toughness of Nanomaterials and Interfaces. *Adv Healthc Mater* **12**, 2203297 (2023).
455. STEMdiff™ Cerebral Organoid Kit Culture medium kit for establishment and maturation of human cerebral organoids.
456. Wilde, P., Mackie, A., Husband, F., Gunning, P. & Morris, V. Proteins and emulsifiers at liquid interfaces. *Adv Colloid Interface Sci* **108–109**, 63–71 (2004).

457. Dickinson, E. Adsorbed protein layers at fluid interfaces: interactions, structure and surface rheology. *Colloids Surf B Biointerfaces* **2**, 161–176 (1999).
458. Zhu, W. *et al.* High level expression and purification of recombinant human serum albumin in Pichia pastoris. *Protein Expr Purif* **147**, 61–68 (2018).
459. Kobayashi, K. *et al.* High level secretion of recombinant human serum albumin by fed-batch fermentation of the methylotrophic yeast, Pichia pastoris, based on optimal methanol feeding strategy. *J Biosci Bioeng* **90**, 280–288 (2000).
460. Murasugi, A. Secretory expression of human protein in the Yeast Pichia pastoris by controlled fermentor culture. *Recent Pat Biotechnol* **4**, 153–166 (2010).
461. Simossis, V. A. & Heringa, J. PRALINE: a multiple sequence alignment toolbox that integrates homology-extended and secondary structure information. *Nucleic Acids Res* **33**, W289–W294 (2005).
462. Mücksch, C. & Urbassek, H. M. Molecular dynamics simulation of free and forced BSA adsorption on a hydrophobic graphite surface. *Langmuir* **27**, 12938–12943 (2011).
463. Mücksch, C. & Urbassek, H. M. Forced Desorption of Bovine Serum Albumin and Lysozyme from Graphite: Insights from Molecular Dynamics Simulation. *J Phys Chem B* **120**, 7889–7895 (2016).
464. Singh, D. K., Sanghi, S. K., Gowri, S., Chandra, N. & Sanghi, S. B. Determination of aliphatic amines by gas chromatography-mass spectrometry after in-syringe derivatization with pentafluorobenzoyl chloride. *J Chromatogr A* **1218**, 5683–5687 (2011).
465. Schrödinger LLC. *The PyMOL Molecular Graphics System, Version~1.8*. (2015).
466. Simard, J. R. *et al.* Locating high-affinity fatty acid-binding sites on albumin by x-ray crystallography and NMR spectroscopy. *Proc Natl Acad Sci U S A* **102**, 17958–17963 (2005).
467. Studier, F. W. & Moffatt, B. A. Use of bacteriophage T7 RNA polymerase to direct selective high-level expression of cloned genes. *J Mol Biol* **189**, 113–130 (1986).
468. Francis, D. M. & Page, R. Strategies to Optimize Protein Expression in E. coli. *Curr Protoc Protein Sci* **61**, 5241 (2010).
469. Miroux, B. & Walker, J. E. Over-production of proteins in Escherichia coli: mutant hosts that allow synthesis of some membrane proteins and globular proteins at high levels. *J Mol Biol* **260**, 289–298 (1996).
470. Vogl, T., Gebbie, L., Palfreyman, R. W. & Speight, R. Effect of Plasmid Design and Type of Integration Event on Recombinant Protein Expression in Pichia pastoris. *Appl Environ Microbiol* **84**, (2018).
471. Kurjan, J. & Herskowitz, I. Structure of a yeast pheromone gene (MF alpha): a putative alpha-factor precursor contains four tandem copies of mature alpha-factor. *Cell* **30**, 933–943 (1982).
472. Lin-Cereghino, G. P. *et al.* The Effect of α-Mating Factor Secretion Signal Mutations on Recombinant Protein Expression in Pichia pastoris. *Gene* **519**, 311 (2013).

473. Brake, A. J. *et al.* Alpha-factor-directed synthesis and secretion of mature foreign proteins in Saccharomyces cerevisiae. *Proc Natl Acad Sci U S A* **81**, 4642–4646 (1984).
474. Thermofisher Scientific. GeneArt Services. https://www.thermofisher.com/order/geneart-dashboard/index.html.
475. GenScript. Rare Codon Analysis Tool. https://www.genscript.com/tools/rare-codon-analysis.
476. Kumar, A. & Kaur, J. Primer Based Approach for PCR Amplification of High GC Content Gene: Mycobacterium Gene as a Model. *Mol Biol Int* **2014**, 1–7 (2014).
477. Peyret, N., Seneviratne, P. A., Allawi, H. T. & SantaLucia, J. Nearest-neighbor thermodynamics and NMR of DNA sequences with internal A.A, C.C, G.G, and T.T mismatches. *Biochemistry* **38**, 3468–3477 (1999).
478. Breslauer, K. J., Frank, R., Blocker, H. & Marky, L. A. Predicting DNA duplex stability from the base sequence. *Proc Natl Acad Sci U S A* **83**, 3746 (1986).
479. Pemberton, I. K., Buc, H. & Buckle, M. Displacement of Viral DNA Termini from Stable HIV-1 Integrase Nucleoprotein Complexes Induced by Secondary DNA-Binding Interactions †. (1998).
480. Technologies, L. Pichia Expression Kit, MAN0000012, RevA.00.
481. pPIC9K A Pichia Vector for Multicopy Integration and Secreted Expression Catalog no. V175-20. (2010).
482. Lin-Cereghino, J. *et al.* Direct selection of Pichia pastoris expression strains using new G418 resistance vectors. *Yeast* **25**, 293–299 (2008).
483. Von Allmen, C. & Lindner, P. Transformation protocol, Protocol No. 4308 915.545 –03/2004.
484. User Manual EasySelect ™ Pichia Expression Kit For Expression of Recombinant Proteins Using pPICZ and pPICZα in Pichia pastoris. (2010).
485. Kumar, R. Simplified protocol for faster transformation of (a large number of) Pichia pastoris strains. *Yeast* **36**, 399–410 (2019).
486. Becker, D. M. & Guarente, L. High-efficiency transformation of yeast by electroporation. *Methods Enzymol* **194**, 182–187 (1991).
487. Suga, M. & Hatakeyama, T. High efficiency transformation of Schizosaccharomyces pombe pretreated with thiol compounds by electroporation. *Yeast* **18**, 1015–1021 (2001).
488. Minning, S. *et al.* Optimization of the high-level production of Rhizopus oryzae lipase in Pichia pastoris. *J Biotechnol* **86**, 59–70 (2001).
489. Anasontzis, G. E., Penã, M. S., Spadiut, O., Brumer, H. & Olsson, L. Effects of temperature and glycerol and methanol-feeding profiles on the production of recombinant galactose oxidase in Pichia pastoris. *Biotechnol Prog* **30**, 728–735 (2014).
490. Babcock, J. J. & Brancaleon, L. Bovine serum albumin oligomers in the E- and B-forms at low protein concentration and ionic strength. *Int J Biol Macromol* **53**, 42 (2013).
491. Jumper, J. *et al.* Highly accurate protein structure prediction with AlphaFold. *Nature 2021 596:7873* **596**, 583–589 (2021).
492. Cull, M. G. & Schatz, P. J. [26] Biotinylation of proteins in vivo and in vitro using small peptide tags. *Methods Enzymol* **326**, 430–440 (2000).
493. Fairhead, M. & Howarth, M. Site-specific biotinylation of purified proteins using BirA. *Methods Mol Biol* **1266**, 171 (2015).

494. Reaction conditions for BirA biotin ligase 1 Basic INSTRUCTIONS FOR USE.
495. Jain, J., Veggiani, G. & Howarth, M. Cholesterol loading and ultrastable protein interactions determine the level of tumor marker required for optimal isolation of cancer cells. *Cancer Res* **73**, 2310–2321 (2013).
496. Sato, T., Terao, K., Teramoto, A. & Fujiki, M. Molecular properties of helical polysilylenes in solution. *Polymer (Guildf)* **44**, 5477–5495 (2003).
497. Sorenson, A. E., Askin, S. P. & Schaeffer, P. M. In-gel detection of biotin–protein conjugates with a green fluorescent streptavidin probe. *Analytical Methods* **7**, 2087–2092 (2015).
498. Wang, G., De Jong, R. N., Van Den Bremer, E. T. J., Parren, P. W. H. I. & Heck, A. J. R. Enhancing Accuracy in Molecular Weight Determination of Highly Heterogeneously Glycosylated Proteins by Native Tandem Mass Spectrometry. *Anal Chem* **89**, 4793–4797 (2017).
499. Tegel, H., Tourle, S., Ottosson, J. & Persson, A. Increased levels of recombinant human proteins with the Escherichia coli strain Rosetta(DE3). *Protein Expr Purif* **69**, 159–167 (2010).
500. Lobstein, J. *et al.* SHuffle, a novel Escherichia coli protein expression strain capable of correctly folding disulfide bonded proteins in its cytoplasm. *Microb Cell Fact* **11**, 1–16 (2012).
501. Green, N. M. Avidin. *Adv Protein Chem* **29**, 85–133 (1975).
502. Moore, R., Radice, G. L., Dominis, M. & Kemler, R. The generation and in vivo differentiation of murine embryonal stem cells genetically null for either N-cadherin or N- and P-cadherin. *INTERNATIONAL JOURNAL OF DEVELOPMENTAL BIOLOGY* **43**, 831–834 (1999).
503. Åkerström, B., Brodin, T., Reis, K. & Björck, L. Protein G: a powerful tool for binding and detection of monoclonal and polyclonal antibodies. *Journal of immunology* **135**, 2589–2592 (1985).
504. Shevde, N. K. & Mael, A. A. Techniques in embryoid body formation from human pluripotent stem cells. *Methods Mol Biol* **946**, 535–546 (2013).
505. Javier-Torrent, M., Zimmer-Bensch, G. & Nguyen, L. Mechanical Forces Orchestrate Brain Development. *Trends Neurosci* **44**, 110–121 (2021).
506. Kerstein, P. C., Nichol, R. H. & Gomez, T. M. Mechanochemical regulation of growth cone motility. *Front Cell Neurosci* **9**, 244 (2015).
507. Delmas, P., Hao, J. & Rodat-Despoix, L. Molecular mechanisms of mechanotransduction in mammalian sensory neurons. *Nature Reviews Neuroscience 2011 12:3* **12**, 139–153 (2011).
508. Sun, Z., Costell, M. & Fässler, R. Integrin activation by talin, kindlin and mechanical forces. *Nature Cell Biology 2019 21:1* **21**, 25–31 (2019).
509. Fu, M. *et al.* The Hippo signalling pathway and its implications in human health and diseases. *Signal Transduction and Targeted Therapy 2022 7:1* **7**, 1–20 (2022).
510. Srivastava, N., Traynor, D., Piel, M., Kabla, A. J. & Kay, R. R. Pressure sensing through Piezo channels controls whether cells migrate with blebs or pseudopods. *Proc Natl Acad Sci U S A* **117**, 2506–2512 (2020).
511. He, L., Si, G., Huang, J., Samuel, A. D. T. & Perrimon, N. Mechanical regulation of stem-cell differentiation by the stretch-activated Piezo channel. *Nature 2018 555:7694* **555**, 103–106 (2018).
512. Woo, S. H. *et al.* Piezo2 is required for Merkel-cell mechanotransduction. *Nature 2014 509:7502* **509**, 622–626 (2014).

513. Pathak, M. M. *et al.* Stretch-activated ion channel Piezo1 directs lineage choice in human neural stem cells. *Proc Natl Acad Sci U S A* **111**, 16148–16153 (2014).
514. Mueller, K. A. *et al.* Hippo Signaling Pathway Dysregulation in Human Huntington's Disease Brain and Neuronal Stem Cells. *Sci Rep* **8**, 11355 (2018).
515. Ha, J. *et al.* Simplified Brain Organoids for Rapid and Robust Modeling of Brain Disease. *Front Cell Dev Biol* **8**, (2020).
516. Zaltsman, Y., Masuko, S., Bensen, J. J. & Kiessling, L. L. Angiomotin Regulates YAP Localization during Neural Differentiation of Human Pluripotent Stem Cells. *Stem Cell Reports* **12**, 869–877 (2019).
517. Zhang, H., Deo, M., Thompson, R. C., Uhler, M. D. & Turner, D. L. Negative regulation of Yap during neuronal differentiation. *Dev Biol* **361**, 103–115 (2012).
518. Cao, X., Pfaff, S. L. & Gage, F. H. YAP regulates neural progenitor cell number via the TEA domain transcription factor. *Genes Dev* **22**, 3320–3334 (2008).
519. Lavado, A. *et al.* The Hippo Pathway Prevents YAP/TAZ-Driven Hypertranscription and Controls Neural Progenitor Number. *Dev Cell* **47**, 576-591.e8 (2018).
520. Tse, J. D. *et al.* Dynamic conversion of cell sorting patterns in aggregates of embryonic stem cells with differential adhesive affinity. *BMC Dev Biol* **21**, 1–15 (2021).
521. Larue, L. *et al.* A role for cadherins in tissue formation. *DEVELOPMENT* **122**, 3185–3194 (1996).
522. Pain, B., Baquerre, C. & Coulpier, M. Cerebral organoids and their potential for studies of brain diseases in domestic animals. *Vet Res* **52**, 1–12 (2021).
523. Gotz, M. & Huttner, W. B. The cell biology of neurogenesis. *Nat Rev Mol Cell Biol* **6**, 777–788 (2005).
524. Kawaguchi, A. Neuronal Delamination and Outer Radial Glia Generation in Neocortical Development. *Front Cell Dev Biol* **8**, 623573 (2021).
525. Pollen, A. A. *et al.* Molecular Identity of Human Outer Radial Glia during Cortical Development. *Cell* **163**, 55–67 (2015).
526. Smart, I. H. M., Dehay, C., Giroud, P., Berland, M. & Kennedy, H. Unique morphological features of the proliferative zones and postmitotic compartments of the neural epithelium giving rise to striate and extrastriate cortex in the monkey. *Cereb Cortex* **12**, 37–53 (2002).
527. Lewitus, E., Kelava, I. & Huttner, W. B. Conical expansion of the outer subventricular zone and the role of neocortical folding in evolution and development. *Front Hum Neurosci* **7**, (2013).
528. Takeichi, M. The cadherin superfamily in neuronal connections and interactions. *Nat Rev Neurosci* **8**, 11–20 (2007).
529. Takeichi, M. Functional correlation between cell adhesive properties and some cell surface proteins. *J Cell Biol* **75**, 464–474 (1977).
530. Takeichi, M. The cadherins: cell-cell adhesion molecules controlling animal morphogenesis. *Development* **102**, 639–655 (1988).
531. Hirano, S. & Takeichi, M. Cadherins in brain morphogenesis and wiring. *Physiol Rev* **92**, 597–634 (2012).

532. Miyamoto, Y., Sakane, F. & Hashimoto, K. N-cadherin-based adherens junction regulates the maintenance, proliferation, and differentiation of neural progenitor cells during development. *Cell Adh Migr* **9**, 183 (2015).
533. Morita, H. *et al.* Nectin-2 and N-cadherin interact through extracellular domains and induce apical accumulation of F-actin in apical constriction of Xenopus neural tube morphogenesis. *Development* **137**, 1315–1325 (2010).
534. Hatta, K. & Takeichi, M. Expression of N-cadherin adhesion molecules associated with early morphogenetic events in chick development. *Nature* **320**, 447–449 (1986).
535. Hirai, Y., Nose, A., Kobayashi, S. & Takeichi, M. Expression and role of E- and P-cadherin adhesion molecules in embryonic histogenesis. II. Skin morphogenesis. *Development* **105**, 271–277 (1989).
536. Rai, S., Leydier, L., Sharma, S., Katwala, J. & Sahu, A. A quest for genetic causes underlying signaling pathways associated with neural tube defects. *Front Pediatr* **11**, 1126209 (2023).
537. Peng, L. & Gautrot, J. E. Growth of Mesenchymal Stem Cells at the Surface of Silicone, Mineral and Plant-Based Oils. *bioRxiv* *2022.08.17.504254* na (2022).
538. Scheraga, H. A. The thrombin-fibrinogen interaction. *Biophys Chem* **112**, 117–130 (2004).
539. Retzinger, G. S., DeAnglis, A. P. & Patuto, S. J. Adsorption of Fibrinogen to Droplets of Liquid Hydrophobic Phases. *Arterioscler Thromb Vasc Biol* **18**, 1948–1957 (1998).
540. Adamczyk, Z., Bratek-Skicki, A., Zeliszewska, P. & Wasilewska, M. Mechanisms of Fibrinogen Adsorption at Solid Substrates. *Curr Top Med Chem* **14**, 702–729 (2014).
541. Wu, X. *et al.* Adsorption properties of albumin and fibrinogen on hydrophilic/hydrophobic TiO2 surfaces: A molecular dynamics study. *Colloids Surf B Biointerfaces* **207**, 111994 (2021).
542. Rowe, S. L., Lee, S. Y. & Stegemann, J. P. Influence of Thrombin Concentration on the Mechanical and Morphological Properties of Cell-seeded Fibrin Hydrogels. *Acta Biomater* **3**, 59 (2007).
543. Milyaeva, O. Y. & Rafikova, A. R. Effect of Low Concentrations of Thrombin on the Dynamic Surface Properties of Fibrinogen Solutions. *Colloid Journal* **84**, 55–63 (2022).
544. Milyaeva, O. Y. & Rafikova, A. R. Dynamic Surface Properties of Fibrin. *Colloid Journal* **85**, 423–432 (2023).
545. Hardy, J. G., Römer, L. M. & Scheibel, T. R. Polymeric materials based on silk proteins. *Polymer (Guildf)* **49**, 4309–4327 (2008).
546. MacQueen, L., Sun, Y. & Simmons, C. A. Mesenchymal stem cell mechanobiology and emerging experimental platforms. *J R Soc Interface* **10**, (2013).